NANOCOMPOSITE SCINTILLATORS FOR NEUTRON CAPTURE MEASUREMENTS

by

Sy Stange

A dissertation submitted in partial fulfillment
of the requirements for the degree of
Doctor of Philosophy
(Nuclear Science)
in The University of Michigan
2011

Doctoral Committee:

        Ernst-Ingo Esch, Los Alamos National Laboratory, Co-Chair
        Professor James Paul Holloway, Co-Chair
        Professor Rachel S. Goldman
        Professor Zhong He

For my parents

ACKNOWLEDGEMENTS

Andy Li has been both a wonderful friend and a valued colleague throughout this process, and I hope that he and I can continue to work together for many years. Melissa Shear is another wonderful friend; she and her family have repeatedly opened their home and their lives to me, and I am grateful. Andrew Cole has provided comic relief and another perspective on getting a doctorate. Conversations with Rebecca Lehman have been a much-needed break. The congregation at the Los Alamos Jewish Center has been interested and helpful throughout the last few years - their endless questions about when I would finish were understood as expressions of support, never pressure.

I need to reach further back in time to thank three more people. When I left the graduate program in plasma physics, I considered leaving science altogether. Sam Cohen gave me a job in his lab that allowed me to begin seeing myself as a scientist again, and forced me to consider spending time at Los Alamos. Jaeyoung Park showed me how fun science could be, and bent over backward to support and help me in applying to graduate school again, without ever pressuring me to do so. And finally, reaching back all the way to my undergraduate days, Stephen Kumar Gregory

remains the best professor I have ever had in my entire, stretched-out, academic career.

I cannot close this section without thanking my family. The enthusiasm and interest shown by Mom, Dad, Bridget, Bill, Alex, Annie, Ben, Heather, and Chris in my work, even when it was hard to understand, has been greatly appreciated. They have put up with my very infrequent visits and preoccupation. I hope to be able to repay all their kindness by spending more time with them, as well as with Amelia and Hudson, in the years to come.

TABLE OF CONTENTS

LIST OF FIGURES

LIST OF TABLES

LIST OF APPENDICES

Appendix

LIST OF ABBREVIATIONS

3HF 3-hydroxyflavone

AFCI Advanced Fuel Cycle Initiative

ASTAR Stopping-Power and Range Tables for Helium Ions

BaF$_2$ barium fluoride

BGO bismuth germanate

CCD charge-coupled device

CeF$_3$ cerium fluoride

CERN European Organization for Nuclear Research

CMS Compact Muon Solenoid

DANCE Detector for Advanced Neutron Capture Experiments

ESTAR Stopping-Power and Range Tables for Electrons

FWHM full width at half maximum

IFMIF International Fusion Materials Irradiation Facility

ITER International Thermonuclear Experimental Reactor

LANSCE Los Alamos Neutron Science Center

LHC Large Hadron Collider

MaRIE Matter-Radiation Interactions in Extremes

MIDAS Maximum Integration Data Acquisition System

NIH National Institutes of Health

NIST National Institute of Standards and Technology

n_TOF neutron Time of Flight

ORELA Oak Ridge Electron Linear Accelerator

PET positron emission tomography

PL photoluminescence spectroscopy

PMT photomultiplier tube

POPOP 1,4-bis(5-phenyloxazol-2-yl)benzene

PPO 2,5-diphenyloxazol

QDC charge-to-digital converter

RL radioluminescence spectroscopy

SRIM Stopping and Range of Ions in Matter

TBP tributyl phosphate

TEM transmission electron microscopy

UV ultraviolet

UV/Vis ultraviolet/visible spectroscopy

WNR Weapons Neutron Research

XRD x-ray diffraction

CHAPTER I

Introduction

Scintillation, or the emission of light from a material that has been struck by radiation, is perhaps the most commonly used method of detecting and characterizing radiation, particularly γ-rays. Scintillating materials are used in laboratories and at accelerators to identify the particles produced in nuclear physics experiments, at border crossings and in the field to detect radioactive materials as part of nonproliferation and security applications, and in hospitals to form images of the body for diagnosing disease.

The interaction of ionizing radiation with a material results in charged particles. The precise methods by which these particles interact with the material vary, but in general, in a scintillator the charged particles create a small amount of light in the process of losing the energy they received from the incident radiation. This light may be collected, amplified, and converted to an electronic signal. Scintillators are an especially useful type of radiation detector because the amount of light emitted is proportional to the energy deposited by the radiation. Since the energy of an incident γ-ray is characteristic of the isotope emitting it, the identity of the radioactive material may thus be determined from the energies of the detected γ-rays.

Both organic scintillators, which are made up of carbon-based compounds, and inorganic scintillators, which consist of single crystals of an inorganic material, are commonly used. Inorganic scintillators have superior resolution and efficiency, but the crystal growth process is time-consuming and prone to defects, so inorganic scintillators are expensive and many are not readily available in large sizes.

Nanocomposite scintillators, consisting of crystals less than 10 nm in diameter suspended in a matrix, are of interest because they may have better resolution and efficiency than organic scintillators, but without the difficulties and expense involved in growing conventional inorganic scintillators. Due to the small size of the nanoparticles, light scattering should be small, allowing for better transmission of scintillation

light than has been observed in composite scintillators incorporating larger particles. They may also make it possible to utilize inorganic scintillating materials that are not currently available in large sizes or quantities.

This document describes the characterization of two novel scintillators: a liquid scintillator loaded with cerium fluoride (CeF_3) nanoparticles for the detection of neutron-capture γ-rays and a liquid scintillator loaded with fissionable material for neutron detection. Both scintillators were prepared as proofs of principle for nanocomposite systems.

The CeF_3 scintillator was intended to detect the γ-rays resulting from neutron capture in nuclear physics experiments. When a neutron is captured on a nucleus of the target, it transfers energy to the nucleus. The nucleus releases some of that energy by emitting γ-rays. Detecting these γ-rays is necessary to determine the cross-section of neutron capture. Every nuclear reaction has a cross-section, or probability of occurring, which depends on the energy of the incoming neutron. Knowing the cross-section for neutron capture is important for a number of areas of scientific research, including improving our understanding of the early universe and interpreting data from nuclear weapons tests. Since the CeF_3-loaded liquid scintillator was the first scintillator incorporating nanoparticles to be characterized in our laboratory, its development was also an opportunity to determine which characterization tools provided the most information about its structural, optical, and radiation-detection properties.

The fissionable scintillator was conceived as a neutron flux monitor for nuclear physics applications. In order to accurately determine the cross-section of any neutron-induced reaction, it is necessary to know the neutron flux, or the rate at which neutrons pass through the target. Unlike the CeF_3 scintillator, the proposed nanoparticles for the fissionable scintillator were not required to scintillate. Instead, they were chosen because they undergo induced fission when struck by a neutron. When the nucleus of a fissionable atom absorbs a neutron, it can change shape and deform until it splits into two pieces. These pieces, the fission fragments, then deposit energy in the liquid scintillator that serves as a matrix material, causing scintillation.

This work begins in Chapter II by discussing in greater detail the concept of a nanocomposite scintillator and the potential applications of the CeF_3-loaded and fissionable scintillators. Chapter III then describes the development and characterization of the liquid scintillator used as a matrix, or material in which the nanoparticles could be suspended, for both systems, as well as the process of fabricating CeF_3 nanoparticles and suspending them in the liquid scintillator. The suite of techniques

used to characterize the structural, optical, and radiation-response properties of the scintillators and the analysis of their data are discussed in Chapter IV. Chapter V contains the results of the characterization of CeF_3 scintillators. It also discusses the development of a CeF_3-loaded detector for experiments performed in a neutron beam line and the results of those experiments. Chapter VI describes the optical and radiation-response characterization of two different fissionable scintillators and the selection of a fissionable molecular complex for incorporation into a detector for beam line experiments. The results of beam line experiments on the fissionable scintillator are given in Chapter VII. Finally, Chapter VIII summarizes the results of the characterization and beam line experiments on both scintillators and suggests directions for future research.

CHAPTER II

Experimental Motivation

2.1   Measurement of Neutron Capture Cross-Sections

Neutron capture cross-sections are often measured using the neutron time-of-flight method at experiments such as DANCE (the Detector for Advanced Neutron Capture Experiments at Los Alamos National Laboratory) and n_TOF (the neutron Time of Flight facility at the European Organization for Nuclear Research (CERN)). [Esc08a] [Abb02] These experiments are designed as a 4π configuration of detectors surrounding a target, as shown in Figure 2.1. Neutrons that are captured in the target excite nuclei, which emit γ-rays in the form of a γ-cascade when they de-excite. The de-excitation energy, or Q-value, is the difference between the masses of the incident neutron and the nucleus before neutron capture and the mass of the nucleus after neutron capture,

$$Q = m_n c^2 + m(A, Z)c^2 - m(A + 1, Z)c^2 \tag{2.1}$$

where m_n is the neutron mass, $m(A, Z)$ is the mass of the target nucleus before neutron capture, and $m(A + 1, Z)$ is the mass of the target nucleus after neutron capture.

The de-excitation energy is typically between 4 and 10 MeV and is a unique value for each isotope. It is emitted in the form of a γ-cascade, multiple γ-rays (usually between 3 and 6) whose total energy sums to Q. [Cou07] Although the Q-value is a constant for each isotope, there are numerous possible combinations of γ-ray energies that can occur. Figure 2.2 shows a generalized and simplified version of two steps in the process. The nucleus may transition from its excited state, with energy $E(A + 1, Z)^*$, to any allowed energy level, as shown by the arrows on the left side of Figure 2.2. This energy transition takes place through the emission of a γ-ray. The right side of Figure 2.2 shows one possible subsequent step, the permitted decays from
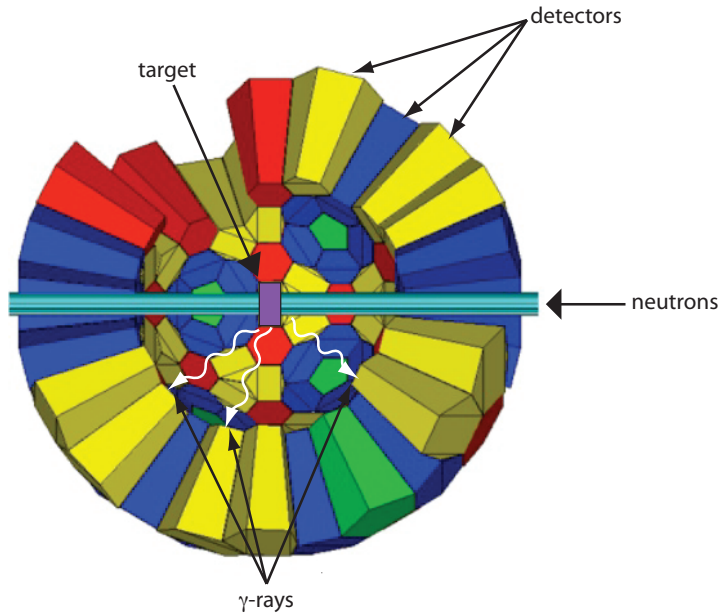
Figure 2.1: The DANCE detector array. A 4π arrangement of BaF_2 detectors surrounding a target (purple). The pale blue line indicates the beam path. Neutron capture events in the target result in the emission of γ-rays. Four different detector shapes are used, indicated by different colors, but all have the same solid angle. [Hei99]

the highest intermediate energy level. The large number of possible combinations of γ-rays means that there is no single characteristic γ-ray emitted following neutron capture. In order to identify a neutron capture event, the entire γ-cascade must be detected so that the Q-value can be accurately calculated. Therefore, neutron capture experiments require a detector array whose solid angle approaches 4π.

The neutron's energy is measured using the time-of-flight technique. This involves using the time the neutron travels to reach the target to determine the its velocity, and hence its kinetic energy. The time of neutron generation is indicated by a signal from the accelerator, while the time the neutron arrives at the target is determined by detecting the γ-cascade. The neutron's velocity and energy are then calculated from this time-of-flight. For example, the distance neutrons travel to reach the target at DANCE is 20.25 m. [Ull05] The neutrons used to measure cross-sections at DANCE have energies from 10 meV to 500 keV. [Esc08a] Therefore, the 500 keV neutrons, which have a velocity of $0.03c$, arrive in 2.25 μs and the 10 meV neutrons, which have a velocity of only $4.6 \times 10^{-6}c$, arrive in 14.6 ms.

Although DANCE and n_TOF are designed with 4π arrays of detector crystals, in
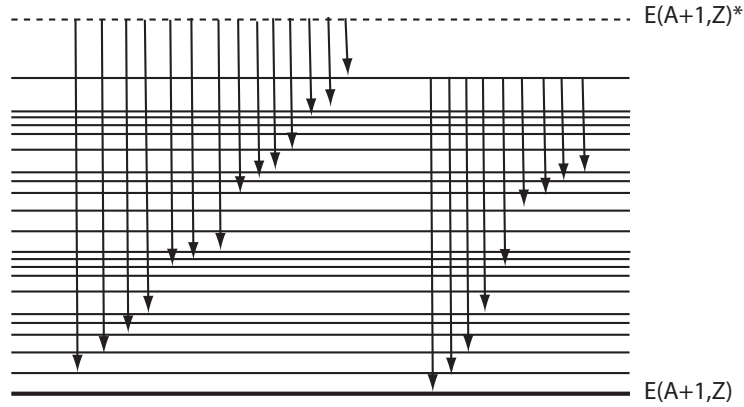
Figure 2.2: Generalized and simplified diagram showing permitted energy levels and transitions of an excited nucleus following neutron capture. The excited nucleus, with energy $E(A+1,Z)^*$, can emit γ-rays that cascade down to the ground state ($E(A+1,Z)$) through any combination of allowed energy states. The left side of the figure shows permitted transitions from the excited state. If the first γ-ray emitted by the nucleus decreases its energy to that of the highest intermediate level, the possible transitions from that level are shown on the right. There are many combinations of γ-rays that sum to the Q-value.

both cases the actual solid angle is less than 4π. Both arrays leave out two crystals to allow the neutron beam to enter and exit, using only 40 of the 42 designed, in the case of n_TOF, and 160 of the 162 designed, in the case of DANCE. [Abb03] [Ull05] In addition, at DANCE the crystals were designed to form a shell with an inner radius of 17 cm, but had to be moved outward by 1 cm to allow for wrapping. [Esc08a] The combination of the larger radius and the removal of two of the crystals reduces the effective solid angle to 3.52π, a loss of 12% of the original solid angle.

Many modern neutron capture cross-section experiments, including n_TOF and DANCE, use spallation neutrons. [Abb03] [Rei04] In spallation, a burst of protons from an accelerator collides with nuclei of a heavy-metal spallation target. A proton deposits its energy through collisions in the nucleons of the nucleus, resulting in the ejection of nucleons and the excitation of the nucleus. In de-exciting, the nucleus emits more particles, the majority of them neutrons, until its excitation energy drops below the nucleon binding energy. [Ler99] It has been calculated that an average of 20 neutrons are produced for each 800 MeV incident proton at the Los Alamos Neutron Science Center (LANSCE). [Lis90] The remaining excitation energy is emitted as α, β,

and γ radiation. Since these γ-rays, called the γ-flash, travel at the speed of light, they reach the experiment target before any neutrons (in the case of DANCE, in 67.5 ns) and can Compton scatter into the detectors. The γ-flash saturates the detectors and causes pile-up in the data acquisition system, preventing the detection of neutron capture γ-rays. In addition, a neutron capture event cannot be definitively identified until enough time has elapsed to ensure that a detected γ-ray does not belong to the γ-flash. The time that must elapse before neutron capture measurements can be made depends on the decay time of the signal generated in a detector by a γ-ray.

The response of a scintillation detector to a typical spallation pulse is shown in Figure 2.3. The arrival of the γ-flash, visible at *Peak Time*= 0, causes pileup in the digitizer because there is insufficient time for the scintillator's light pulse to fully decay before the arrival of the next γ-ray. The voltage settings that the data acquisition software uses to detect the beginning and end of a peak are determined based on the baseline output, so until the light output of the scintillator decays almost completely, no new peaks can be detected. Therefore, the entire γ-flash and the higher-energy neutrons are grouped into a single event, which in Figure 2.3 begins at 0 μs and ends near 70 μs. The baseline does not return to its original value until near 120 μs, however, so events between 70 μs and 120 μs also produce pileup, resulting in fewer detected pulses than expected.

A neutron capture detector must have high γ-efficiency to maximize the probability of capturing all the γ-rays of the γ-cascade. The detector must also have a low sensitivity to neutrons, since it will be placed in a neutron-rich environment. Finally, the detector must have a fast signal decay time. Both DANCE and n_TOF use barium fluoride (BaF_2), whose signal decays with a 0.6 ns fast component and a 630 ns slow component, as shown in Figure 2.4. [Hei00][Abb02] The long time required to collect photons from the slow component of the decay, which contains 80% of the total photons produced, gives the detector a recovery time that limits it to measuring target samples with half-lives greater than a few hundred days.

This limit arises in part from the increased neutron flux needed to measure short-lived targets, which results in a larger gamma flash, and in part from the limit on the number of atoms of a radioisotope that can be used as a target. The limit on the number of atoms is derived from the maximum number of events that can be tolerated by the detectors. In addition to events resulting from neutron capture, a large number of events are also generated in the detectors as the target decays. These decay events present a problem because random coincidence γ-rays make it difficult to identify neutron capture events. Existing neutron capture experiments are also limited by
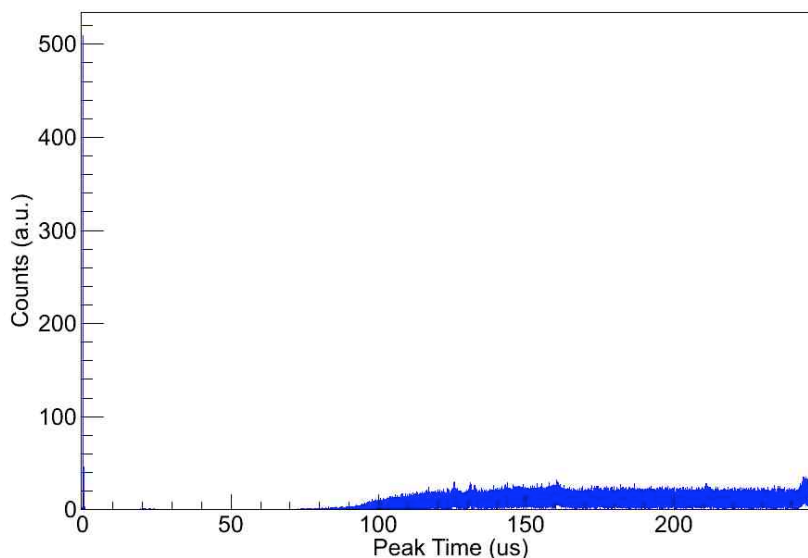
Figure 2.3: Response of a scintillation detector to a spallation pulse. The arrival of the γ-flash is shown at 0 μs. Due to pileup from γ-rays, the detector signal does not return to its baseline value until more than 100 μs later. During this time, the data acquisition system is unable to identify pulses, since they are offset from the expected baseline, so no data is collected. This data was taken at LANSCE as part of the experiments discussed in Chapter V.

the number of atoms that can be used as a target. The flux required to measure the neutron capture cross-sections of a number of radioisotopes of astrophysical interest has been calculated by Couture and Reifarth, and is shown graphically in Figure 2.5. [Cou07]

The red circles in Figure 2.5 represent radioisotopes for which no neutron capture cross-section measurements have been performed, while the white circles represent radioisotopes for which some data (not necessarily complete) has been taken. Comparing the flux required for the measurement (indicated by the y-axis) with the capabilities of existing neutron capture experiments makes the limitations of current facilities obvious. Even DANCE, which at 3×10^5 n/s/cm^2/decade has the highest neutron flux of existing experiments, is unable to measure the neutron capture cross-sections of many short-lived isotopes of interest to the nuclear astrophysics community, among them ^{95}Zr (64 days), ^{147}Nd (11 days), and ^{185}W (75 days). [Lug03][Rei03][Son03] Neutron capture cross-section measurements are also needed to calculate criticality and waste production estimates for the Advanced Fuel Cycle Initiative (AFCI) (^{238,239}Np (2 days) and ^{237}U (11 days)) and to continue radiochemical interpretation of debris
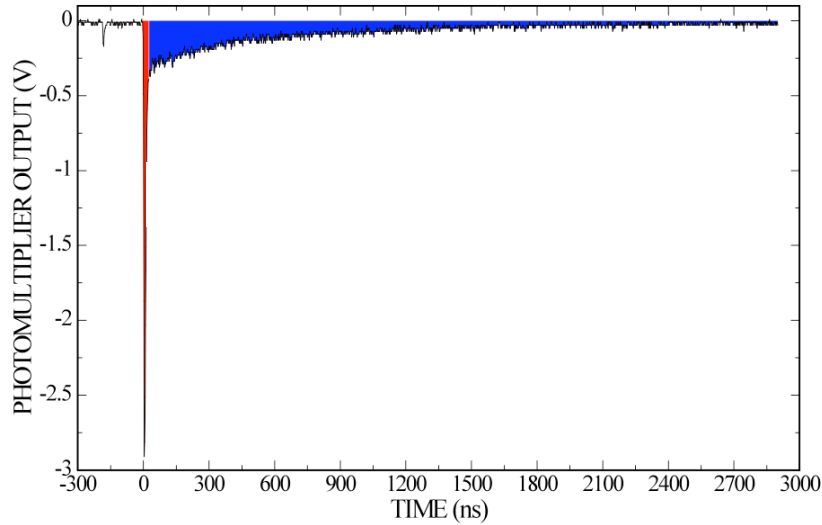
Figure 2.4: Pulse from BaF_2 scintillator, with fast component (decay time 0.6 ns) in red and slow component (decay time 630 ns) in blue. [Esc08b]

from nuclear weapons tests. [Ali06] One way of increasing the neutron flux that can be used at a facility would be to select a detector material with a faster decay time (and therefore a shorter recovery time) than BaF_2.

2.2   Early Development of Cerium Fluoride

The scintillation properties of cerium fluoride (CeF_3) were discovered two decades ago almost simultaneously by D.F. Anderson [And89] and by W.W. Moses and S.E. Derenzo [Mos89], while testing crystals supplied by Optovac of North Brookfield, MA. Like BaF_2, the scintillation pulse from CeF_3 has a two-component decay, but with a fast component of 3 ns and a slow component of 27 ns. CeF_3 was immediately identified as a good candidate material for applications requiring a scintillator with a fast decay time and high density.

2.2.1   Cerium Fluoride for Medical Physics

One potential application was positron emission tomography (PET). In PET, a positron-emitting radionuclide is introduced into the body. Positrons annihilate

9
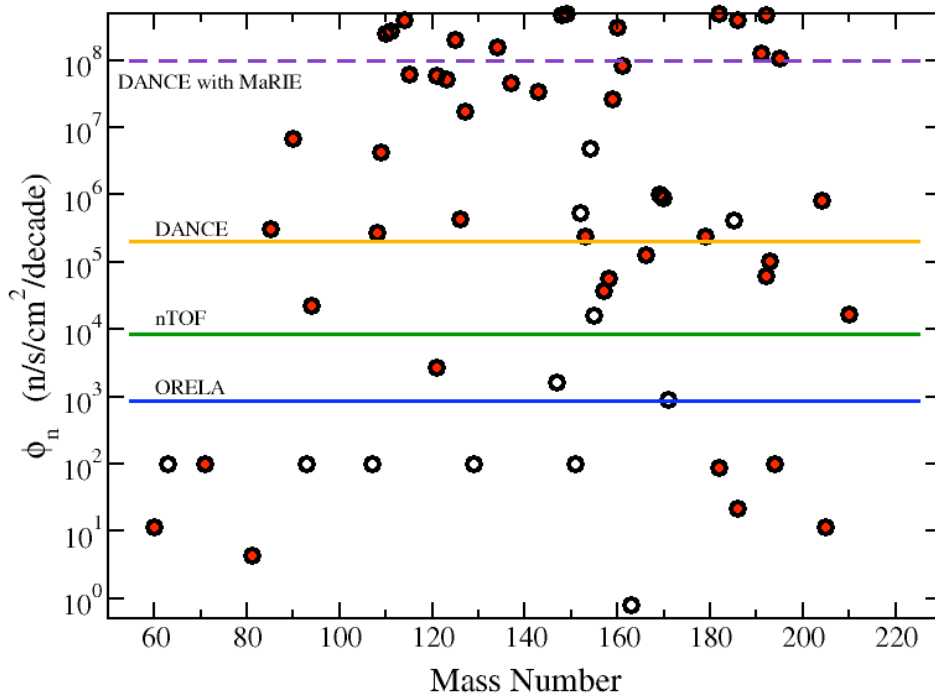
Figure 2.5: Required flux for neutron capture cross-section measurements. White circles indicate measurements for which some data has been taken; red circles indicate measurements for which no data exists. Solid lines show the highest neutron flux achievable by existing neutron capture experiments DANCE, n_TOF, and the Oak Ridge Electron Linear Accelerator (ORELA). The dashed line shows the predicted highest neutron flux achievable by DANCE utilizing the proposed Matter-Radiation Interactions in Extremes (MaRIE) facility. Figure provided by A.J. Couture using [Cou07].

within a short distance, producing two γ-rays traveling at 180° relative to one another. The detection of these coincident γ-rays allows the user to identify a positron decay event. The ideal detector for PET must therefore have high efficiency and a quickly-decaying scintillation light pulse, in addition to good time and energy resolution. [Dow06]

Bismuth germanate ($Bi_4Ge_3O_{12}$, BGO) was then and remains until today the most commonly used scintillator for PET due to its high intrinsic efficiency and probability of photoelectric effect. [vE02] However, its 300 ns decay time limits the rate at which coincident γ-rays can be detected. The faster decay time of CeF_3 made it a possible alternative to BGO for high-rate PET, despite its lower density and poorer light yield.

	CeF_3	BaF_2	CsF	BGO
Density	6.16	4.89	4.61	7.13
Radiation Length [cm]	1.7	2.1	2.6	1.1
Decay Constant [ns]				
short	5	0.6	5	300
long	30	620		
Peak Emission [nm]				
short	310	220	390	480
long	340	310		
Index of Refraction				
(at peak emission)	1.68	1.56	1.48	2.15
Light Yield				
(NaI(Tl) = 100)	4-5	5	4	7-10

Table 2.1: Properties of CeF_3 and related scintillators [All80][And90][Chi94]

[And90]

In addition, at the time CeF_3 was discovered there was interest in time-of-flight PET techniques, which use the interval between the detection of the coincident γ-rays to more precisely locate the positron-emitting isotope. [Mul81] The faster decay times of CsF (cesium fluoride) and the fast component of BaF_2, compared with BGO, drew early interest despite their lower stopping power. [All80][Won84] In the case of BaF_2, the RC timing constant of the photomultiplier tube resulted in the production of distinct pulse shapes by the fast and slow components of the scintillation light, enabling the fast pulses to be separated and utilized. [Won84] However, the 225 nm wavelength of the fast emission of BaF_2 required expensive quartz photomultiplier tubes (PMTs).

CeF_3 was suggested as a slightly slower alternative to BaF_2 whose 310 nm fast emission could likely be detected using less costly borosilicate glass PMTs. [And89] Experiments found, though, that the energy resolution at 511 keV (the annihilation photon energy) using borosilicate glass was only 57%, compared with 30% for quartz and 27% for ultraviolet (UV) glass. [Miy94] In addition, simulations of the coincidence sensitivity of BGO and CeF_3 indicated that in order to achieve a sensitivity of 92% relative to BGO it was necessary to increase the length of the CeF_3 crystal by 50% and increase the energy threshold from 150 keV to 350 keV. Due to its lack of superior performance compared with BaF_2, CsF, and BGO, research into CeF_3 for time-of-flight PET was soon abandoned. Shortly afterwards, research into BaF_2 and CsF for this application was halted as well, as the high stopping power of BGO made it the industry standard. [Mos06]

2.2.2 Cerium Fluoride for Calorimetry

Calorimetry for high-energy physics experiments was quickly identified as a possible application for CeF_3. [And89] Interest was primarily focused on the electromagnetic calorimeter for the Compact Muon Solenoid (CMS) experiment for the Large Hadron Collider (LHC) at CERN. The LHC was predicted to require a scintillator with excellent energy resolution, small granularity, good photon angle measurement capability, radiation hardess, and a fast signal decay time. [Sch94] The first three of these properties can be achieved by careful design, engineering, and manufacturing, but the radiation hardness and signal decay time can only be controlled through crystal selection. NaI:Tl, CsI:Tl, and BGO had been used in previous high-energy calorimeters, but their radiation hardness and signal decay speed were insufficient for the proposed LHC calorimeter. BaF_2 had been proposed for use at the Semiconducting Supercollider, but its slow component and mediocre density disqualified it from consideration at the LHC. [Cry96a]

Simulations indicated that the electromagnetic calorimeter in the CMS would experience extremely high radiation doses, up to 4 Mrad/y in its forward region. The calculated maximum hadron dose was equivalent to 3.6×10^{13} one-MeV neutrons/cm^2. [Aar93] Thus, the radiation hardness of candidate scintillator materials for the electromagnetic calorimeter, including CeF_3, became a topic of great interest to the high energy physics community. Early research into the radiation hardness of CeF_3 showed a 4.8% loss in transmission per unit radiation length at 375 nm for a dose of 10^7 rad, comparable that observed in BaF_2, and 19% per unit radiation length for 10^8 rad. [Maj87][Kob91] The photoluminescence spectrum appeared unchanged after the full 10^8 rad dose.

The Crystal Clear Collaboration, in their extensive study of the optical and radiation properties of CeF_3 crystals, also examined the effect of high-dose γ-radiation (10^5 rad). [Cry93] The purest of the irradiated crystals showed no damage, as indicated by a lack of change to the photoluminescence spectrum or the light yield, at these doses, consistent with earlier research. [Kob91] However, the less pure crystals developed several absorption bands. The Crystal Clear Collaboration also irradiated a CeF_3 crystal at a low dose (120 rad/h) typical of that expected for the LHC, up to an accumulated dose of 530 ± 110 krad, with no damage.

Tests of the effects of neutron irradiation, a substitute for the expected hadron irradiation from the LHC, were also performed on CeF_3 crystals. [Cry93] Measurements of the effect of neutron irradiation up to an integrated fluence of 2×10^{13} cm^{-2} on transmission showed no effect on one crystal and resulted in a 25% decrease in

transmission in the ultraviolet region in another. After performing more extensive neutron irradiation experiments, Chipaux et al. concluded that CeF_3 crystals were resistant to neutron damage from fluences up to 5×10^{13} cm^{-2}. [Chi94]

The performance of CeF_3 crystal arrays in high-energy particle beams was found to be suitable for high-energy physics experiments. [Cry96b] However, lead tungstate ($PbWO_4$) rather than CeF_3 was selected as the CMS scintillator because of its very high density and economical production. [Bay94] In addition, the useful properties of the small CeF_3 crystals were difficult to reproduce in larger crystals, and it proved to be difficult to grow long crystals with reproducible results. [Cry96a] [Ina00]

2.3   Recent Work on Cerium Fluoride

Following the 1994 decision to use $PbWO_4$, rather than CeF_3, in the CMS calorimeter, the pace of research on CeF_3 slowed. [Bay94] However, the high-energy physics community retained an interest in the potential of CeF_3 for future calorimeters, provided large crystals with reproducible results could be grown. [Cry96a]

CeF_3 has become the focus of calorimetry research again in recent years, as it has become apparent that $PbWO_4$ suffers cumulative damage in response to the type of high-energy hadron interactions expected at the LHC. [Huh05] For proton fluence rates above 10^{12} cm^{-2}, the light transmission though the crystals decreases significantly. The transmission of one $PbWO_4$ crystal dropped from over 70% at 700 nm before irradiation, to about 65% after 1.3×10^{13} cm^{-2} and to about 40% after 5.4×10^{13} cm^{-2}. The transmission falls off even more dramatically at lower wavelengths. The lowest wavelength at which light is transmitted is 350 nm before irradiation, 375 nm after 1.3×10^{13} cm^{-2}, and 400 nm after 5.4×10^{13} cm^{-2}. This is very different from the effect of γ-irradiation, which causes a decrease in transmission but does not affect location of the band edge.

2.4   Nanocomposite Scintillators

Nanocomposite scintillators consist of nanoscale (<100 nm diameter) particles of a scintillating material suspended in a matrix material. [McK07b] This concept combines two areas of scintillator research: composite scintillators and nanoparticle scintillators.

2.4.1 Composite Scintillators

Composite scintillators have typically been proposed as novel neutron detectors. They were first developed in the early 1950s. The first composite consisted of ZnS (zinc sulfide) powder molded into a Lucite matrix. [Hor52] The efficiencies observed were greater than those of contemporary neutron detectors using ZnS. [Mou49] However, the efficiency was severely limited for mass loadings over 6% due to the opacity of the detectors. This was attributed to the amount of ZnS powder used, but research by our team suggests that the large size of the powder (8-25 μm) was a more likely cause. [McK07b] A variation on the ZnS composite detector involved suspending the powder in heated liquid paraffin, then allowing the paraffin to cool and solidify while shaking constantly to ensure that the powder remained evenly dispersed. [Emm54] Higher mass loadings and higher efficiencies were achieved using this method, but the detector thickness was still limited by the opacity of the composite, and neither method of producing a ZnS composite scintillator was readily scalable to larger sizes. [Kub88]

In the past two decades, several other groups have tested composite scintillators using particles with sizes <100 μm. [Kub88] [Vas03] [Vas04] [Bud07a] [Bud07b] [Wal07] [Gal09] These scintillators have typically displayed good pulse-shape discrimination potential, efficiency, and neutron sensitivity. However, their thickness is limited by short light attenuation lengths.

2.4.2 Nanoparticle Scintillators

The potential uses of nanoparticle scintillators have attracted attention in recent years, as an alternative to the expensive and difficult processes required to grow large single crystals. [An02] [Dai02] The material properties of nanoparticles, which often differ from those of the bulk material, also make them attractive foci of basic and applied research. [McK07a] In particular, differences between the luminescence of scintillator nanoparticles and the luminescence of microparticles and bulk quantities have been the subject of a great deal of research in recent years.

The luminescence lifetime in nanoparticles is longer than in microparticles. [Mel99] In addition, the luminescence intensity depends on particle size, with the luminescence efficiency increasing inversely with the particle size, even for particles with sizes as small as a few nanometers in diameter. [Erd95][Gol97] Using nanoscale particles, as opposed to microscale particles, should give the detectors long optical attenuation lengths, as shown in Figure 2.6, and eliminate the need for index matching. [McK07b]
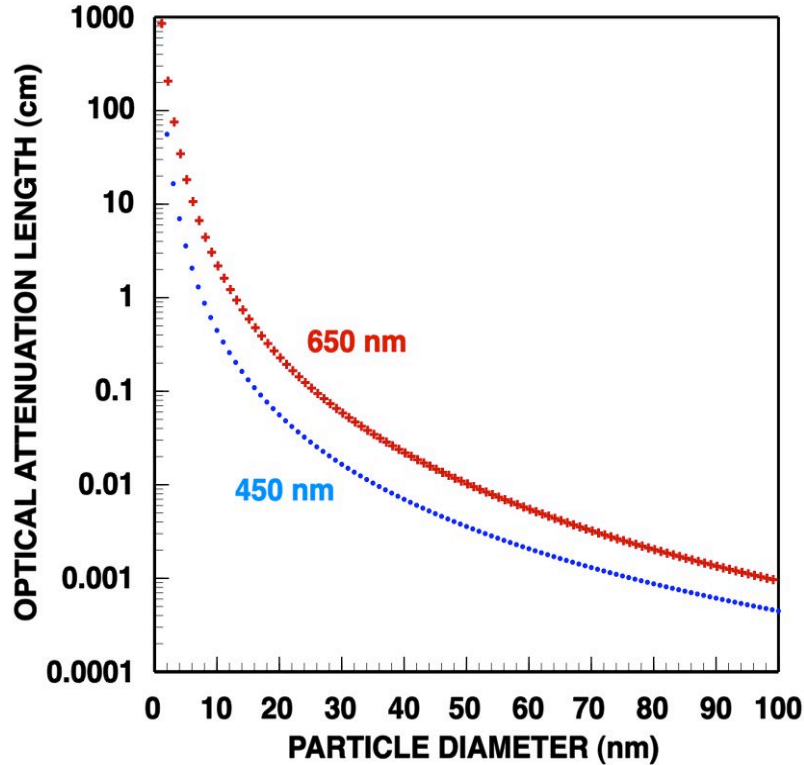
Figure 2.6: Optical attenuation length at two wavelengths as a function of nanoparticle diameter. The short optical attenuation lengths observed in composite scintillators result from the large particle sizes. To optimize the attenuation, scintillator particles should be less than 10 nm in diameter. [McK07b]

2.5   Cerium Fluoride Nanocomposite Detectors for Neutron Capture Measurements

One area of research described in this work is the development of a CeF_3 nanocomposite detector. Due to their faster signal decay time, detectors made of CeF_3 could accurately detect neutron capture γ-rays from short-lived radioisotopes whose neutron capture cross-sections cannot be measured using BaF_2. However, CeF_3 single-crystal detectors are not currently available in large sizes or quantities. This problem could be circumvented through the use of a nanocomposite detector. The goal of this work was to produce CeF_3 nanocrystals, characterize their structural, optical, and radiation detection properties, load them into a matrix material, and test their response to beam line neutrons.

2.6 The Scintillation Process in Inorganic Scintillators

The scintillation behavior of inorganic materials arises from the crystal structure. In a crystalline material, the quantum levels of the outermost electrons in an atom are perturbed by the nearness of other electrons. The quantum levels spread out, becoming bands of allowed states separated by forbidden bands in which electrons are not found. The highest-energy filled band, known as the valence band, is the source of scintillation electrons. When an electron in the valence band absorbs energy, such as that from incident radiation, it may be excited into the empty band above the forbidden band, known as the conduction band, as shown in Figure 2.7. This results in not only a free electron, but also a free hole in the valence band. Alternatively, the electron may be excited into the exciton band, a set of states slightly below the bottom of the conduction band, and remain bound to its hole. The electron-hole pair is called an exciton and may travel freely through the crystal. [Leo94]

Luminescence results from the transfer of the electron back to the valence band. However, luminescence in the visible range requires the presence of an impurity, an excess ion of one of the atoms composing the crystal, or a defect in the pure crystal. [Bir64] Any of these may introduce permitted energy states, or centers, in the otherwise forbidden band. When an electron and hole recombine in one of these centers, they de-excite to the ground state energy through either a radiationless transition or the emission of a photon. Electrons and holes may also fall into separate metastable states, called traps, from which there are no direct radiation-producing transitions to the valence band. Rather, electrons may be excited back into the conduction band through the acquisition of thermal energy or may undergo a radiationless transition to the valence band. [Bir64]

Many of the crystals most commonly used as scintillators possess luminescence centers due to the presence of impurities. Examples are thallium-doped sodium iodide and cesium-iodide and cerium-doped lanthanium chloride and lanthanum bromide.

2.7 The Scintillation Process in Organic Scintillators

The scintillation of conjugated and aromatic organic compounds arises from their electron configurations, which are determined by quantum mechanics. The Pauli exclusion principle states that no two fermions may have the same quantum numbers. [Pau25] An electron has one quantum number associated with its spin, with two possible values ($+1/2$ or $-1/2$), so only two electrons, one with each quantum number,
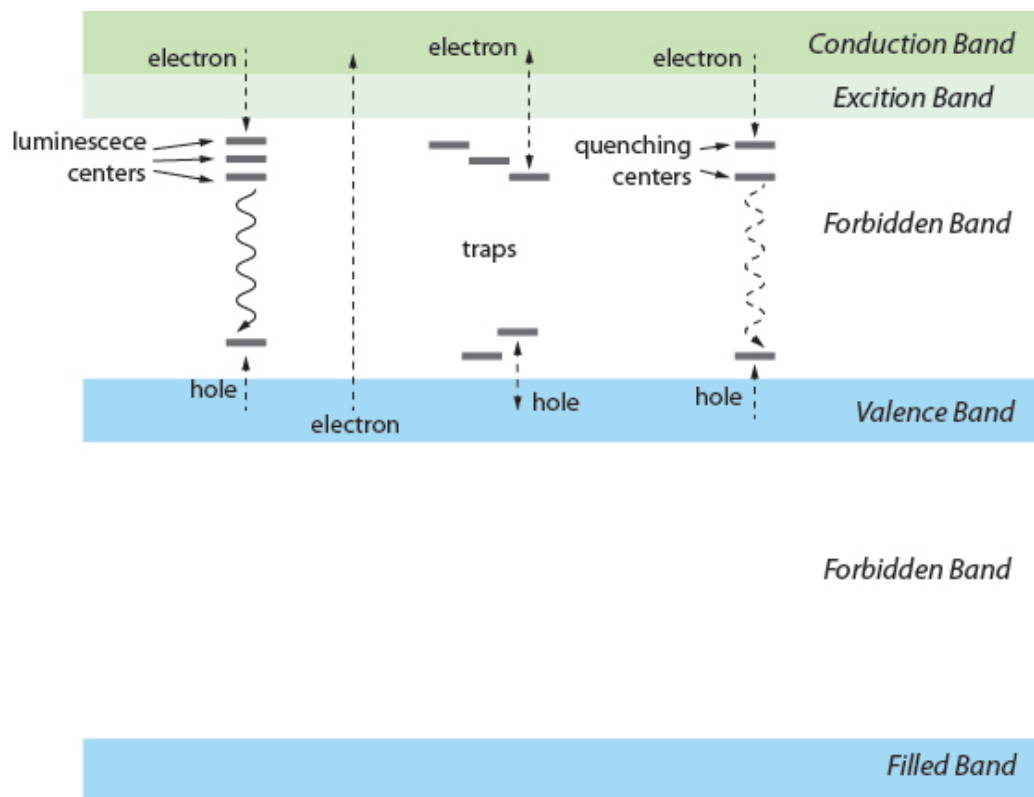
Figure 2.7: Possible transitions between energy bands in an inorganic crystal. Electrons in the valence band may be excited into the conduction band, leaving behind holes, or may be excited to the exciton band and remain bound to their holes. Excited electrons travel freely in the conduction band, and may return to the valence band by combining with a hole at a luminescence or quenching center. Both electrons and holes may also become trapped in metastable levels.

may exist in one orbital. Carbon has six electrons. The first two electrons are placed in the lowest orbital, the $1s$ shell. The next two are placed in the next orbital, the $2s$ shell. The final two electrons of carbon go into the $2p$ shell. Thus, the ground state of carbon has a $1s^2 2s^2 2p^2$ configuration. However, the $2p$ shell can actually contain up to six electrons (two each in the $2p_x$, $2p_y$, and $2p_z$ shells) because its quantum function exists on three planes. Hence, a bound carbon atom can be considered to have a configuration of $1s^2 2s^1 2p^3$, with one electron from the $2s$ shell excited into the $2p$ shell. In an organic molecule, the $2s$ and $2p$ orbitals combine to form hybrid orbitals in three possible configurations, two of which can lead to scintillation. [Str76]

In the sp^3 configuration, four hybrid orbitals form on the corners of a hypothetical tetraheron. In the sp^2 configuration, two p orbitals and the single s orbital combine to form three hybrid orbitals at angles of $120°$. These orbitals are called σ-electrons.

17

The remaining p orbital is called a π-electron. Due to its presence, the carbon atom forms a double bond. In the sp configuration, two σ-orbitals form at angles of $180°$ to one another. The remaining two π-orbitals form a triple bond. [Bir70]

Since π-electrons are not strongly bound to an atom, they are more easily excited. The absorption of energy excites a π-electron in the singlet ground state, S_0, into one of the singlet excited states, shown in Figure 2.8 as S_1, S_2, and S_3. As shown in Figure 2.8, each state may have multiple vibrational levels, and an electron may be excited into any of them, but excitation takes place only from equilibrium of the ground state. [Bir64] Electrons that are excited into the S_2, S_3, and higher singlet states undergo radiationless transition to lower singlet states or the ground state. The prompt luminescence, or fluorescence, of an organic molecule results only from radiation-producing transitions between the S_1 and S_0 states. Since the vibrational period is 4-5 orders of magnitude smaller than the lifetime of the first excited state, S_1, the electron will always reach equilibrium before de-exciting, but may transfer to any of the ground vibrational states. [Bir64] Transitions between S_1 and the vibrational states of S_0 are indicated by peaks in the observed optical luminescence.

Electron excitation directly into a triplet state from S_0 is spin-forbidden. However, when the energy states of a singlet level overlap with those of a triplet level an electron may undergo intersystem crossing into the triplet state. Intersystem crossing occurs most commonly between the lowest excited singlet and triplet states, S_1 and T_1, as shown in Figure 2.8. [Kas50] From T_1, the electron may return to the singlet ground state. [Lew44] The radiation emitted during this process is called phosphorescence and has a longer lifetime than fluorescence, tens of milliseconds or longer as compared with nanoseconds or tens of nanoseconds. [Bir64] Electrons in T_1 or another triplet state may also gain enough thermal energy to return to the singlet states, in which case the wavelength of the subsequent luminescence is identical to that seen in fluorescence, but the emission time is several orders of magnitude longer.

An organic scintillator system may consist of one or several luminescent molecules. The liquid scintillator that was formulated and characterized as a part of this work was a ternary system, utilizing two organic dyes in toluene. In a binary, ternary, or higher-order organic scintillator system, the primary observed luminescence is that of the component having the highest-wavelength emission. However, the rise-time or decay time of the luminescence may be slightly longer than that of the emitting component alone, due to the time required for energy transfer between the scintillator components.

When incident radiation deposits energy in an organic scintillating molecule, the
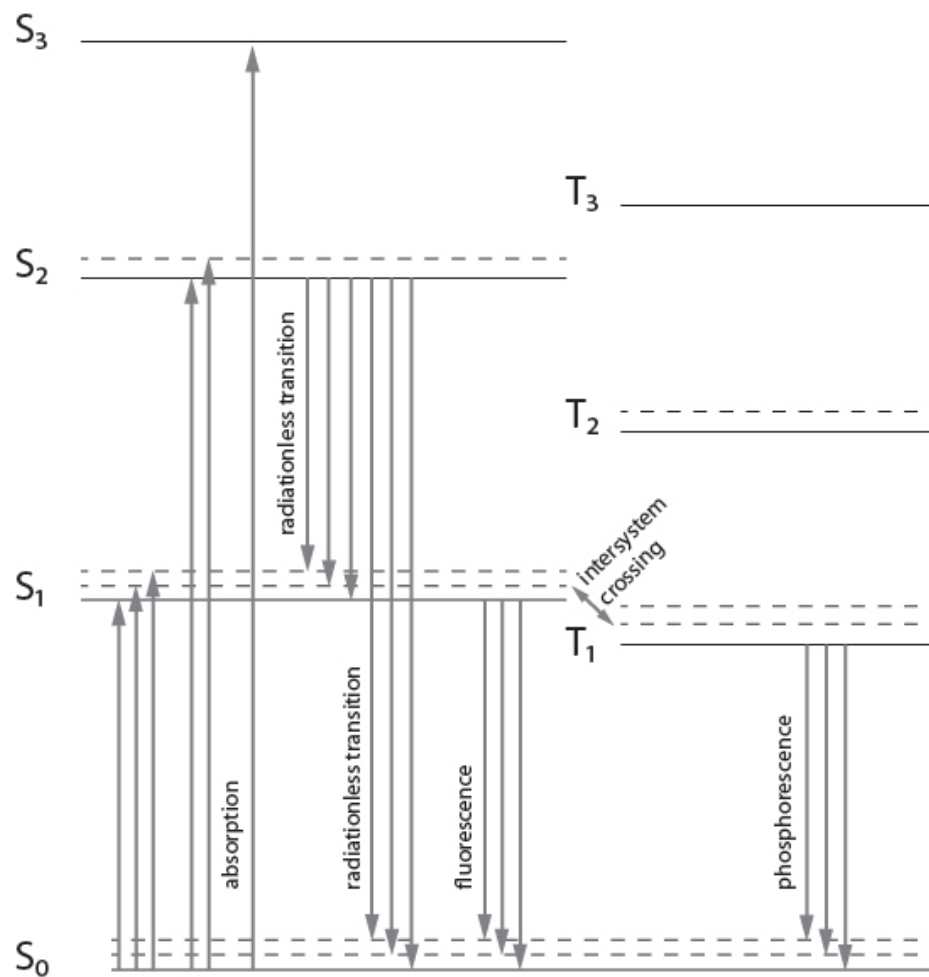
Figure 2.8: Generalized energy level diagram for π-electrons in an organic molecule. Absorbed energy from incident radiation excites electrons from the singlet ground state, S_0, to the singlet excited states. From the singlet states, electrons may undergo intersystem crossing to triplet states. Not all possible transitions are shown. Figure based on Birks. [Bir64]

fraction of that energy that is converted to scintillation light depends on the mass of the incident particle. As the energy of a massive particle decreases, it becomes subject to ionization quenching, in which the number of molecules that may be excited by the particle is reduced because a large proportion of the surrounding molecules have already been ionized or excited. Ionization quenching affects all massive particles, but becomes more pronounced as the particle mass increases. The highest efficiency scintillation results from photons, with photons in the ultraviolet range converting 50-90% of their energy to scintillation. Electrons have a scintillation efficiency of only $\sim$4%, and protons and α-particles have even smaller efficiencies of $\sim$2% and $\sim$0.4%, respectively. [Bir64] Since the reduction in efficiency is more marked for

fluorescence than phosphorescence, the difference in the relative intensities of the two components may be used to discriminate between a less-massive and a more-massive form of radiation.

2.8 Fission Chambers

Calculation of the cross-sections of neutron-induced reactions requires accurate measurements of the neutron flux incident on the target as a function of energy. Since the energy of incident neutrons in many accelerator-based experiments changes with time, neutron flux detectors for use in such experiments must produce a sufficiently high count rate to provide a statistically accurate picture of the flux, without affecting experimental systems in the beam line by changing the characteristics of the incident beam or adding noticeable background events. [Wen93]

Fission chambers have been used to detect neutron flux for nuclear physics experiments since the beginning of the nuclear age. [Deu44] With the development of nuclear reactors, fission chambers were modified for use as reactor monitoring devices. [Ave54] Miniature fission chambers have also been proposed more recently as neutron diagnostics in fusion experimental facilities and reactors, such as International Thermonuclear Experimental Reactor (ITER) and the International Fusion Materials Irradiation Facility (IFMIF). [Cab10] [Rap09] Two fission chambers currently in use at LANSCE are shown in Figure 2.9. A fission chamber consists of an ionization chamber containing a surface that has been coated with a fissionable material. When an incoming neutron fissions in the coating, the fission fragments create trials of ionized particles in the gas. An applied voltage allows the electrons to be collected and the fission event to be identified.

Early fission chambers were assembled by preparing foils or grids coated with a thin layer of thorium, uranium, plutonium, or neptunium. Most commonly, solutions of nitrates of fissionable oxides, alcohol, and a cellulose varnish were prepared. [Ave54] [Deu46] These solutions were then most often painted onto a foil or grid destined for the fission chamber, [Ave54] [Bro54] although Deutsch and Ramsey, in preparing a gridded detector, actually painted the solution onto mica and floated it off after drying. [Deu46] However, the painting method resulted in extremely uneven coatings, so has it been abandoned in modern fission chambers. Certain high-performance applications make use of the highly-uniform coatings that may be obtained through vacuum evaporation. [Lov09] [BJ88] However, in most of the fission chambers in use currently, the fissionable coating has been applied to the foils by means of electro-
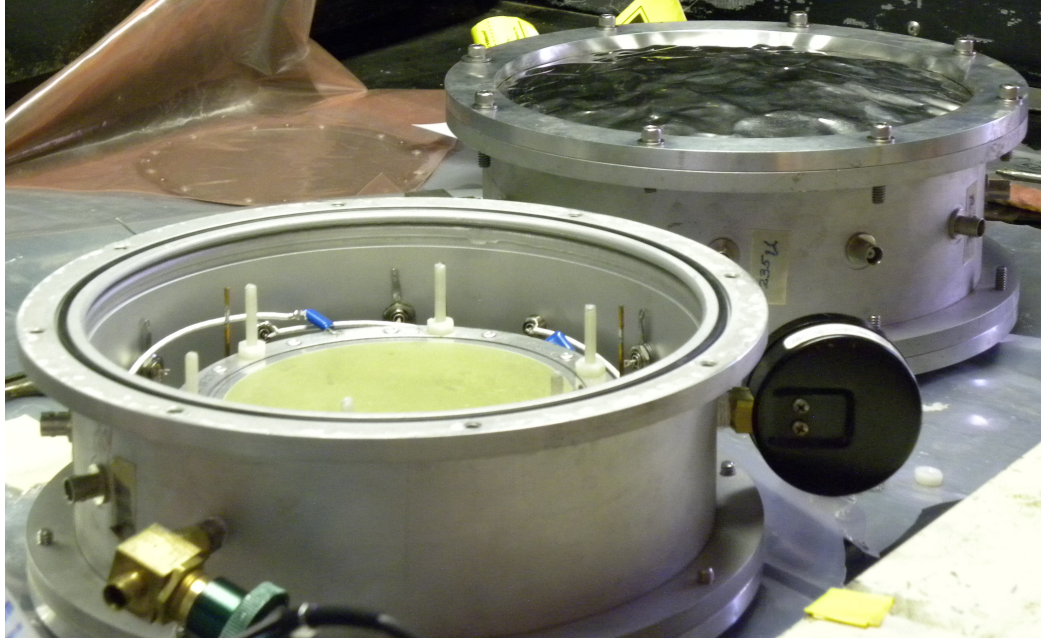
Figure 2.9: Two fission chambers used at LANSCE, both constructed according to the method described by Wender. [Wen93]. The chamber in the foreground has been opened to show the top foil, which is coated with ^{235}U.

plating. [Wes68] [Wen93]

The thickness of the fissionable coating on the foils has a direct effect on the fission chamber efficiency. As its thickness increases, the likelihood of an incident neutron fissioning in the foil also increases. However, the fission fragments must exit the foil in order to be detected, which limits the optimal coating thickness. Therefore, the fissionable coating is typically no more than 2-3 mg/cm^2, [Bar65] resulting in relatively low efficiencies and requiring that experiments in low-neutron-flux environments either utilize very large effective areas or be conducted over long periods of time.

The fill gas used in fission chambers is typically 90-98% argon, with the remainder consisting of a quench gas such as carbon dioxide or methane. [Bro54] [Deu46] [Ham95] [Wen93] The quench gas is necessary because argon has a relatively high excitation energy, so the photons emitted as ions de-excite ionize the cathode, resulting in a continuous discharge. [Leo94] A quench gas absorbs a sufficient number of de-excitation photons to prevent a continuous discharge from developing. Since electrons produced when fission fragments ionize the fill gas must travel through the gas to the anode to be detected, fission chambers have relatively long pulse rise times, on the order of microseconds. [Kno00] Fission chambers are therefore prone to pulse

pile-up in high-neutron-flux environments.

2.9 Scintillators Loaded with Fissionable Nanoparticles for Neutron Detection

The second area of research described in this work is the development of a scintillator loaded with fissionable material for use as a neutron flux detector. The use of an organic scintillator loaded with fissionable nanoparticles would address many of the disadvantages of fission chambers. The fast decay time of the organic matrix, typically at least two orders of magnitude faster than the rise time of a fission chamber, would make the detector less susceptible to pulse pile-up, while the use of fissionable material well-dispersed in the matrix would permit a higher loading of fissionable material than can be used in fission chambers, making the detector more effective in low-flux environments.

As a proof-of-principle for this concept, a fissionable molecular complex was selected, developed, and dissolved in an organic scintillator. The optical and radiation detection properties of this fissionable scintillator were characterized, and a sample was tested in the beam line to assess its response to high-energy neutrons.

CHAPTER III

Fabrication of Nanocomposite Scintillators

3.1 Introduction

Preparing samples of CeF_3 nanoparticles for characterization is a three-step process, involving fabricating the nanoparticles, washing them to remove excess capping ligands and solvents, and loading them into a liquid matrix in the desired concentration. The nanoparticles are synthesized by combining sodium fluoride and cerium nitrate, resulting in the precipitation of CeF_3 particles, whose size is limited by the addition of oleic acid, which acts as a capping ligand. The product of the synthesis reaction is a thick gel consisting of CeF_3 nanoparticles suspended in excess oleic acid and solvents. Typically, the extra material is removed before characterization, using a washing process that involves precipitation and centrifuging to isolate the nanoparticles.

The matrix used for most characterization measurements is a liquid scintillator. A liquid scintillator with an excitation wavelength near 300 nm and an emission wavelength near 420 nm was developed by adding wavelength-shifting dyes to toluene. Light yield measurements were used to optimize the relative concentrations of the dyes.

Samples of CeF_3 nanoparticles suspended in liquid scintillator displayed lower light yields than expected. Several theories were tested against this phenomenon. Neither the difference between the light yields of liquid scintillator and CeF_3, nor variations in the energy deposition, were sufficient to account for the decreased light yield. Instead, experiments indicated that oleic acid has a significant quenching effect on the liquid scintillator.
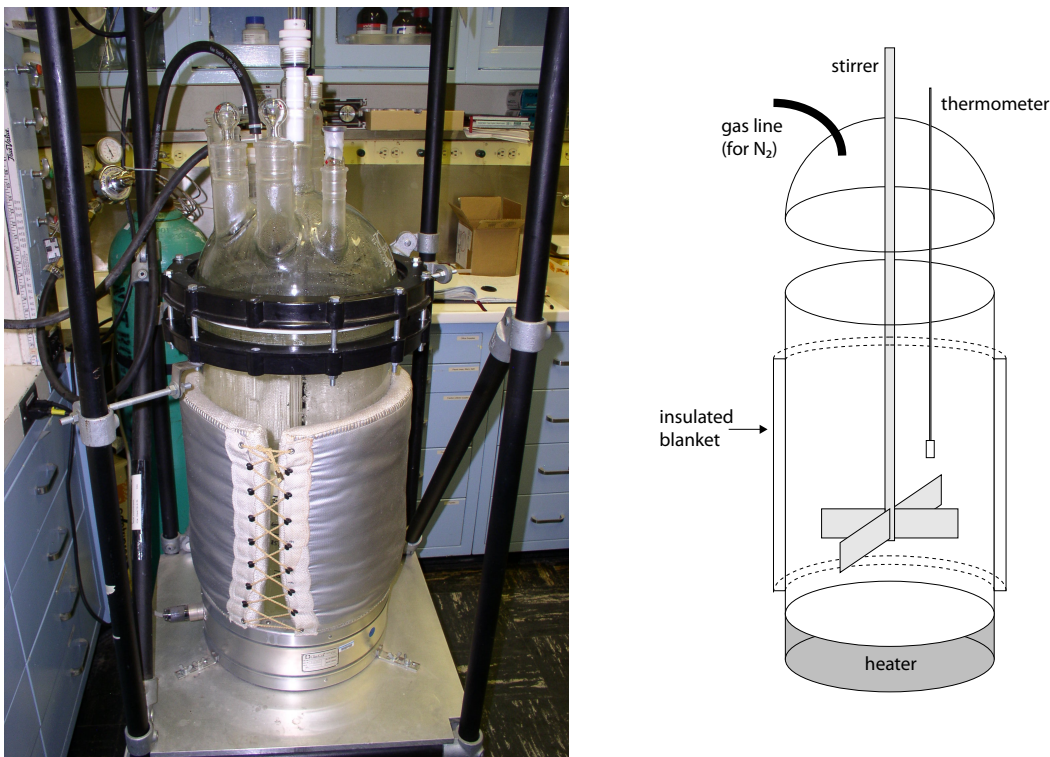
Figure 3.1: Left: Glass reactor vessel used for fabrication of CeF$_3$ nanoparticles, sitting on top of heater and surrounded by insulated blanket. Right: Diagram of reactor vessel, illustrating locations of heater, insulated blanket, stirring rod, and thermometer.

3.2   Synthesis of Cerium Fluoride Nanoparticles

Nanoparticles are prepared using a precipitation reaction performed in the reactor pictured in Figure 3.1. 130 g of sodium fluoride (NaF) dissolved in 8 L of water is combined in the reactor vessel with 230 g oleic acid mixed with 8 L of ethanol. The reactor is then filled with nitrogen to create an inert atmosphere, since the reaction is performed around and above the flash point of ethanol, which is 13° C. [Lid09] A heater is used to gradually raise the temperature to around 80° C, just below the boiling point of an ethanol/water solution, over a 24 hour period. Once the temperature has stabilized, a solution consisting of 440 g cerium nitrate (Ce(NO$_3$)$_3$) in 6 L water is added dropwise at an approximate rate of 20 mL per minute. This results in the formation of CeF$_3$ through the reaction

$$3NaF + Ce(NO_3)_3 \rightleftharpoons CeF_3 + 3NaNO_3 \tag{3.1}$$
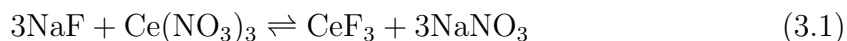
Figure 3.2: Left: Sodium fluoride/oleic acid solution before the addition of cerium nitrate. Stirrer is visible in center, thermometer is visible on right. Right: Sodium fluoride/oleic acid solution after the addition of cerium nitrate. Solution has turned white due to the formation of oleic-capped cerium fluoride particles.

Since the reaction is exothermic, and is performed in a heated solvent bath, the CeF_3 molecules have sufficient thermodynamic energy to assemble in their most thermodynamically stable structure, which is the crystal. Although this reaction can run in either direction, the forward direction dominates because CeF_3 is not soluble in ethanol or water, so it precipitates out of the solution. The $Ce(NO_3)_3$ is added slowly to allow the drops to disperse before the reaction occurs, to discourage the formation of large CeF_3 crystals. Crystal growth is also inhibited by the addition of oleic acid to the solution. Oleic acid prevents crystal development by attaching to nucleation sites, locations on the CeF_3 crystals where growth can occur. This can be seen in Figure 3.2, which shows that after the addition of $Ce(NO_3)_3$ the solution turns white due to the formation of oleic-capped CeF_3 particles. Oleic acid was initially chosen as the capping agent based on reports of its use in the successful fabrication of LaF_3 and $NaYF_4$ nanoparticles. [Zha05] [Boy06]

Once all of the $Ce(NO_3)_3$ has been added, the heater is turned off and the precipitate and supernatant are allowed to cool overnight ($\sim$15 hours), while still stirring and purging with N_2. After cooling, the supernatant is pumped out of the reactor, leaving the precipitated CeF_3 nanoparticles stuck to the sides and bottom of the reactor vessel and the stirrer paddle. The isolated nanoparticles are allowed to sit for several days as the remaining solvents evaporate. Before the reactor is opened, it is purged with N_2 for two hours to remove ethanol vapors. The nanoparticles are then removed and weighed, as shown in Figure 3.3. Excess oleic acid is removed by adding
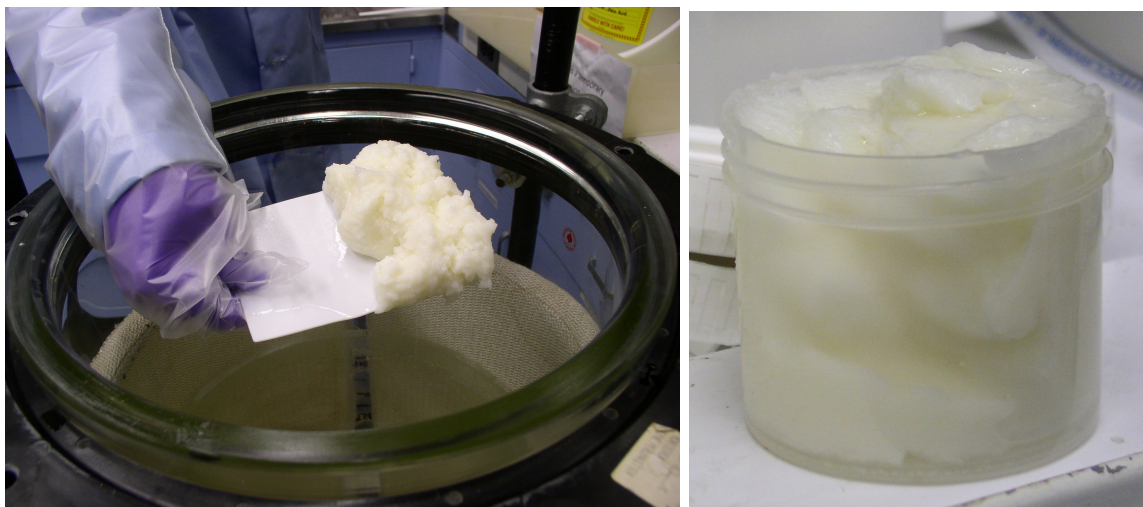
Figure 3.3: Left: The precipitate, a mixture of CeF_3 nanoparticles and oleic acid, is removed from the reactor. Right: CeF_3 precipitate before weighing. The precipitate is wetter than the end product will be, due to ethanol and water that will be removed by centrifuging. The yellow color is the result of excess oleic acid.

a 90% ethanol solution at a ratio of 0.62 mL ethanol per gram of gel and sonicating for one hour to disperse the nanoparticles. The dispersion is then centrifuged at 200 rpm for 20 minutes. The precipitate mixed with ethanol is shown before and after centrifuging in Figure 3.4. Following centrifuging, the supernatant is decanted and the nanoparticles are left in the hood for several days to dry, as shown in Figure 3.5.

Ten batches of CeF_3 nanoparticles were prepared at different times using this process. The characterization measurements described in this document were primarily performed using CeF_3 from batches five through eight.

3.3 Preparation of Samples

The precipitate that remains after drying is a gel consisting of oleic-capped CeF_3 nanoparticles mixed with free oleic acid left over from the fabrication process. Before a batch of CeF_3 gel is characterized, the amount of free oleic acid present is measured. This process involves measuring the initial mass of the gel, then removing the free oleic acid through a washing process similar to that used to remove oleic acid after fabrication and measuring the mass of the product.

In the first step of the washing procedure, the gel is combined with toluene at a ratio of 3.5 mL toluene per gram of gel. Although pure CeF_3 is insoluble in toluene,
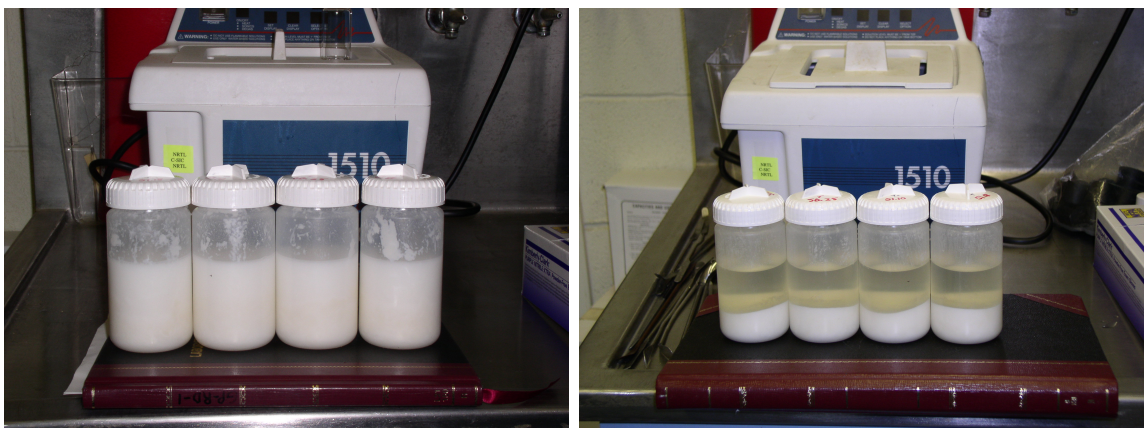
Figure 3.4: Left: CeF$_3$ precipitate, mixed with ethanol, before sonication and centrifuging. The precipitate has been divided into four roughly equal masses for the centrifuge. Right: CeF$_3$ precipitate after sonication and centrifuging. The yellowish liquid is a mixture of ethanol and oleic acid.

Figure 3.5: CeF$_3$ nanoparticles drying in the hood after washing

the oleic acid capping ligand, which is soluble, makes it possible to disperse the nanoparticles. The nanoparticle gel and the toluene are shaken vigorously, either by hand or using a mechanical shaker, until they form a dispersion. Methanol is then added, at a ratio of 3.5 mL per gram of gel, and the container is shaken several times to disperse it. Since the oleic acid-capped CeF_3 nanoparticles are not soluble in methanol, they begin to precipitate out, while the free oleic acid remains in solution with the toluene and methanol. The mixture is centrifuged at 3300 rpm for 8 minutes to complete the precipitation process. Following centrifugation, the supernatant, a mixture of toluene, methanol, and oleic acid, is decanted. This process can be repeated to further reduce the free oleic acid content. Once the nanoparticles have been washed, the remaining methanol and toluene are evaporated off by leaving the containers in the hood for 48 hours. The initial mass of the nanoparticles in their container is compared with the final mass; the reduction in mass is due to the removal of oleic acid through the washing process. One round of washing reduced the mass of a sample by 28-36%, depending on the batch of CeF_3 gel used. The washing process also changes the appearance of the CeF_3 nanoparticle gel. The translucent gel in which the nanoparticles are originally suspended is entirely removed, leaving behind the oleic acid-capped nanoparticles in the form of a pure white substance.

To determine what proportion of the free oleic acid is removed during one round of the washing process, three samples were prepared. The first sample was washed once using the procedure described above, the second sample was washed twice, and the third sample was washed three times. Suspending the nanoparticles in toluene after the first and second rounds of washing required much more vigorous shaking for a longer period of time than was initially needed to suspend the gel. The mass of the first sample was 28% less than the initial mass, while the masses of the second and third samples were both 31% less than the initial mass. Assuming that no capping ligands are removed by the washing process, this indicates that one round of washing removes 90% of the free oleic acid, and a second round of washing removes virtually all of the remaining 10%. Since the majority of the free oleic acid was removed by the first washing, a single washing was used for most nanoparticle samples.

For characterization purposes, the washed nanoparticles were dispersed in a matrix. The matrix most frequently used was a liquid scintillator consisting of toluene with two wavelength-shifting dyes, 2,5-diphenyloxazol (PPO) in a concentration of 7.5 mg per milliliter toluene and 1,4-bis(5-phenyloxazol-2-yl)benzene (POPOP) in a concentration of 1 mg per milliliter toluene. The absorption and emission spectra of these three components are shown in Figures 3.6, 3.7, and 3.8. Toluene was selected
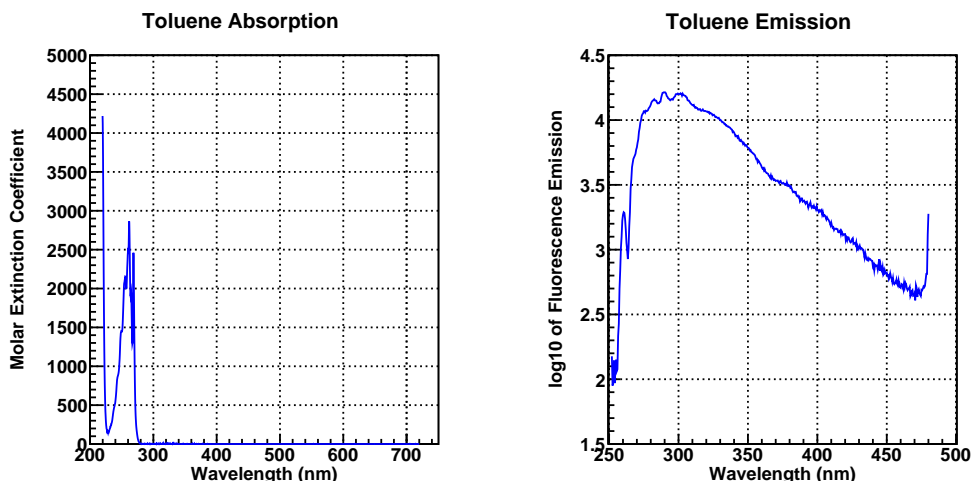
Figure 3.6: Spectra showing the wavelengths of light absorbed and emitted by toluene (data from PhotochemCAD database [Du98])
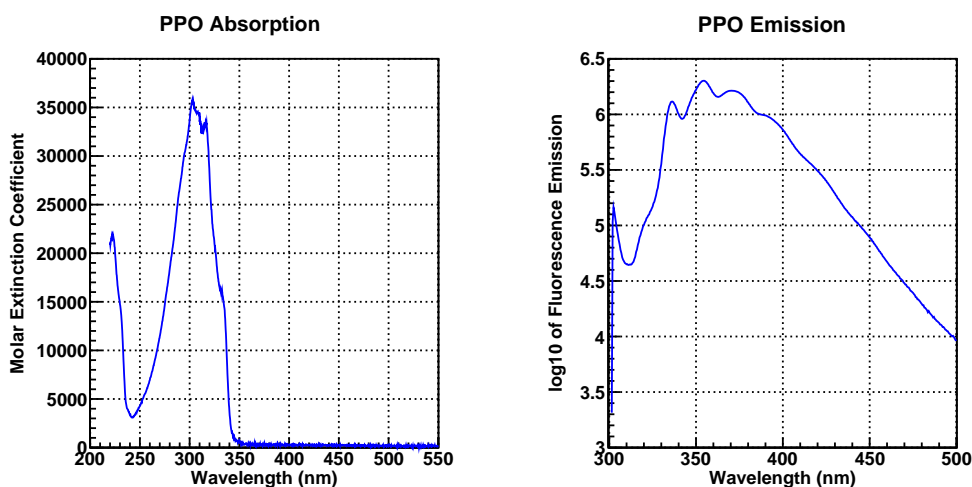
Figure 3.7: Spectra showing the wavelengths of light absorbed and emitted by PPO (data from PhotochemCAD database [Du98]). Light emitted by toluene around 300 nm (Figure 3.6) is absorbed by PPO and re-emitted around 350 nm.

as the primary scintillator due to the similarity between the wavelength of its emission and that of CeF_3. Due to this similarity, the same wavelength-shifting dyes are able to absorb and re-emit light from both toluene and CeF_3.

The use of two dyes, a primary and a secondary, allowed the light to be shifted from 300 nm to around 410 nm, the wavelength at which the quantum efficiency of the PMT used, which is shown in Figure B.1, is optimal. Since the emission spectrum of
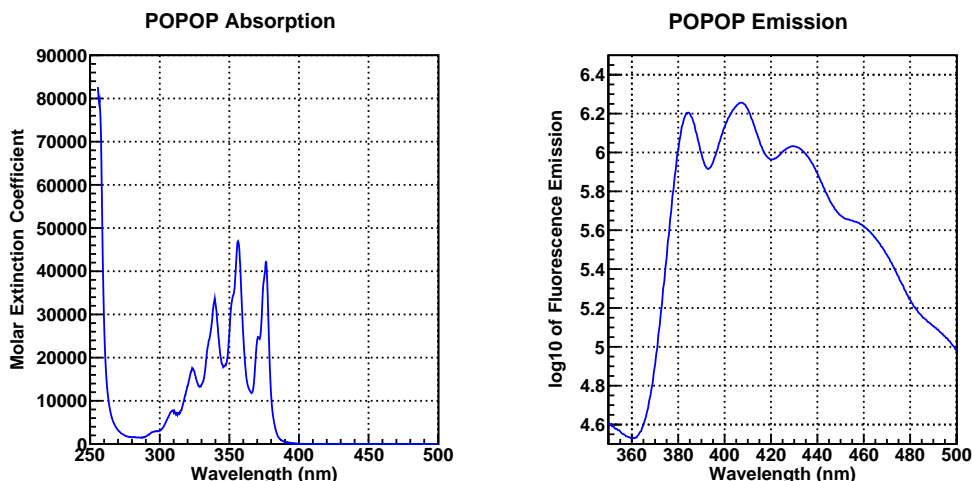
Figure 3.8: Spectra showing the wavelengths of light absorbed and emitted by POPOP (data from PhotochemCAD database [Du98]). Light emitted by PPO around 350 nm (Figure 3.7) is absorbed by POPOP and re-emitted around 410 nm.

toluene overlaps the absorption spectrum of PPO, light emitted by toluene is absorbed by PPO and re-emitted at a higher wavelength. Due to the breadth of its emission spectrum, some of the light produced by PPO is emitted at wavelengths for which the PMT quantum efficiency is high. However, in order to obtain an emission with a larger fraction of emitted light in this range, a secondary dye was used. As shown by the overlap between the wavelengths of PPO emission and POPOP absorption, the light emitted by PPO is absorbed by POPOP and re-emitted at over a higher wavelength range. The broad PPO emission, with maximum light yield between 380 nm and 430 nm, is a good match for the peak quantum efficiency of the PMT.

The dyes both shift the wavelength of the emitted light and increase its intensity, as depicted by the radiolumenescence spectra of toluene and the standard liquid scintillator mixture in Figure 3.9. The addition of the wavelength-shifting dyes not only moves the wavelength of maximum emission from 300 nm to 410 nm, it also increases the magnitude of the emission by a factor of twenty-five, as discussed in Chapter II.

3.4   Liquid Scintillator Optimization

PPO and POPOP were selected primarily because their excitation and emission wavelengths were good matches for one another and for toluene. In addition, the
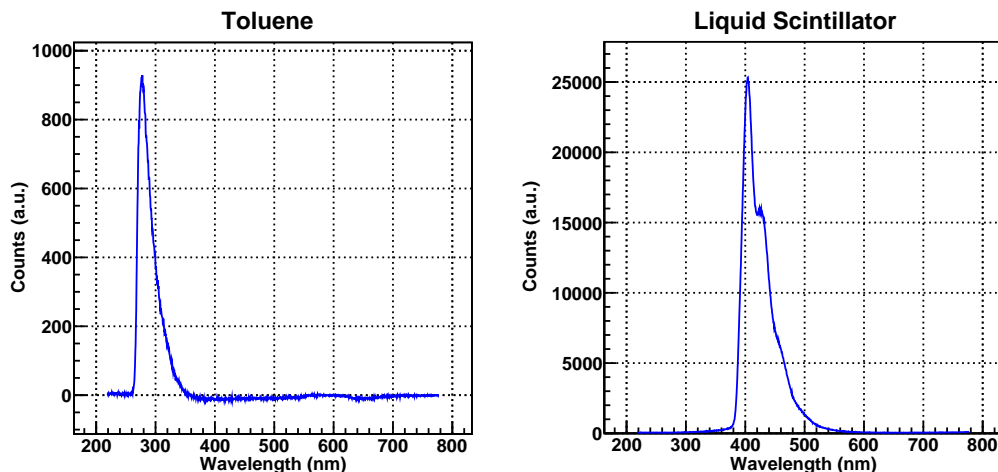
Figure 3.9: Radiolumenescence spectra of toluene and liquid scintillator (toluene with 7.5 mL PPO and 1 mL POPOP per mL toluene). The liquid scintillator is more than an order of magnitude brighter than toluene alone. In addition, the wavelength of its maximum emission has been shifted from 300 nm to 420 nm.

emission wavelength of POPOP is well-matched for the PMTs used - the most commonly used PMT in this system, the Hamamatsu R2059, has a wavelength range of 160-650 nm, with a peak sensitivity at 420 nm.

3.4.1 Optimization of p-terphenyl/POPOP Scintillator

Early samples suspended CeF_3 in a liquid scintillator that used p-terphenyl (1,4–di-phenylbenzene), rather than PPO, as the primary shifter. As can be seen by comparing Figures 3.7 and 3.10, the absorption and emission peak wavelengths of p-terphenyl are about 10 nm lower than those of PPO. However, due to the breadth of the emission peaks (both those of PPO and p-terphenyl, and that of toluene), the overlap between the p-terphenyl emission and the POPOP absorption is essentially unchanged.

In order to optimize the light output of the liquid scintillator, the effects on solubility and light yield with respect to the relative concentrations of the two wavelength-shifting dyes were tested. The initial liquid scintillator recipe consisted of 20 mL toluene, 200 mg p-terphenyl, and 40 mg POPOP, and was chosen based on the work of Bross and Pla-Dalmau on doped polystyrene scintillators. [Bro92] [Bro93] The amounts of toluene, p-terphenyl, and POPOP used in the first set of optimization samples are given by Table 3.1. To minimize errors in the amount of POPOP added to each sample, a toluene/POPOP solution was prepared that contained the total

31
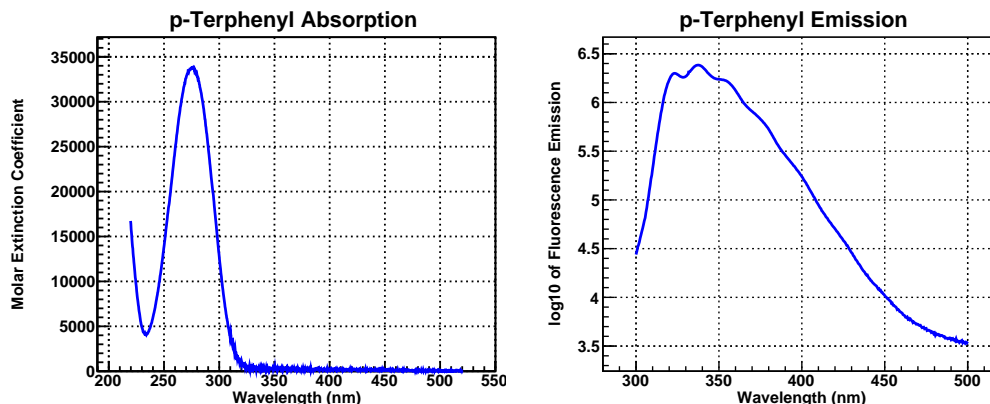
Figure 3.10: Spectra showing the wavelengths of light absorbed and emitted by p-terphenyl (data from PhotochemCAD database [Du98]). Light emitted by toluene around 290 nm (Figure 3.6) is absorbed by p-terphenyl and re-emitted around 350 nm.

amount of POPOP required for all of the samples. 200 mg POPOP was added to 100 mL toluene and stirred using a magnetic stirrer until the solution was colorless and transparent. 20 mL each of the combined solution was designated as samples 012007A, 012007B, and 012007C, 15 mL was designated as sample 012007D, and 10 mL was designated as sample 012007E. Toluene was added to samples 012007D and 012007E to increase the total volume to 20 mL (the contribution of the POPOP to the solution volume was negligible). The required amount of p-terphenyl was then added to each sample, and the samples were sonicated for one hour, after which they were found to be colorless and transparent. After resting approximately 12 hours, however, all of the samples except sample 012007E contained a yellow, thread-like precipitate, with samples 012007A, 012007B, and 012007C containing significantly more precipitate than sample 012007D. Further sonication was only able to remove the precipitate temporarily; only sample 012007E remained in solution over several days.

The presence of precipitate in all of the first set of samples except for sample 012007E indicated that the concentration of wavelength-shifting dyes exceeded the solubility limit. The yellow color of the precipitate, which is characteristic of POPOP, suggested that the POPOP concentration was higher than optimal. The second set of optimization samples was designed to determine whether the POPOP concentration should be decreased from the 1 mg per milliliter toluene level used for sample 012007E, as well as to determine whether the 5 mg per milliliter toluene concentration of p–terphenyl used in sample 012007E was optimal. The compositions of the nine

Sample	Toluene (mL)	p-Terphenyl (mg)	POPOP (mg)
012007A	20	200	40
012007B	20	150	40
012007C	20	100	40
012007D	20	150	30
012007E	20	100	20

Table 3.1: Composition of the first set of samples used to optimize the relative concentrations of toluene and two wavelength-shifting dyes, p-terphenyl and POPOP. The initial dye concentrations were chosen based on a recipe used for doped plastic scintillators. [Bro92]. Only the solution incorporating the smallest amount of POPOP, solution 012007E, was stable for longer than a few hours.

Sample	Toluene (mL)	p-Terphenyl (mg)	POPOP (mg)
030107E	20	100	20
030107F	20	100	24
030107G	20	100	16
030107H	20	100	12
030107I	20	100	8
030107J	20	120	20
030107K	20	80	20
030107L	20	60	20
030107M	20	40	20

Table 3.2: Composition of the second set of samples used to optimize the relative concentrations of toluene and two wavelength-shifting dyes, p-terphenyl and POPOP. Note that sample 030107E in this set is identical to sample 012007E in the first set of samples (Table 3.1), which was the only stable sample in that set.

samples prepared are given in Table 3.2; note that sample 030107E in this set is identical to sample 012007E in Table 3.1.

As was done previously, to minimize the errors involved in measuring the relatively small quantities of POPOP, the total amount of POPOP required was divided between two volumes of toluene and mixed using magnetic stirrers until the POPOP was well-dispersed. The first solution contained 100 mL toluene and 100 mg POPOP and was evenly divided among samples 030107E, 030107J, 030107K, 030107L, and 030107M. The second solution contained 100 mL toluene and 120 mg POPOP. 20 mL of this solution was designated as sample 030107F, 13.3 mL was designated as sample 030107G, 10 mL was designated as sample 030107H, and 6.6 mL was designated as sample 030107I. Toluene was added to samples 030107G, 030107H, and 030107I to

bring the total volume to 20 mL. The required amount of p-terphenyl was added to each solution, and the solutions were sonicated for one hour, after which all samples were colorless and transparent.

At the time when the p-terphenyl/POPOP scintillator was optimized, the only technique typically used to assess the light output of scintillator solutions involved determining the channel of the Compton edge in the energy spectrum produced by the scintillator in response to a ^{137}Cs γ-source. This technique is described in detail in Section 4.4.1. The Compton edge channel was located using the reduced chi-square, whose general form is

$$\frac{\chi^2}{\nu} = \frac{\sum\limits_{i=1}^{n} \left(\frac{x_i - \mu_i}{\sigma_i} \right)^2}{\nu} \tag{3.2}$$

where ν is the number of degrees of freedom of the n independent variables x_i with means μ_i and standard deviations σ_i. When the Gaussian fit to a distribution is good, the reduced chi-square should approach unity. [Leo94] The independent variables x_i are the n individual data points of the spectrum, the σ_i are their errors, and the number of degrees of freedom ν is the number of data points minus the number of free parameters (three, in the case of a Gaussian fit). The other component of Equation 4.18, μ_i, is calculated from the fitting function: μ_i is the expected value of each data point. The data analysis framework ROOT [Bru97] was used to plot the energy spectrum, generate a Gaussian fit for the Compton edge region, and calculate the chi-square and number of degrees of freedom. An example of this process is shown in Figure 3.11, for sample 052107F. Absolute light yields were unnecessary for liquid scintillator optimization, since comparisons were only made between spectra measured using identical parameters during a short period of time. Therefore, no correction was made for the charge-to-digital converter (QDC) pedestal, as it resulted in the same light yield offset for all spectra in a set.

The results of the analysis are given in Table 3.3. To assist in analysis, the centroid bin numbers were converted to relative light yields, as displayed in Figure 3.12. In order to accurately calculate the relative light yield, a 41-channel pedestal was subtracted from each of the centroid values given in Table 3.3. Sample 030107E, which contained 100 mg p-terphenyl and 20 mg POPOP, was selected as the baseline sample, having a relative light yield of 1. As shown in Figure 3.12, there were no trends observed in the light yield as a result of varying the quantity of wavelength-shifting dyes. As a result, sample 030107E was selected as the standard p-terphenyl/POPOP liquid scintillator recipe.
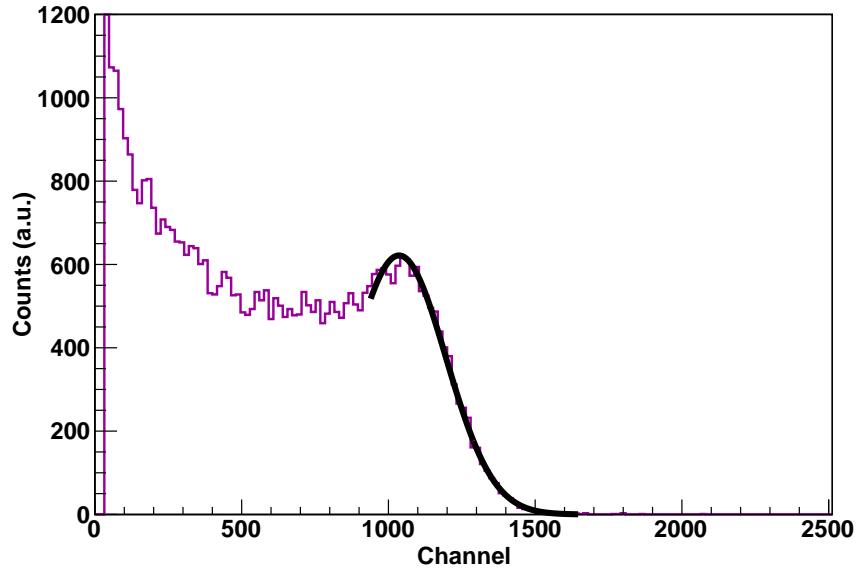
Figure 3.11: Spectrum of sample 052107F and Gaussian fit to Compton edge. The range of the fit, which here extends from channel 936 to channel 1650, is chosen so as to bring the reduced chi-square, Equation 4.18 as close to unity as possible. The QDC pedestal, visible on the far left of the spectrum, was uncorrected for liquid scintillator optimization measurements, since it was identical for all measurements in a set and comparisons were not made between spectra from different sets.

Sample	Fit Range	Reduced χ^2	Centroid
030107E	146-440	0.9950	186
030107F	116-415	1.064	157
030107G	201-465	0.9360	220
030107H	126-350	1.017	147
030107I	146-450	1.039	205
030107J	191-384	1.022	241
030107K	41-300	0.9673	58
030107L	131-465	1.248	170
030107M	186-525	0.9446	208

Table 3.3: Parameters used for Gaussian fits of Compton edges of liquid scintillators utilizing p-terphenyl and POPOP, including range of Gaussian fit (in bins), location of Gaussian centroid, and value of reduced chi-square (Equation 4.18).

35
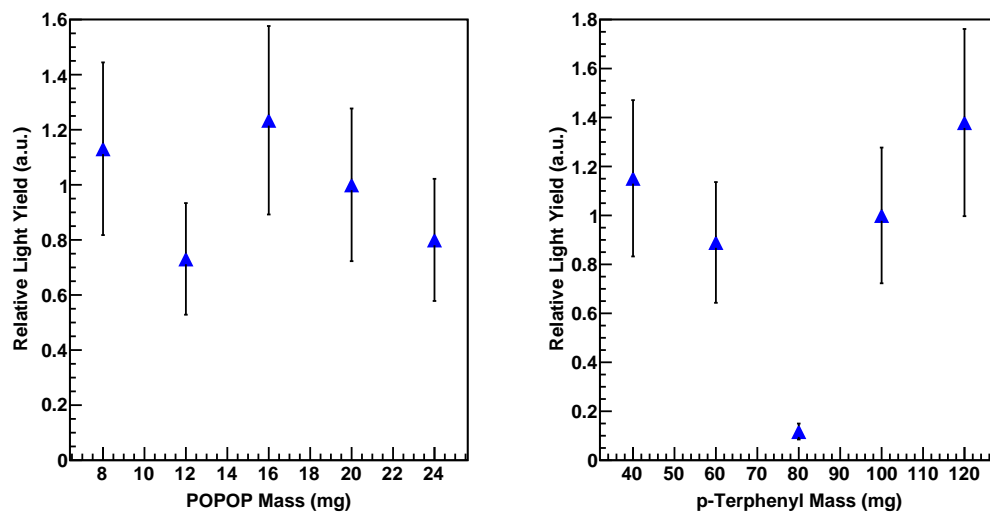
Figure 3.12: Relative light yields of p-terphenyl/POPOP scintillators, based on Compton edge locations. Light yields are relative to the light yield of solution 030107E, which contained 100 mg p-terphenyl and 20 mg POPOP. The light yield shown for solution 030107K, which contained 80 mg p-terphenyl and 20 mg POPOP, was unusually low, probably due to errors in sample preparation.

3.4.2 Optimization of PPO/POPOP Scintillator

When CeF$_3$ nanoparticles were added to the p-terphenyl/POPOP liquid scintillator, a precipitate formed. To identify the insoluble component, the wavelength-shifting dyes were varied. When the p-terphenyl was replaced by the same amount of PPO, the dyes remained soluble even after the addition of nanoparticles. The relative concentrations of PPO and POPOP were optimized by mixing a set of samples, as outlined in Table 3.4.

As with the earlier scintillator samples, the first step in preparing these samples involved the preparation of a solution containing the total amount of POPOP that would be required. 200 mg POPOP was added to 100 mL toluene and stirred using a magnetic stirrer until the POPOP was well-dispersed. While stirring, 10 mL of the dispersion was added to sample 051607A, 10 mL was added to sample 051607B, 10 mL was added to sample 051607C, 15 mL was added to sample 051607D, and 20 mL was added to sample 051607E. Toluene was added to samples 051607A, 051607B, 051607C, and 051607D to bring the total volume to 20 mL. The required amount of PPO was then added to each solution. The PPO went into solution more readily than p-terphenyl, requiring little mixing. All of the solutions were sonicated for one

36

Sample	Toluene (mL)	PPO (mg)	POPOP (mg)
051607A	20	100	20
051607B	20	150	20
051607C	20	200	20
051607D	20	100	30
051607E	20	100	40

Table 3.4: Composition of samples used to optimize the relative concentrations of toluene and two wavelength-shifting dyes, PPO and POPOP. PPO was selected as a replacement for p-terphenyl, which was insoluble when combined with CeF_3 nanoparticles. The baseline sample, sample A, used the same proportions as the final formulation of the scintillator incorporating toluene, p-terphenyl, and POPOP.

Sample	Fit Range	Reduced χ^2	Centroid
051607A	1021-1619	1.333	1055
051607B	941-2010	0.8985	1025
051607C	1061-2010	1.334	1100
051607D	1061-1579	0.9955	1133
051607E	901-2010	1.005	972

Table 3.5: Fit range, fit quality, and location of Compton edge for 051607 series of liquid scintillators based on toluene, PPO, and POPOP.

hour, at which point they were colorless and transparent.

The radiation responses of all five solutions displayed a Compton continuum only, due to the low-Z composition of the liquid scintillator and the small size of the detectors, quartz cuvettes containing ~3.5 mL of the solution. The ranges of the Gaussian fits to the Compton edges of the spectra and the reduced chi-square values are given in Table 3.5. Samples 051607C and 051607D displayed the highest light yields, as indicated by the location of the Compton edge. However, when samples 051607C, 051607D, and 051607E were reproduced, along with an additional sample containing 50 mg POPOP and 100 mg PPO, all of the samples containing more than 20 mg POPOP required lengthy sonication and would not remain in solution for more than a few hours.

In response to the solubility problems experienced when using more than 1 mg POPOP per milliliter toluene, the next set of sample scintillators was formulated with lower POPOP concentrations. This batch was designed to determine whether 10 mg or 20 mg POPOP would perform better in 20 mL toluene and to determine the ideal PPO-to-POPOP ratio. The compositions of the individual scintillators are given in Table 3.6.

Sample	Toluene (mL)	PPO (mg)	POPOP (mg)
052107A	20	100	10
052107B	20	200	10
052107C	20	100	20
052107D	20	200	20
052107E	20	150	10
052107F	20	150	20

Table 3.6: Composition of series of toluene/PPO/POPOP scintillators designed to determine the optimum amount of POPOP and relative concentration of PPO. Due to solubility problems experienced with the previous series of scintillator samples, the POPOP concentration was limited to no more than 1 mg/mL toluene.

Sample	Fit Range	Reduced χ^2	Centroid
052107A	986-1830	1.227	1070
052107B	776-1900	1.009	886
052107C	911-1900	1.072	1007
052107D	796-1800	1.229	890
052107E	926-1800	1.010	995
052107F	936-1650	1.043	1037

Table 3.7: Fit range, fit quality, and location of Compton edge for 052107 series of liquid scintillators using toluene/PPO/POPOP. Amounts of wavelength-shifting dyes in each sample are given in Table 3.6.

As in previous scintillator preparations, the total amount of POPOP required for all samples was combined with toluene to minimize measurement errors. 90 mL POPOP was added to 90 mL toluene and stirred using a magnetic stirrer until the POPOP was well-dispersed. While still stirring, 60 mL of the dispersion was removed, divided into three 20 mL samples, and designated as samples 052107C, 052107D, and 052107F. The remaining 30 mL of the dispersion was divided into three 10 mL samples. 10 mL additional toluene was added to each of these samples, and they were designated as samples 052107A, 052107B, and 052107E. PPO was added to each solution in the required quantity, and the samples were sonicated for 25 minutes, at which point they were colorless and transparent.

The light yields of the PPO/POPOP scintillators were measured. Their fit characteristics are given in Table 3.7. The two samples that contained 200 mg PPO, 052107B and 052107D, had much lower light yields than the other samples. Of the remaining three samples, 052107F, with 150 mg PPO and 20 mg POPOP, was chosen as the liquid scintillator standard.
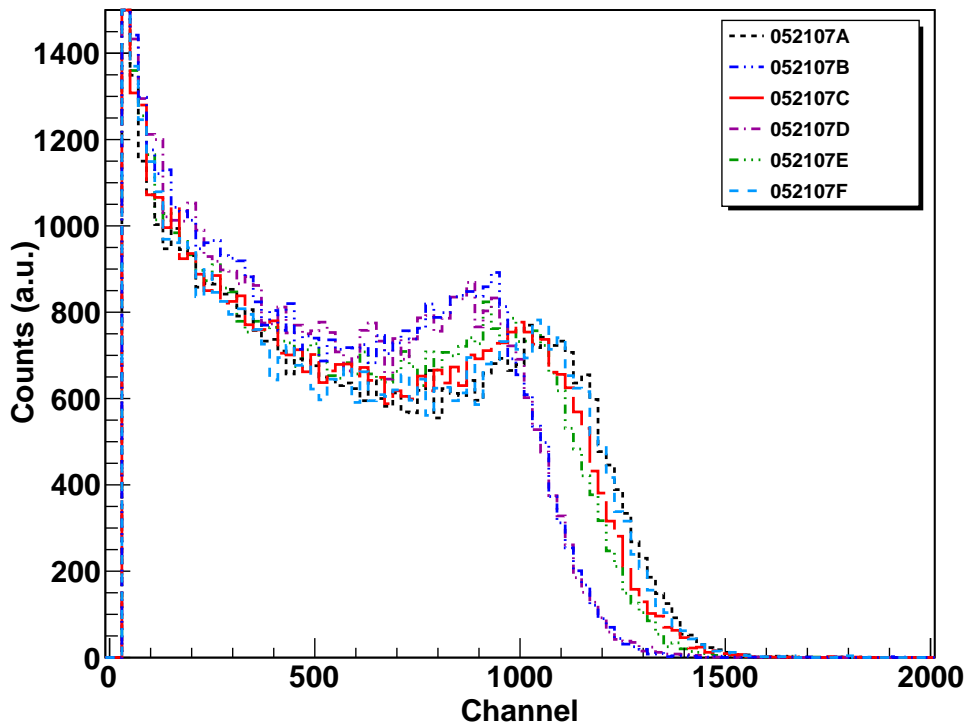
Figure 3.13: Energy spectra produced by final batch of toluene/PPO/POPOP scintillators in response to γ-rays from ^{137}Cs. Samples 052107B and 052107D, which contained the highest concentrations of PPO, had noticeably lower light yields, while the remaining samples produced similar spectra.

At the time this work was performed, the Compton edge technique for measuring light yield was the standard method used. However, later measurements of light yield utilized radioluminescence spectroscopy, as described in Section 4.3.2. Radioluminescence spectra show the wavelength range and intensity of emitted light, making it possible to discern whether the relative concentrations of the liquid scintillator components are optimal. For example, if the concentration of PPO were too high, relative to the POPOP concentration, the radioluminescence spectrum would feature the characteristic emissions of both components, indicating that not all of the light emitted by PPO was absorbed by POPOP. The use of radioluminescence spectroscopy might have simplified the process of optimizing the liquid scintillator, by providing additional information about its emission. However, the end result obtained using the Compton edge technique is a good liquid scintillator, and its radioluminescence spectrum indicates that there is no significant mismatch between the concentrations of its components.

3.5 Liquid Scintillator Quenching

As part of the radiation characterization of CeF_3 suspensions discussed in Chapter V, five solutions containing a standard liquid scintillator mixture and varying mass concentrations of CeF_3 nanoparticles were prepared. The nanoparticles were suspended in an oleic acid gel that was 64.5% (by mass) nanoparticles. Sufficient gel was added to each liquid scintillator sample to produce solutions that contained 0%, 5%, 10%, 20%, and 30% CeF_3 by mass. The preparation of more concentrated solutions was attempted, but the nanoparticles did not stay in suspension.

Measurements indicated that the light yield, represented by the channel in which the Compton edge was observed, decreased as the CeF_3 concentration increased, as shown in Figure 3.14. Several theories were developed and tested in the process of explaining this behavior.
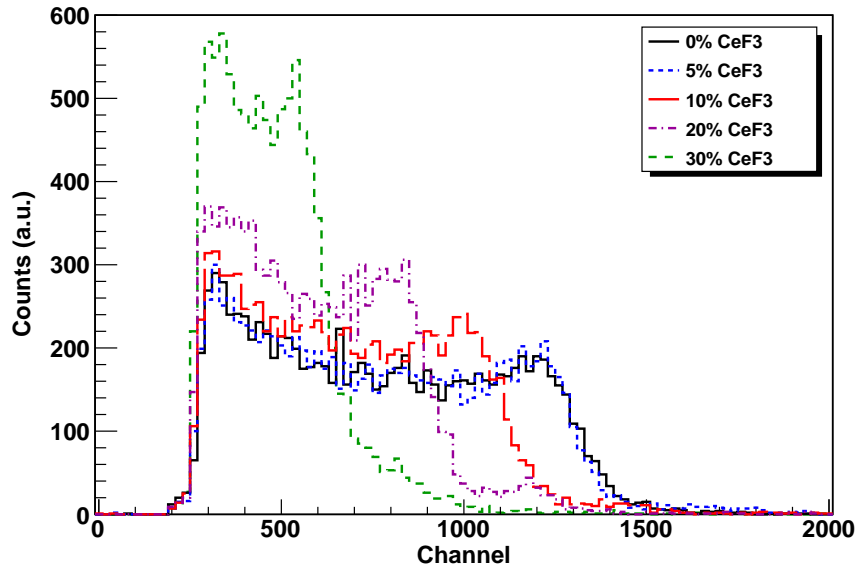
Figure 3.14: Energy spectra of liquid scintillator solutions with varying CeF_3 concentrations. The light yield, indicated by the Compton edge, decreases as the CeF_3 concentration increases.

The first theory assumed that the lower light yield resulted from the smaller number of photoelectrons produced by CeF_3 compared with liquid scintillator. The light yield of CeF_3 was known to be 4.4 photons/keV of deposited energy. [Mos89] Since measuring the light yield of the standard liquid scintillator solution using a QDC produced only a bin number for the location of the Compton edge, this was

converted to a quantitative value by comparison with scintillation crystals whose light yields were known.

In order to convert bin numbers to light yields, it was necessary to determine the number of photoelectrons in the Compton edge or photopeak. The deposited γ-ray energy is related to the light yield by the expression

$$\frac{E_{dep} \times LY \times QE \times G \times q}{\text{charge/channel}} + \text{pedestal} = \text{channel} \tag{3.3}$$

where E_{dep} is the deposited γ-ray energy, LY is the light yield in photons/keV, QE is the quantum efficiency, G is the gain, and q is the Coulomb constant. The pedestal is produced by the charge-to-amplitude stage of the QDC, and results in a baseline output signal that is present any time a gate signal is applied to the QDC. The QDC used, a Caen V965, whose specifications are given in Table C.8, has two ranges. Each channel of the high range represents 200 fC of deposited charge. The quantum efficiency of the PMT, a Hamamatsu R2059 with base E2979-500, depends on the wavelength of the scintillator emission and can be determined using Figure B.1. The number of channels in the pedestal is determined using the expression

$$\text{pedestal} = \frac{I_P \times \text{gate width}}{\text{charge/channel}} \tag{3.4}$$

where I_P is the pedestal current, which was left at its default setting of approximately 82.5 μA for all measurements. As with Equation 3.3, the charge per channel of the QDC was 200 fC for the high range utilized here. Thus, the pedestal depended on the gate width. All measurements discussed here utilized a 500 ns gate width, which resulted in a 206 channel pedestal.

The PMT gain at the -2200 V operating voltage used to measure the spectra seen in Figure 3.14 had to be determined experimentally. Rather than relying on a single measurement at this voltage, three calculations of the gain were performed at -1550 V, -2200 V, and -2400 V. Three different crystals were used, because obtaining a spectrum across this voltage range required a variety of light yields. A LaBr$_3$ crystal was used for the measurement at -1550 V. The light yield of LaBr$_3$ was reported by the manufacturer to be 63 photons/keV [Roz09] This is consistent with the light yield of 61 ± 5 photons/keV reported for LaBr$_3$ doped with 0.5% Ce^{3+}, [vL01] so the light yield of the crystal used was assumed to be 63 ± 5 photons/keV. The number of charge carriers produced as a result of the photoelectric absorption of a 661.7 keV γ-ray was therefore 41,687.1 $\pm$ 3,308.5. At the 380 nm wavelength of the LaBr$_3$

emission, according to Figure B.1 the PMT quantum efficiency is 0.27 ± 0.02. These figures can be used with Equation 3.3 to obtain the gain at -1550 V:

$$1972 \text{ channels} = 206 \text{ channels}$$
$$+ \frac{661.7 \text{ keV} \times 63 \text{ /keV} \times 0.27 \times 1.602 \times 10^{-19} \text{ C} \times G}{200 \text{ fC/channel}} \tag{3.5}$$

$$G = 1766 \text{ channels} \times \frac{200 \text{ fC/channel}}{1.803 \text{ fC}} = 1.96 \times 10^5 \tag{3.6}$$

The errors of the various quantities may be propagated through to obtain the error in the gain. The light yield had statistical error due to variations in the number of charge carriers produced, while errors in the quantum efficiency and photopeak channel were systematic. The error in the photopeak channel was not measured; however, similar measurements had errors of ~ 5 channels.

$$\sigma_G^2 = \left(\frac{\partial G}{\partial \text{channel}}\right)^2 \sigma_{\text{channel}}^2 + \left(\frac{\partial G}{\partial LY}\right)^2 \sigma_{LY}^2 + \left(\frac{\partial G}{\partial QE}\right)^2 \sigma_{QE}^2 \tag{3.7}$$

$$\left(\frac{\sigma_G}{G}\right)^2 = \left(\frac{\sigma_{\text{channel}}}{(\text{channel} - \text{pedestal})}\right)^2 + \left(\frac{\sigma_{LY}}{LY}\right)^2 + \left(\frac{\sigma_{QE}}{QE}\right)^2$$
$$= \left(\frac{5}{1972 - 206}\right)^2 + \left(\frac{3308.5}{41687.1}\right)^2 + \left(\frac{0.02}{0.27}\right)^2 \tag{3.8}$$
$$= 0.012$$

$$\sigma_G = 0.11 \times 1.96 \times 10^5 \Rightarrow G = (1.96 \pm 0.22) \times 10^5 \tag{3.9}$$

A BC-408 scintillator was used to obtain the measurement at -2200 V. The scintillator manufacturer quoted a light yield equivalent to 64% that of anthracene, or 10 photons/keV. [Sai08b] [Elj] The variation in photons produced was assumed to be 1 photon/keV, consistent with other scintillators produced by the manufacturer. At the 425 nm emission wavelength, the PMT quantum efficiency is given by Figure B.1 to be 0.24 ± 0.02. The Compton edge, equivalent to 477.4 keV, was observed in channel 1767 ± 5. Using these quantities, Equations 3.3 and 3.7 give a gain of $(1.70 \pm 0.22) \times 10^6$.

The measurement at -2400 V was performed using a BGO crystal. The light yield quoted by the manufacturer was 8-10 photons/keV. [Sai08a] This range was consistent with the 8.2 photons/keV reported by Holl [Hol88], so the light yield used for calculations was 9 ± 1 photons/keV. At the 480 nm wavelength reported for the BGO emission, the quantum efficiency of the PMT, as estimated from Figure B.1, is

0.17 ± 0.02. The photopeak was observed in channel 2052 ± 5. The gain at -2400 V can then be calculated as $(2.50 \pm 0.40) \times 10^6$.

The gain of a PMT can be written as

$$G = (KV_d)^n = \left(\frac{KV_b}{n}\right)^n \tag{3.10}$$

where K is a constant, V_d is the dynode voltage (assuming the same voltage is applied to each dynode), V_b is the voltage applied to the PMT base, and n is the number of stages. [Leo94] The number of stages needed to describe the behavior of a PMT is not equal to its number of dynodes; rather, it is a fraction of that number. [Kno00] Equation 3.10 was used to develop a fit for the measured PMT gains, and resulted in the expression

$$G = \left(\frac{(0.0298 \pm 0.00243) \times V_b}{5.95 \pm 0.380}\right)^{(5.95 \pm 0.380)} \tag{3.11}$$

which has an error that depends on the dynode voltage,

$$\sigma_G^2 = \left(\frac{\partial G}{\partial K}\right)^2 \sigma_K^2 + \left(\frac{\partial G}{\partial n}\right)^2 \sigma_n^2$$

$$= \left[\frac{n}{K}\left(\frac{KV_b}{n}\right)^n\right]^2 \sigma_K^2 + \left[-\left(\frac{KV_b}{n^2}\right)\left(\frac{KV_b}{n}\right)^n \ln\left(\frac{KV_b}{n}\right)\right]^2 \sigma_n^2 \tag{3.12}$$

$$\left(\frac{\sigma_G}{G}\right)^2 = \left(\frac{n}{K}\right)^2 \sigma_K^2 + \left[-\left(\frac{KV_b}{n^2}\right) \ln\left(\frac{KV_b}{n}\right)\right]^2 \sigma_n^2$$

$$= 0.235 + 0.144 \times [0.000842 \cdot V_b \ln(0.00501 \cdot V_b)]^2 \tag{3.13}$$

Equation 3.11 is a good fit to the observed behavior, as can be seen in Figure 3.15. This expression was used to calculate the expected gain at -2200 V, the voltage at which the spectra in Figure 3.14 were measured, to be $(1.59 \pm 2.68) \times 10^6$. However, it should be noted that the value for n produced by the fit, 5.95, is smaller than expected for a 12-dynode PMT. Knoll states that typical values of n measured for a 10-dynode PMT range between six and nine - based on this, a value between approximately seven and eleven was expected. [Kno00]

Calculating the gain made it possible to determine the light yield of the liquid scintillator. According to Figure B.1, the quantum efficiency at the 410 nm measured wavelength of maximum emission is 0.26 ± 0.02. The Compton edge was measured in channel 1183 ± 5. Equations 3.3 and 3.7 were used to determine the light yield of
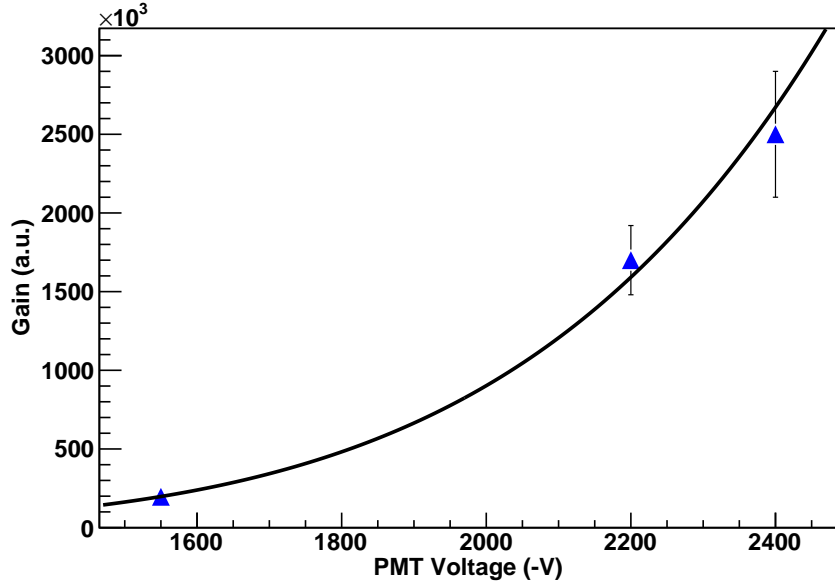
Figure 3.15: Gain observed for Hamamatsu R2059 PMT with E2979-500 base at -1550 V, -2200 V, and -2400 V. Equation 3.10 was used to fit the data, with K and n as free parameters. The final fit, given by Equation 3.11, is a good match for the data, but the value for n, the number of stages, is a much smaller fraction of the number of dynodes present (12) than expected.

the liquid scintillator and its error,

$$1183 \text{ channels} = 206 \text{ channels}$$
$$+ \frac{477.4 \text{ keV} \times LY \times 0.26 \times 1.602 \times 10^{-19} \text{ C} \times 1.59 \times 10^6}{200 \text{ fC/channel}} \quad (3.14)$$

$$LY = 977 \text{ channels} \times \frac{200 \text{ fC/channel}}{31.6 \text{ pC keV}} = 6.18 \text{ photons/keV} \quad (3.15)$$

$$\left(\frac{\sigma_{LY}}{LY}\right)^2 = \left(\frac{\sigma_{\text{channel}}}{\text{channel} - \text{pedestal}}\right)^2 + \left(\frac{\sigma_G}{G}\right)^2 + \left(\frac{\sigma_{QE}}{QE}\right)^2$$
$$= \left(\frac{5}{1183 - 206}\right)^2 + \left(\frac{2.68 \times 10^6}{1.59 \times 10^6}\right)^2 + \left(\frac{0.02}{0.26}\right)^2 \quad (3.16)$$
$$= 2.85$$

$$\sigma_{LY} = 1.69 \times LY = 10.4 \Rightarrow LY_{LS} = 6.18 \pm 10.4 \text{ photons/keV} \quad (3.17)$$

The theoretical light yield of the solutions was determined by calculating the relative volume concentrations of the scintillator components. This revealed that oleic

CeF$_3$ by mass	CeF$_3$ by volume	toluene by volume	oleic by volume
0%	0%	100%	0%
5%	0.7%	96%	3.3%
10%	1.5%	93%	5.5%
20%	3.0%	85%	12.0%
30%	4.7%	77%	18.3%

Table 3.8: Volume concentrations of CeF$_3$ nanoparticles, toluene, and oleic acid in the five scintillator solutions whose light yields are shown in Figure 3.14. The wavelength-shifting dyes PPO and POPOP are not included because their contributions to the mass and volume are negligible.

acid, which does not scintillate, made up a significant fraction of the total volume, as shown in Table 3.8. The nanoparticle gel used to make these solutions contained 64.5% CeF$_3$ by mass and 35.5% free oleic acid.

The first theory assumed that γ-rays deposited no energy in the oleic acid. According to this theory, as the volume of liquid scintillator in a cuvette of constant volume was replaced by CeF$_3$, the light yield of the solution would decrease. As shown in Figure 3.16, this theory predicted a less pronounced decrease in light yield than was observed experimentally. The errors in the experimental data, which were calculated based on the 19.6% average resolution of the 5%, 10%, and 20% CeF$_3$ spectra shown in Figure 3.14, show that the difference between the data and theory are significant for the 20% and 30% CeF$_3$ solutions.

The second theory assumed that energy was deposited in the oleic acid, in addition to the liquid scintillator and CeF$_3$. This further reduced the expected light output, since energy deposited in oleic acid does not result in scintillation. Rather than assigning to each material a fraction of the deposited energy equivalent to its volume concentration, as was done for the first theory, the slowing-down of electrons produced by the photoelectric effect in the material was modeled. The electron stopping power over the energy range from 10 keV to 1 GeV was obtained for each material from the National Institute of Standards and Technology (NIST) Stopping-Power and Range Tables for Electrons (ESTAR) database, and splines were calculated to provide data for intermediate energies. [oSa] Electrons in the model had an initial energy of 661.7 keV. For each step, the distance traveled through each material, in proportion to their concentrations, was calculated and used with the splines to determine the amount of energy lost. As shown in Figure 3.17, this theory produced slightly lower estimated light yields than were produced by the theory shown in Figure 3.16. However, the observed light yields were still much less, particularly for the 20% and 30%
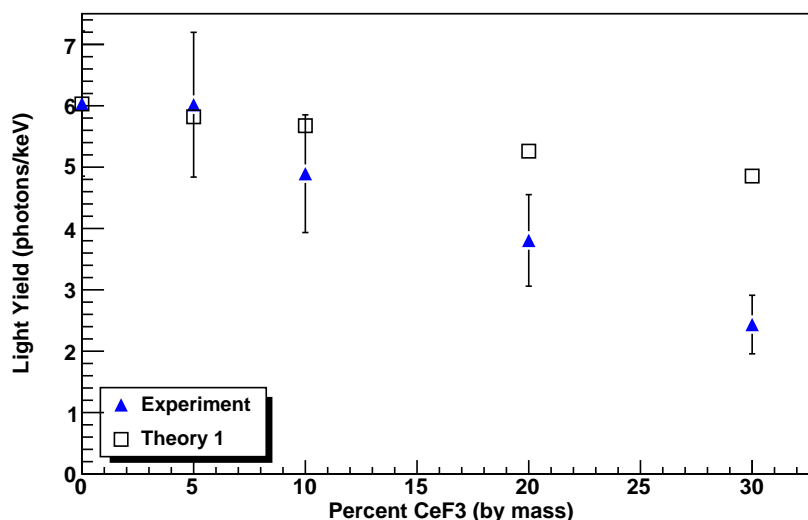
Figure 3.16: Calculations of the expected light yield based on the volume concentrations of liquid scintillator and CeF_3, and assuming that oleic acid has no effect, predict a decrease in light yield with increasing CeF_3 concentration that is smaller than that observed experimentally.

CeF_3 solutions.

Finally, the effect of adding oleic acid to a liquid scintillator solution was examined experimentally. Adding oleic acid to liquid scintillator in the concentration that would have been found in a composite scintillator containing 30% by mass CeF_3 resulted in the data point shown in Figure 3.18. The observed light yield of the liquid scintillator and oleic acid solution was 2.06 photons/keV, slightly below the 2.43 photons/keV measured for the 30% CeF_3 solution.

The 66% reduction in light yield observed in the liquid scintillator solution following the addition of oleic acid indicated a quenching effect. To confirm this phenomenon, reagent grade (99% purity) oleic acid was added dropwise to a cuvette containing ∼1.5 mL liquid scintillator. Radioluminescence spectroscopy, performed as described in Section 4.3.2, showed that oleic acid dramatically decreased the luminescence, as shown in Figure 3.19.

Some reduction in radioluminescence is expected from the addition of an inert substance to liquid scintillator. The predicted decrease in radioluminescence was calculated based on the assumption that it decreases as the proportion of the volume
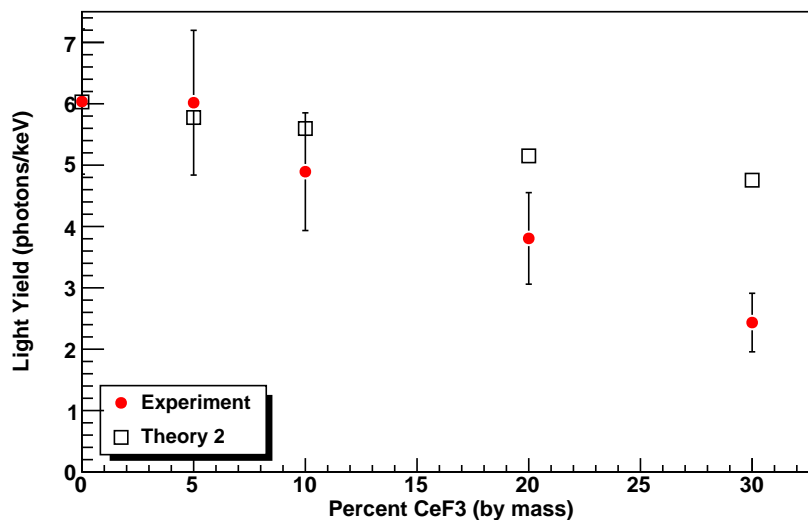
Figure 3.17: Calculations of the expected light yield, based on the second theory, displayed a reduced light yield compared with that shown Figure 3.16. However, the experimentally observed light yield was still lower. The light yields were calculated based on a model utilizing data from the NIST ESTAR database.[oSa] The errors were calculated using the resolution measured by the Gaussian fitting routine.

consisting of liquid scintillator decreases,

$$\text{Total RL} = I_0 \times \frac{V_{LS}}{V_{LS} + V_O} \tag{3.18}$$

where I_0 is the radioluminesence of the original liquid scintillator solution before the addition of oleic acid, V_{LS} is the volume of liquid scintillator present, a constant, and V_O is the volume of oleic acid. However, Figure 3.20 shows that the actual reduction is much more significant. Even following the addition of four drops of oleic acid, equivalent to only 6% of the volume of liquid scintillator present, the decrease in radioluminescence is greater than can be attributed solely to the added volume.

Two possible explanations were developed to explain the quenching of the scintillation light by oleic acid. The first explanation was a chemical reaction between one of the wavelength-shifting dyes and oleic acid. This was ruled out by confirming the quenching effect of oleic acid on toluene alone. High-purity oleic acid was added dropwise to a cuvette that had been filled halfway with toluene, a volume of approximately 1.5 mL. Following the addition of each drop of oleic acid, the stopper was replaced in the cuvette and the cuvette was shaken. The addition of oleic acid
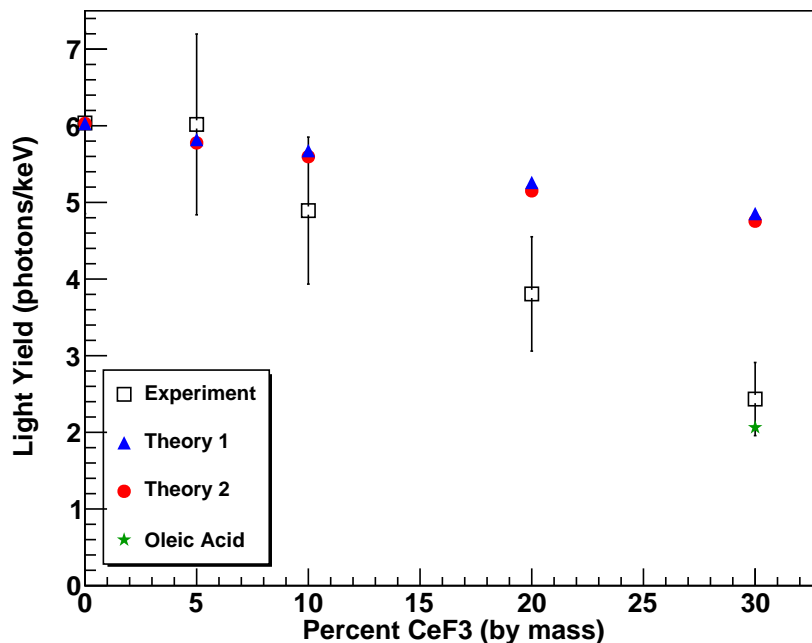
Figure 3.18: Comparison between experimentally observed light yield, light yield as predicted in Figures 3.16 and 3.17, and oleic acid in liquid scintillator without CeF_3 nanoparticles. The mass of oleic acid calculated to be present in the 30% CeF_3 solution was added to a liquid scintillator solution, resulting in the single point shown. This point suggests that the reduction in light yield from the predicted values was due to excess oleic acid remaining from the CeF_3 synthesis.

quenched the radioluminescence of toluene, as shown in Figure 3.21.

The second explanation for the observed quenching was a transfer of energy from the toluene to the oleic acid. This explanation was the best fit for the observed behavior. The precise energy-transfer mechanism responsible was not identified; however, two possible quenching mechanisms are oxygen quenching and non-radiative energy transfer to oleic acid. Oxygen has a quenching effect on many organic solvents, including toluene. [Pri53] [LB66] Atmospheric oxygen, dissolved in a toluene-based scintillator solution, competes with the transfer of energy from toluene to solutes. [Bar58] There are several mechanisms by which the presence of oxygen can affect the luminescence of an aromatic molecule. Energy can be transferred from toluene to oxygen as the result of a collision. The paramagnetism of a nearby oxygen molecule can enable toluene to transition from the singlet state to the otherwise-forbidden triplet state. Or the excited states of toluene can be quenched directly, as energy is transferred to oxygen, which has no luminescent transitions to its ground state.
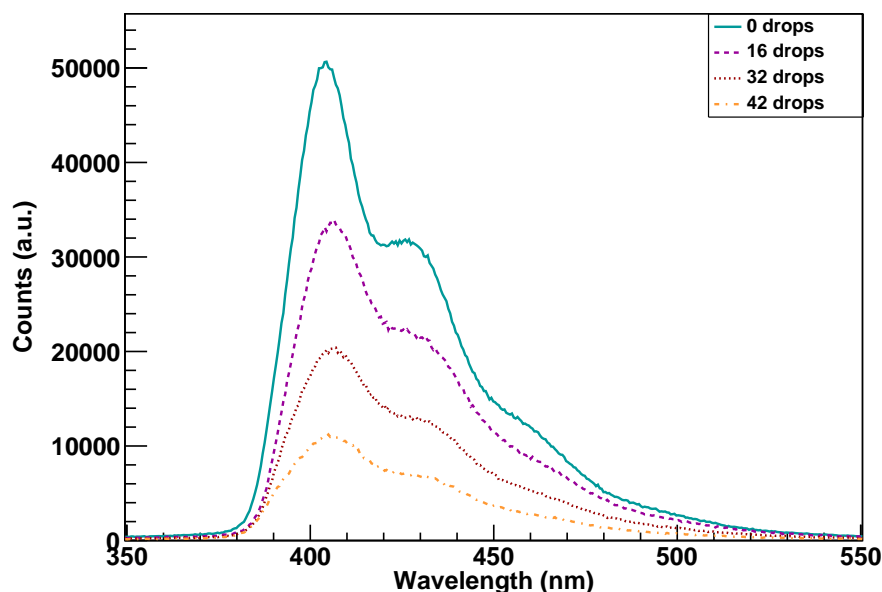
Figure 3.19: Radioluminescence of liquid scintillator alone and after the addition of 16, 32, and 42 drops of high-purity oleic acid. A figure containing spectra for intermediate amounts of oleic acid is available in Appendix A.

[Bir70]

Both dissolved atmospheric oxygen and the oxygen incorporated in oleic acid are present in liquid scintillator solutions containing CeF_3 nanoparticles. The mole fraction solubility of oxygen in toluene is 9.22×10^{-4}. [Fie74] Therefore, a cuvette containing 3.5 mL of toluene (the concentrations of PPO and POPOP are negligible, so this applies to liquid scintillator as well) contains 0.033 moles of toluene and 3×10^{-5} moles of atmospheric oxygen. The amount of oleic acid present as capping ligands on CeF_3 nanoparticles can be estimated. Oleic acid molecules bond to nanoparticle nucleation sites by means of their carboxylic acid groups, which can be seen in the chemical structure shown in Figure 3.22. A typical length for a carbon-oxygen bond is 1.432 Å. [Lid09] Assuming that a carboxylic acid group covers a circular region of a CeF_3 nanoparticle whose diameter is equal to three times the bond length, to account for the two carbon-oxygen bonds and the distance to the next capping ligand, results in a covered area of 0.145 nm^2. The total surface area of a 10 nm diameter spherical nanoparticle is 314 nm^2, so 2167 oleic acid ligands are required to cap each nanoparticle particle. The 30% mass-loaded solution contains 7.504 g CeF_3, equivalent to 0.038 moles. Therefore, 82.3 moles of oleic acid are present

49
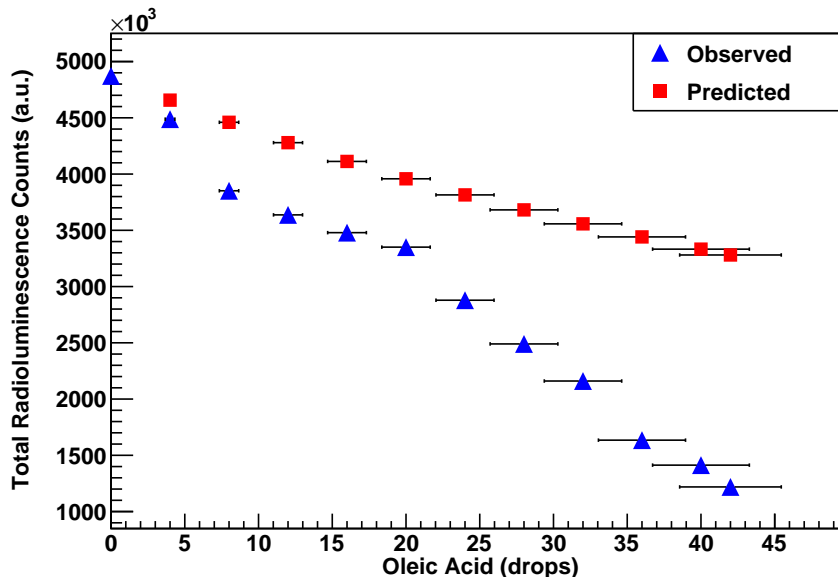
Figure 3.20: Total number of counts in radioluminescence spectra, as shown in Figures 3.19 and A.1, as a function of the number of drops of oleic acid added to the cuvette. The observed decrease in the radioluminescence was greater than the decrease due to the volume of oleic acid, as predicted by Equation 3.18, leading to the conclusion that oleic acid quenches the liquid scintillator. The error in the drop size was determined by measuring the masses of an ensemble of 100 drops of oleic acid, which resulted in a normal distribution with a mean mass of 20.64 mg and a standard deviation of 1.68 mg. Variations in the drop size were the dominant source of error.

as ligands, resulting in 164.7 moles of oxygen.

The mechanisms by which oxygen reduces the luminescence of toluene, particularly the effects due to paramagnetism, may conceivably be inhibited by the presence of carbon, hydrogen, cerium, and fluorine atoms surrounding the oxygen of the carboxylic acid group. Likewise, the bond configurations of the carboxylic acid oxygen atoms may result in different direct energy transfer mechanisms than are observed for dissolved atmospheric oxygen. Nevertheless, the amount of oxygen added to the liquid scintillator when CeF_3 nanoparticles are introduced is so much greater than the amount absorbed from the atmosphere, that if even a fraction of the typical oxygen quenching occurs for oleic acid, this phenomenon could account for the observed decrease in luminescence.

Another potential quenching mechanism is the non-radiative transfer of energy from excited toluene molecules to the π-bonds of oleic acid. As seen in Figure 3.22,
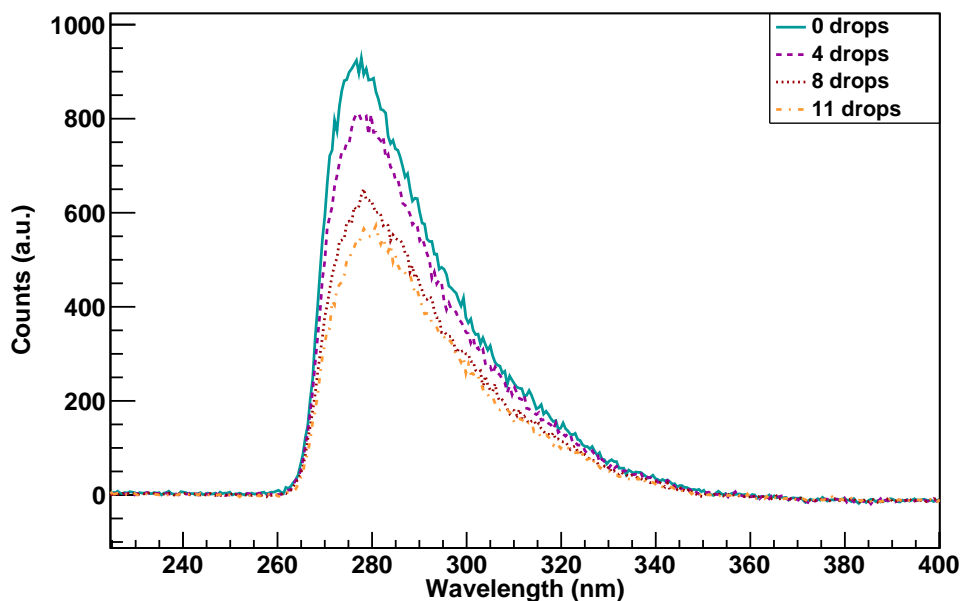
Figure 3.21: Radioluminescence of toluene alone and after the addition of 4, 8, and 11 drops of high-purity oleic acid, showing a substantial decrease in radioluminescence. This indicates that the quenching effect of oleic acid on liquid scintillator does not result from a chemical reaction between oleic acid and either of the wavelength-shifting dyes.
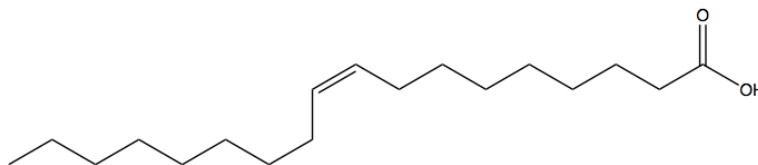
Figure 3.22: Atomic structure of oleic acid. An oleic acid molecule bonds to CeF_3 nanoparticles by means of its carboxylic acid [-COOH] group. Possible quenching mechanisms involve either the oxygen atoms present in the carboxylic acid group or the two double bonds.

oleic acid has two double bonds, each of which incorporates a π-bond as described in Section 2.7. As in any other organic compound containing a double or triple bond, the absorption of energy by a π-electron results in a transition to an excited state. However, the de-excitation processes available to oleic acid do not result in luminescence. Therefore, the transfer of energy from excited toluene molecules to either free or bound oleic acid molecules would decrease the observed luminescence.

The negative effect of oleic acid on the liquid scintillator light yield indicates that extra care must be taken in selecting capping ligands for scintillating nanoparticles. The CeF_3 dispersions that were characterized and tested in the beam line at LANSCE were prepared before the quenching had been attributed to the capping ligand.

CHAPTER IV

Characterization Techniques

4.1   Introduction

The characterization techniques described here are used primarily to answer two questions about samples of nanocomposite scintillators: the size of the particles, and the quality and quantity of light they emit. As discussed in Section 4.2, the size of the fabricated material is critical to allow transmission of light through the scintillator. The primary methods of determining particle size are structural characterization techniques, such as x-ray diffraction (XRD) and transmission electron microscopy (TEM), but ultraviolet/visible spectroscopy (UV/Vis), an optical technique, can also provide valuable information. Using multiple methods to determine particle size is advantageous because together they provide greater certainty and additional information about size variation.

Optical and radiation characterization provides information on the quantity of scintillation within the nanocomposite and the quality of the light produced. Optical characterization techniques, such as photoluminescence spectroscopy (PL), radioluminescence spectroscopy (RL), and UV/Vis, produce data on the wavelengths of light that are excited, emitted, and transmitted, in response to both optical and radiation stimulation. Since only samples that respond to RL may respond to γ-rays, this technique also indicates whether radiation characterization is likely to produce useful results. For samples with noticeable RL, radiation characterization is used to determine the light yield, resolution, and peak-to-Compton ratio. Together, these techniques produce a broad array of critical information about samples of scintillating materials.

4.2 Structural Characterization Techniques

In order to detect radiation interactions in a scintillator, the scintillation light must be collected. Ideally, even scintillation photons emitted deep within a scintillator should be detectable by a light-collection device at its surface. This requires a highly transparent scintillator material. Nanocomposite scintillators use a matrix material that is transparent, meaning that scintillation light is neither absorbed nor scattered by it. [McK07b]

Due to their small size, the scattering mechanism for the nanoparticles present in a nanocomposite scintillator can be approximated by Rayleigh scattering. Rayleigh scattering occurs when light is scattered by particles whose diameters are at least several orders of magnitude smaller than the wavelength of the light, and can be described by

$$\frac{I_s}{I_i} = \frac{8\pi^4 N}{\lambda^4 r^2} \left(\frac{d}{2}\right)^6 \left|\frac{m^2 - 1}{m^2 + 2}\right|^2 (1 + \cos^2 \theta) \tag{4.1}$$

where I_s/I_i is the ratio of scattered to incident light, N is the number of particles, λ is the wavelength of the light, r is the distance from the particle to the detector, d is the particle diameter, m is the ratio of the index of refraction of the particles to the index of refraction of the medium, and θ is the scattering angle. [Boh83] Since light scattering decreases with the particle diameter raised to the sixth power, nanoparticles suspended in a matrix should exhibit very little scattering, regardless of the difference between indices of refraction.

Since the high transparency to scattering of nanoparticles is an advantage of nanocomposite scintillators, determining the size of fabricated particles was extremely important. The nanoparticle size was measured using two techniques: transmission electron microscopy and x-ray diffraction.

4.2.1 Transmission Electron Microscopy

In TEM, a beam of electrons from an emission source is directed at a sample.[Ege05] The transmitted electrons are collected and used to form an image of the sample through the optical process shown in Figure 4.1.

The electrons needed for TEM are produced using either a thermionic source or a field-emission gun and are accelerated by an anode. A series of condenser lenses are used to create a near-parallel electron beam incident on the specimen. The atoms of the specimen scatter some of the electrons. Electrons exiting the specimen are dispersed and recombined by the objective lens, forming an image. After passing
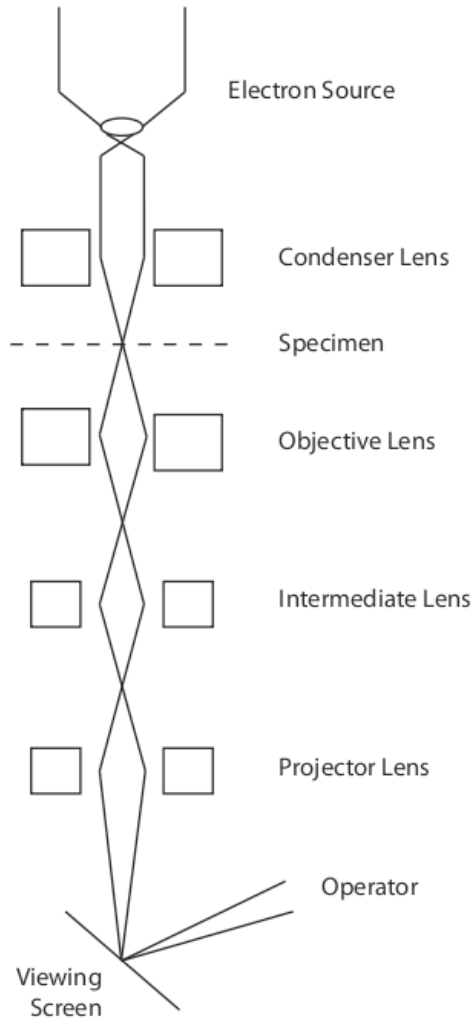
Figure 4.1: Generalized diagram of the optical process used to produce TEM images of a specimen. Electrons produced by an electron source are directed onto the specimen by the condenser lens. The scattered electrons are diffracted and recombined by the objective lens to form an image of the specimen. The projector lenses enlarge the image produced by the objective lens, before it is projected onto a fluorescent viewing screen.

through a series of intermediate and projector lenses, the image is projected onto a fluorescent viewing screen.[Wil09] The transmission electron microscope used for this work was a JEOL JEM-300F Field Emission Electron Microscope with a maximum obtainable resolution of 0.17 nm. In this machine, electrons are produced by a tungsten field-emission gun and accelerated to 300 kV.

Specimens for TEM analysis were prepared from samples of nanoparticles suspended in liquid scintillator or other solvents. A single drop of the suspension was dropped onto a 400-mesh copper grid, and the solvent was allowed to evaporate. Nanoparticles in the grid spaces could be examined using the TEM.

TEM images have higher resolution than can be obtained using a light microscope. The maximum obtainable resolution of a light microscope, imposed by the wavelength range of visible light, is 330 nm. [Wil09] In a TEM apparatus, resolution is derived instead from the wavelength of the electrons. The electron wavelength is calculated using the relativistic form of the de Broglie equation

$$\lambda = \frac{h}{p} = \frac{h}{\sqrt{2m_0 K \left(1 + \frac{K}{2m_0 c^2}\right)}} \tag{4.2}$$

where h is Planck's constant, p is the electron momentum, m_0 is the electron rest mass, K is the electron kinetic energy, and c is the speed of light. So for a TEM machine, such as the one used for this work, that is capable of accelerating electrons to 300 kV, the theoretical maximum resolution is 1.97 pm. However, the actual resolution obtainable using existing TEM machines is limited by lens aberrations, and the best obtained resolution reported at the time of this writing is 50 pm. [Ern09]

4.2.2   Analysis of Transmission Electron Microscopy Images

The analysis process for TEM images of nanoparticles, such as the one shown in Figure 4.2, involves using software to increase the contrast of the image, locate particles, and measure their sizes. The program used to perform this task is ImageJ, a public-domain image-processing code developed at the National Institutes of Health (NIH). ImageJ is widely used for analysis of digital images. The use of software allows TEM image analysis to be performed more quickly and with greater reproducibility than analysis using the human eye, but still possesses some limitations.

The first step of the analysis process is the setting of upper and lower thresholds for the image brightness. ImageJ assigns each pixel of the image a brightness value on a scale from 0 to 256, where a pixel with a brightness value of 0 is black. Areas
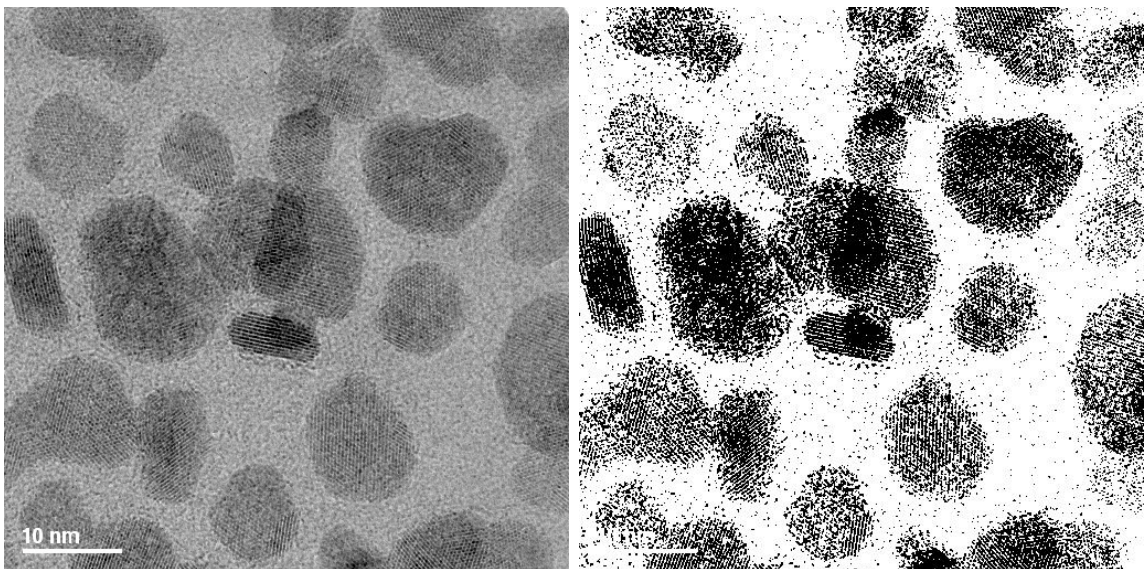
Figure 4.2: A sample TEM image of CeF$_3$ nanoparticles, before (left) and after (right) setting thresholds. The upper threshold has been set to 104 (on a 256-bit scale) and the lower threshold has been set to 0. ImageJ highlights pixels whose brightness values fall within the threshold range. The poor contrast between nanoparticles and background makes it difficult to highlight nanoparticles without also highlighting background pixels.

of the image with brightness values greater than or equal to the lower threshold and less than or equal to the upper threshold are identified as objects of interest, and are highlighted to distinguish them from the background, as shown in Figure 4.2. In analyzing images of nanoparticles, the lower brightness threshold is always set to zero. Areas of nanoparticles may appear darker because their orientation is favorable for Bragg scattering or because they are thicker than surrounding objects. Although thickness may be an indicator of overlapping nanoparticles, there is no need to exclude darker particles from the analysis.

Selecting the best value for the upper brightness threshold is challenging. If the threshold is set too low, not enough pixels in some particles will be highlighted for the particles to be recognized by ImageJ's analysis routine. If the threshold is set too high, the particle sizes calculated by the analysis routine may be inaccurate due to the addition of background pixels and the software's inability to distinguish between neighboring particles. Both of these sources of error are demonstrated by Figure 4.2. Several particles have not been completely highlighted, and will be missed by the analysis routine, while the central cluster of particles will be treated as if it were a

single particle.

One method used to select the upper brightness threshold was to determine the value which resulted in the largest number of particles identified by the analyzer. Sample results of this method are shown in Figure 4.3 for the image shown in Figure 4.2 and for another image featuring more particles. In both cases, the number of particles found by ImageJ initially increases with the threshold, as more particles are identified. However, beyond a certain threshold value, the number of particles found decreases as particles are combined. The optimum upper brightness threshold was near 100 for both of the images shown in Figure 4.3.

Once the upper and lower thresholds have been set, particles are identified using ImageJ's particle analysis routine. This routine locates objects within specified size and circularity ranges and provides information about their areas. A demonstration of the objects identified is shown in Figure 4.4. The particle analysis routine includes an option to ignore particles that intercept the edge of the image, which is useful when there are many particles that are only partially visible. To enable ImageJ to accurately calculate the area, it is necessary to provide it with information about the image scale. Generally, the scale bar on the TEM image is used for this purpose - once ImageJ has been informed of the length of the scale bar in both pixels and nanometers, it is able to provide all measurements in either set of units.

Figure 4.4 illustrates the difficulty of accurately measuring nanoparticle areas using TEM. Even using the optimum brightness threshold, determined by the method shown by Figure 4.3, the particle outlines determined for many of the particles by ImageJ are smaller than their actual sizes. This problem arises from the lack of contrast between the particles and the background material, due to the small size of the particles. The lack of contrast between nanoparticles and their background material, as shown for decreasing particle sizes in Figure 4.5, results from the dependance of the scattering mechanisms utilized in TEM on particle size.[Pyr08] For this reason, TEM measurements were not used as the sole indicator of particle size, but were analyzed in conjunction with results from XRD and UV/Vis. TEM images were also a useful tool for qualitatively assessing the amount of variation in particle size through visual inspection.

TEM images provide information on the variation in particle sizes present in a sample. However, because each image only captures a small segment of the sample, data is not necessarily representative. For this reason, XRD, which can be used to estimate the average particle size, was employed as well.
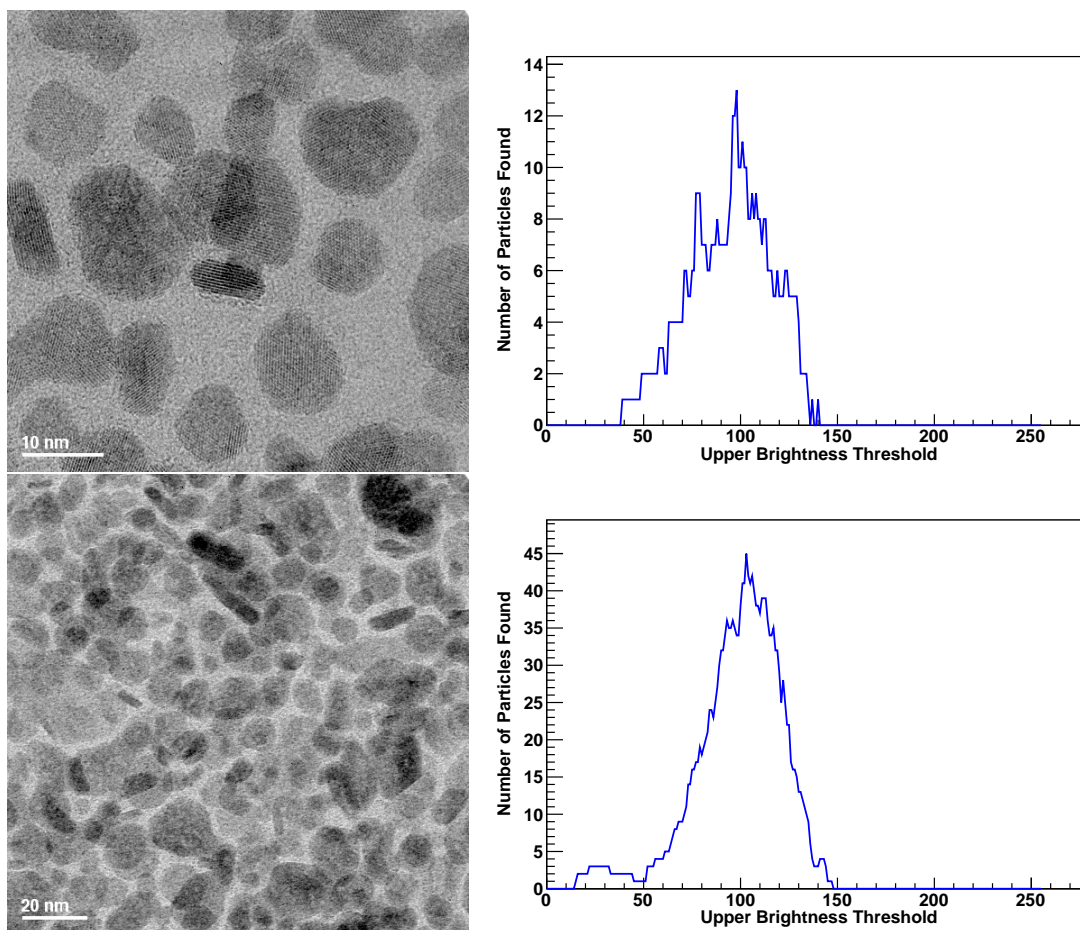
Figure 4.3: Variation in the number of particles identified by ImageJ. As the upper brightness threshold is raised, the number of particles found initially increases, as lighter particles are highlighted. However, if the upper brightness threshold is raised too far, spaces between particles are filled in, resulting in a decrease in the number of particles identified. Despite the difference in the number of particles in these two images, their optimum brightness thresholds are similar - the largest number of particles are found for a brightness of 98 for the upper image and 103 for the lower image. For these measurements, the lower brightness threshold was set to 0 and allowable particle sizes ranged from 4 nm^2 to infinity. The minimum allowable particle size was selected based on experimentation - allowing particles with sizes less than 4 nm^2 resulted in the misidentification of background regions in these low-contrast images.
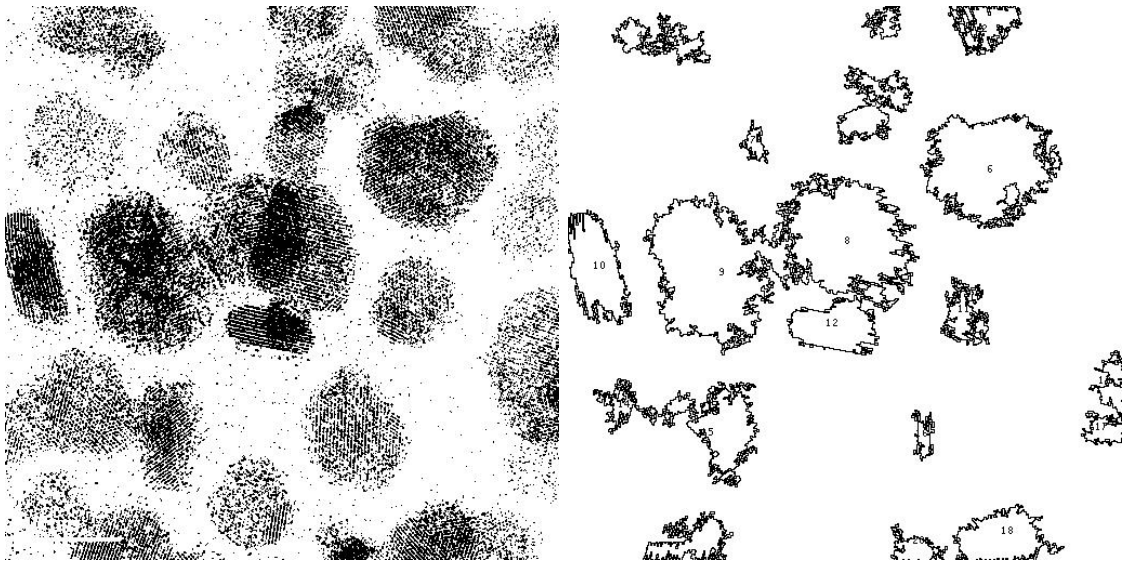
Figure 4.4: Particles identified by the particle analysis routine. The upper brightness threshold is set to 98 and the lower brightness threshold is set to 0, to maximize the number of particles identified in the right-hand image. Running the particle analysis routine with allowable particle sizes of 4 nm^2 to infinity and any degree of circularity results in the identification of the particles outlined in the left-hand image. Note that even with optimized brightness thresholds, the sizes of many of the computer-identified particles are significantly smaller than the sizes of the actual particles.
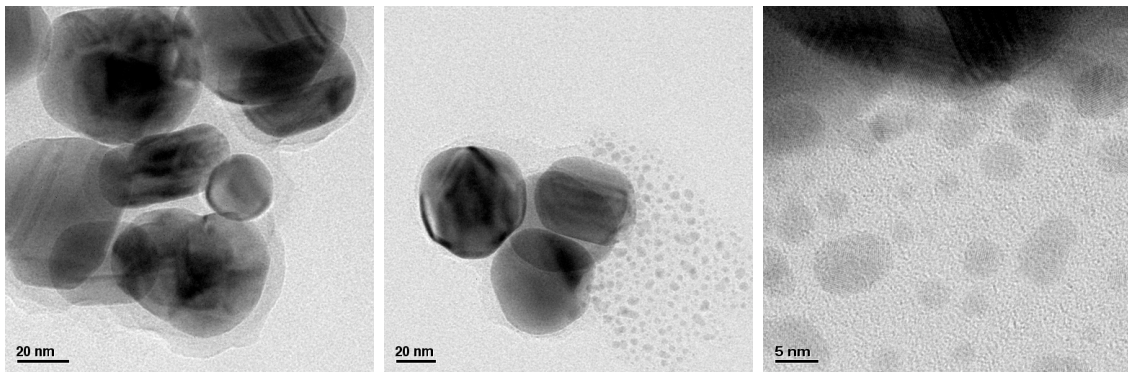
Figure 4.5: Crystalline silver nanoparticles coated with amorphous silica, in three different sizes. (The scale bar in the left-hand and middle images is 20 nm long; the scale bar in the right-hand image is 5 nm long.) Note that the image contrast decreases with particle size. Images provided by Leif Brown.
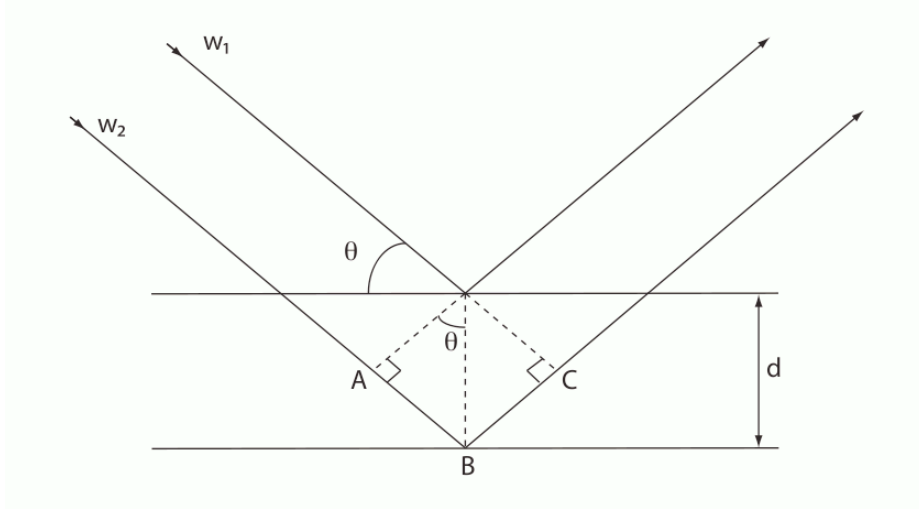
Figure 4.6: Waves with wavelength λ are incident on two planes of a crystal. As described by Equation 4.3, constructive interference requires that the additional distance, $\overline{ABC}$, traveled by wave w_2 be an integer multiple of λ. Otherwise, the waves will be out of phase as they exit the crystal, resulting in destructive interference. Figure drawn based on Cullity. [Cul56]

4.2.3 X-Ray Diffraction

In XRD, a beam of monoenergetic x-rays is diffracted by the crystal layers of a sample. The machine used for this work was a Siemens D5000 X-Ray Diffractometer.

The wavelengths of x-rays diffracted by a crystal obey the Bragg law, which describes the necessary conditions for constructive interference. Figure 4.6 shows two incoming waves, both having a wavelength λ, one of which is reflected off the crystal surface and one of which is reflected off the a layer of the crystal lattice that is a distance d below the surface. Since wave w_2 travels an additional distance $\overline{ABC}$, constructive interference requires that $\overline{ABC}$ be an integer multiple of the wavelength. Some straightforward trigonometry results in the Bragg law,

$$\overline{ABC} = n\lambda = 2d\sin\theta \qquad (4.3)$$

where θ is the angle of incidence of the waves. This equation applies to crystals with any number of planes. Therefore, x-rays that exit the crystal with wavelengths that are an integer multiple of one another interfere constructively, while x-rays that exit the crystal out of phase with one another interfere destructively. [Cul56]

Since x-rays are diffracted by multiple planes of a crystal, based on Equation 4.3 we would expect the overall effect to be destructive interference at all angles other

than those described by the Bragg law. However, this effect depends on the number of crystal planes and the path difference for two waves scattered from adjacent planes. If the path difference is significantly different from the wavelength or an integer multiple of it, then even waves reflected from planes near one another will have very different phases, and will interfere destructively. However, if the path difference for two waves scattered from adjacent planes is close to an integer multiple of their wavelength, then the phases of the reflected waves will be similar. Achieving a large enough difference in path lengths for complete destructive interference of a wave reflected from a layer close to the surface will require a very large number of crystal planes. For small particles, then, which possess a relatively small number of crystal planes, at angles close to the Bragg angle the destructive interference is imperfect.

4.2.4   Analysis of X-Ray Diffraction Data

The characteristics of the intensity distribution produced by small particles because of incomplete destructive interference can be described using the Debye-Scherrer equation

$$t = \frac{0.9\lambda}{\text{FWHM}\cos\theta} \tag{4.4}$$

where t is the thickness of the sample, λ is the wavelength of the incident x-rays, FWHM is the full width in radians of the intensity distribution at half its maximum value, and θ is the angle of the incident x-rays relative to the crystal surface. The full width at half maximum is inversely related to the sample thickness; thus, as the sample thickness (equal to the number of crystal planes multiplied by the distance between them) increases, the width of the diffraction curve decreases, approaching a delta function at the Bragg angle, as shown in Figure 4.7.

XRD spectra such as the one shown in Figure 4.8 can be used to calculate the approximate size of the sample nanoparticles, by assuming that a nanoparticle's thickness is identical to its diameter. However, corrections are necessary to obtain the correct x-ray wavelength. $K\alpha$ x-rays are emitted with two slightly different energies, resulting from the fine structure of the atom. $K\alpha_1$ x-rays are emitted following transitions from the L_3 level ($n=0$, $l=1$, $j=3/2$) to the K level ($n=1$, $l=0$, $j=1/2$), while $K\alpha_2$ x-rays are emitted following transitions from the L_2 level ($n=0$, $l=1$, $j=1/2$) to the K level. The wavelengths of the two x-ray lines are generally separated by about half a picometer - the copper $K\alpha_1$ and $K\alpha_2$ x-rays used in our system have wavelengths of 154.0 pm and 154.4 pm, respectively, corresponding to transition energies of 8048 eV and 8028 eV. [oSc] Therefore, accurate interpretation of an XRD spectrum
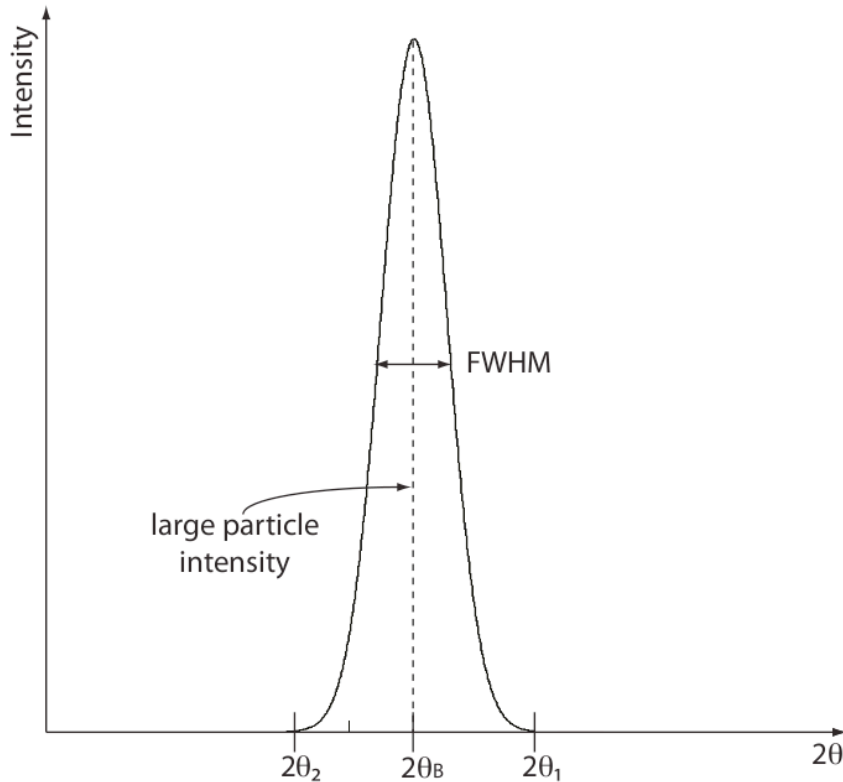
Figure 4.7: Intensity of diffracted light, as a function of twice the incident angle, for
small particles. As described by Equation 4.4, the destructive interfer-
ence is incomplete for angles close to the Bragg angle, θ_B, resulting in
broadening of the intensity peak. In comparison, light is diffracted from
a large particle only when the angle of incidence is exactly equal to the
Bragg angle, as shown by the dashed line.

requires that one component of the doublet be eliminated. [Coo74] The $K\alpha_1$ line is
more intense, so features attributable to $K\alpha_2$ x-rays are removed using a method
derived from the technique originally suggested by Rachinger. [Rac48] Rachinger's
technique assumes that the overlapping $K\alpha_1$ and $K\alpha_2$ peaks have the same shape and
that the region where the intensity of the $K\alpha_2$ peak is zero can be used to predict the
shapes of both peaks for all other regions.

Following the removal of the $K\alpha_2$ peak, remaining features are fitted to deter-
mine the full width at half maximum needed to apply the Debye-Scherrer equation.
The pseudo-Voigt function, a convolution of the Gaussian and Lorentzian distribu-
tions, is generally considered to be the optimal choice for fitting XRD data due
to its ability to model broadening from both experimental and physical sources.
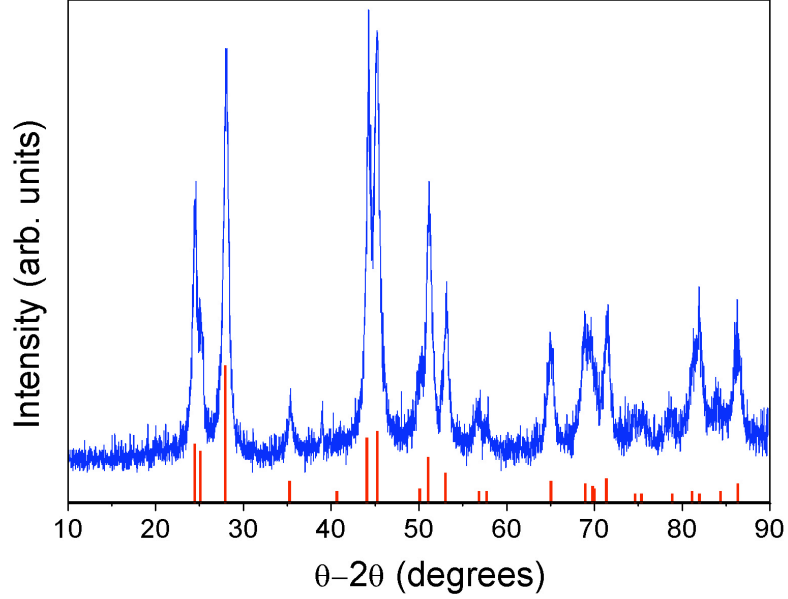
Figure 4.8: Sample XRD of CeF$_3$ nanoparticles (blue) and library spectrum (red). The library spectrum shows the angles at which Bragg diffraction is expected for CeF$_3$ crystals; here it verifies the identity of the fabricated material. Peak broadening is visible for peaks above about 60°.

[Tho87][Wer74][You82] It can be written as

$$f(\Gamma, \eta, x) = \eta \left/ \left[1 + \left(\frac{x - x_0}{0.5\Gamma} \right)^2 \right] + (1 - \eta) \exp \left[- \left(\frac{x - x_0}{b\Gamma} \right)^2 \right] \right. \qquad (4.5)$$

where $b = 0.5\sqrt{\ln 2}$, Γ is the full width at half the maximum intensity, and η is the fraction of the distribution that is described by a Lorentzian distribution (making (1-η) the fraction described by a Gaussian). [Wer74] A fitting routine was developed based on Equation 4.5 and employing four parameters: Γ, η, the centroid x_0, and a scaling factor I. The user-specified fitting range was used to determine the initial values of the centroid and Γ; the centroid was set at the midpoint of the fitting range and Γ was set as half the length of the fitting range. During the fitting process, the centroid was allowed to vary anywhere within the fitting range and Γ was allowed to range from zero to the entire length of the fitting range. The initial value for η was set at 0.5, and it was allowed to vary from zero to one. The scaling factor I, which represented the intensity of the peak, was user-specified and was allowed to vary within 10% of its initial value.

A sample fit is shown in Figure 4.9. The Pseudo-Voigt fit was applied between $2\theta=25.9°$ and $2\theta=28.3°$; these values were chosen to bring the reduced chi-square as

close to unity as possible, while requiring the fit to extend through the full width at half maximum. The intensity of the peak (in arbitrary units) was 5093.3 ± 0.275, and its centroid was located at $2\theta = 27.84° \pm 1.96 \times 10^{-5}$. Errors for the intensity and centroid were obtained from the Pseudo-Voigt fit. This fit is entirely Lorentzian, returning a value of 1 for η. The full width at half maximum was $(6.29 \pm 0.00132) \times 10^{-3}$ radians and the wavelength of the copper $K\alpha_1$ x-rays was 154.0 pm (the $K\alpha_2$ x-rays were removed before analysis). The Debye-Scherrer equation was used to estimate the particle size,

$$t = \frac{0.9 \times 154 \text{ pm}}{(6.29 \times 10^{-3}) \cos{(27.84/2)}} = 22.70 \text{ nm} \tag{4.6}$$

The error in the particle size may be calculated by propagating the errors in the full width at half maximum and centroid.

$$\sigma_t^2 = \left(\frac{\partial t}{\partial x_0}\right)^2 \sigma_{FWHM}^2 + \left(\frac{\partial t}{\partial \theta}\right)^2 \sigma_\theta^2$$
$$= \left(-\frac{0.9\lambda}{(\text{FWHM})^2 \cos\theta}\right)^2 \sigma_{FWHM}^2 + \left(\frac{0.9\lambda}{\text{FWHM}} \frac{\sin\theta}{\cos^2\theta}\right)^2 \sigma_\theta^2 \tag{4.7}$$

$$\left(\frac{\sigma_t}{t}\right)^2 = \left(\frac{\sigma_{FWHM}}{\text{FWHM}}\right)^2 + \left(\frac{\sigma_\theta \sin\theta}{\cos\theta}\right)^2$$
$$= \left(\frac{1.32 \times 10^{-6}}{6.29 \times 10^{-3}}\right)^2 + \left(\frac{(0.5 \times 1.96 \times 10^{-5}) \sin(27.84/2)}{\cos(27.84/2)}\right)^2 \tag{4.8}$$
$$= 4.40 \times 10^{-8}$$

$$\sigma_t = (2.10 \times 10^{-4})(22.70 \text{ nm}) \Rightarrow t = 22.70 \pm 0.0048 \text{ nm} \tag{4.9}$$

The estimated sample thickness, 22.70 ± 0.0048 nm, is considered to be equivalent to the particle size. Since XRD spectra include refraction from many particles, this is an average size over the entire sample.

4.3   Optical Characterization Techniques

The light emitted by the CeF_3 nanoparticles in solution was characterized using PL, RL, and UV/Vis. These three methods of optical characterization provide distinct types of information on the solution. PL provides information on the excitation and emission wavelengths and their relative intensities. RL allows the response of the sample to one form of radiation, x-rays, to be observed and its wavelength and relative intensity to be measured. UV/Vis examines which wavelengths of light are
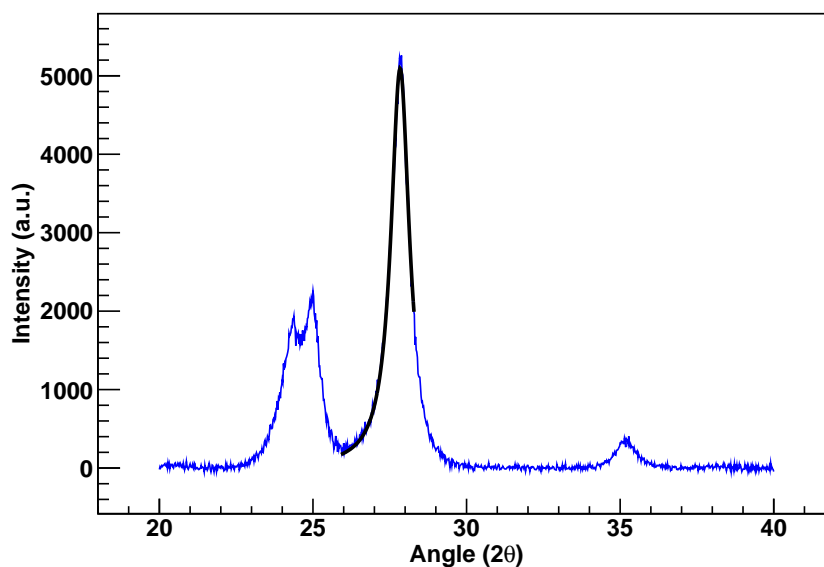
Figure 4.9: Pseudo-Voigt fit of peak in XRD spectrum of CeF$_3$. Fit was applied between 2θ=26.5 and 2θ=29; initial value of peak intensity was 5500.

transmitted through the sample, and which are absorbed by it. By assuming that the particles are small, so that they Rayleigh scatter light, we can also use UV/Vis to estimate the particle size.

4.3.1 Photoluminescence Spectroscopy

PL stimulates samples with light to determine the wavelength ranges of excitation and emission. When the energy of the incident light corresponds to an amount of energy required to excite an atom, energy (light) is absorbed. When the atom returns to its lower-energy state, a few nanoseconds later, a photon is emitted with an energy equal to the difference between the two states.

Light for the PL apparatus is generated by a lamp and directed into the excitation monochromer, as shown in Figure 4.10. Light entering the monochromer is directed onto a parabolic mirror. The flat wave front of light reflected by the mirror is directed at an adjustable diffraction grating. A diffraction grating is a mirror with many grooves etched into it at regular intervals, called the grating period, which determine the direction that incident light is reflected. The angle between the incident and diffracted beams is expressed by

$$\sin\theta = \frac{m\lambda}{l} \tag{4.10}$$
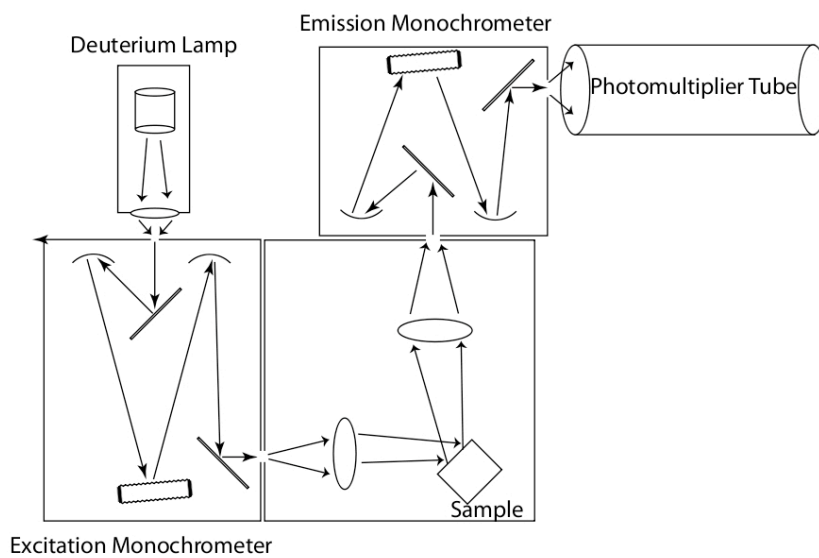
Figure 4.10: Light for the photoluminescence system is generated by a deuterium lamp. A series of lenses and mirrors directs the light onto a monochrometer and, from there, onto the sample. Light emitted by the sample also passes through a monochrometer before entering the detector, a photomultiplier tube.

where θ is the angle between the incident and diffracted light, λ is the light's wavelength, l is the grating period, and m is an integer. Since the angle of diffraction is a function of the light's wavelength, a diffraction grating spreads out the light. Light of the desired wavelength can then be directed onto the sample. Light emitted by the sample is also directed onto a monochrometer, and from there into a photomultiplier tube.

In order to determine the emission wavelength, the diffraction grating in the excitation monochrometer is tuned to a specific wavelength using a computer-controlled stepper motor. The emission monochrometer is then tuned through a range of wavelengths. The resulting spectrum shows the emission corresponding to the chosen excitation. The reverse is true in measuring the excitation wavelength - the emission monochrometer is tuned to a specific value, and the excitation wavelength is varied.

A sample PL spectrum, of the toluene-based liquid scintillator whose development is described in Chapter III, is shown in Figure 4.11. Two main peaks are visible in the emission, at 411 nm and 433 nm. Each peak corresponds to a different excitation wavelength (the hump in the spectrum near 460 nm likely indicates a third, minor,
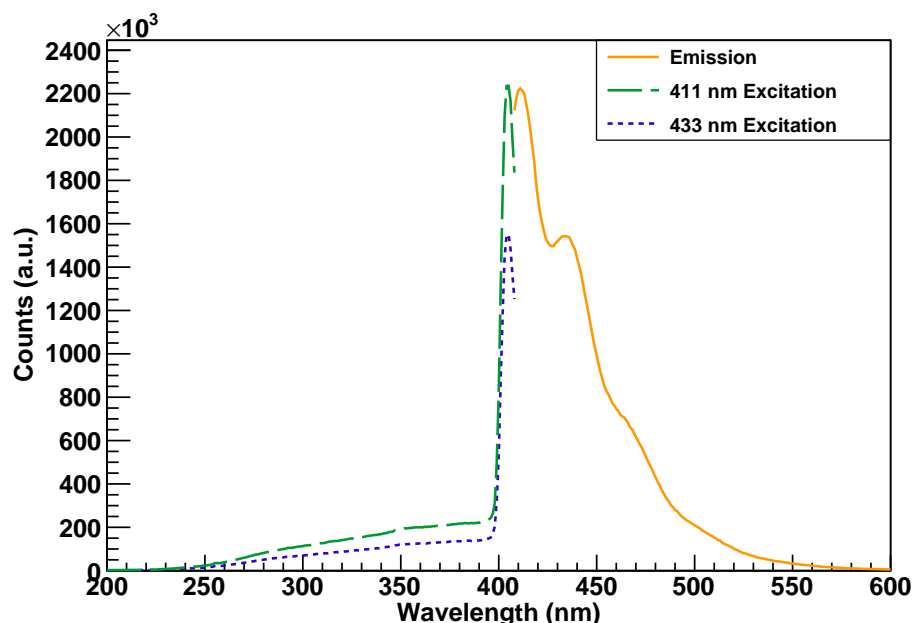
Figure 4.11: Photoluminescence of a toluene-based scintillator containing PPO and POPOP. The two primary peaks visible in the emission spectrum are produced by incident light at two different wavelengths.

excitation). The narrowness of the excitation peaks is typical of liquid scintillators.

The Photon Technology International TimeMaster steady-state fluorimeter and lifetime spectrometer was used for all of the PL measurements described here. As built, the apparatus is capable of utilizing light from 200 to 800 nm.

4.3.2 Radioluminescence Spectroscopy

RL measures the intensity of the luminescence of a sample across a specified wavelength range in response to x-ray absorption. The RL of a sample is a better predictor of its γ-ray response than its PL, thus, it was one of the most frequently used characterization techniques for this research.

In RL, a sample cuvette is placed in one of two positions in the x-ray enclosure, as shown in Figure 4.12. In the standard sample position, the cuvette is normal to both the x-ray tube and the liquid light guide. In the second position, used to measure the surface luminescence, the sample is placed at a 45° angle relative to both the x-ray tube and the liquid light guide. X-rays are generated from an x-ray tube with a molybdenum target. The Kα_1 and Kα_2 x-rays are emitted at energies 17.479 and 17.374 keV, respectively. [oSc] The scintillation light produced by the sample in response to the x-rays travels to the monochrometer, a Princeton Instru-

68
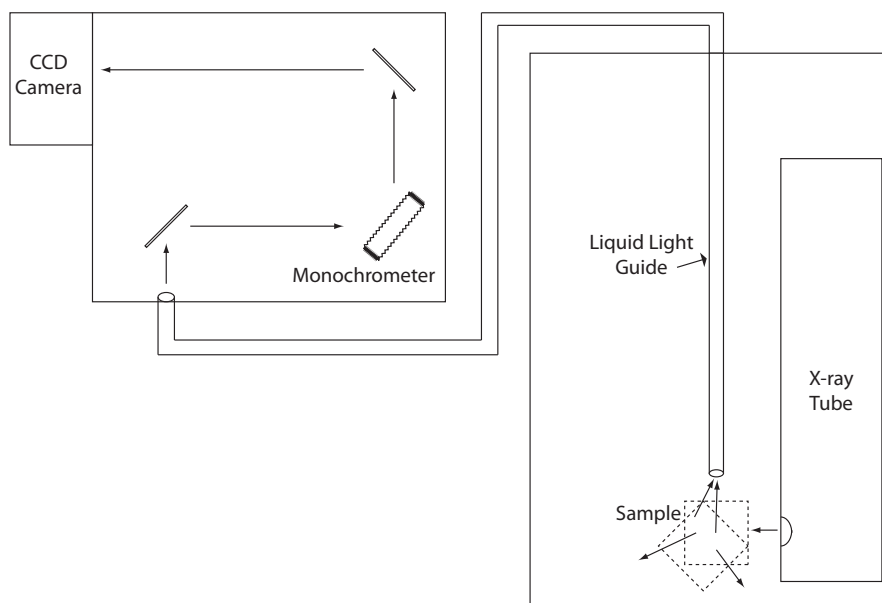
Figure 4.12: In the RL system, luminescence is induced by x-rays. The scintillation light passes through a fiber-optic cable into a monochrometer system, and from there into a CCD for detection.

ments/Acton SpectraPro 2300i, through the light guide. The monochrometer grating typically used allows a broad range of light to pass, so the entire spectrum of interest, 200 nm to 800 nm, can be measured without changing the monochrometer position. From the monochrometer, light enters a CCD for collection. The monochrometer grating focuses the entire spectrum onto the CCD, making it possible to integrate the radioluminescence over time, an option not available with the PL system.

A sample RL spectrum is shown in Figure 4.13. The material, PPO, POPOP, and CeF_3 nanoparticles in a poly(methyl acrylate)-poly(styrene)-poly(divinylbenzene) polymer, has a maximum RL near 420 nm, similar to the RL wavelength observed for liquid scintillator. Background subtraction was performed for all RL spectra.

4.3.3 UV-Visual Spectroscopy

UV/Vis measures the transmission of light through samples. The spectrometer used for these measurements was a Varian Cary 5000 UV-Vis-NIR Spectrophotometer. The principle behind its operation is shown in Figure 4.14.

Light generated by a lamp is directed into a double monochrometer. Two lamps are used, a deuterium lamp for the ultraviolet range and a quartz halogen lamp for
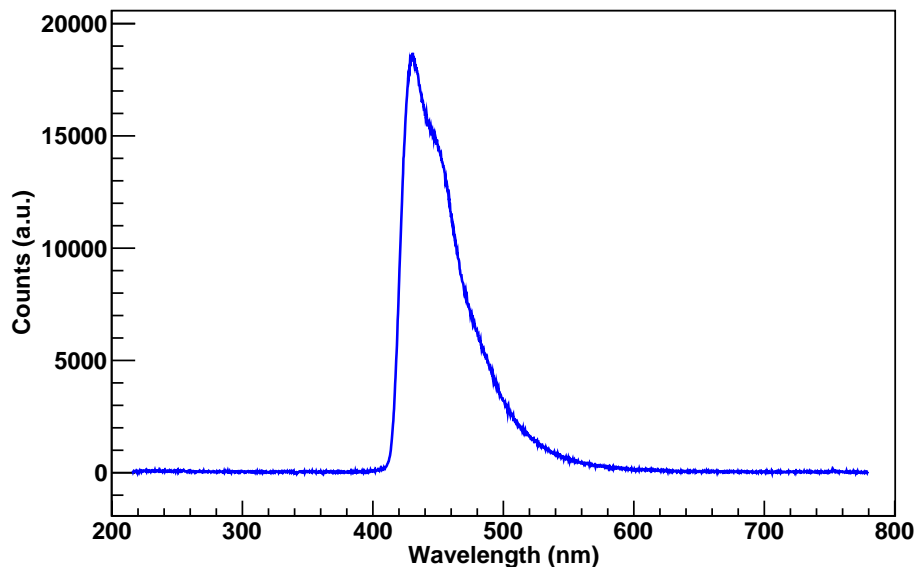
Figure 4.13: Radioluminescence of CeF_3 nanoparticles, PPO, and POPOP suspended in a poly(methyl acrylate)-poly(styrene)-poly(divinylbenzene) polymer.
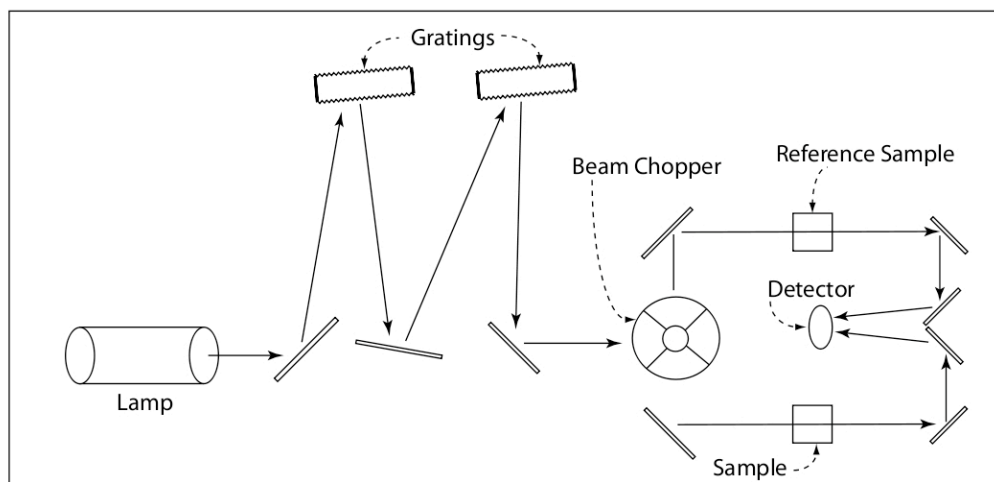
Figure 4.14: The UV/Vis system measures the transmission of light through a sample. Light is generated using a deuterium lamp in the ultraviolet range and a quartz halogen lamp in the visible range. The light passes through a double monochrometer, required because of the broad range of wavelengths to be examined. The light exiting the monochrometers is split and travels along two paths, one through the sample and one through a reference. The difference between the light detected from the two paths is used to determine the relative transmission.

70

the visible range; the apparatus switches lamps at 335 nm. A double monochromer is required to cover the entire wavelength range. The monochromer scans through the wavelength range selected by the user. For each wavelength, the light from the monochromer is directed onto a beam chopper. The beam chopper alternates the beam path along which the light is permitted to travel.

There are two beam paths, one passing through the sample and one passing through a reference sample, used to determine the relative transmission. After passing through the sample, the light enters a detector. The fractional intensity is determined by comparing the light transmitted through the sample with the light transmitted through the reference, generally a blank sample. Baseline subtraction is performed; the baseline can be measured at any time, and is typically repeated before each set of measurements. Once the background has been subtracted from the relative transmission, the spectrometer produces a transmission spectrum for the sample.

Particle size can also be measured using transmission spectra by modeling the expected scattering of light. By integrating the general expression for Rayleigh scattering, we are able to derive a cross-section

$$\sigma_{RS} = \tag{4.11}$$

$$= \int_0^{2\pi} \int_0^{\pi} \frac{(2\pi)^4}{2r^2\lambda^4} \left(\frac{d}{2}\right)^6 \left|\frac{m^2-1}{m^2+2}\right|^2 \left(1+\cos^2\theta\right) r^2 \sin\theta d\theta d\phi \tag{4.12}$$

$$= \frac{2\pi^5}{3} \frac{d^6}{\lambda^4} \left|\frac{m^2-1}{m^2+2}\right|^2 \tag{4.13}$$

where d is the nanoparticle diameter, λ is the light wavelength, and m is the ratio of the refractive indices of the nanoparticle and the matrix material. The Rayleigh scattering cross-section can be related to the observed transmission using the expression

$$\frac{I}{I_0} = e^{-N\sigma\ell} \tag{4.14}$$

$$= \exp\left[-\frac{v_{frac}}{\frac{4}{3}\pi\left(\frac{d}{2}\right)^3} \frac{2\pi^5}{3} \frac{d^6}{\lambda^4} \left|\frac{m^2-1}{m^2+2}\right|^2 \ell\right] \tag{4.15}$$

$$= \exp\left[-4\pi^4 v_{frac} \frac{d^3}{\lambda^4} \left|\frac{m^2-1}{m^2+2}\right|^2 \ell\right] \tag{4.16}$$

where I/I_0 is the fractional transmission, N is the number of particles present, σ is the interaction cross-section, and ℓ is the distance traveled by the light through the

particles. The number of particles present, N, is calculated by dividing the fractional volume of nanoparticles, v_{frac}, by the nanoparticle volume Since UV-visual spectroscopy is performed using a standard quartz cuvette, ℓ was equal to one centimeter for all measurements.

A fitting routine was developed to fit transmission data to the Rayleigh scattering expression as a function of two parameters: the nanoparticle diameter d and a scaling factor A

$$\frac{I}{I_0} = A \exp\left[-4\pi^4 v_{frac} \frac{d^3}{\lambda^4} \left|\frac{m^2 - 1}{m^2 + 2}\right|^2 \ell\right]. \tag{4.17}$$

An example of a fit, using data from CeBr$_3$ nanoparticles, is shown in Figure 4.15. The figure also displays the results of a fit using Equation 4.17, which was applied between 350 and 800 nm. The fitting function produced an estimated particle diameter of 11 nm $\pm$ 51.6 fm and a scaling factor of $0.776 \pm 4.61 \times 10^{-6}$. Rayleigh scattering is a poor fit to the experimentally observed transmission below 350 nm. Samples of nanoparticles measured using UV/Vis were typically suspended in the standard liquid scintillator solution or in another scintillating matrix. The Rayleigh scattering model does not take into account scintillation, so the absorption and isotropic emission of incident light appears as a lower-than-expected transmission.

4.4 Radiation Characterization Techniques

Since the goal of the CeF$_3$ nanoparticle research was to construct a detector for neutron-capture γ-rays, the radiation detection properties of the nanoparticles and potential matrix materials were of great interest. Measurement of the pulse height spectrum was used as a first check of samples, to determine whether γ-rays were detected and whether a photopeak was present. An associated measurement was the determination of the light yield, used to assess whether scintillation light was able to reach the PMT.

Pulse height spectra for liquid composite scintillators were obtained using the setup shown in Figure 4.16. The PMT (a Hamamatsu R2059 tube with a Hamamatsu E2979-500 socket, specifications given in Appendix B) was connected to a high-voltage power supply. During the course of the experiments, three different power supplies were used. The power supply used for most measurements of spectra was a LeCroy 1454 High Voltage Mainframe. Occasionally, a Caen A1733 12 channel HV board connected to a Caen SY1527 LC Universal Multichannel Power Supply System was used. Specifications for all electronics used are given in Appendix C. At typical
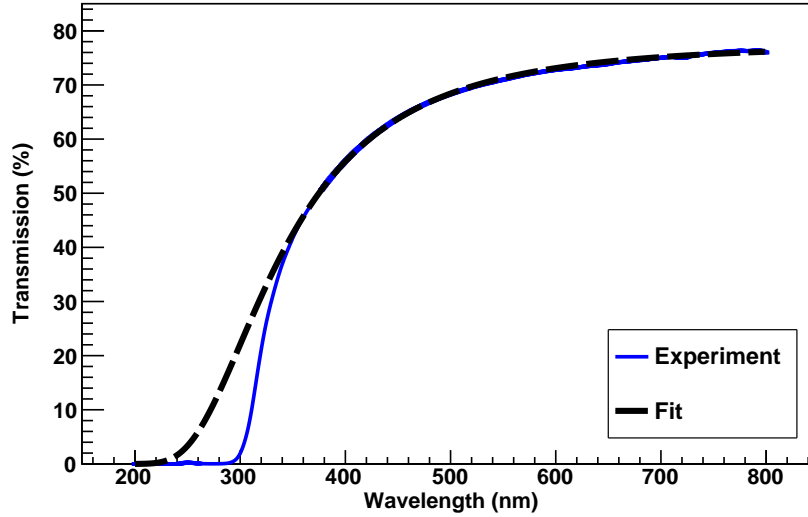
Figure 4.15: Transmission of light through CeBr$_3$ nanoparticles, and Rayleigh scattering fit. The Rayleigh scattering equation is not a good fit for the observed behavior below 350 nm, because it does not account for the absorption and re-emission of light through scintillation. The fit, based on Equation 4.17 and applied between 350 and 800 nm, has a scaling factor of $0.776 \pm 4.61 \times 10^{-6}$ and a particle diameter of 11 nm $\pm$ 51.6 fm.

operating voltages of 1500-3000 V, the LeCroy power supply had a voltage ripple of less than 100 mV peak-to-peak and the output voltage was within $0.1\% + 1.5$ V of the voltage setting. The Caen system had a voltage ripple of less than 30 mV peak-to-peak and the output voltage was within $0.3\% + 0.25$ V of the setting. Thus, at the PMT's recommended operating voltage of 2500 V, the expected output voltage of the LeCroy was between 2496 and 2504 V and the expected output voltage of the Caen system was between 2492.25 and 2507.75 V. Since both power supplies are expected to produce a voltage within one half of one percent of the requested voltage, no distinction was made between them during the data analysis.

The anode of the PMT was connected to a Caen V925 Quan Linear Fan-In Fan-Out Board. One channel from the fan-in fan-out was connected to a Caen V812 16-Channel Constant Fraction Discriminator. From the discriminator, the signal entered a Caen V462 Dual Gate Generator. Both channels of the gate generator were utilized to set the gate delay and the gate width. The output of the gate generator was connected to the trigger channel of a Caen V965 QDC. Another channel from the fan-in fan-out was connected to a 99-foot BNC cable, and from there to an input channel of the QDC. The 147-ns delay introduced by the BNC cable provided
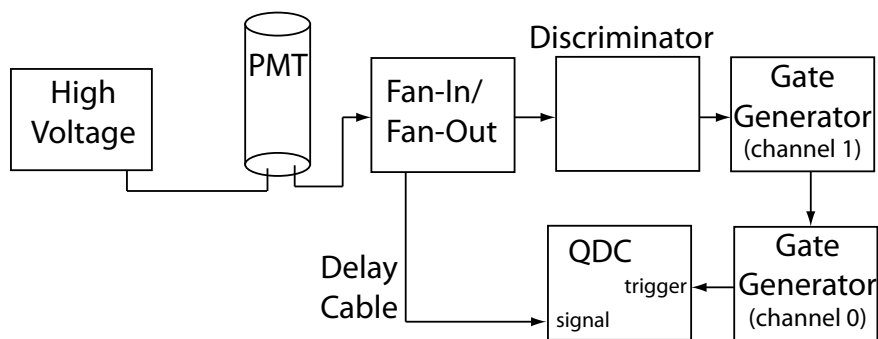
Figure 4.16: Electronics configuration for measurement of spectra. The signal from the PMT is split using a fan-in fan-out board. One output of the fan-in fan-out is used as a trigger signal for the QDC. A discriminator is used to set a minimum pulse height for triggering. A dual gate generator is used to delay the trigger signal and to set the length of the trigger. Another output of the fan-in fan-out is used as the signal input for the QDC. A 99-foot BNC cable is used to ensure that the signal arrives at the same time as the corresponding trigger.

sufficient time for the trigger signal to pass through the discriminator and the gate generator. However, it also resulted in signals with more prolonged rise and fall times than observed in the original pulses.

A standard quartz cuvette containing 3 - 3.5 mL of the composite to be measured was mounted on the PMT in one of two positions, as shown in Figure 4.17. In the first configuration, the PMT was positioned vertically and the cuvette was placed on its face. In this configuration, light had to pass through the 1 cm^2 bottom of the cuvette to enter the PMT. A silicon-based optical grease, Bicron BC-630, was applied between the cuvette and the PMT. In the second configuration, the PMT was positioned horizontally and optical grease was used to mate the side of the cuvette to the glass. The cuvette and PMT were placed in a darkbox.

Typically, a collimated ^{137}Cs source with an activity of approximately 287 μCi was used to measure the spectrum. Based on the pulse height spectrum, the energy resolution, light yield, and peak-to-Compton ratios were determined.

Vertical Configuration

Cuvette

Horizontal Configuration

PMT

PMT Base

Signal Cable   HV Cable
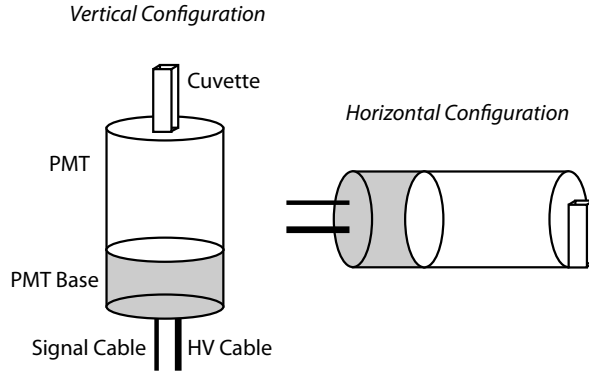
Figure 4.17: Vertical and horizontal configurations of the PMT and cuvette. In the vertical configuration, the 1 cm^2 cuvette base is in contact with the PMT surface. In the horizontal configuration, the 3.5 cm^2 side of the cuvette is in contact with the PMT surface. The path length traveled by light to reach the PMT is shorter in the horizontal configuration, which is an advantage when measuring solutions with poor transmission. However, for cuvettes that are not completely filled, the horizontal configuration positions the air-filled section of the cuvette against the PMT.

4.4.1 Characterization of Pulse Height Spectra

For samples containing little or no high-Z material, such as liquid scintillator alone or samples with low volumes of CeF$_3$ nanoparticles, the location of the Compton edge was used to determine the light yield. The channel of the Compton edge was calculated using a Gaussian fit, generated using the ROOT data analysis framework developed by CERN. Parameters governing the fit were the starting and ending bins. The goodness of the fit was judged using the reduced chi-square,

$$\frac{\chi^2}{\nu} = \frac{\sum\limits_{i=1}^{n} \left(\frac{x_i - \mu_i}{\sigma_i} \right)^2}{\nu} \tag{4.18}$$

where ν is the number of degrees of freedom of the n independent variables x_i with means μ_i and standard deviations σ_i. A good fit results in a reduced chi-square that approaches unity from above or below. [Leo94] Built-in commands in ROOT were used to determine the chi-square, based on a method suggested by Gagunashvili, and the number of degrees of freedom. [Gag05] [Gag] In order to ensure an appropriate range for the fit, its starting bin was required to fall in a lower channel than the centroid calculated by the fitting routine, and the fit was required to extend through

75

the end of the Compton continuum.

For samples whose spectra displayed both a Compton edge and a photopeak, the preferred method of determining the light yield used both features. These samples were typically compared with samples lacking a photopeak, so the Compton edge location was the primary figure of interest; however, fitting the photopeak as well improved the accuracy of the fit. Software was written to fit the Compton edge and photopeak with a double Gaussian function

$$f(x) = H_{PP} \exp \left\{ -\frac{1}{2} \left(\frac{x - x_{0,PP}}{\sigma_{PP}} \right)^2 \right\} + H_{CE} \exp \left\{ -\frac{1}{2} \left(\frac{x - x_{0,CE}}{\sigma_{CE}} \right)^2 \right\} \quad (4.19)$$

where the photopeak and Compton edge have heights H_{PP} and H_{CE}, respectively, centroids $x_{0,PP}$ and $x_{0,CE}$, and standard deviations σ_{PP} and σ_{CE}. However, the number of free parameters is four, not six, since the photopeak centroid and standard deviation depend upon the corresponding Compton edge characteristics,

$$x_{0,PP} = x_{0,CE}/0.72 \qquad\qquad \sigma_{PP} = \sigma_{CE}/\sqrt{0.72} \qquad (4.20)$$

The routine located the Compton edge and photopeak by looking for their characteristic changes in slope and fit individual Gaussian functions to them. The parameters of these fits were then used as initial parameters for H_{PP}, H_{CE}, $x_{0,CE}$, and σ_{CE} The fitting routine as permitted to vary these parameters, as long as they remained within one half of the initial value. An example of the final fit produced by this software is shown in Figure 4.18.

This fitting routine was only successful when applied to a spectrum with a well-defined photopeak. In addition, poorly-defined Compton edges, such as those seen in spectra from samples containing high concentrations of CeF_3 nanoparticles, could not be located by the software, and had to be fitted by manually selecting the limits of the fit range and providing initial conditions.

Although the fitting process can be used to calibrate the spectrum, an uncalibrated spectrum must be used to determine the light yield. The light yield is calculated by comparing the channel in which the Compton edge or photopeak appears for a sample with the location of the same feature in another sample or a scintillator of known light yield.

The resolution is calculated from the photopeak using the standard expression

$$R = \frac{\text{FWHM}}{E_0} \qquad (4.21)$$

76
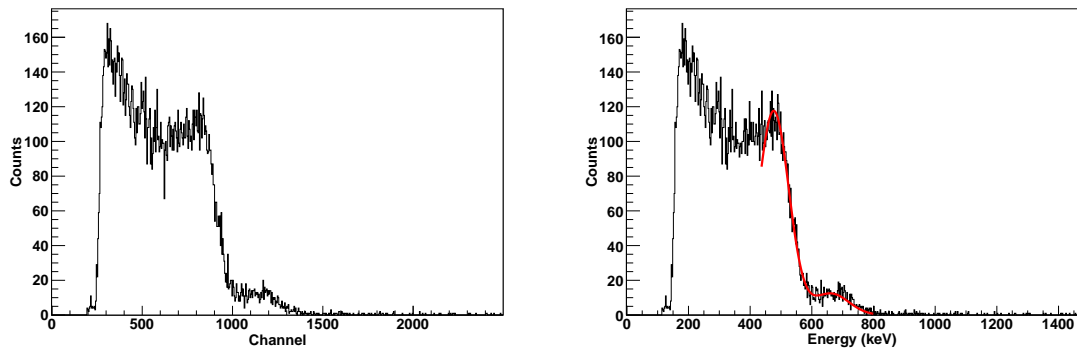
Figure 4.18: Spectrum of CeF$_3$ nanoparticles in liquid scintillator, before (left) and after (right) applying a fitting routine that uses the Compton edge and the photopeak to develop Gaussian fits for the entire range. Note that the fitting routine also uses the known photopeak energy (a ^{137}Cs source was used to obtain this spectrum) to calibrate the horizontal axis, replacing channel numbers with energy values.

where FWHM is the full width of the Gaussian distribution at half its maximum and E_0 is the centroid energy, usually 661.7 keV since a ^{137}Cs source was used for most characterization.

CHAPTER V

Characterization of Cerium Fluoride Nanocomposite Scintillators

5.1   Introduction

CeF$_3$ nanoparticles were characterized using the techniques described in Chapter IV in order to quantify the average particle size, evaluate its light yield, and determine whether and in what concentration the nanoparticles could be incorporated into a detector for beam line testing. Characterization using TEM provided little quantitative information regarding particle size. XRD and UV/Vis indicated that the average particle diameter was <20 nm and were in good agreement regarding the sizes of nanoparticles from different fabrication batches. The average particle size varied only by about one standard deviation between most batches of CeF$_3$, indicating that the fabrication process was reproducible. XRD and UV/Vis data were also used to examine the effect of the washing process on nanoparticle size and provided conflicting results, with XRD indicating that washing the nanoparticles to remove excess oleic acid did not result in agglomeration, and UV/Vis showing that a dispersion of washed nanoparticles had significantly lower transmission.

CeF$_3$ nanoparticles did not show significant light yield. The PL, RL, and UV/Vis of CeF$_3$ nanoparticles dispersed in liquid scintillator was dominated by the characteristic liquid scintillator emission; the CeF$_3$ emissions at 286 nm, 300 nm, and 340 nm, if present, excited the components of the liquid scintillator.
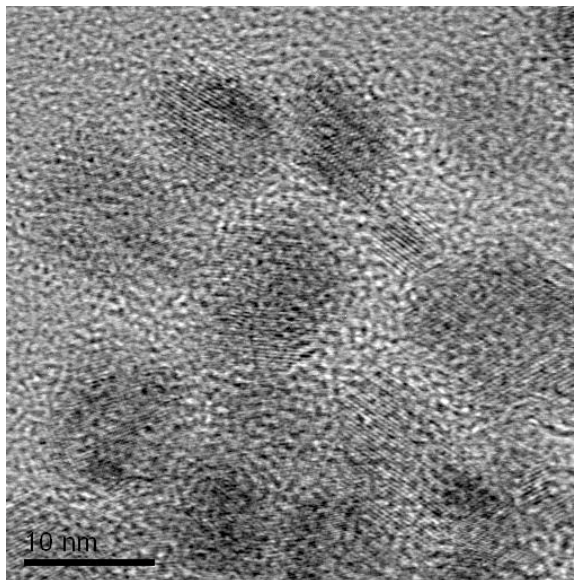
Figure 5.1: TEM of early sample of CeF_3 nanoparticles. The poor resolution of the image, which results from the small size of the particles, makes the nanoparticle boundaries difficult to discern, but most of these particles are less than 10 nm in diameter. There is greater variation in particle size than is seen in Figure 5.2.

5.2 Size Measurements Using Transmission Electron Microscopy

TEM of early batches of CeF_3 was performed sporadically. Two images taken soon after experimentation with CeF_3 nanoparticle fabrication had begun are shown in Figures 5.1 and 5.2. Both images show that the nanoparticles are ellipsoid in form and have diameters of less than 10 nm. Figure 5.2 also shows a single nanoparticle at high magnification, allowing the lattice structure of the crystal to be distinguished. The coherent lattice structure indicates that the nanoparticle is a single crystal.

Unfortunately, only a few TEM images were taken for each of these samples. The resolution of the image in Figure 5.1 makes the particles difficult to distinguish against the background, but a greater degree of size variation is evident than is seen in Figure 5.2. Since each TEM image captures only a small part of the sample, one of the disadvantages of the technique is the difficulty of determining whether an image is typical of the sample as a whole. Eight TEM images of one of these early batches of CeF_3 were analyzed to determine the particle distribution. A total of 263 particles were identified, with areas between 4 nm^2 and 5743 nm^2. The majority of the particles had areas in the lower part of this range, with $99\% \pm 0.6\%$ of particles
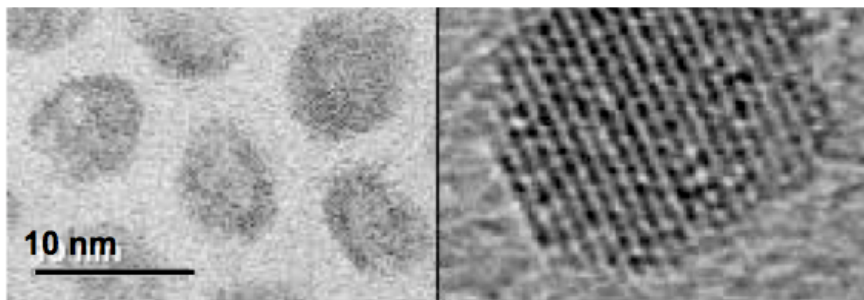
Figure 5.2: Right: Standard TEM of CeF$_3$ nanoparticles, showing that particles have similar sizes and diameters are about 10 nm. Left: High-magnification view of one of the CeF$_3$ nanoparticles shown in the image on the right. The lines visible on the particle are its lattice structure, and indicate that this is a nanocrystal, not an amorphous clump of CeF$_3$ molecules.

having areas less than 3002 nm^2 and 95% $\pm$ 1.3% of particles having areas less than 245 nm^2. As indicated by the TEM images, the particles are elliptical. Figure 5.3 shows the ratio of the particle axes, as determined from the fits generated by ImageJ. The minor axis is typically slightly more than half the length of the major axis, with a mean ratio of 0.58 and standard deviation of 0.20. The distribution of ratios did not change noticeably when limited to only the smallest 95% of particles.

To gain an understanding of the variation in particle size across a TEM sample, 15 images were taken for each of two batches of CeF$_3$ nanoparticles, batches 6 and 7, from locations all across the copper grids on which the samples had been loaded. The nanoparticles were suspended in toluene, which evaporates quickly, so the only particles visible in the TEM image were CeF$_3$ nanoparticles. The images were analyzed using the particle maximization technique described in Section 4.2.1.

A total of 700 particles were identified and analyzed in the images of batch 6. As discussed in Section 4.2.1, the particle maximization technique has difficulty distinguishing between particles that are located very close to one another. For that reason, the areas of particles from batch 6 were spread across five orders of magnitude, ranging from 4 nm^2 (the lower limit applied during the image analysis process) to 20530 nm^2. However, 99% $\pm$ 0.4% of the particles had areas less than 1500 nm^2. Furthermore, 95% $\pm$ 0.8% of the particles had areas less than 240 nm^2. The mean ratio of the minor axis to the major axis was 0.61 $\pm$ 0.18.

A total of 213 particles were identified and analyzed in the images of batch 7, with sizes ranging from 4 nm^2 to 11582 nm^2. Ninety-nine percent $\pm$ 0.7% of the particles had areas smaller than 644 nm^2 and 95% $\pm$ 1.5% of the particles had areas less than
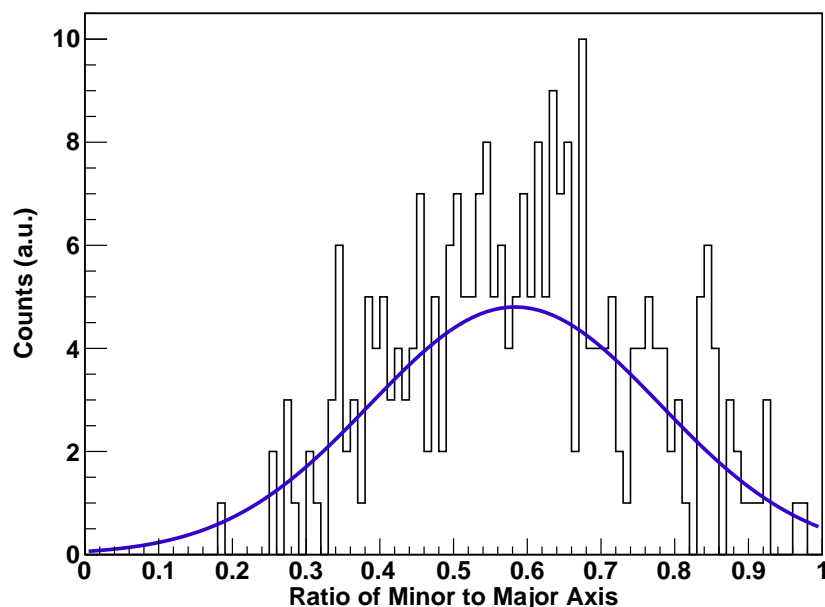
Figure 5.3: Ratio of minor to major axis for particles in an early batch of CeF_3, as calculated by ImageJ. Fitting the ratio with a Gaussian curve results in a mean of 0.58 and a standard deviation of 0.20.

171 nm^2. The mean ratio of the major to the minor axis was 0.60 ± 0.20.

Samples of batches 6 and 7, as well as a sample from an early batch of fabricated CeF_3 nanoparticles, displayed similar size characteristics, insofar as it was possible to determine using TEM. They also displayed very similar degrees of ellipticity. $95\% \pm 0.7\%$ of the particles in the early batch and in batch 6 were smaller than about 240 nm^2. For a particle whose minor axis is 0.6 times the length of the major axis, the approximate mean value for the batches studied, this corresponds to a particle with a major axis of 11.3 nm and a minor axis of 6.77 nm. The particles in batch 7 were smaller, with $95\% \pm 1.5\%$ having an area less than 171 nm^2, corresponding to a particle with a major axis of 9.52 nm and a minor axis of 5.71 nm.

5.3 Sample Identification and Size Measurements Using X-Ray Diffraction

XRD was performed on samples of several batches of CeF_3 in order to determine the average particle size. The identification of the fabricated nanoparticles as CeF_3 was verified by comparing the locations and relative intensities of XRD peaks with reference values, as shown in Figure 5.4. [fDDnt] The locations of the XRD peaks
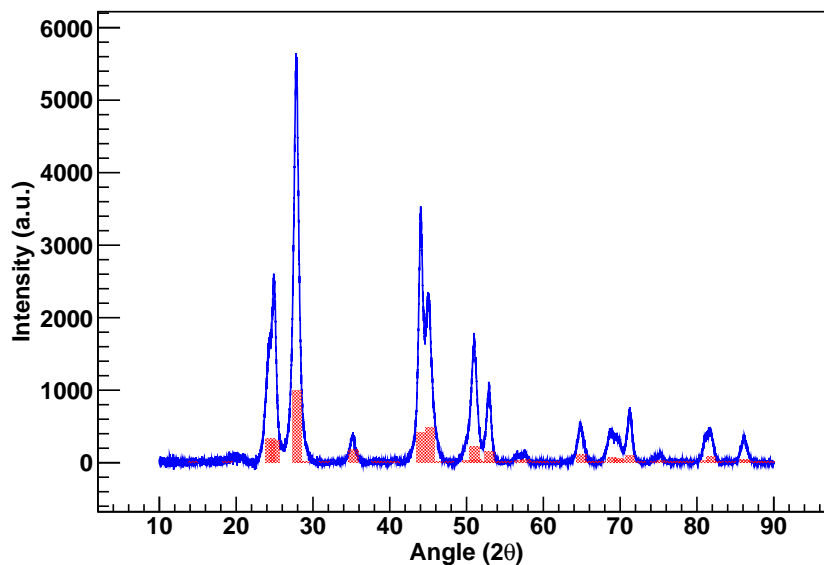
Figure 5.4: XRD spectrum of unwashed CeF_3 nanoparticles (blue line) and locations and relative intensities of expected CeF_3 peaks (red bars). Intensities of reference peaks have been scaled so that the most intense peak has an intensity of 1000. The angles at which peaks were observed appear to coincide with the locations at which peaks were expected. Reference data obtained from the International Centre for Diffraction Data. [fDDnt]

were an excellent match for the expected values, occurring within 1% of the 2θ given by the reference data.

In order to determine the range of variation in particle size between batches, spectra were taken of samples of unwashed CeF_3 nanoparticles from synthesis batches six, seven, eight, and nine, suspended in oleic acid. The measurements began at $2\theta=10°$ and continued through $2\theta=90°$, except for the spectrum of batch 6, shown in Figure 4.9, which due to instrumental error consisted only of the angles between $2\theta=20°$ and $2\theta=40°$. Peaks with intensities equal to at least 10% of the highest-intensity peak in the reference spectrum were characterized, as shown in Table 5.1. (A list of the locations and intensities of all peaks in the reference spectrum is available in Appendix D.) The mean particle size was calculated for all four batches by applying the Debye-Scherrer equation, Equation 4.4, to these peaks. The results, given in Table 5.2, show that there is no significant variation in particle size between batches. All four batches have means fall between 18 nm and 21 nm, and all are within one another's error bars.

The XRD spectrum of batch 7 was compared with a spectrum from a sam-

Reference		Batch 6			Batch 7			Batch 8			Batch 9		
2θ (deg.)	I	2θ (deg.)	I	Size (nm)	2θ (deg.)	I	Size (nm)	2θ (deg.)	I	Size (nm)	2θ (deg.)	I	Size (nm)
24.459	34	24.400	34	13.848	24.505	32	10.273	24.419	31	11.130	24.339	30	10.976
25.014	30	24.958	42	24.436	24.914	46	21.261	24.900	45	22.116	24.864	42	22.693
27.899	100	27.848	100	24.620	27.824	100	19.582	27.793	100	19.487	27.745	100	21.500
35.267	18	35.182	7	20.130	35.163	7	16.210	35.136	7	15.980	35.086	7	18.547
44.060	41	—	—	—	44.046	62	22.794	44.040	66	21.134	43.994	68	22.681
45.228	48	—	—	—	45.018	42	15.610	44.962	44	14.126	44.919	46	15.033
51.033	23	—	—	—	50.984	30	19.042	50.957	32	18.554	50.917	32	19.354
52.959	15	—	—	—	52.933	18	20.933	52.881	20	21.797	52.837	20	20.578
64.982	11	—	—	—	64.843	9	16.955	64.815	10	18.762	64.775	11	19.846
71.277	10	—	—	—	71.240	13	21.141	71.213	14	22.248	71.188	14	21.696

Table 5.1: Locations and relative intensities of major XRD peaks, obtained from CeF$_3$ reference data and measured for four batches of unwashed CeF$_3$ nanoparticles.[fDDnt] All intensities have been normalized to the peak at $2\theta = 24.899$. Nanoparticle sizes have been calculated using the Debye-Scherrer equation.

Batch	# Peaks Used	Mean Size (nm)	Error (nm)
6	4	20.756	2.278
7	10	18.380	1.353
8	10	18.522	1.361
9	10	19.290	1.389

Table 5.2: Mean size of particles in synthesis batches 6, 7, 8, and 9, measured by applying the Debye-Scherrer equation to peaks in the XRD spectrum with intensities greater than or equal to 10% of the maximum intensity.

Reference	Batch 7 Unwashed		Batch 7 Washed	
2θ (deg.)	2θ (deg.)	Size (nm)	2θ (deg.)	Size (nm)
27.899	27.824	19.582	27.793	15.491
35.267	35.163	16.201	35.125	15.036
44.060	44.046	22.794	44.050	16.393
45.228	45.018	15.610	44.954	12.585
51.033	50.984	19.042	50.921	15.967
52.959	52.933	20.933	52.850	16.275
64.982	64.843	16.955	64.792	14.991
71.277	71.240	21.141	71.181	17.399

Table 5.3: Locations of major XRD peaks, obtained from CeF_3 reference data and measured for unwashed and washed samples of CeF_3 nanoparticles from synthesis batch 7.[fDDnt] Nanoparticle sizes have been calculated using the Debye-Scherrer equation.

ple of batch 7 that had been washed once, using the process described in Section 3.3. The objective of this comparison was to determine whether the washing process affected the nanoparticle size. As shown in Table 5.3, the measured particle size did not increase as a result of the washing process. The eight XRD peaks whose widths were measured produced an average nanoparticle diameter of 15.51 nm $\pm$ 1.39 nm, significantly smaller than the mean diameter of the unwashed sample from batch 7, 18.38 nm $\pm$ 1.35 nm.

5.4 Transmission and Size Measurements Using Ultraviolet/ Visible Spectroscopy

The UV/Vis spectra of three 1 cm $\times$ 3 cm OD CeF_3 crystals obtained from Scionix can be seen in Figure 5.5. (A fourth crystal had an unpolished face that precluded UV/Vis measurements.) The sharp falloff in transmission below about 280 nm is consistent with the behavior seen in CeF_3 crystals by other investigators. [And89]
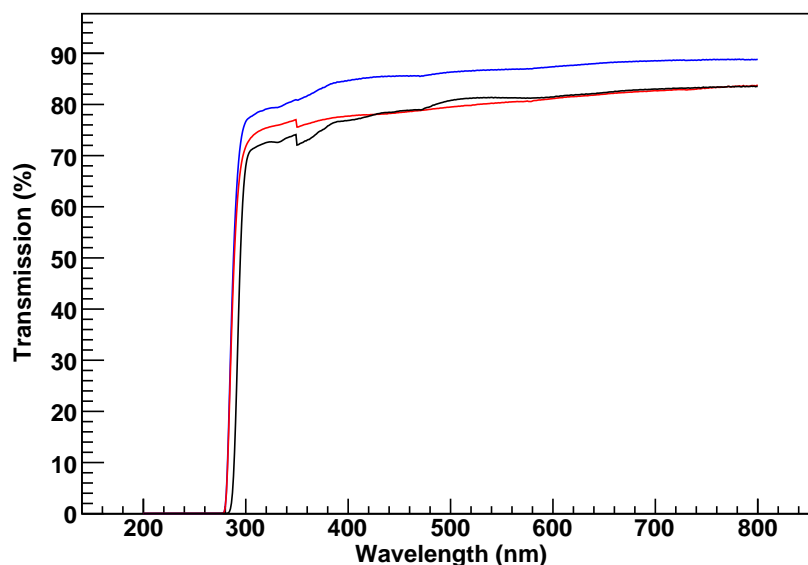
Figure 5.5: Transmission of light through three commercial CeF_3 crystals. The abrupt falloff of transmission below 280 nm and high transmission of light above that wavelength agree with the behavior observed by other investigators.

[Cry93] [Sch94] [Cry96a] It results from the presence of CeF_3 excitation bands at 250 nm and 286 nm. [Cry96a] The smoothness of the transmission curves indicates that the crystals are high-purity; the presence of impurities such as neodymium and oxygen, which were found in early CeF_3 crystals, would be indicated by absorption peaks in the high-transmission region or by poor transmission overall. The sharp increase in transmission seen in the crystals near 340 nm is an artifact of the spectrophotometer, which changes from a quartz halogen lamp to a deuterium lamp at that wavelength.

The transmission of light through solutions loaded with CeF_3 nanoparticles produced a much different spectrum, as shown in Figure 5.6, which overlays the spectra from three samples made using different batches of CeF_3 and the spectrum of liquid scintillator. All three CeF_3 samples consist of unwashed nanoparticles suspended in the standard liquid scintillator, but the CeF_3 concentrations vary, with the samples of batches 6 and 7 containing 8.8% by mass and the sample of batch 8 containing 20% by mass. All of the CeF_3 nanoparticle UV/Vis spectra are characterized by an abrupt falloff in the transmission just above 400 nm. This reflects the behavior of the liquid scintillator, and results from the absorption of lower-wavelength light by toluene, PPO, and POPOP.
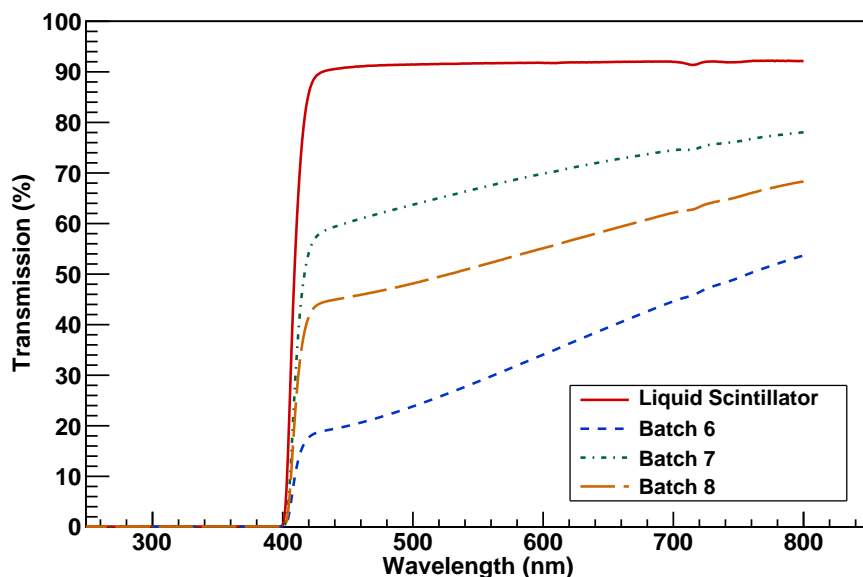
Figure 5.6: UV/Vis of CeF$_3$ nanoparticles from batches 6, 7, and 8 suspended in liquid scintillator. The transmission cutoff results from the absorption of light by the liquid scintillator components. The poor overall transmission of the solutions and

The overall transmission of the samples containing nanoparticles is both lower than the transmission through liquid scintillator alone and lower than the 88% ± 2% maximum theoretical transmission of CeF$_3$ crystals. [Cry96a] Poor transmission overall, as well as a gradual decrease in transmission with decreasing wavelength, can indicate the presence of an impurity. The Crystal Clear Collaboration, in one of their later papers on CeF$_3$, show the UV/Vis spectrum of a CeF$_3$ crystal contaminated with oxygen, which shows a decrease in transmission of about 20% between 400 nm and 700 nm, comparable to the scale of the variation seen in the CeF$_3$ nanoparticle solutions. [Cry96a] This suggests that oxygen or another contaminant may be present in fabricated CeF$_3$ nanoparticles.

UV/Vis was also used to explore the question of whether the washing process described in Section 3.3, which removed excess oleic acid, caused nanoparticles to agglomerate by also removing oleic acid capping ligands. Two samples were prepared, each using 2.54 g of CeF$_3$ nanoparticle gel from batch 6. For the unwashed solution, the gel was taken up directly into liquid scintillator. For the washed solution, the gel was taken up into toluene and crashed out using methanol as per the usual washing process, then taken up into liquid scintillator. Since light scattering measurements were also performed on these samples, both were filtered through a 2.7 μm filter as a

86
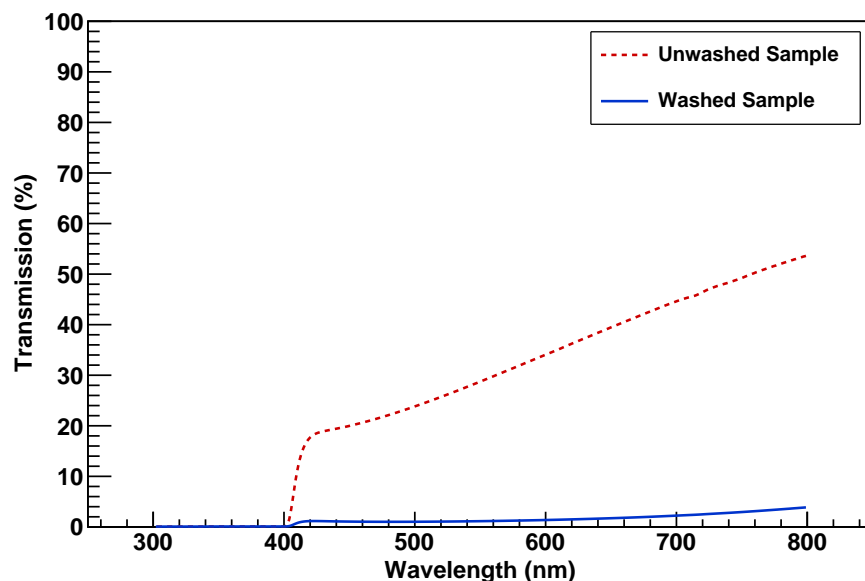
Figure 5.7: UV/Vis of washed and unwashed samples of CeF_3 nanoparticles from batch 6 suspended in liquid scintillator. The washed sample shows significantly lower transmission.

final step. As shown in Figure 5.7, the spectrum of the washed sample displayed much lower transmission, never higher than 4% over the wavelength range of interest. Since the only difference between the samples was the washing process, the conclusion was that the washing created agglomerated particles in sufficient concentration to prevent the transmission of light. XRD size measurements of the washed nanoparticles did not increase, compared with the unwashed particles, because agglomeration does not affect the nanocrystal structure.

UV/Vis can be used to provide information on the nanoparticle size, as described in Section 4.3.3. Typically, Rayleigh-scattering fits to the UV/Vis spectra of CeF_3 nanoparticles were of poorer quality than fits to the spectra of other nanoparticles, such as the Rayleigh scattering fit shown for $CeBr_3$ nanoparticles in Figure 4.15. An example of a Rayleigh scattering fit for CeF_3 nanoparticles from batch 7 suspended in liquid scintillator may be seen in Figure 5.8. The fit was applied from the maximum wavelength of 800 nm to the edge of the transmission cutoff at 425 nm, and produced an estimated nanoparticle size of 18.16 nm $\pm$ 4.24 $\times$ 10^{-4} nm with a scaling factor of 0.746. Fits to dispersions using CeF_3 nanoparticles from batches 6 and 8 may be seen in Figures 5.9 and 5.10. In all cases, the fit was calculated based on the transmission curve between the maximum wavelength of 800 nm and the 425 nm transmission cutoff, but has been shown for the entire measured range.
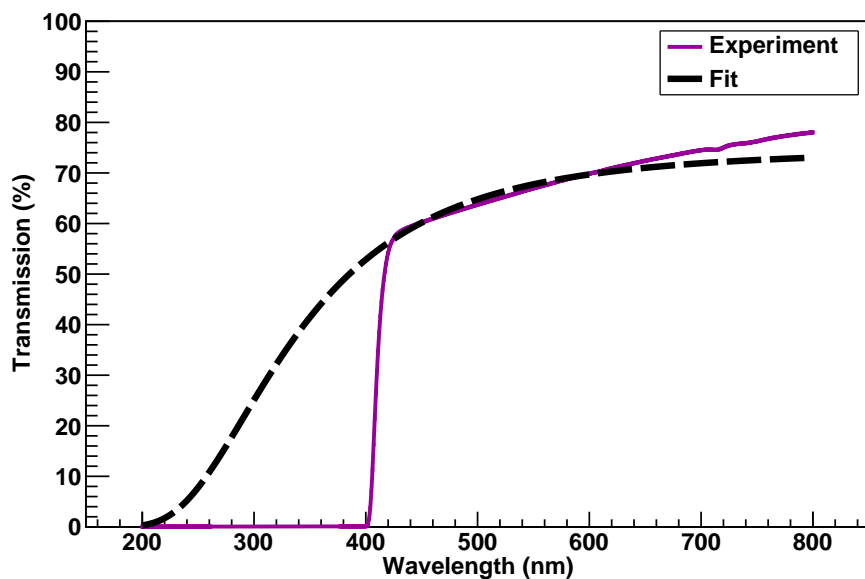
Figure 5.8: Rayleigh scattering fit to transmission of light through CeF_3 nanoparticles from batch 7 suspended in toluene. According to the fit, the nanoparticles have an average diameter of 18.16 nm $\pm$ 423.8 fm with a scaling factor of 0.746.
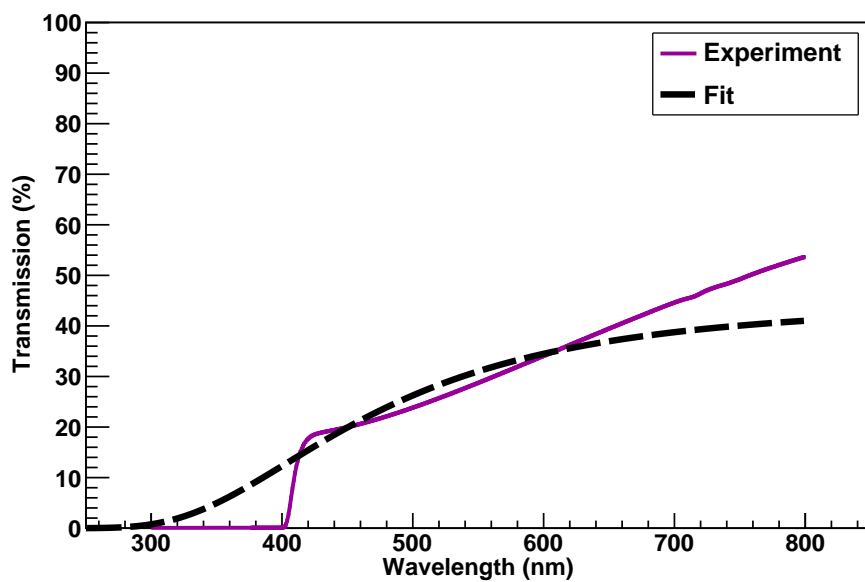
Figure 5.9: Rayleigh scattering fit to transmission of light through CeF_3 nanoparticles from batch 6 suspended in toluene. According to the fit, the nanoparticles have an estimated diameter of 28.17 nm $\pm$ 459.9 fm with a scaling factor of 0.445.
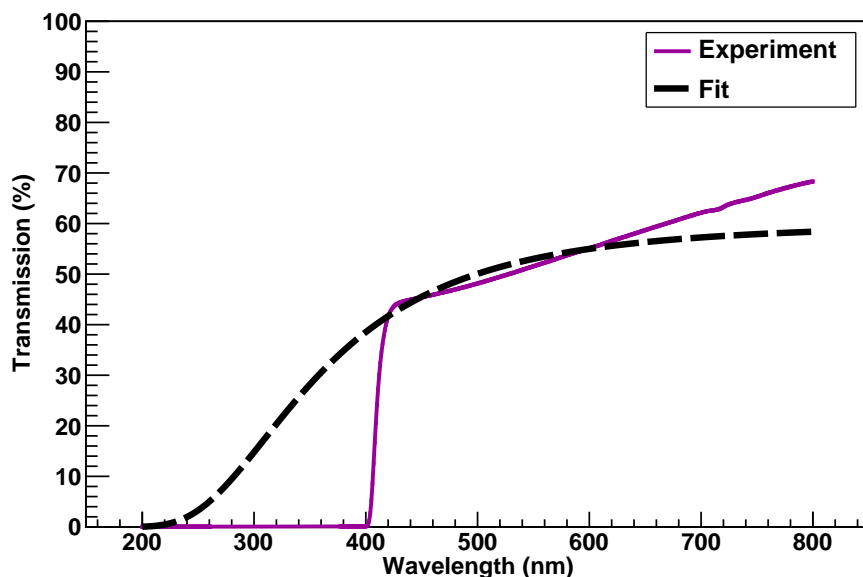
Figure 5.10: Rayleigh scattering fit to transmission of light through CeF_3 nanoparticles from batch 8 suspended in toluene. According to the fit, the nanoparticles have an estimated diameter of 19.75 nm $\pm$ 468.4 fm with a scaling factor of 0.600.

The particle sizes estimated by UV/Vis for nanoparticles from batches 7 and 8 are consistent with the average sizes calculated for these batches using XRD, as shown in Table 5.4. In both cases, the Rayleigh scattering model diameter is within the error bar of the XRD diameter. However, the particle size calculated for batch 6 using Rayleigh scattering is significantly higher than the size produced by XRD. It may be observed from Figures 5.8, 5.9, and 5.10 that as the maximum transmission of the sample decreases and its slope becomes more pronounced, its divergence from the behavior predicted by Rayleigh scattering increases. The poor quality of the Rayleigh scattering fit is the most likely explanation for the discrepancy between the particle sizes calculated using XRD and UV/Vis for CeF_3 nanoparticles from batch 6.

5.5   Characterization of Photoluminescence Spectra

Early characterization of the CeF_3 luminescence identified a single emission wavelength of 340 nm. [Mos89] As research into CeF_3 continued, however, it became clear that a lower-wavelength component was also present. The lower-wavelength emission was measured at 310 nm by Anderson and at 300 nm by the Crystal Clear Collaboration. [And90] [Chi94] The discrepancy in the identification of the lower-wavelength

Batch	XRD		UV/Vis	
	Size (nm)	Error (nm)	Size (nm)	Error (fm)
6	20.756	2.278	28.17	459.9
7	18.380	1.353	18.16	423.8
8	18.522	1.361	19.75	428.4

Table 5.4: Comparison of average particle sizes calculated by analyzing XRD spectra with particle sizes generated using Rayleigh scattering fits to UV/Vis spectra. For CeF_3 nanoparticles from batches 7 and 8, the particle sizes predicted by the Rayleigh scattering model are within the error bars of the particle sizes calculated using XRD. The Rayleigh scattering model is a poor match for the UV/Vis spectrum produced by a sample of CeF_3 nanoparticles from batch 6, and produces a significantly larger size estimate than the one generated using XRD.

emission arises from two sources. First, emission wavelengths are frequently rounded to the nearest 10 nm. For example, Chipaux et al. observed an emission at 303 nm but quote the wavelength as 300 nm in their 1994 paper. [Chi94] Second, PL peaks produced by solids are sufficiently wide to allow for a discrepancy of a few nanometers in the identified wavelength. The value for the lower-wavelength emission that is quoted most often in recent literature is 300 nm. [Bel03] [Ina00] [Koz04] [Mar06] The CeF_3 luminescence results from a transition of Ce^{3+} from an excited 5d level to the ground 4f level. [Ped92] The typical emission wavelengths of cerium are around 286 nm and 300 nm. In addition, cerium ions that are perturbed by defects in the crystal lattice emit light around 340 nm. [Nik94]

The PL of CeF_3 nanoparticles suspended in liquid scintillator is dominated by the PL of the liquid scintillator. A typical spectrum, as shown in Figure 5.11, displays excitation and emission at the same wavelengths and with the same relative intensities as are observed in the PL of liquid scintillator alone, which is shown in Figure 4.11. Liquid scintillator exhibits two emissions, at 411 nm and 433 nm, both of which are excited by 405 nm. The wavelengths observed for excitation and emission in the CeF_3 nanoparticle-loaded liquid scintillator differ by only a few nanometers, which is within instrumental error. Since the transmission cutoff of the liquid scintillator is slightly higher than 400 nm, any light emitted by CeF_3 at its characteristic 286 nm, 300 nm, or 340 nm wavelengths would be absorbed by the liquid scintillator.
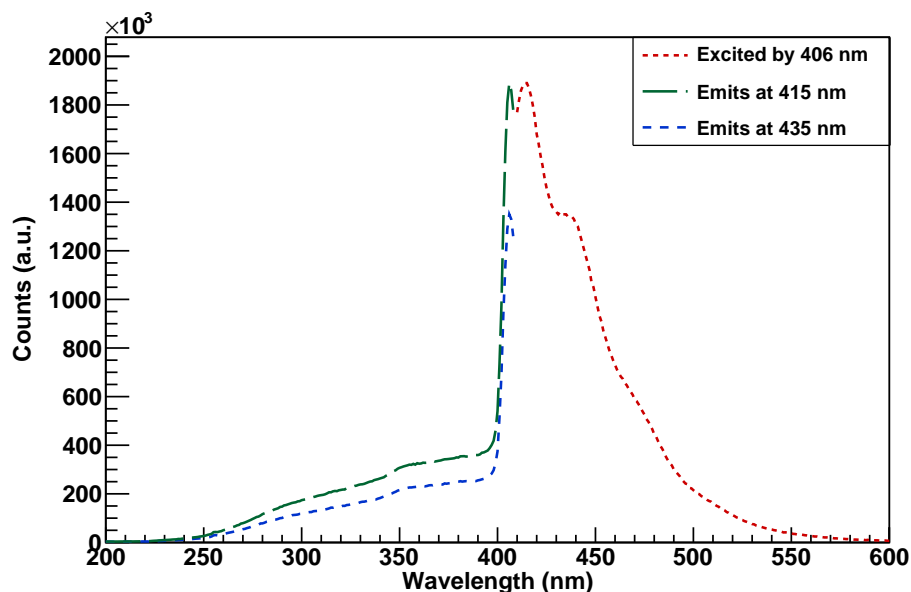
Figure 5.11: PL/PLE of CeF_3 nanoparticles in liquid scintillator, showing similar excitation and emission locations and relative intensities to those observed in liquid scintillator alone.

5.6   Characterization of Radioluminescence Spectra

Of the three characteristic CeF_3 emissions reported for PL, the emission at 300 nm dominates for RL of the bulk crystal. [Cry96a] When RL is performed at a 90° angle, the majority of the observed emission is produced by transitions deep within the crystal, rather than at the surface. Therefore, light emitted near 286 nm is reabsorbed before escaping from the crystal, and since fewer crystal defects are found in the interior of the crystal, few perturbed sites contribute to the luminescence. The RL spectra of the four CeF_3 crystals obtained from Scionix are shown in Figure 5.12. These measurements were performed with the crystals at a 45° angle, because of the way the crystals had been cut and polished, so the spectrum shows the luminescence generated at the surface. They therefore resemble the photoluminesence spectra seen by Schneegans [Sch94] and by the Crystal Clear Collaboration [Cry93] [Cry96a] more than the radioluminescence spectra seen by them. The differences in overall RL intensity and in the relative intensities of the 286 nm, 300 nm, and 340 nm emissions result from variations in the prevalence of defects in the crystals.

The characteristic CeF_3 emissions are completely absent from RL of CeF_3-loaded liquid scintillator, as shown in Figure 5.13. The CeF_3 emissions fall within the excitation ranges of the toluene, PPO, and POPOP in the liquid scintillator. However,
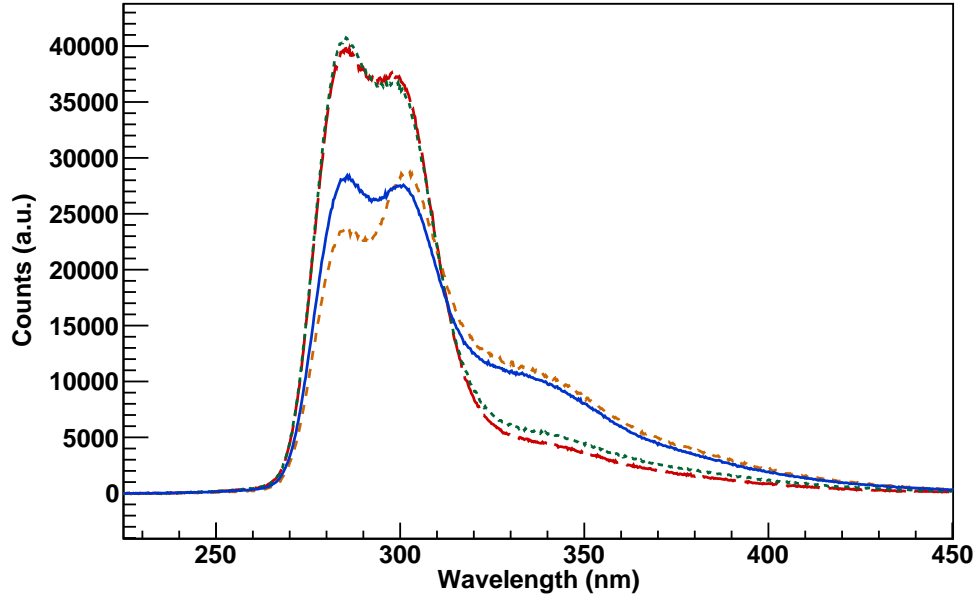
Figure 5.12: RL of four CeF$_3$ crystals. Since the RL was performed at a 45° angle, excitation and emission occurred near the surface of the crystals, so all three of the characteristic CeF$_3$ emissions are visible, near 286, 305, and 340 nm.

the sample loaded with CeF$_3$ nanoparticles is 200% brighter, having an emission over all wavelengths of 6.6×10^6 counts/s, compared with 2.2×10^6 counts/s for liquid scintillator alone. The increased emission could result from a higher photoelectric cross-section due to the presence of high-Z material, or could result from the excitation of the liquid scintillator by luminescing CeF$_3$ nanoparticles.

The photoelectric effect is a function of the atomic number of the atom,

$$\sigma_{PE} \propto \frac{Z^n}{E_\gamma^{3.5}} \tag{5.1}$$

where n is a number between 4 and 5 and E_γ is the energy of the incident photon, here the x-ray energy. The photoelectric cross-section in toluene is 0.273 cm^{-1} for 17.374 keV x-rays and 0.268 cm^{-1} for 17.479 keV x-rays. [oSd] To prepare the CeF$_3$-loaded liquid scintillator, 2 g of CeF$_3$ were added to 8.86 mL of liquid scintillator, which was assumed to be equivalent to 7.68 g of toluene. Assuming the density of CeF$_3$ nanoparticles to be equal to the 6.16 g/cm^3 observed for the bulk material [And89], the density of the dispersion was 9.68 g in 9.18 mL, or 1.05 g/cm^3. The photoelectric cross-sections of the x-rays emitted by the RL system in a mixture
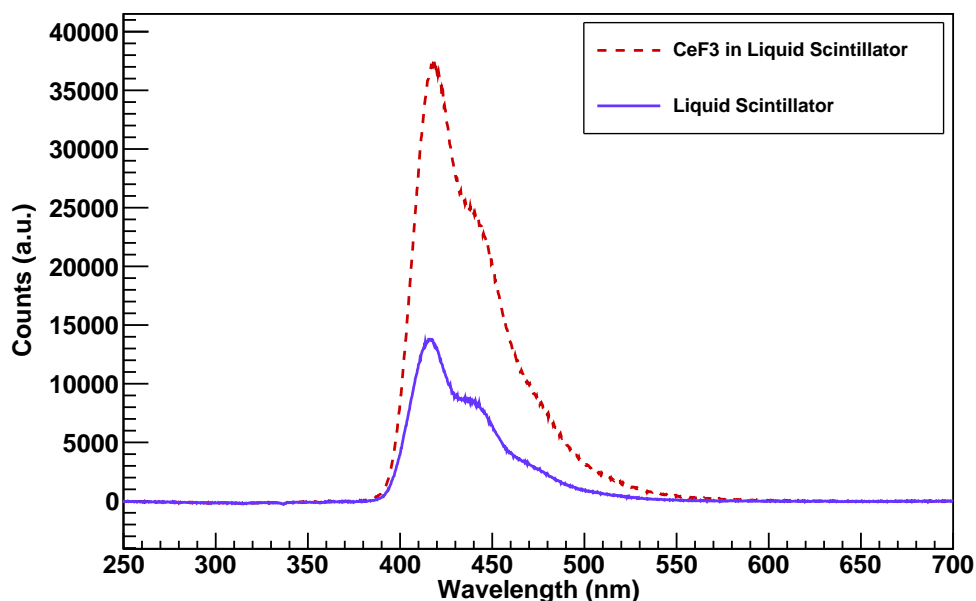
Figure 5.13: RL of CeF$_3$-loaded liquid scintillator, compared with liquid scintillator alone.

consisting of 20.66% by mass CeF$_3$ and 79.34% by mass toluene were 7.15 cm^2/g, or 7.51 cm^{-1}, for 17.374 keV x-rays and 7.03 cm^2/g, or 7.38 cm^{-1}, for 17.479 keV x-rays. [oSd] Thus, the cross-section for the photoelectric effect in the CeF$_3$-loaded solution is 26 times greater than the cross-section for the photoelectric effect in toluene alone. However, the observed RL is an order of magnitude smaller. The smaller-than-expected increase in RL may result from charged particles depositing energy in the less-luminescent CeF$_3$ or may reflect the finite number of x-ray photons produced by the apparatus.

5.7   Response of Cerium Fluoride Nanocomposites to Gamma Radiation

In order to determine the optimum mass loading of CeF$_3$ nanoparticles in liquid scintillator, six dispersions were prepared, each containing a different mass of 64.5% CeF$_3$ gel suspended in liquid scintillator. Their CeF$_3$ mass concentrations were 0%, 5%, 10%, 20%, 30%, and 40%. The dispersions were washed using the process described in Section 3.3, then taken up into liquid scintillator and filtered. The 30% solution required two filters; the 40% solution required six and produced only a few milliliters of the final dispersion, indicating that the liquid scintillator

93
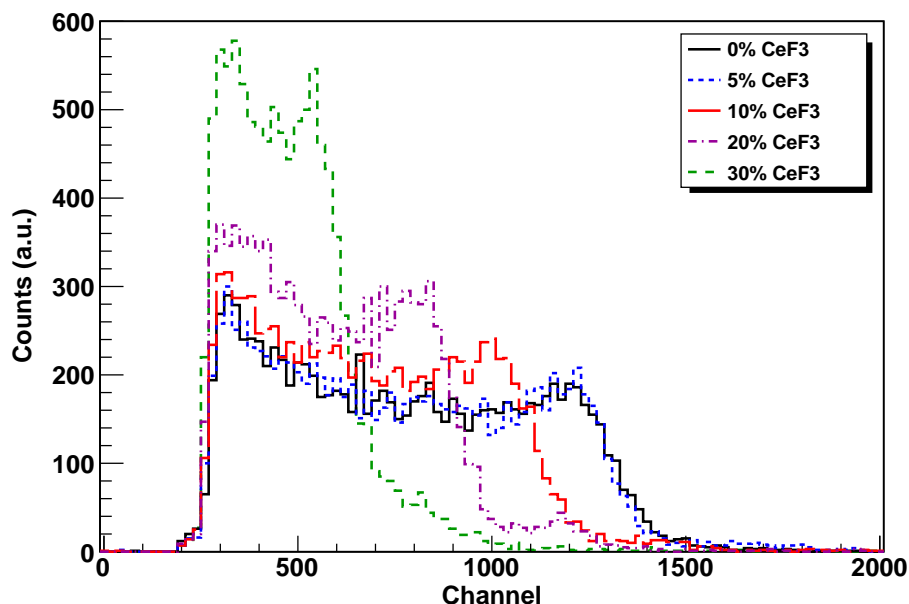
Figure 5.14: Energy spectra of liquid scintillator dispersions with different mass concentrations of CeF$_3$ nanoparticles. The light yield, indicated by the Compton edge, decreases as the CeF$_3$ concentration increases.

was saturated. The 20%, 30%, and 40% dispersions were noticeably whiter than the lower-concentration dispersions, and produced precipitate when allowed to stand overnight.

Due to the small amount of the 40% CeF$_3$ dispersion produced and its instability, its γ-ray response was not measured. The responses of the other dispersions to ^{137}Cs γ-rays are shown in Figure 5.14. The data acquisition software used for these measurements was designed to accumulate data until a set number of counts was reached; thus, each spectrum contains 10,200 counts, but no information was retained on the duration of the measurement. The decrease in light yield with increasing CeF$_3$ concentration, as indicated by the position of the Compton edge, was eventually attributed to quenching by oleic acid and is discussed in detail in Section 3.5. The resolution of each spectrum was determined by fitting the photopeak and Compton edge, as described in Section 4.4.1. The photopeak of the 30% sample could not be fit because of its low light yield, but the resolutions of the other samples are shown in Table 5.5.

The resolutions in Table 5.5 are consistent with the resolution measured of a test sample for the beam line CeF$_3$ detector. This sample contained 2 g of CeF$_3$ from batch 8 in 8.86 mL of liquid scintillator, equivalent to 20% mass loading. The response of 3 mL of this dispersion to a ^{137}Cs source was measured for 30 minutes, producing

% CeF3	Resolution(%)	Error (keV)	FWHM	Reduced χ^2
5	18.61	1.604	123.1	1.128
10	20.45	1.358	135.3	1.199
20	19.72	1.495	130.5	0.934

Table 5.5: Resolution and FWHM of the 661.7 keV ^{137}Cs photopeak, fit error in the photopeak location, and overall goodness of the fit for 5%, 10%, and 20% CeF$_3$ nanoparticles in liquid scintillator. Each spectrum contained 20,401 counts.
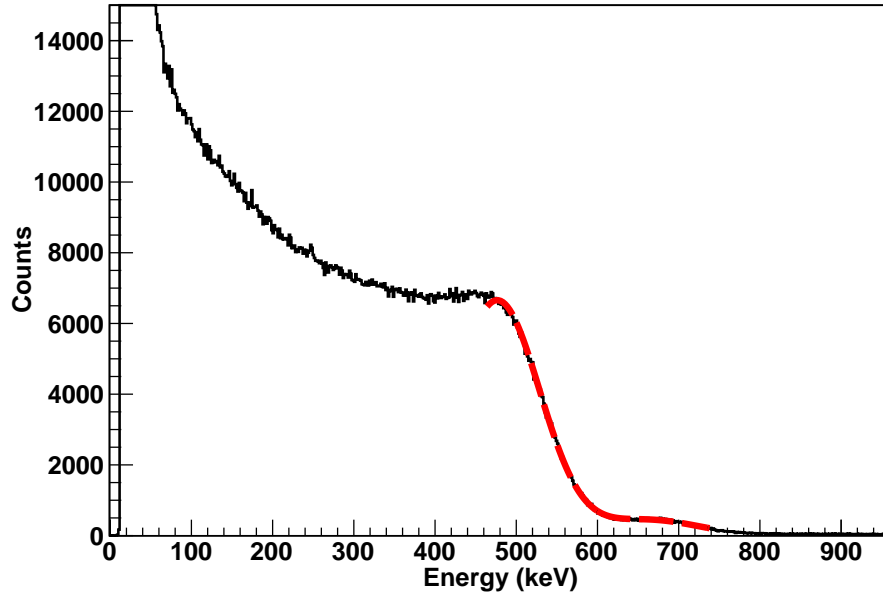
Figure 5.15: Energy spectrum of 20% CeF$_3$ dispersion in response to γ-rays from ^{137}Cs over 17 hours. The Compton edge and photopeak have been fitted using the automated routine described in Section 4.4.1, resulting in a resolution of 22.08% $\pm$ 0.12%.

116,174 counts. The resolution, produced by fitting the Compton edge and photopeak, was 23.61% $\pm$ 0.0061%, with a FWHM of 156.2 $\pm$2685. The error in the photopeak location was 1.27 keV and the reduced chi-square for the fit was 1.273. Following the characterization of the test sample, the beam line detector dispersion was prepared by adding 15.79 g of CeF$_3$ gel from batch 8 to 70 mL of liquid scintillator, for a mass loading of 20%. A few milliliters of this suspension were removed and characterized by measuring their response to a ^{137}Cs source for 17 hours. The resolution of this sample was 22.08% $\pm$ 0.12%, with a FWHM of 146.11 $\pm$ 509.47, a photopeak error of 0.277 keV, and a reduced chi-square of 2.13.
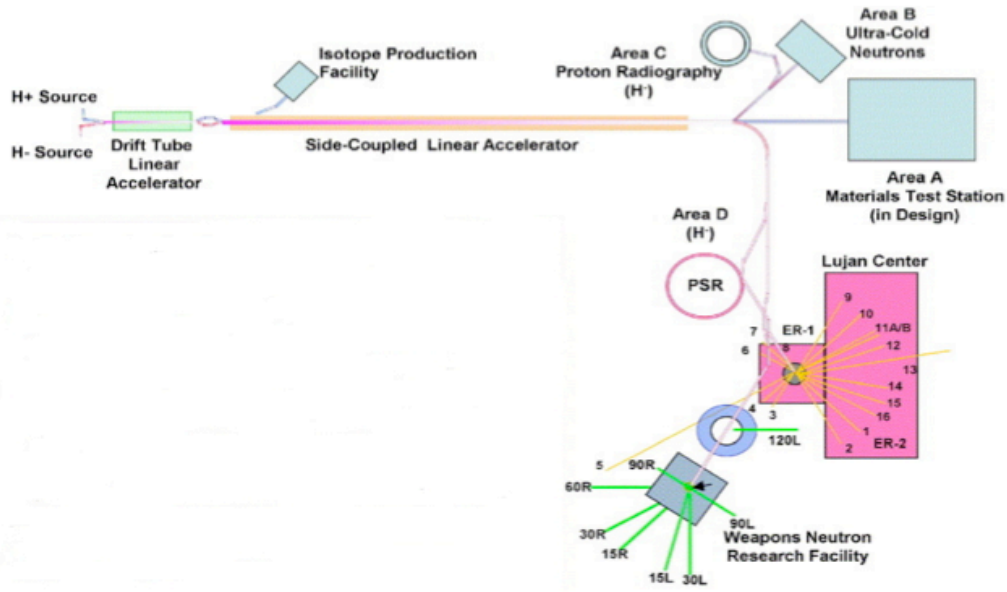
Figure 5.16: The Los Alamos Neutron Science Center, showing linear accelerators, proton storage ring, and experimental flight paths. Experiments on CeF_3-loaded detectors were conducted at flight path 5; experiments on fissionable scintillators were conducted at flight path 90L.

5.8 Beam Line Experiments on CeF_3 Nanocomposite Detectors

Characterization of the radiation detection properties of CeF_3 is sufficient to evaluate its ability to detect monoenergetic γ-rays in low-background environments. However, the detectors in neutron capture experiments must reliably detect γ-rays in environments with high neutron backgrounds.

These experiments were performed at LANSCE, the Los Alamos Neutron Science Center, which is shown in Figure 5.16. H^+ and H^- ions are produced by Cockcroft-Walton accelerators and accelerated to 750 keV before being injected into a drift tube linear accelerator that accelerates them to 100 MeV. A side-coupled linear accelerator then accelerates the ions to 800 MeV. The beam is directed into a proton storage ring, which builds a compressed 250 ns pulse out of 450 μs of continuous proton delivery by allowing protons into the ring in 250 ns intervals separated by 110 ns gaps. Since the 800 MeV protons travel around the ring in 360 ns, this results in compressed 100 μA bursts of protons that are used to produce neutrons through spallation. [Lis90]

Experiments on liquid scintillators loaded with CeF_3 were performed at flight path 1FP5. For this flight path, the distance traveled by γ-rays and neutrons between the

96
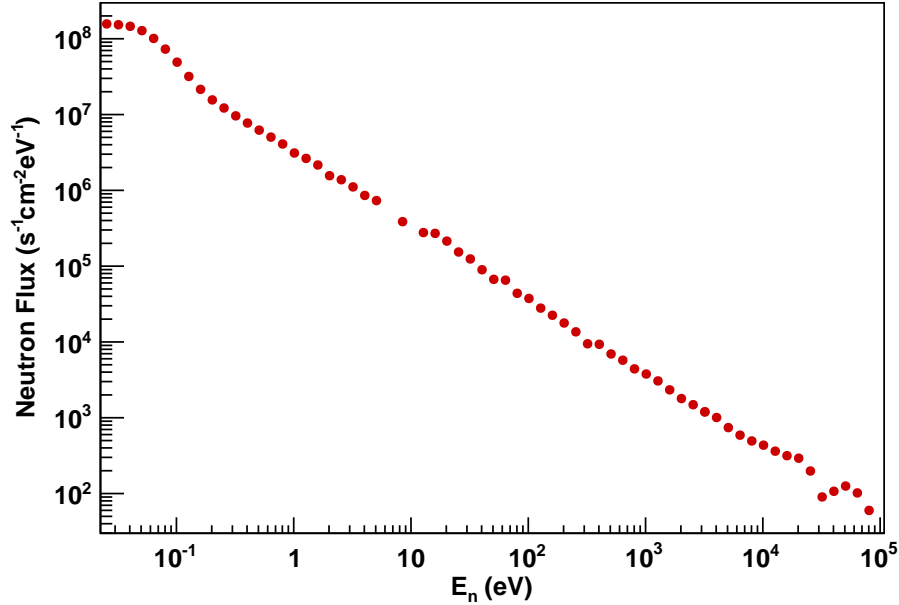
Figure 5.17: Neutron flux profile at flight path 1FP5, measured using a fission chamber. [Tov09] Data provided by Fredrik Tovesson.

spallation target and the detector is 8 m. As shown in Figure 5.17, the beam profile for 1FP5 contains neutrons with energies from subthermal to 200 keV. [Tov09]

The experimental setup used to characterize the response of CeF_3-loaded detectors in the beam line is shown in Figure 5.18. Two quartz detector bottles containing $\sim$60 mL liquid scintillator (7.5 mg PPO and 1 mg POPOP per mL toluene) and loaded with 20% by mass CeF_3 nanoparticles from batch 8 were wrapped in teflon tape and mounted vertically on Hamamatsu R2059 photomultiplier tubes with Hamamatsu E2979-500 socket assemblies and Hamamatsu E989-05 permalloy magnetic shields. Technical specifications for the PMT assembly are given in Appendix B. Covers were constructed to protect the entire assembly from light. The detectors were placed $\sim$1.5 feet apart on either side of the neutron beam flight path 1FP5, about 7 m from the spallation target. Targets were suspended between the detectors, in the neutron beam. A BaF_2 detector module from DANCE was also included in the experiment, for comparison. The three PMT sockets were powered by a LeCroy 1454 High Voltage Mainframe with a LeCroy 1461 12-Channel High Voltage Board 1461N, described in Appendix C. Signals were collected by an Acqiris DC265 8-bit digitizer in an Acqiris CC015 crate. The digitizer was controlled using the Maximum Integration Data Acquisition System (MIDAS) software.

The target materials chosen were tantalum, cobalt, carbon, and gold, because the

beam path

HV Power Supply

Negative Board

CeF$_3$ Detector

CeF$_3$ Detector

PMT

Target

PMT

Accelerator
t$_0$ Signal

BaF$_2$ Detector
and PMT

Trigger   3   2   1

Digitizer
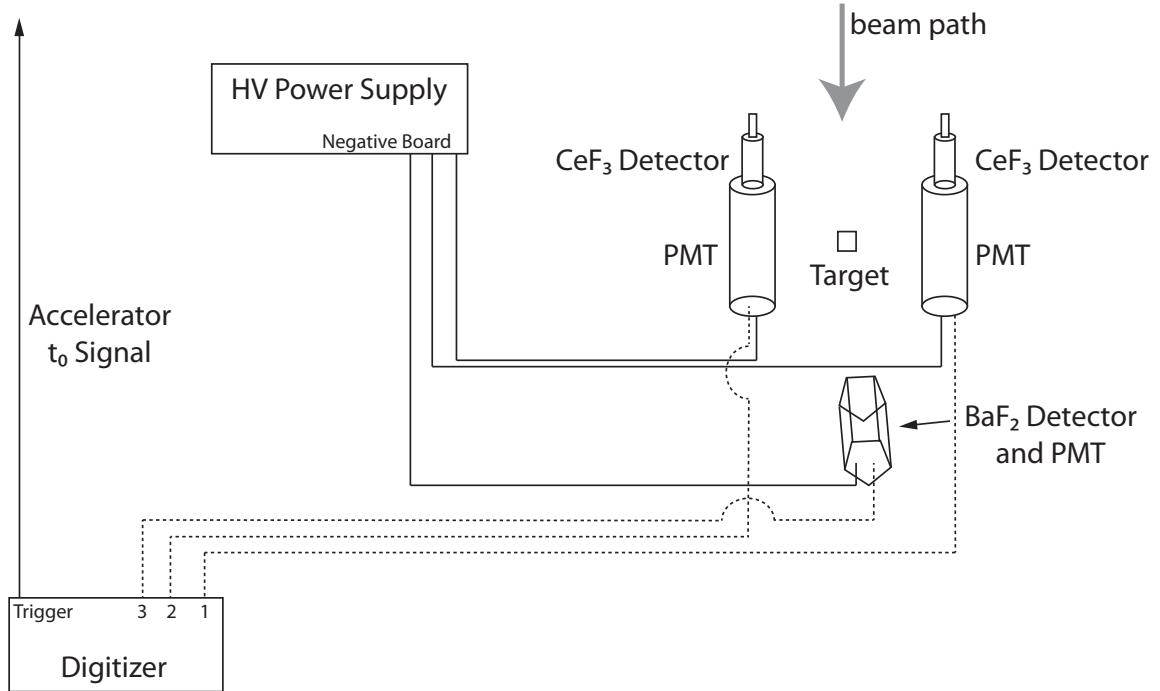
Figure 5.18: Diagram of experimental setup of CeF$_3$-loaded and BaF$_2$ single-crystal detectors at flight path 1FP5. Following each trigger, signals produced by all three detectors in response to the γ-flash, beam neutrons, and neutron capture on the target are digitized.

responses of these materials to neutrons are well known. Since carbon has a very low neutron capture cross-section and a large neutron scattering cross-section, its response was used to perform background subtraction on the spectra produced using other target materials. A comparison of the response of one of the CeF$_3$ nanocomposite detectors to neutron capture on a tantalum target with the response of the BaF$_2$ detector module is shown in Figure 5.19. The spectrum from the CeF$_3$ detector displays lower-resolution peaks than the BaF$_2$ spectrum. However, the CeF$_3$-loaded scintillator was capable of detecting neutron capture resonances corresponding to much higher-energy neutrons than the BaF$_2$ detector. Due to the lengthy period it required to recover from the arrival of the γ-flash, the BaF$_2$ detector was blind to capture γ-rays produced by neutrons with energies higher than 40 eV, while the CeF$_3$ detector was able to detect resonances produced by neutrons with energies up to 400 eV.
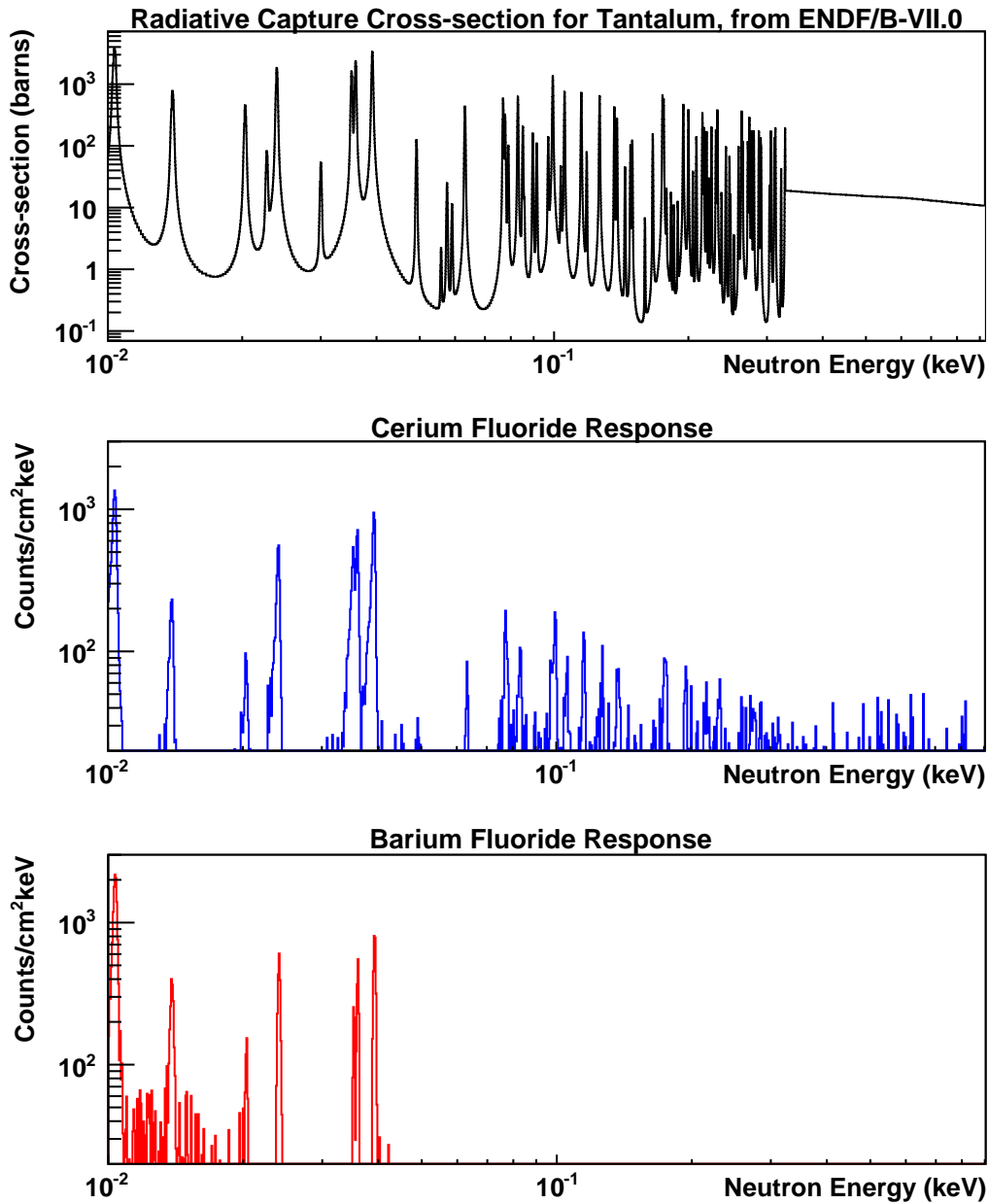
Figure 5.19: Comparison of spectra produced by a CeF_3 nanocomposite detector and a BaF_2 single-crystal detector in response to neutron capture on tantalum. Due to its long signal decay time following the arrival of the γ-flash, the BaF_2 detector was unable to detect γ-rays resulting from the capture of neutrons with energies above ∼40 eV. Although the spectrum from the CeF_3 detector shows significant noise, likely from neutron interactions with the liquid scintillator, neutron capture resonances can be seen for neutrons with energies up to ∼400 eV.

CHAPTER VI

Characterization of Fissionable Scintillators

6.1 Introduction

An ideal molecule for incorporation into a fissionable scintillator would have no luminescence at wavelengths that could interfere with the liquid scintillator and would have an established method for nanoparticle synthesis. ^{238}U was chosen as a candidate isotope because a nanoparticle fabrication method exists for Bi_2O_3 that could be extended to U_3O_8. [Li06] Additionally, it was hoped that the uranium luminescence could reduce the need for wavelength-shifting dyes in the scintillating matrix.

As shown in Figure 6.1, ^{238}U has a fission cross-section that is greater than 0.1 b only for neutrons with energies over ~1.35 MeV and decreases quickly for lower energies. ^{235}U has a fission cross-section that is 7-8 orders of magnitude higher for low-energy neutrons. However, materials with threshold fission energies serve an important purpose in neutron flux measurements. At the LANSCE 4FP90L flight path where fissionable scintillators were tested, the fastest neutrons measured have energies approaching 800 MeV. Neutrons with energies as low as 200 keV may be detected between γ-flashes, which arrive every 1,786.6 ns. Neutrons with energies below ~200 keV form the neutron wrap around, on top of which means the next neutron pulse is laid. Neutron flux spectra from detectors utilizing radioisotopes that do not fission in response to low-energy neutrons, such as ^{238}U or ^{232}Th, may be used to determine which portion of the spectrum measured by materials such as ^{235}U results from high-energy neutrons in the current pulse. [Fow47]

Regardless of which isotope is used, the uranyl moiety luminesces. It was hoped that this luminescence would eliminate the need for wavelength-shifting dyes in the scintillator. However, both the luminescence and the yellow coloration of the uranyl molecules interfered with the escape of light produced by the liquid scintillator. Attempts were made to address these issues by varying the wavelength-shifting dyes
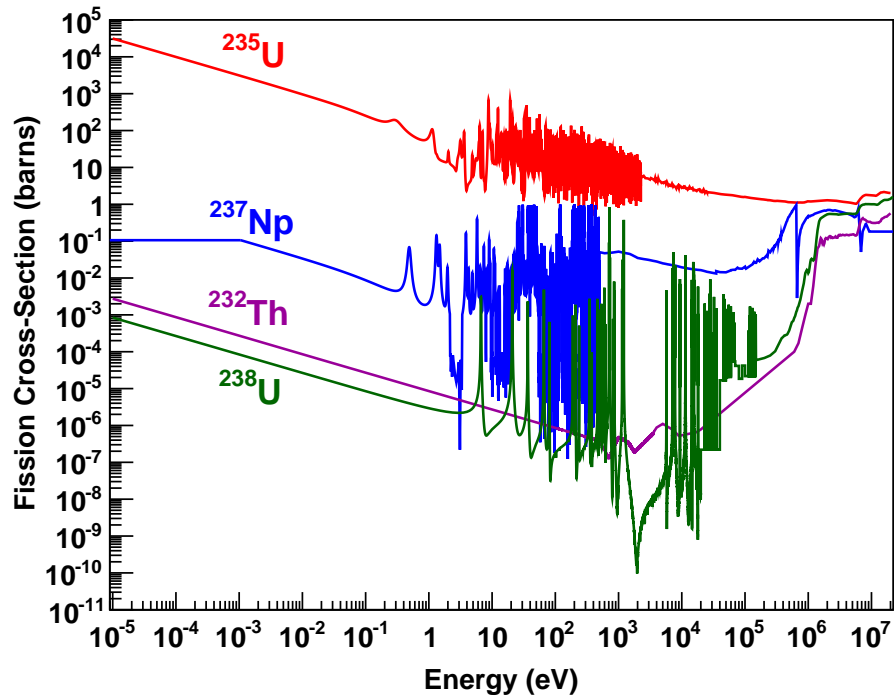
Figure 6.1: Fission cross-sections of ^{235}U, ^{237}Np, ^{238}U, and ^{232}Th. ^{235}U and ^{237}Np are the most suitable isotopes for a fission flux monitor, since they have no threshold neutron energy for fission, unlike ^{238}U and ^{232}Th. Cross-sections for ^{235}U, ^{237}Np, and ^{238}U were obtained from the Evaluated Nuclear Data File (ENDF); cross-sections for ^{232}Th were obtained from the Japanese Evaluated Nuclear Data Library (JENDL).

and their concentrations. Eventually, ^{232}Th was identified as an alternative candidate. Like ^{238}U, ^{232}Th has a threshold neutron energy - only neutrons with energies greater than 1.5 MeV have a fission cross-section greater than 0.1 b. However, unlike those of ^{238}U, the oxides of ^{232}Th are colorless and do not luminesce. Characterization of thorium-loaded liquid scintillator solutions showed optical properties that were comparable to those of liquid scintillator, so ^{232}Th was selected for incorporation into the scintillators fabricated for testing in the beam line.

6.2   Characterization of Uranium Solutions

A high mass loading of fissionable material was desirable to maximize the likelihood of fission interactions. However, if the mass loading was too high, detections of α-particles from the decay of the fissionable material would dominate the signal, resulting in pulse pileup. To estimate the maximum tolerable activity, the decay time

of the liquid scintillator was conservatively estimated at 50 ns, and ten decay times, or 500 ns, were allowed for the complete decay of the pulse. To minimize pileup, the average time between the beginning of a true gamma or neutron pulse in the liquid scintillator and the next alpha decay event should be greater than 500 ns. This can be treated as an interval between two random events, the previous and next α-decays of the fissionable material. If a random point in time is chosen between these two events, the average time to the next event is $1/r$, where r is the α-decay rate. [Kno00] The average time to the next event can therefore be written as a function of constants specific to the isotope,

$$\frac{1}{r} = \frac{1}{\lambda N} = \frac{t_{1/2}M}{mN_A \ln 2} \tag{6.1}$$

where λ is the decay constant, N is the number of atoms of the radioisotope present, $t_{1/2}$ is its half-life, M is its atomic weight, m is its mass in grams, and N_A is Avogadro's number. For a solution containing 1 g of ^{238}U, Equation 6.1 predicts a decay rate of 12,432 decays/s, so the average time between the arrival of a γ-ray or neutron and an α-particle decay is 80.44 μs. The accidental coincidence rate, r_{acc}, may be described using the equation,

$$r_{acc} = r_1 r_2 t_r \tag{6.2}$$

where r_1 and r_2 are the two decay rates and t_r is the time required by the system to resolve the pulse. [Leo94] Assuming a resolving time of 500 ns and a sample rate of 12,432 decays/s, Equation 6.2 predicts 77.3 coincidences/s between two α-particles. The rate of neutron interactions in a uranium-loaded liquid scintillator, r_{ntot}, may be calculated as

$$r_{ntot} = \Phi \sigma_{ntot} \rho \tag{6.3}$$

where Φ is the neutron flux, σ_{ntot} is the total neutron interaction cross-section, and ρ is the atomic density of the solution. Over the 90L energy range, the total neutron interaction cross-section for the elements present in the uranium-loaded liquid scintillator ranges from approximately 2 barns to 20 barns, with hydrogen having the highest cross-section. [Shi] For the purpose of preparing a conservative estimate of the event rate, the cross-section of the solution as a whole was assumed to be 20 barns. Its atomic density was assumed to be identical to that of toluene, which has a density of 0.8669 g/mL and atomic weight of 92.14 g/mol, hence contains 5.666×10^{21} atoms/mL. At the 90L flight path, the neutron flux over all energies is 8.584×10^7 neutrons/s/cm^2. [Tov09] The estimated rate calculated using Equation 6.3 was therefore 9.727×10^6 interactions/s/mL, or 9.727×10^8 interactions/s in

a 100-mL detector. Therefore, a conservative estimate of the rate of accidental coincidences between neutrons and α-particles according to Equation 6.2 is 6.046×10^6 /s. This is two orders of magnitude smaller than the neutron event rate, so the pileup due to 1 g of uranium in a 100-mL detector was deemed acceptable.

A molecular complex incorporating uranyl nitrate and tributyl phosphate (TBP), $UO_2(NO_3)_2(TBP)_2$, was selected as the fissionable component of the uranium-loaded scintillator. Since the desired mass of uranium was one gram in a 100 mL detector, 35 mg of ^{238}U in the form of the uranium complex was dissolved in approximately 3.5 mL of the standard liquid scintillator described in Chapter III. In addition, 35 mg of uranium incorporated into $UO_2(NO_3)_2(TBP)_2$ was dissolved in 3.5 mL of toluene to determine whether it could substitute for one or both of the wavelength-shifting dyes used in the liquid scintillator.

Compounds containing uranyl ions have long been known to emit light in the yellow-green range of the spectrum, and were even discussed by Stokes in his seminal paper describing the Stokes shift. [Sto52] The uranyl emission typically appears as four to six bands about 20-30 nm apart between roughly 470 nm and 600 nm. [dA03] All of these bands result from the excitation of an electron from the UO_2^{2+} molecular orbital to the uranium $5f$ atomic orbital. [Hna10] The vibrational structure in the luminescence indicates that there are several possible methods of de-excitation: electron transfer to the ground state or to a symmetric or anti-symmetric state of the uranyl ion. [Leu99] [Hna10] The precise locations of the emission bands vary slightly depending on which ligand is bound to the uranyl ion. [Jør82] All of the uranium-loaded solutions were yellow, as illustrated by Figure 6.2.

6.2.1   Characterization of Uranium Complex in Toluene

The first solution characterized consisted of the uranium complex in toluene. Both surface and normal RL from the uranium-loaded toluene were essentially absent, as shown by Figure 6.3. The failure to observe any luminescence indicated that any light emitted by either the uranyl oxide or the toluene was absorbed by the solution.

The uranium-loaded toluene also displayed only weak PL, shown in Figure 6.4. The characteristic toluene excitation at 260 nm and broad emission around 280 nm, shown in Figure 3.6, were entirely absent. Instead, the solution displayed weak luminescence at 467 nm and 548 nm. The observed emission peaks must result from the uranium complex; since TBP does not luminesce, uranyl nitrate must be the source. [Zha09] The observed PL emission peaks for $UO_2(NO_3)_2(TBP)_2$ are consistent with the spectra reported for uranyl nitrate hydrates, $UO_2(NO_3)_2 \cdot nH_2O$, both

Figure 6.2: Uranium complex dissolved in liquid scintillator, showing the yellow coloration characteristic of uranyl oxides.

alone [Leu99] and with phosphonic acid ligands [Hna10]. However, at least four bands are typically observed in the PL of uranyl compounds; the locations of the peaks in Figure 6.4 suggest that additional peaks would be expected near 494 nm and 521 nm. These peaks were not obvious in the broad PL scans used in the initial analysis of a material with unknown excitation and emission wavelengths.

Although only two bands of the vibrational structure were observed in the PL of uranium-loaded toluene, its UV/Vis displayed extensive structural fluctuations, as shown in Figure 6.5. Here, the vibrational structure extends throughout the region from 350 nm to 500 nm. The number of fluctuations reflect the presence of the complicated, multi-peak structures that are often associated with each band due to vibrational levels of the singlet state. [Leu99] The peak centered at 376 nm is indicative of a broad luminescence from the uranyl complex; the toluene luminescence was not observed due to the high absorption cutoff resulting from the yellow coloration of the solution.
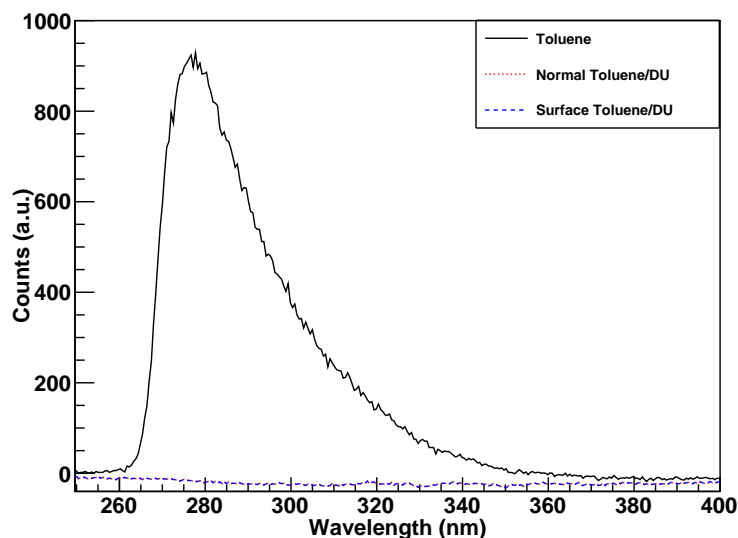
Figure 6.3: Radioluminescence of toluene compared with radioluminescence of toluene/uranium solution. The uranium-containing solution was expected to have a radioluminescence spectrum identical to toluene, but instead emitted almost no light. The RL of the uranium-loaded solution appears negative due to fluctuations in the background during the 2 s measurement compared with the subtracted background.
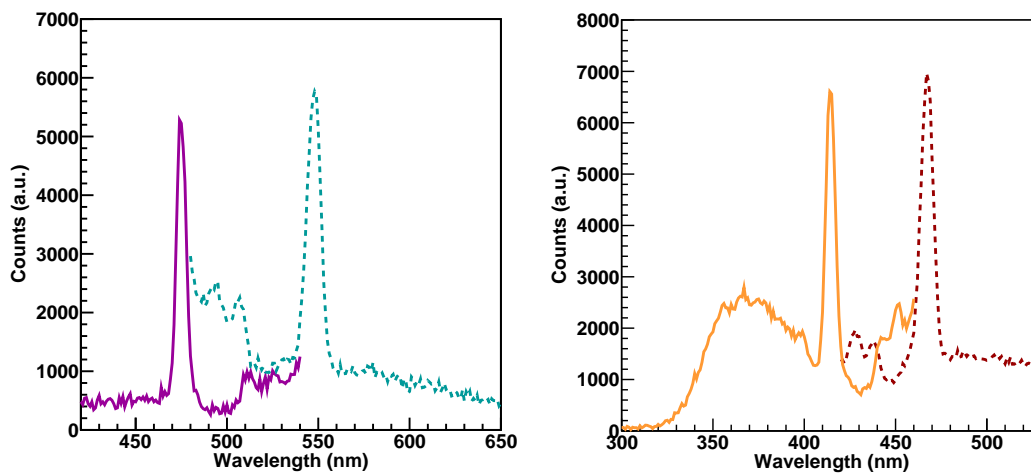
Figure 6.4: Excitations (solid lines) and corresponding emissions (dashed lines) of uranium complex in toluene. Weak photoluminescence of the uranium complex in toluene, showing excitation at 415 nm and 475 nm, with corresponding emissions at 467 nm and 548 nm. Pure toluene absorbs light around 260 nm and emits it in a broad spectrum around 300 nm, as shown in Figure 3.6.
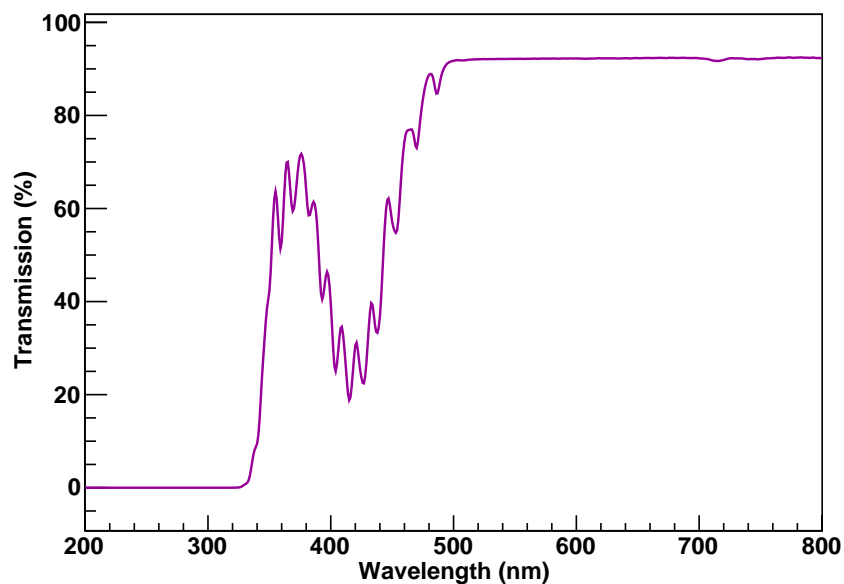
Figure 6.5: UV/Vis of uranium-loaded toluene. Uranyl vibrational structure is evident. Toluene luminescence, which would be expected near 280 nm, cannot be seen due to the absorption cutoff.

6.2.2 Characterization of Uranium Complex in Liquid Scintillator

Initially, the uranium complex was suspended in the liquid scintillator whose development is described in Chapter III. However, as shown in Figure 6.6, RL of the uranium-loaded solution was significantly less intense than that of liquid scintillator alone. The total intensity of the uranium-loaded solution over all wavelengths was 5.0×10^5 counts/s, compared with 2.3×10^6 counts/s from the liquid scintillator. In addition, the emission of the uranium-loaded scintillator was spread over a broader wavelength range. Together, these observations suggested that some of the energy emitted by the liquid scintillator excited the uranium complex.

The vibrational structure of the uranyl oxide singlet state was visible in the UV/Vis spectrum, shown in Figure 6.7. The transmission rapidly falls off from ∼90% at wavelengths above 500 nm to almost zero for wavelengths below 400 nm. The vibrational structure of the uranyl oxide singlet state which appears in this region was also observed in the PL spectrum, shown in Figure 6.8.

Like the solution shown in Figure 6.2, all of the uranium-containing solutions were yellow due to the presence of uranyl oxide. It was suspected that the yellow solution was absorbing some of the blue-violet emission of the liquid scintillator. This theory was supported by energy spectra taken using ^{137}Cs and ^{60}Co sources, shown in
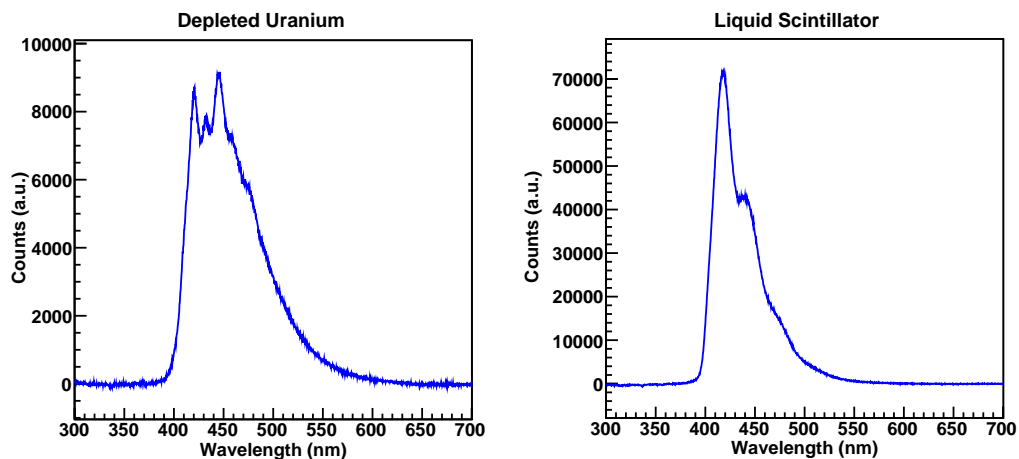
Figure 6.6: Radioluminescence of uranium in liquid scintillator (left) and of liquid scintillator alone (right). The decreased efficiency and increased wavelength range of the scintillation from the uranium-loaded scintillator suggest that energy is transferred from an excited state of one of the liquid scintillator components to uranium, which then de-excites through an emission at higher wavelengths than is observed in the liquid scintillator.
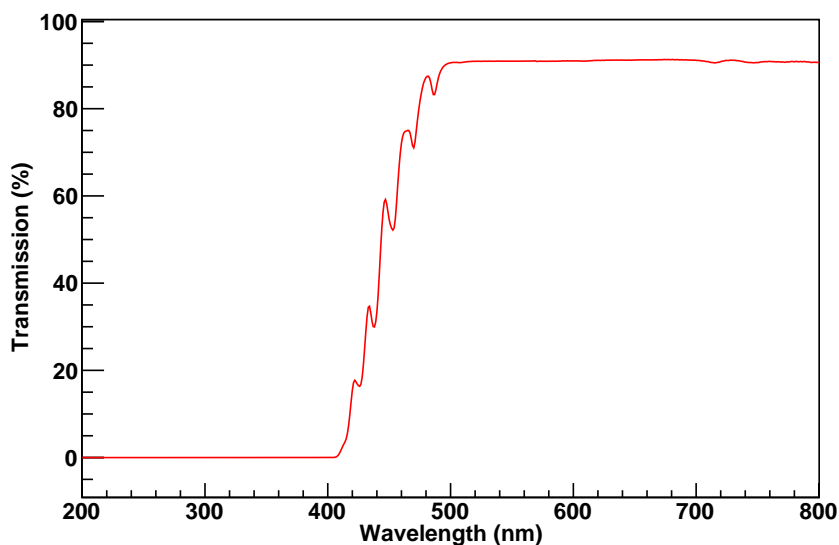
Figure 6.7: Ultraviolet/visible spectroscopy of liquid scintillator/uranium solution.

107
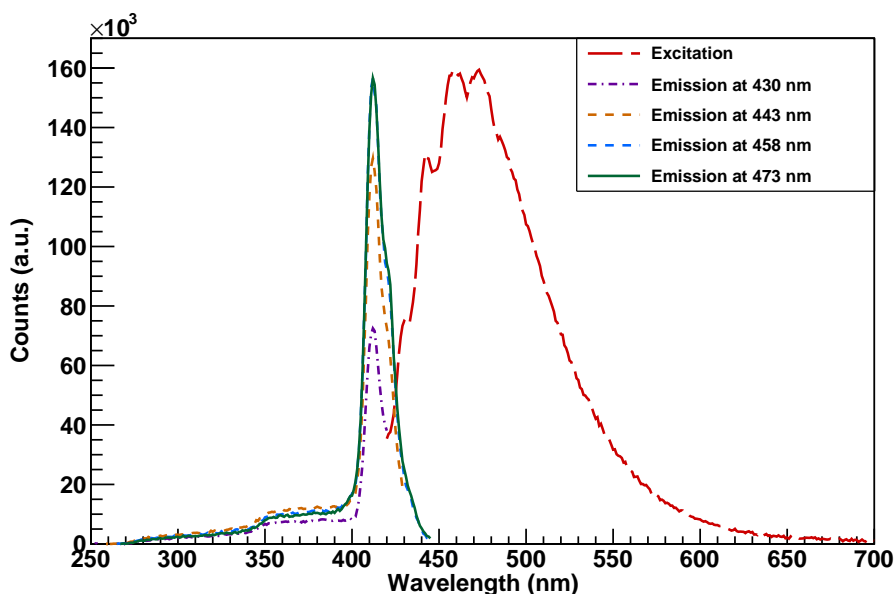
Figure 6.8: Photoluminescence of uranium in liquid scintillator. The wavelength range of the emission is typical of uranyl complexes. The humps in the emission curve result from vibrational states in the uranyl oxide.

Figure 6.9. The RL of uranyl nitrate in PPO and toluene was 1.1×10^6 counts/s, almost half the number of counts observed from liquid scintillator alone, so a noticeable response to γ-rays was expected, but instead the spectra displayed far fewer counts than expected and did not include characteristic Compton edge, photopeak, or α-particle response features.

During the 5-minute run without a source, 141,297 counts were measured. In comparison, a 5-minute run with a ^{60}Co source contained 140,733 counts, 2σ fewer than the background, and the 5-minute run with the collimated ^{137}Cs source contained 139,473 counts, 5σ fewer. The α-particles produced through the decay of ^{238}U with branching ratios greater than 0.01 have energies of 4.151 MeV and 4.198 MeV. [1] Assuming the liquid scintillator to be equivalent to toluene, the NIST Stopping-Power and Range Tables for Helium Ions (ASTAR) database gives continuous slowing down approximation ranges of 2.685×10^{-3} g/cm^2 and 2.731×10^{-3} g/cm^2 for α-particles with these energies. [oSb] Dividing the toluene density by these values produces ranges of 30.97 μm for 4.151 MeV α-particles and 31.50 μm for 4.198 MeV α-particles. Therefore, all α-particles generated in the 1 cm $\times$ 1 cm $\times$ 4 cm cuvette may be

assumed to be detected. The α-event rate was

$$\frac{dN}{dt} = -\lambda N = \frac{(0.09 \text{ g})(6.022 \times 10^{23} \text{ atoms/mol})}{238.02981 \text{ g/mol}} \times \frac{\ln 2}{1.411 \times 10^{17} \text{ s}}$$

$$= 1118.537 \text{ decays/s}$$

(6.4)

where λ is the decay constant and N is the number of atoms of ^{238}U present in the cuvette. Thus, 335,561 counts due to α-particle interactions should have occurred in the detector during each 5-minute measurement period.

To determine the activity expected from the collimated 287 μCi source, a 30-minute spectrum was obtained using an Amptek GAMMA-RAD detector with a 76 mm $\times$ 76 mm NaI(Tl) crystal. Exclusive of the noise bin, the spectrum contained 6,327,500 counts. In comparison, a 30-minute background spectrum contained 1,271,012 counts. The detected counts from the ^{137}Cs source were therefore 5,056,488 counts $\pm$ 2,757 counts. The collimator was placed against the front face of the detector, so its solid angle was assumed to be totally subsumed by the NaI crystal. The absorption coefficient, $1/\lambda$, for ^{137}Cs γ-rays in NaI is 0.0765 ± 0.0003 cm^2/g. [How54] The fraction of γ-rays absorbed by the crystal was

$$1 - \frac{I}{I_0} = 1 - e^{-t/\lambda} = 1 - e^{-(3.67 \text{ g/cm}^3)(7.6 \text{ cm})0.0765 \text{ cm}^2/\text{g}} = 0.88$$

(6.5)

where I_0 and I are the initial and final intensities, respectively, and t is the thickness of the crystal in g/cm^2. Therefore, the actual number of γ-rays emitted by the collimated ^{137}Cs source during the 30-minute run was 5,746,009.

A cuvette filled with liquid scintillator and placed in at a typical measurement distance from the ^{137}Cs source for 10 minutes measured 24,183 counts, indicating that it detected 1.26% of the γ-rays emitted during that period. Therefore, during the 5-minute measurement of the thorium-loaded liquid scintillator with the collimated ^{137}Cs source, 12,091 γ-rays should have been detected, in addition to the 335,561 α-decay events in the scintillating solution, for a total of 347,652 expected events. The 139,473 counts measured with the ^{137}Cs source present represent only 40% of those expected, and the 141,297 counts measured without a source represent only 42% of the α-particle decays during that period.

This low detection efficiency, as well as the preponderance of low-energy events in the energy spectrum, indicate that light produced by the scintillator was absorbed by the highly-colored solution. Photons produced at the surface of the cuvette were able to escape into the PMT, but photons generated deep within the solution were
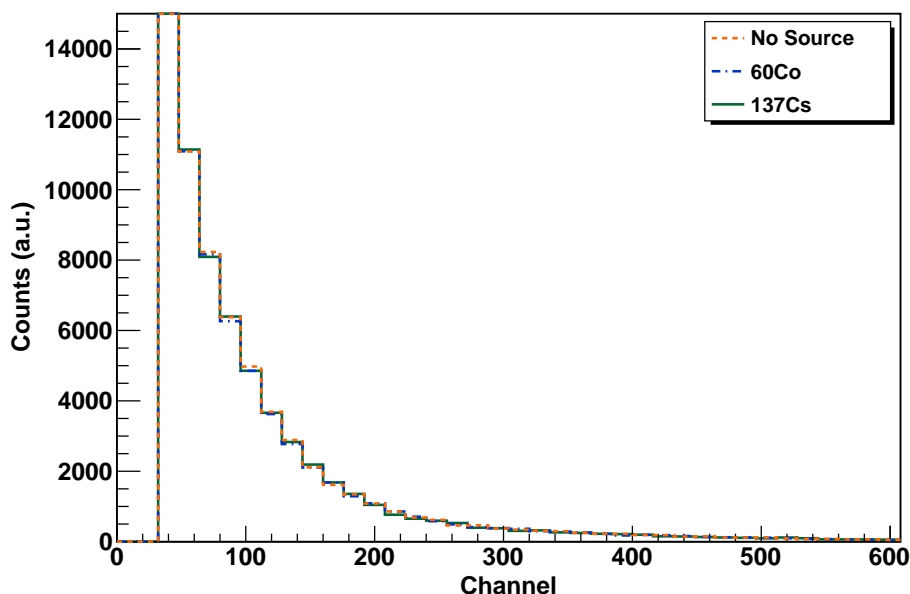
Figure 6.9: Energy spectra of uranyl nitrate in toluene and PPO in response to ^{60}Co and ^{137}Cs sources do not show characteristic features of γ-ray interaction.

self-absorbed.

For this reason, it was decided to attempt to shift the scintillation light into a higher wavelength region by changing the secondary dye of the liquid scintillator. Two samples were prepared, one containing the uranium complex in toluene and PPO, the standard primary dye of the liquid scintillator, and one containing the uranium complex in toluene, PPO, and 3-hydroxyflavone (3HF). 3HF was selected as a secondary dye because its absorption peak, located near 340 nm, was close to the peak PPO emission at 350 nm and its emission, near 530 nm, results in green light, which would not be absorbed by the yellow solution. [Sen79] Since the optimum concentration of 3HF was not known, the solution was prepared using 1 mg per milliliter toluene, the same concentration used for POPOP.

As shown in Figure 6.10, the substitution of 3HF for POPOP in the uranium-loaded liquid scintillator did not improve the emission intensity. The total intensity of the emission, 5.2×10^5 counts/s, was comparable to the 5.0×10^5 counts/s observed for a conventional liquid scintillator loaded with uranium. Furthermore, the emission was split into two peaks, one around the 3HF emission wavelength of 530 nm and one overlapping with the emission of a uranium-loaded liquid scintillator with PPO only. The intensity of the emission in the PPO region of 340 nm to 490 nm dropped from 1.1×10^6 counts/s to 2.8×10^5 counts/s, a reduction of 8.3×10^5 counts/s, 74.5%
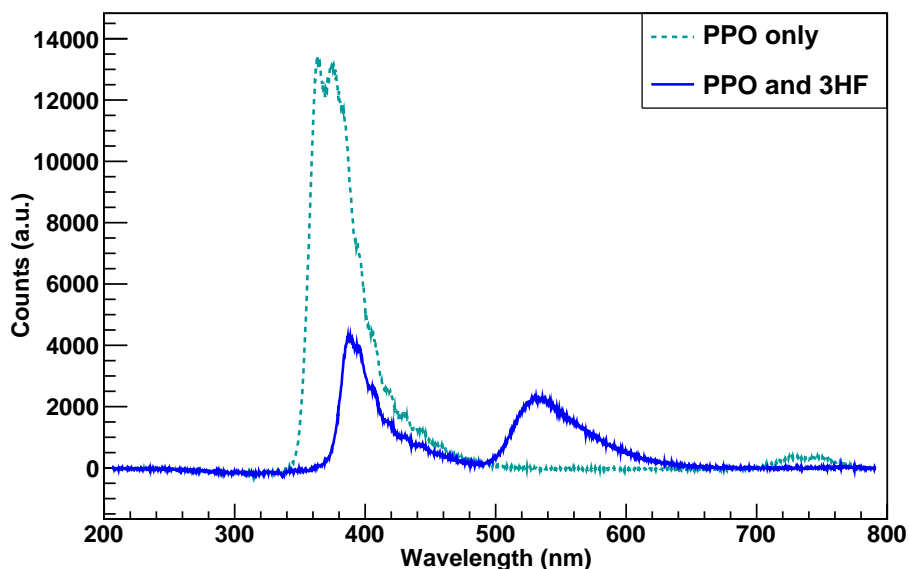
Figure 6.10: Radioluminescence of uranium-loaded toluene-based liquid scintillators during a 2 second window. Some of the light emitted by PPO excites the 3HF dye and is re-emitted at a higher wavelength.

of the original emission. Only 2.6×10^5 counts/s, 31.7% of those missing from the PPO peak, appeared in the 3HF region from 490 nm to 650 nm.

To determine whether the low light output from 3HF indicated that the concentration of dye used was incorrect, an additional test was performed. The 3HF concentration was increased from 1 mg/mL toluene to 2 mg/mL toluene. As shown by the RL spectrum in Figure 6.11, the increased concentration resulted smaller peaks in both the PPO and 3HF regions. Its total intensity, 2.1×10^5 counts/s, was only half that observed for a solution containing half as much 3HF. In addition, the decrease in both peaks of the spectrum indicated that the transfer of energy from PPO to 3HF was not an efficient process, so 3HF was eliminated as a dye. Other dyes with emissions in the 500-600 nm wavelength range were considered. However, due to the difficulty of finding a dye with such a large range between its excitation and emission wavelengths, a decision was made to switch to a different fissionable material.

6.3 Characterization of Thorium Solutions

Due to the poor light yield of liquid scintillator loaded with a uranium complex, resulting from both the uranium excitation and the yellow coloration of the solution, the decision was made to develop a proof-of-principle scintillator utilizing a thorium
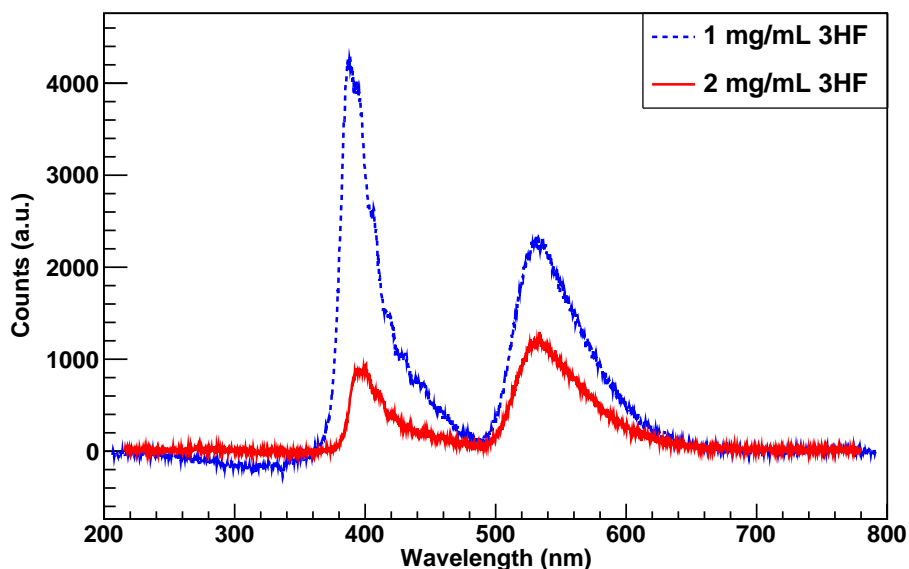
Figure 6.11: Effect on the radioluminescence of increasing the 3HF concentration from 1 mg/mL toluene to 2 mg/mL toluene. Both solutions also contain 7.5 mg PPO per mL toluene. RL was measured over a 2-second window.

complex instead. ^{232}Th, used as $Th(NO_3)_4(TBP)_2$, was selected because the molecular complex is colorless and does not luminesce. In addition, the desired concentration of fissionable material was increased to 2 g in a 100 mL detector. According to Equation 6.1, a detector containing 2 g of ^{232}Th would have an average gap between α-decay events of 122.7 μs, more than two orders of magnitude greater than the 500 ns allowed for the decay of a γ-ray or neutron pulse. Applying Equation 6.2 to the conservatively estimated resolving time of 500 ns and the estimated neutron interaction rate of 9.727×10^8 interactions/s, and assuming an α-particle interaction rate of 8,150 /s predicts an accidental coincidence rate of 3.96×10^6 /s. Since the accidental coincidence rate of α-particles and neutrons is more than two orders of magnitude smaller than the overall interaction rate, the pileup due to 2 g of thorium in the 100-mL detector was considered to be tolerable.

Two 4 mL solutions containing 0.08 g each of thorium were prepared, one using toluene as the solvent and one using liquid scintillator, as well as toluene and liquid scintillator reference solutions. TBP, which was not expected to affect the properties of the liquid scintillator, was added to the reference solutions in order to ensure that any observed effects were due to the thorium nitrate. As shown in Figures 6.12 and 6.13, the thorium-loaded liquid scintillator behaved exactly as desired. Its PL is identical to that of liquid scintillator: the excitation and emission wavelengths are

112
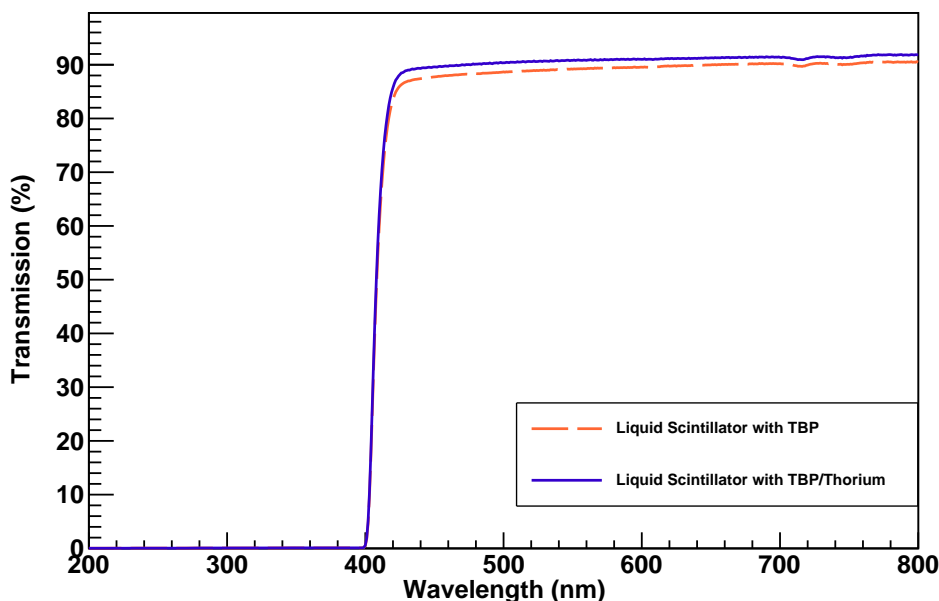
Figure 6.12: UV/Vis of liquid scintillator loaded with thorium, compared with liquid scintillator alone. The thorium-loaded scintillator displays the same transmission cutoff as the regular liquid scintillator. Its increased transmission may result from the increase in effective refractive index.

the same, as are their relative intensities. The colorless solution possesses the same UV/Vis cutoff as liquid scintillator. The thorium-loaded solution displayed a higher peak transmission, peaking at 91.89%, compared with a maximum transmission of 90.57% for the unloaded scintillator, possibly due to the increase in the effective index of refraction and decrease in dispersion of the solution.

The RL of the thorium-loaded solution is 10% brighter than that of liquid scintillator alone, as shown in Figure 6.14, an increase from 2.9×10^6 counts/s to 3.2×10^6 counts/s. It was theorized that the increased RL resulted from a higher photoelectric cross-section due to the presence of the high-Z thorium molecules. As discussed in Chapter V, liquid scintillator can be treated like toluene alone, since the wavelength-shifting dyes contribute a negligible amount to its mass. The photoelectric cross-section of RL x-rays in toluene is 0.273 cm^{-1} for 17.374 keV x-rays and 0.268 cm^{-1} for 17.479 keV x-rays. [oSd] The thorium-loaded scintillator contained 80 mg of thorium, equivalent to 3.448×10^{-4} moles, or 349.14 mg of the thorium complex dissolved in 4 mL of liquid scintillator, which may be assumed to be equivalent to 4 mL, or 3.47 g, of toluene. Assuming that the density of the thorium complex is substantially equal to the 11.7 g/cm^3 density of thorium, the solution
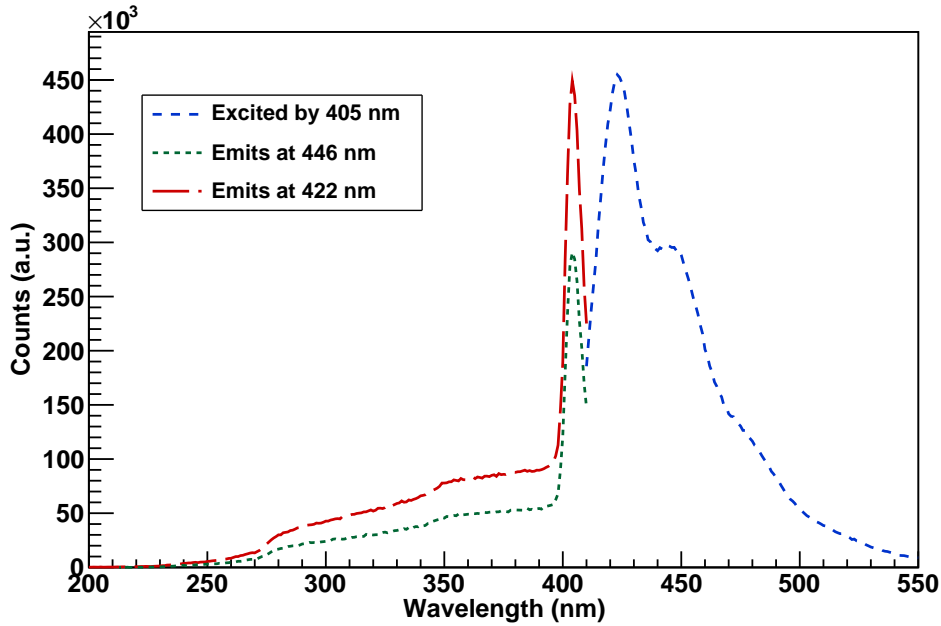
Figure 6.13: PL of thorium in liquid scintillator, showing characteristic liquid scintillator excitation and emissions

has a density of 3.82 g in 4.03 mL, or 0.948 g/cm^3. The photoelectric cross-sections are 2.34 cm^2/g, or 2.22 cm^{-1}, for 17.374 keV x-rays and 2.30 cm^2/g, or 2.18 cm^{-1}, for 17.479 keV x-rays. [oSd] Thus, 7.13 times more photoelectric interactions are expected in the thorium-loaded scintillator, while only about 10% more counts were actually observed. However, the x-ray production of the RL apparatus limits the potential reaction rate in the sample. Typical organic scintillators absorb ∼30% of the x-rays produced, so the RL response for a thorium-loaded scintillator should not be more than a few times the response for a liquid scintillator sample. [Li] In addition, high-Z material may negatively affect the light output of the scintillator, through the deposition of energy by charge carriers in the non-scintillating component.

The spectrum produced by the thorium-loaded liquid scintillator in response to γ-rays from ^{137}Cs had the same shape as the background spectrum, as shown in Figure 6.15. It actually displayed slightly fewer counts than the background spectrum, but was within 1σ. During a 10-minute measurement, 218,400 counts were measured in the background, compared with 218,203 counts, 0.42σ fewer, when the ^{137}Cs source was present. In comparison, a sample containing the same volume of unloaded liquid scintillator produced 24,183 counts in 10 minutes. The expected α-decays can easily
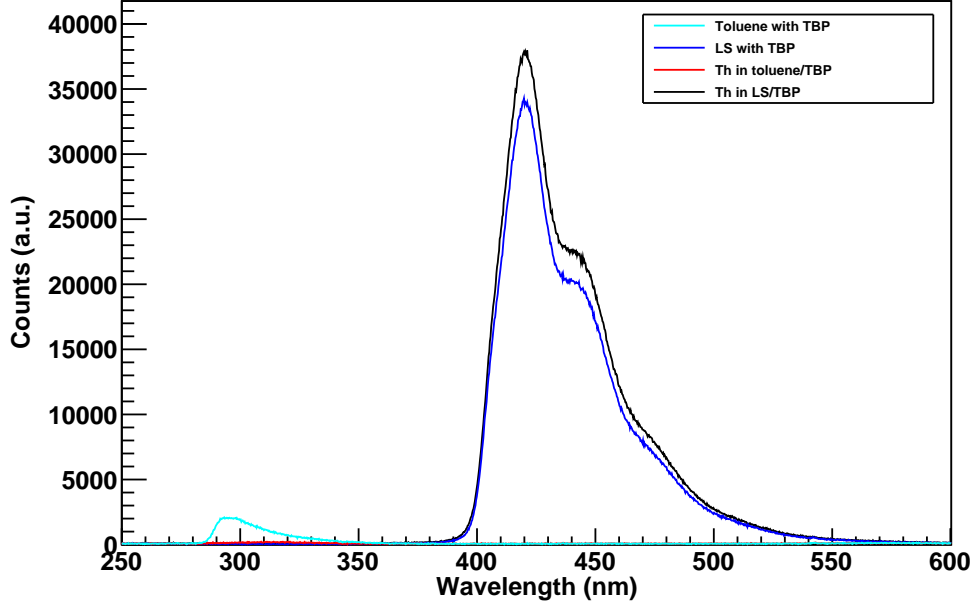
Figure 6.14: RL of liquid scintillator and toluene solutions, each containing 2% (0.08 g) molecular thorium, compared with RL of the same solutions without thorium. The TBP whose presence is noted is the capping ligand used on the thorium; TBP was added to the pure toluene and liquid scintillator solutions to duplicate any quenching effect. The increase in light output of the liquid scintillator solution after the addition of thorium results from the presence of high-Z material.

be calculated,

$$\frac{dN_{Th}}{dt} = -\lambda_{Th}N_{Th} = \frac{(0.08 \text{ g})(6.022 \times 10^{23} \text{ atoms/mol})}{232.038 \text{ g/mol}} \times \frac{\ln 2}{4.420 \times 10^{17} \text{ s}} \quad (6.6)$$

$$= 325.600 \text{ decays/s}$$

where λ_{Th} is the decay constant and N_{Th} is the number of atoms of ^{232}Th present in the cuvette. During a ten-minute measurement, Equation 6.6 predicted 195,360 α-particle decays. The expected β-decays from the ^{228}Ra daughter can likewise be calculated, assuming that no ^{228}Ra is present initially, using the equations

$$\lambda_1 = \frac{\ln 2}{4.420 \times 10^{17} \text{ s}} = 1.568 \times 10^{-18} \text{ s}^{-1} \quad (6.7)$$

$$\lambda_2 = \frac{\ln 2}{1.815 \times 10^8 \text{s}} = 3.819 \times 10^{-9} \text{ s}^{-1} \quad (6.8)$$

115
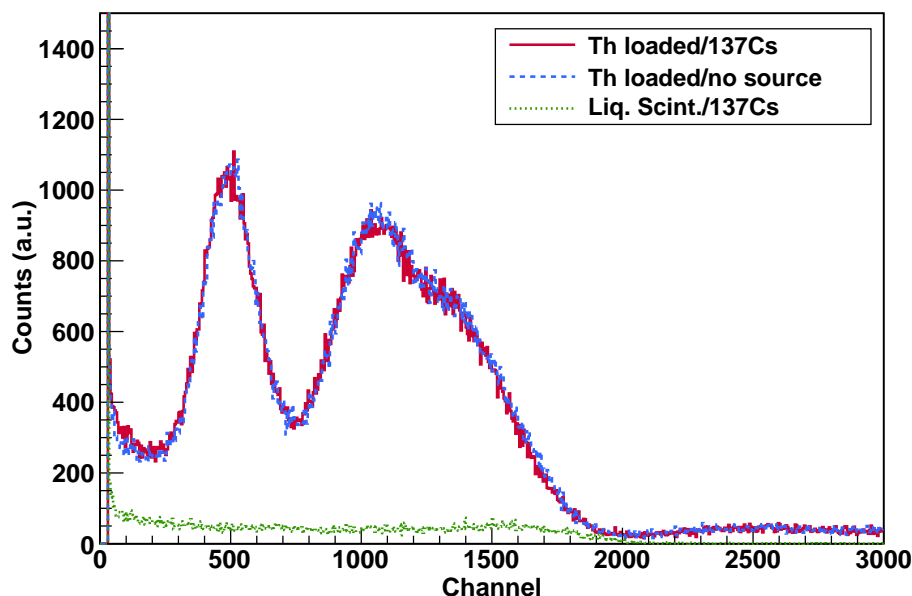
Figure 6.15: Response of thorium-loaded liquid scintillator to ^{137}Cs γ-rays, compared with self-activity of sample and γ-ray response of unloaded liquid scintillator.

$$N_{Ra} = \frac{\lambda_1}{\lambda_2 - \lambda_1} N_0 (e^{-\lambda_1 t} - e^{-\lambda_2 t}). \tag{6.9}$$

where N_0 is the number of ^{232}Th atoms initially present and λ_1 and λ_2 are the decay constants of ^{232}Th and ^{228}Ra, respectively. Since the parent and daughter isotopes were not in equilibrium when the spectra were measured, 12 ± 2 days after the samples were prepared, the ^{228}Ra decay rate cannot be treated as a constant. The decay rate during the measurement period may be calculated by multiplying Equation 6.9 by the ^{228}Ra decay rate. This results in 1.072 decays/s with an error of 16.6% due to uncertainty in the elapsed time since synthesis. Even at the maximum possible rate, 1.500 decays/s, only 900 counts due to β-decays of ^{228}Ra should have been recorded. Thus, the total predicted counts due to α- and β-decays during the ten-minute measurement was 196,260 counts, 10% fewer than actually observed. The increased count rate may indicate a higher-than-expected ^{232}Th concentration - 89 mg of ^{232}Th, rather than the 80 mg expected to be present in the solution, would produce the observed counts.

The consistent count rate observed regardless of whether a source was present may result from the deposition of energy in the non-scintillating thorium complex or may indicate a limitation in the data acquisition software in use at the time. [Coo10]

Due to its good optical characterization results, the thorium complex was selected as the fissionable material to be incorporated into a larger detector for beam line tests, as described in Chapter VII.

CHAPTER VII

Beamline Experiments on Fissionable Scintillators

7.1 Introduction

The optical and radiation detection characterization described in Chapter VI established that the thorium-loaded scintillator emitted light at the typical liquid scintillator wavelength of 410 nm in response to x-ray excitation and α-decay of ^{232}Th. However, in order to assess its capability to detect the fragments produced by inducted fission of ^{232}Th, experiments in a neutron beam were needed. Beamline experiments were conducted at LANSCE with the goal of quantifying the neutron detection of the fissionable scintillator, compared with an unloaded liquid scintillator. An increased count rate, attributable to fission, was observed in the thorium-loaded detector.

7.2 Experiment Setup and Data Acquisition

Two scintillator modules were prepared for the first round of experiments in the beam line. Since the optimum configuration for a liquid scintillator detector and PMT is a vertical configuration, with the air bubble in the detector far from the PMT surface, the detectors had to be leak tight. A detector container with a volume of 150 mL was designed for the experiment, as shown in Figure 7.1. The detector was machined out of teflon, to allow scintillation light to reflect off of its interior walls. The detector window, a quartz disc with a 3-inch diameter and 1/8-inch thickness, was purchased from Technical Glass Products and made leak-tight with a fluorocarbon o-ring.

One of the scintillator modules was filled with 2 ± 0.175 g of thorium, in the form $Th(NO_3)_4(TBP)_2$, suspended in the standard liquid scintillator solution, consisting of 1.125 g PPO and 150 mg POPOP in 150 mL toluene. For comparison purposes, the other scintillator module was filled with liquid scintillator, to which an amount of
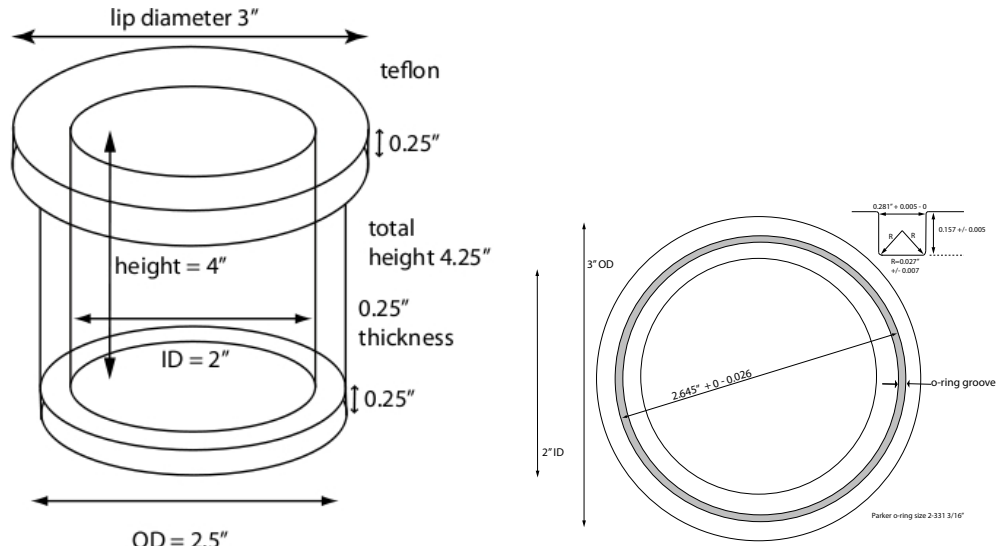
Figure 7.1: 150 mL detector designed for beam line liquid scintillator experiments. The detector was machined from teflon, to maximize the reflection of scintillation light off the interior surface; the outside was wrapped in black electrical tape to make it light tight.

TBP equal to the amount in the thorium-loaded solution had been added, in order to ensure that the only difference between the two solutions was the presence or absence of the thorium nitrate molecule. A fission chamber containing several foils coated with ^{235}U was also used as a comparison detector, as well as to provide a measurement of the neutron flux.

Measurements were performed at the 4FP90L flight path at LANSCE. The locations of the experimental components relative to the spallation source are shown in Figure 7.2. The 4FP90L flight path is part of the Weapons Neutron Research (WNR) Facility, which has a different pulse structure than the Lujan Center, where detectors loaded with CeF_3 were tested. A simplified diagram of the pulse structure is shown in Figure 7.3. Macropulses are delivered to the WNR target at a rate of 100 Hz and have widths of ∼700 μs. Each macropulse contains micropulses that are ∼150 ps wide, which for the duration of this experiment were separated by 1.7866 μs, although spacings several times that are not uncommon. [Tov07] The t_0 pulse used for triggering is generated with each micropulse. Due to the high sensitivity of the liquid scintillators, collimation was used to reduce the neutron beam spot to ∼1 cm in diameter.

The experimental setup is shown in Figure 7.4. Measurements with the two liquid-scintillator-based detectors were performed sequentially. The detector was mounted vertically on a Hamamatsu R2059 PMT with a Hamamatsu E2979-500 socket. Tech-
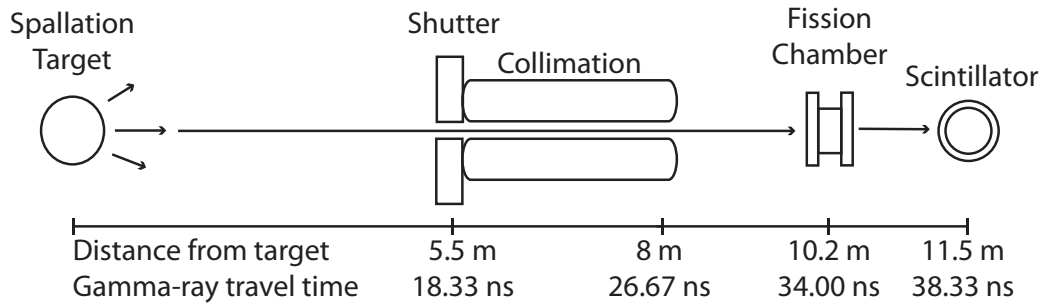
Figure 7.2: Distance of flightpath components from the spallation target and time required for spallation γ-rays to reach them. The accessible area of the 4FP90L flight path begins at the shutter; collimation can be adjusted by the user. The scintillator was placed near the end of the accessible area of the flight path.
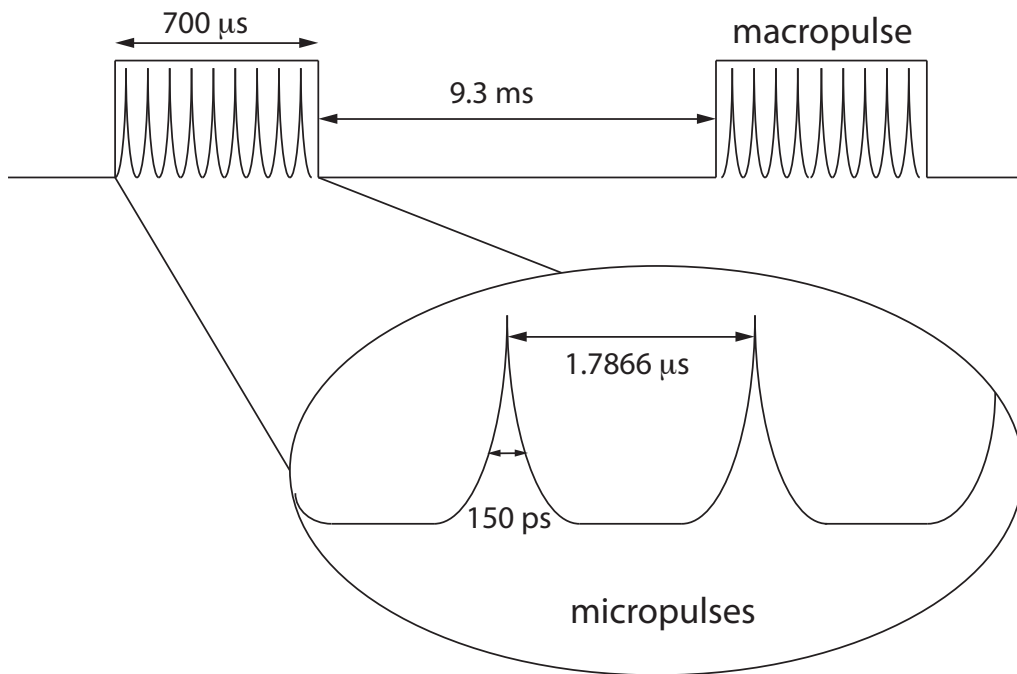
Figure 7.3: Structure of proton pulses delivered to WNR target (not to scale). Macropulses with widths of $\sim$700 μs and containing micropulses typically separated by $\sim$1.8 μs are delivered to the target at a rate of 100 Hz.

120
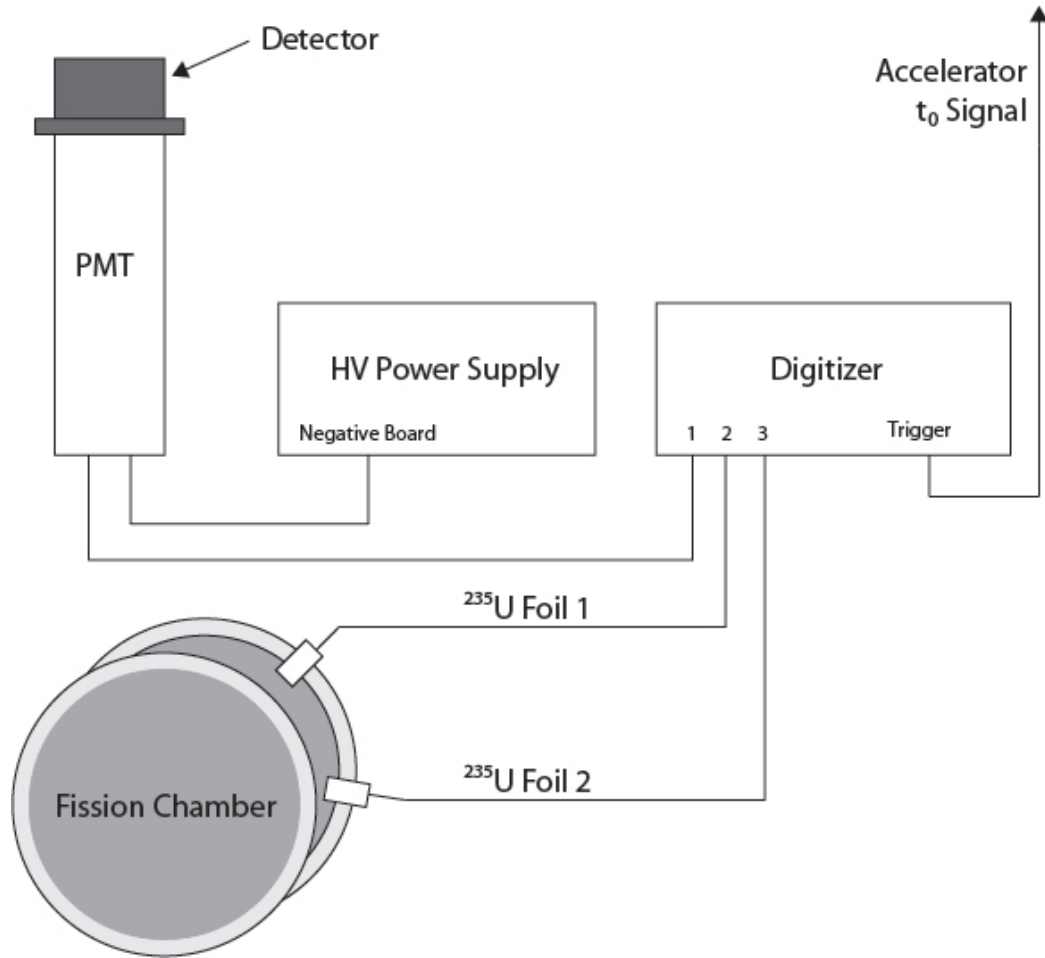
Figure 7.4: Experimental setup for beam line experiments conducted at 4FP90L. Following each trigger signal, the digitizer collected a 250 μs waveform from the scintillator and two foils of the fission chamber.

nical specifications for these components are given in Appendix B. The PMT socket was powered by a LeCroy 1454 High Voltage Mainframe with a LeCroy 1461 12-Channel High Voltage Board 1461N, described in Appendix C. Signals from the PMT were acquired by an Acqiris DC265 8-bit digitizer in an Acqiris CC015 crate. The Acqiris was controlled using the MIDAS software.

Following the arrival of the t_0 signaling the first micropulse in a macropulse, the Acqiris collected a 250 μs waveform for each channel in 2 ns bins. The Acqiris had a selectable full scale of 100 mV, 200 mV, 500 mV, 1 V, 2 V, or 5 V; after examining output pulses from the PMT on an oscilloscope, the 1 V range was chosen for scintillator waveforms to maximize the resolution while minimizing the number of pulses that would be too high for the scale. Since the pulses produced by the PMT were negative, the center of the 1 V range was set at -0.48 V, resulting in a full
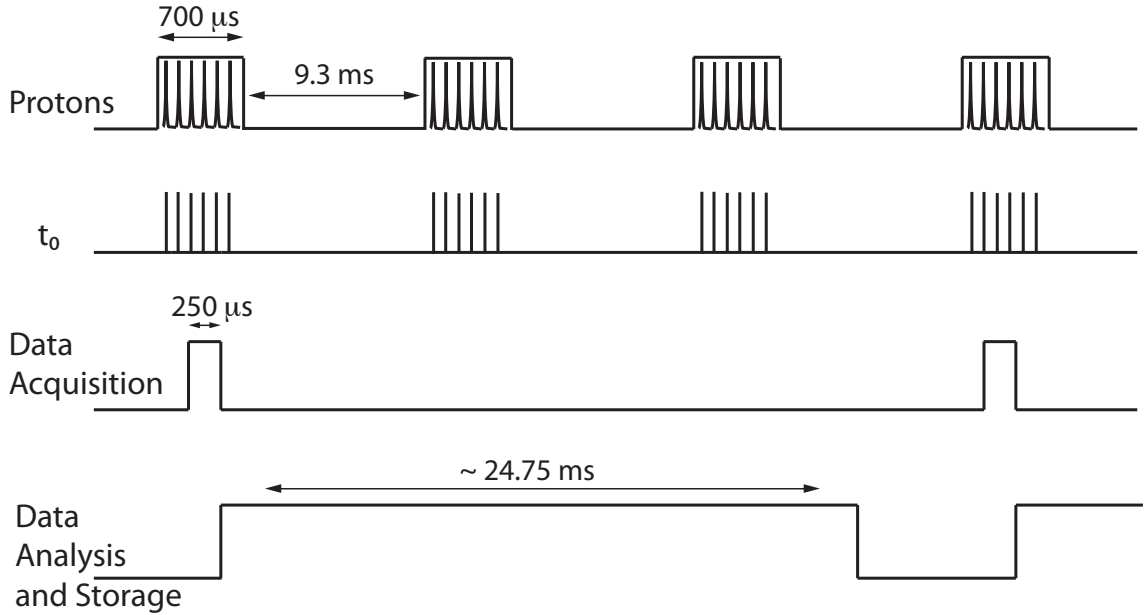
Figure 7.5: Timing diagram for data acquisition system. Each proton micropulse (see Figure 7.3 for more details on the macropulse and micropulse timing) is accompanied by a t_0 signal. Following the arrival of the first t_0 of the macropulse, the Acqiris collects a 250 μs waveform for each channel. Analysis and storage of the waveforms take $\sim$24.75 ms, resulting in a collection and analysis rate of $\sim$40 acquisitions/s.

scale that ran from -0.98 V to 0.02 V. For the two channels recording pulses from the fission chamber, the full scale used was 500 mV, with the midpoint set at -150 mV because of significant noise. Following waveform collection, the data was analyzed by MIDAS. For waveforms from the scintillator, both the results of the MIDAS analysis and the full waveform were saved. All MIDAS analyses performed on waveforms detected from the fission chamber were saved, but due to space constraints only every hundredth waveform from each of the two channels was recorded. Following analysis of the data and writing it to file, the Acqiris was triggered by the first micropulse in the next macropulse. As indicated by Figure 7.5, the total time required for acquisition, analysis, and storage of the waveforms was $\sim$25 ms, so 40 triggers/s resulted in acquired waveforms.
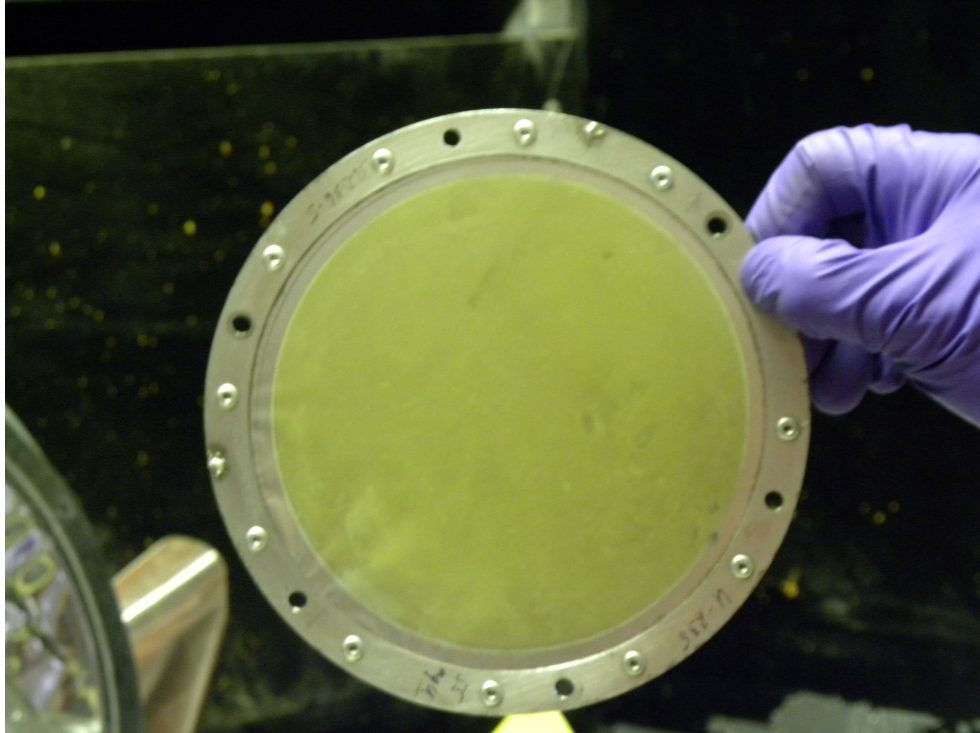
Figure 7.6: A uranium-coated foil from the fission chamber used to monitor the neutron flux during characterization of the thorium-loaded detector. The total mass of ^{235} coated on the foil is 50 mg. Electroplating of the uranium onto the stainless steel foil results in a non-uniform coating.

7.3   Analysis of Fission Chamber Measurements

A fission chamber was mounted in the flight path to provide neutron flux information and to serve as a comparison neutron detector. The chamber had been constructed according to the design described by Wender, [Wen93] and contained three stainless-steel foils that had been coated with ^{235}U, two of them 13 cm in diameter and one of them 10 cm in diameter. One of the foils is shown in Figure 7.6. Since the ^{235}U was deposited by electroplating, the coating is non-uniform, but a total mass of 50 mg of ^{235}U was coated on each of the larger foils and 15 mg was coated on the smaller foil.

Voltage was applied to the fission chamber through a fast preamplifier. Spectra from the two foils coated with 50 mg ^{235}U were collected using the Acqiris digitizer. Due to the low efficiency of the fission chamber and the small beam diameter, less than 10% of recorded spectra contained a fission event. Only every hundredth spectrum produced for each foil was saved, however, peak information for every spectrum was collected using MIDAS. In calculating the neutron arrival rate, it was desirable to

Scintillator	Number of Runs	Triggers	Ch2 Events	Ch3 Events
Thorium-Loaded	251	7,117,657	$287,455 \pm 536$	$317,393 \pm 563$
Unloaded	237	6,918,164	$287,446 \pm 536$	$297,679 \pm 546$
Ratio	1.059	1.029	1.000 ± 0.002	1.066 ± 0.003

Table 7.1: Fission events recorded for the ^{235}U foils connected to channels 2 and 3, for all analyzed thorium-loaded and unloaded liquid scintillator runs. The ratio of events in each channel for the two detectors did not agree with the ratio of triggers, indicating that the beam intensity varied while data was being taken. The difference in fission event ratio between the two channels resulted from a bad solder connection inside the fission chamber.

use the information on peaks found by MIDAS, since recorded spectra containing a fission event provided such a small sample size. This required that the quality of peaks found by MIDAS be assessed.

Fission chamber spectra displayed considerable noise due to α-particle decay of the ^{235}U coating and γ-ray events. The negative-polarity pulses from the fission chamber were measured on a scale from 0.1 V to -0.4 V, with the threshold for the MIDAS peak-finding algorithm set at -0.085 V. Examination of recorded spectra revealed that fission event pulses typically had pulse heights several times the peak threshold; no fission events were found to have produced pulses smaller than the threshold. Since MIDAS occasionally misidentified fluctuations in the decay of fission pulses as peaks, only those peaks which did not occur within 100 bins, or 200 ns, of a previous peak were accepted as legitimate.

The peaks located by the MIDAS peak finding routine could be used to determine the relative neutron flux incident on each detector by comparing the number of fission events in all unloaded liquid scintillator experimental runs with the number of fission events in all thorium-loaded scintillator runs. However, preliminary analysis of the fission chamber data, as summarized in Table 7.1, indicated that the fission event ratios differed for the two foils measured, and neither agreed with the ratio of trigger (t_0) events. The difference in fission event ratios between the two foils resulted from a faulty solder connection inside the fission chamber, which was discovered after the experiment had concluded. Unfortunately, it was not known which channel corresponded to the bad connection, and visual examination of stored waveforms from the two channels did not find obvious indications.

The discrepancy between the trigger event ratio and the fission event ratio indicated that the beam current varied during the experimental runs. While the use of the beam t_0 ensured that no data was recorded during beam outages, decreased

beam current would have resulted in a smaller number of fission events per trigger. To accurately compare the fission event ratio in the two detectors would require using only runs with similar beam currents. An indication of the beam current could be obtained by calculating the rate of fission events per trigger event for each experimental run.

The rate of fission events per t_0 trigger in each recorded data file is shown in Figure 7.7. Fluctuations in the event rate indicate times when the beam current varied. For example, the event rate in both channel 2 and channel 3 decreases for runs 1170 through 1300, indicating a reduction in the beam current. To evaluate the quality of the foil response, a region of typical beam current was needed. The number of runs used to determine the true rate was calculated based on the requirement that there be no greater than 1% error due to statistical variation in the number of fission events,

$$\frac{\sqrt{x}}{x} = \frac{1}{\sqrt{x}} = 0.01 \tag{7.1}$$

$$x = \left(\frac{1}{0.01}\right)^2 = 10,000. \tag{7.2}$$

Since a run typically contained slightly more than 1,000 fission events in each channel, ten runs would be sufficient to reduce the statistical error to less than 1%. Figure 7.7 was used to identify twenty measurement runs for each detector that were performed with full beam current: runs 1080-1099 for the thorium-loaded detector and runs 1310-1329 for the unloaded scintillator.

As shown in Table 7.2, the ^{235}U foil whose signal was measured by channel 3 displayed a fission event ratio that was consistent with the ratio of trigger events in the thorium-loaded and unloaded scintillators. Based on this data, it was concluded that channel 2 was connected to the foil with the faulty solder connection. This conclusion was also supported by Figure 7.7, which showed a reduced event rate between runs 850 and 1000 for channel 2, while the rate in channel 3 remained normal. Therefore, the combined time-of-flight and other spectra for the 237 unloaded liquid scintillator runs were scaled by 1.066, the ratio of fission events in channel 3 for the two scintillators.

7.4 Overview of Waveform Analysis

The 250 μs waveforms collected for the unloaded and thorium-loaded scintillators were analyzed to locate individual pulses and collect data on those pulses. A sample
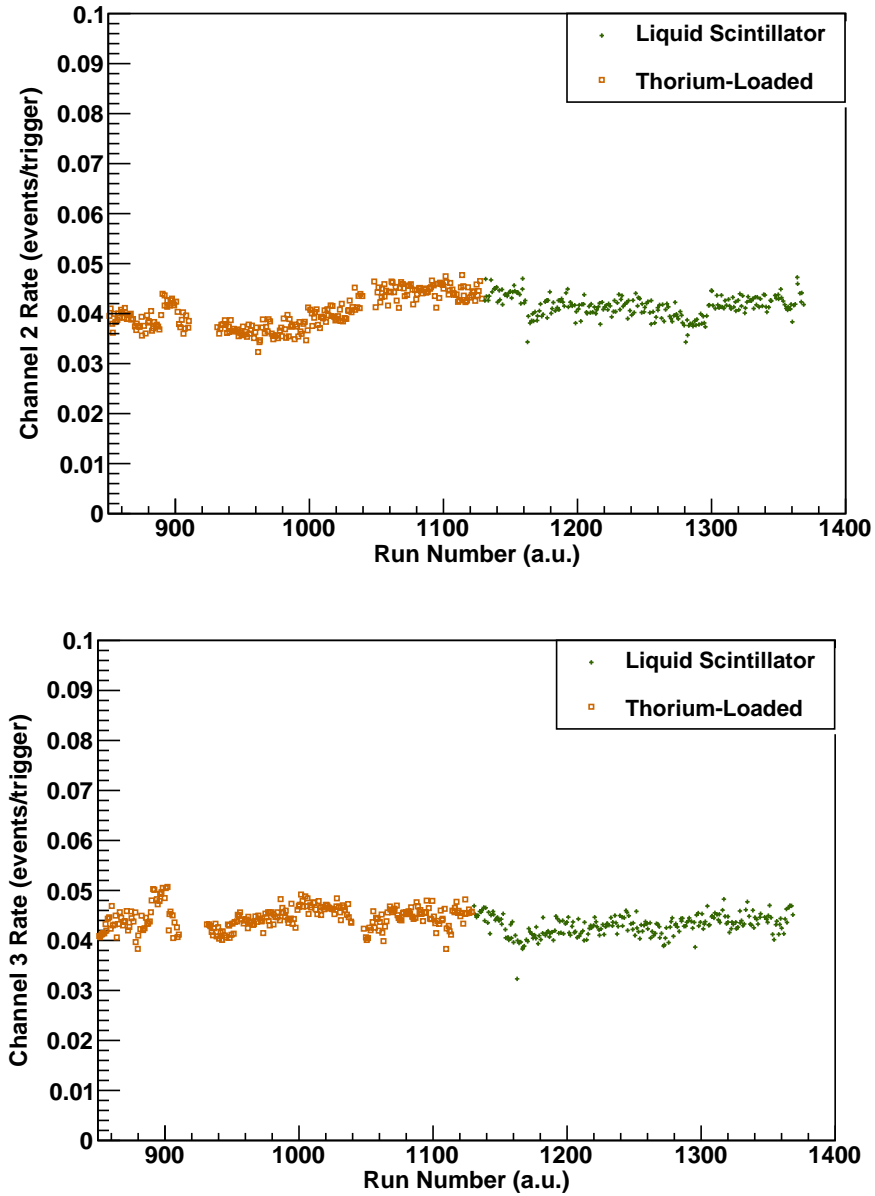
Figure 7.7: Fission events per trigger in channels 2 and 3 for all liquid scintillator and thorium-loaded scintillator experimental runs. Based on the comparison of full-beam-current events summarized in Table 7.2 and the low beam current observed in Channel 2 between runs 850 and 1000, Channel 3 was determined to be the more accurate indicator of the fission event rate.

Scintillator	Number of Runs	Triggers	Ch2 Events	Ch3 Events
Thorium-Loaded	20	564,340	$25{,}700 \pm 160$	$25{,}640 \pm 160$
Unloaded	20	581,600	$24{,}560 \pm 157$	$26{,}560 \pm 160$
Ratio	1	0.970	1.046 ± 0.009	0.965 ± 0.009

Table 7.2: Fission events recorded for the ^{235}U foils connected to channels 2 and 3, for thorium-loaded scintillator runs 1080-1099 and unloaded liquid scintillator runs 1030-1329. By comparing the fission event ratio for each detector with the trigger event ratio, it was determined that the foil connected to channel 3 provided a more accurate indication of the neutron flux.

waveform is shown in Figure 7.8. The background was observed to vary by 1-2 steps (out of 256 steps total) from the baseline, so a minimum pulse height cutoff was set at 3 steps above the baseline. A maximum pulse height cutoff, set at 248 steps, was used to identify pulses that had exceeded the maximum digitizer voltage. These pulses were discarded since accurate height and area information could not be obtained. For pulses whose maximum heights fell between the two cutoffs, the beginning of the pulse was set at the first time bin with a count rate above the 3 step threshold and the end of the pulse was set at the last time bin with a signal of 2 or more steps above the baseline. For each pulse analyzed, the starting time bin, number of bins between starting and ending bins, area, maximum height, and number of bins before the next peak were collected.

A number of methods were explored for discrimination between γ-ray, neutron, and α-particle events based on the fractional areas of pulses produced. However, none of these techniques were able to reliably differentiate γ-ray and neutron pulses. The difficulty in distinguishing between γ-rays and neutrons resulted from two factors. First, the digitizer used to acquire pulses was capable of recording only eight bits of data. Successful pulse shape discrimination has been more frequently reported using digitizers having at least 12 bits. [Poz09] Using a digitizer with a small number of bits results in little detail in the pulse shape of quickly-decaying signals. Second, neither of the liquid scintillator modules tested had been sparged to remove oxygen. Oxygen quenching in organic scintillators suppresses the luminescence of the triplet state, which is responsible for the longer decay time. [Ber61] This reduction in triplet luminescence has been observed to impede pulse shape discrimination by making the pulses produced by different radiations more uniform. [Pat98]

The location of each event within its 1,786.6 ns micropulse was determined by creating a time-of-flight spectrum. Each data file contained 28,000-30,000 waveforms, each 250 μs long and containing slightly more than 139 micropulses. A single 250 μs
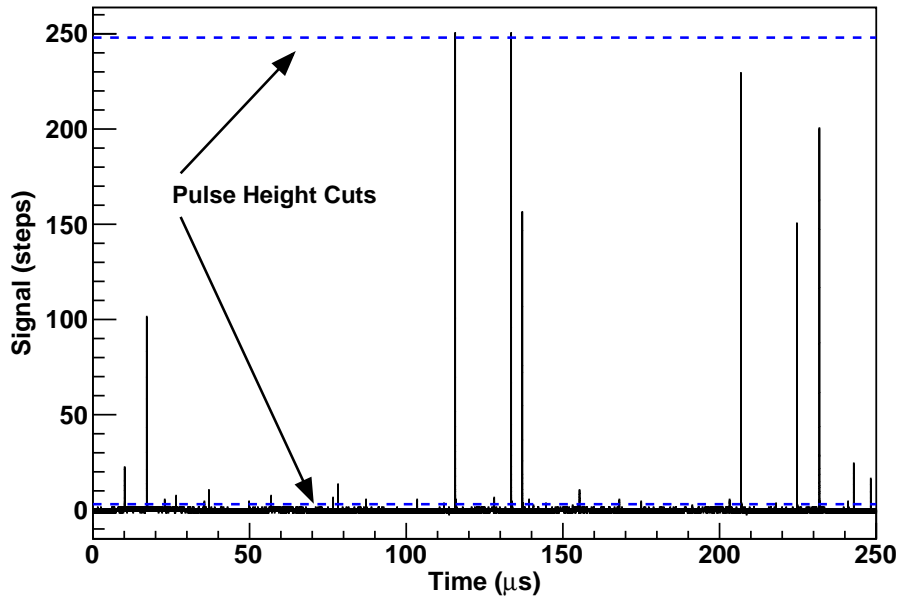
Figure 7.8: Sample 250 μs waveform collected from the unloaded liquid scintillator using the Acqiris digitizer. Analyzed pulses had maximum pulse heights between the two cuts shown, at 3 steps and 248 steps.

waveform, such as the one shown in Figure 7.8, contains too few events to distinguish the micropulse structure, but when the events in all waveforms in a data file are combined into a single time distribution, the locations in time of the micropulses become obvious, as shown in Figure 7.9. The first spallation products to arrive in each micropulse are the γ-rays, since they have the greatest velocity. The γ-flash results in a large number of counts within a short period of time ($<$12 ns). The neutrons, which begin arriving $\sim$5 ns after the end of the γ-flash, result in a much smaller event rate, always less than 150 counts, so the γ-flashes were identified by locating peaks in the summed spectrum with heights greater than 300 counts. The time-of-flight of each event relative to the γ-flash was determined by calculating its distance in time from the preceding γ-flash. In addition to the 139 whole micropulses captured in each waveform, partial micropulses were recorded at the beginning and end of the 250 μs acquisition period; events in these two micropulses were not included in further analyses.

In analyzing the neutron interactions responsible for the time-of-flight spectrum, it is sometimes more useful to have a spectrum that is a function of incident neutron energy. In order to convert a time-of-flight spectrum to neutron energy, each location in time must be converted to its equivalent neutron energy. Since all neutrons with
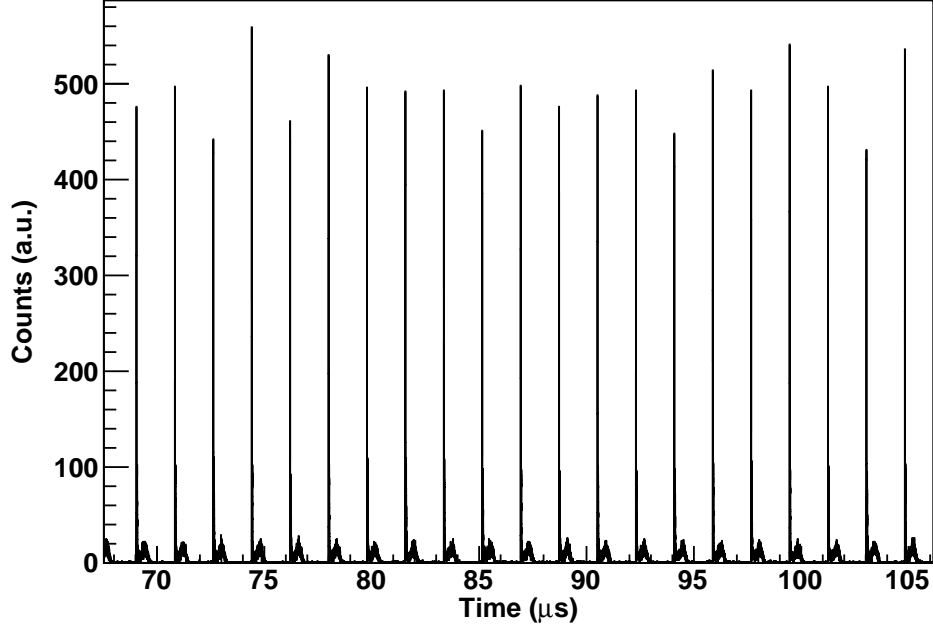
Figure 7.9: Section of the time distribution of pulses detected in 29,113 runs, each 250 μs long. Micropulses are characterized by a tall ($>$300 counts) peak due to the γ-flash, followed by events due to neutron interactions. The relative location in time of each event was determined by its distance from the preceding γ-flash peak.

energies greater than 46 keV have velocities greater than 1% of the speed of light, and all neutrons with energies greater than 4.7 MeV have velocities greater than 10% of the speed of light, the calculation must be performed using relativistic relationships. A series of equations may be used to convert a bin corresponding to a time t_{tof} following the arrival of the γ-flash to the corresponding neutron energy, E_n.

$$t_n = L/c + t_{tof} \tag{7.3}$$

$$v_n = \frac{L}{t_n c} \tag{7.4}$$

$$p_n = \frac{m_n v_n}{\sqrt{1 - v_n^2/c^2}} \tag{7.5}$$

$$E_n = \sqrt{(p_n c)^2 + (m_n c^2)^2} - m_n c^2 \tag{7.6}$$

where L is the flight path length, the distance between the spallation target and the detector, c is the speed of light, m_n is the neutron rest mass energy, and t_n, v_n, and p_n are the calculated neutron arrival time, velocity, and momentum, respectively. The
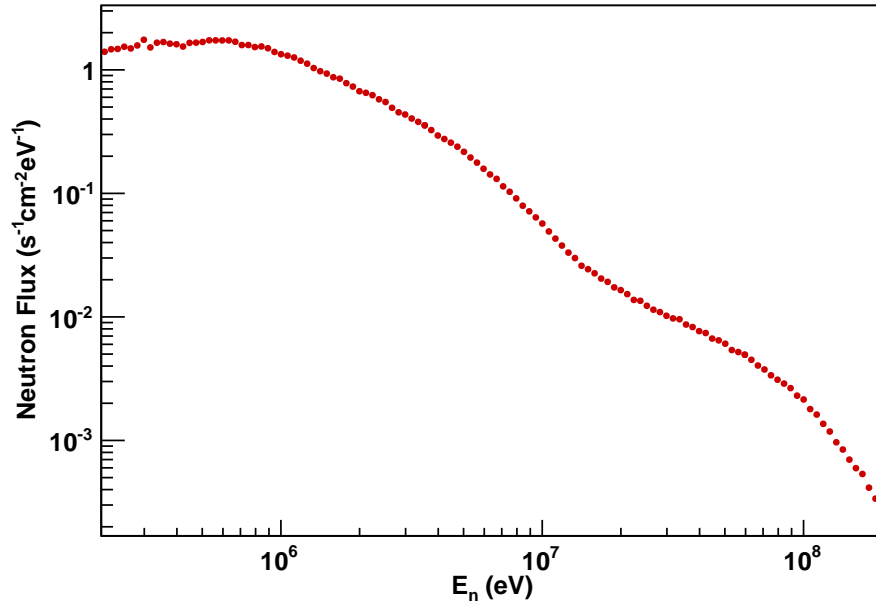
Figure 7.10: Neutron flux profile at flight path 4FP90L, measured using a fission chamber. [Tov09]. Data provided by Fredrik Tovesson.

distance between the spallation target and the end of the experimental area in the flight path was 11.5 m. The neutron energy was calculated only for bins preceding or following the γ-flash, which was centered at $t = 0$, by at least 6 ns. This time was chosen to eliminate the majority of γ-ray events while still providing information about as many neutron events as possible. Since Equations 7.3 through 7.6 produced a series of energy bins with variable widths, the contents of each bin of the resulting histogram were divided by the bin width to produce a count rate per unit energy. Additionally, the neutron time-of-flight spectrum was normalized according to be beam profile. The count rate in the fission chamber was not high enough to provide a statistically accurate measurement of the beam profile at 4FP90L, so a previously measured profile of the neutron flux at the 4FP90L flight path was used for the normalization and is shown in Figure 7.10. [Tov09]

7.5 Measurement of Time-of-Flight Spectra

A typical time-of-flight spectrum recorded for the liquid scintillator is shown in Figure 7.11. The arrival of the γ-flash is visible at 0 ns, with neutrons beginning to arrive shortly afterwards. The feature at 225 ns does not correspond to any expected reaction in the detector, its container, or surrounding materials. To test the hypoth-

130
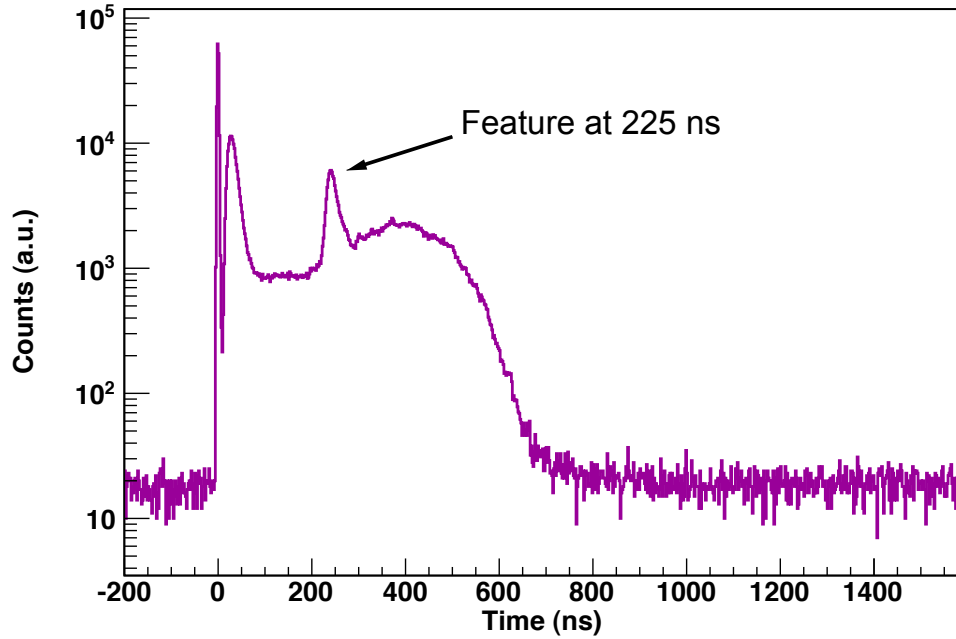
Figure 7.11: Combined spectrum of pulses arriving during 29,113 runs. The 139 micropulses captured during each 250 μs run have been overlaid to show the characteristic spectrum.

esis that it was caused by electronic noise and resulted directly from an echo of the high-energy neutron events visible near 15 ns, the time between each pulse and the next pulse was calculated.

Of the 709,693 pulses represented in Figure 7.11, in 38,839 cases, or 5.47% of the time, the next pulse arrived between 202 ns and 216 ns later. In comparison, 1,488 pulses, or 0.21% of the total, were followed by a pulse that arrived between 186 ns and 200 ns later. The effect was even more marked for higher-energy pulses. Of the 95,669 pulses in the run with heights greater than 100 (where the maximum height was 248), 37,546 pulses, or 39.2%, were followed by a pulse that arrived between 202 ns and 216 ns later. The effect of pulse height on the location of the next pulse is summarized by Figure 7.12. In general, as the energy of a pulse, as indicated by its height, increased, the likelihood of the next pulse falling between 202 ns and 216 ns later also grew. For pulses with heights greater than 240 on a scale of 248, over 94% of the next pulses fell within this range.

The echo pulses could be removed from spectra during analysis by identifying pulses that were preceded by another pulse within the time range of interest. The time-of-flight spectrum of these pulses, together with the time-of-flight spectrum of all pulses in the run, is shown in Figure 7.13. The original peak in the time-of-flight
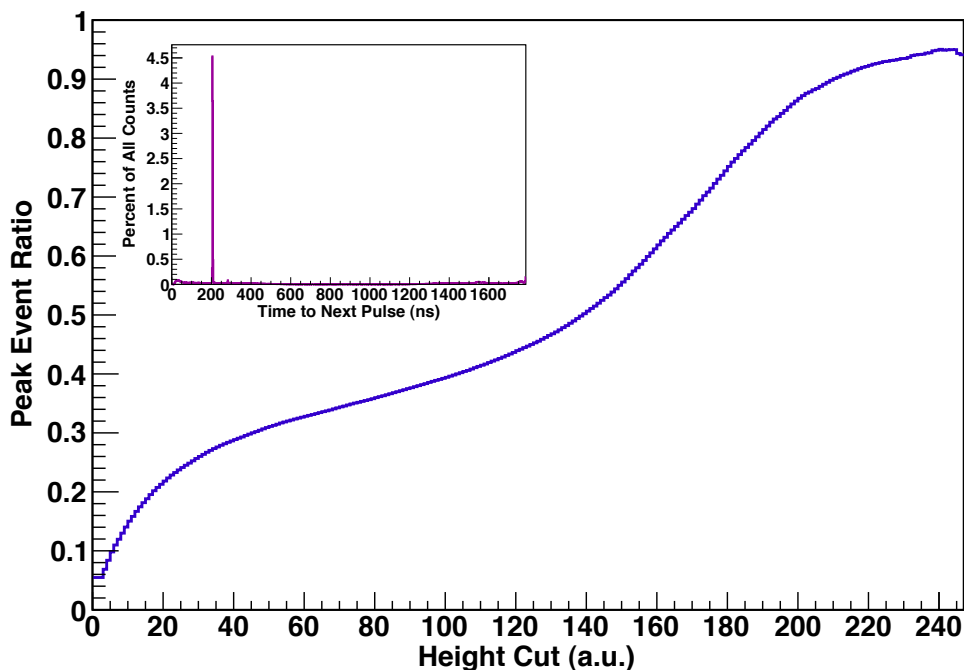
Figure 7.12: Fraction of pulses followed by a pulse that arrived between 202 ns and 216 ns later, as a function of pulse height. As the pulse height, which is an indicator of pulse energy, increases, the fraction of next pulses falling within the region of interest also increases, to as high as 94% for pulses with heights greater than 240 on a scale of 248. Inset: Time between neighboring pulses, showing disproportionate number of pulses arriving ∼202 ns after the previous pulse.

spectrum begins its rise at 10 ns, peaks at 26 ns, and declines gradually until becoming indistinguishable from the rest of the spectrum at 75 ns. Based on this location, and using the observation that echo events occur between 202 ns and 216 ns later, the echo pulse would be expected between 212 ns and 291 ns. Integrating the spectrum reveals that 90.9% of all echo pulses occur during this time period. The time-of-flight spectrum of echo pulses also reveals another peak, which overlaps with the 414 nm to 507 nm range that would be expected for a secondary echo. 5.1% of pulses occur during the secondary echo region, meaning that 96% of all echo pulses are attributable to primary or secondary echoes of the peak at 26 ns. Furthermore, 99.8% of echo pulses occur between 200 ns and 600 ns, possibly indicating the presence of additional high-energy events in the original peak after it merges with the rest of the spectrum near 75 ns. This supposition is consistent with the observed shape of the primary echo peak, which appears to continue its gradual fall-off well beyond the 291 ns cutoff applied based on the primary peak, to at least 350 ns.

By eliminating from the spectrum all pulses preceded by another pulse 202-216 ns earlier, 9.6% of all pulses were removed, including some that were random occurrences rather than true echoes. The fraction of pulses removed from the region between 220 ns and 290 ns, which is characterized by a large pulse echoing the early arrival of high-energy neutrons, was 54.6%. The modified spectrum is shown in Figure 7.14. The expected rate of randomly occurring coincident pulses between 202 ns and 216 ns after a preceding pulse may be calculated by applying Equation 6.2 and treating the 14 ns echo window as a resolving time. Figure 7.14 shows that the rate of background events is $(5 \pm 3) \times 10^{-6}$ counts/ns. The γ-flash region, between -10 ns and 10 ns, would be expected to have the highest number of random coincidences because of its high event rate, which peaks at $(1.5 \pm 0.2) \times 10^{-2}$ counts/ns. The expected coincidence rate is

$$
\begin{aligned}
r_{acc} = r_1 r_2 t_r &= [(5 \pm 3) \times 10^{-6} \text{ ns}^{-1}][(1.5 \pm 0.2) \times 10^{-2} \text{ ns}^{-1}](14 \text{ ns}) \quad (7.7) \\
&= (1.05 \pm 0.645) \times 10^{-6} \text{ coincidences/ns} \quad (7.8)
\end{aligned}
$$

Multiplying the coincidence rate by the neutron pulses represented in Figure 7.13, 4,041,564, results in a prediction of 4.24 ± 2.62 counts/ns in each bin displaying the peak γ-event rate. Examination of Figure 7.13 reveals that the two 2-ns bins in which the γ-flash peaks contain 12 and 13 events, indicating coincidence rates of 6.0 and 6.5 coincidences/s, respectively, within the expected range.

7.6 Calculation of Relative Light Yields and the ^{232}Th α-Particle Background

The combined time-of-flight spectra for all thorium-loaded and unloaded liquid scintillator runs can be seen in Figure 7.15. The unloaded scintillator spectrum has been scaled by 1.066 to compensate for the greater neutron flux observed for the thorium-loaded runs. The thorium-loaded detector displays a higher background count rate than the unloaded scintillator due to α-particles from the decay of ^{232}Th. The spectra shown in Figure 7.15 also suggest that the detectors have different light yields. The region between 400 ns and 700 ns has a smaller event rate in the thorium-loaded detector, indicating that the same number of neutrons produce fewer detectable events. The addition of material with lower or no light yield to liquid scintillator had previously been observed to result in reduced light yield, as seen with CeF_3 nanoparticles.
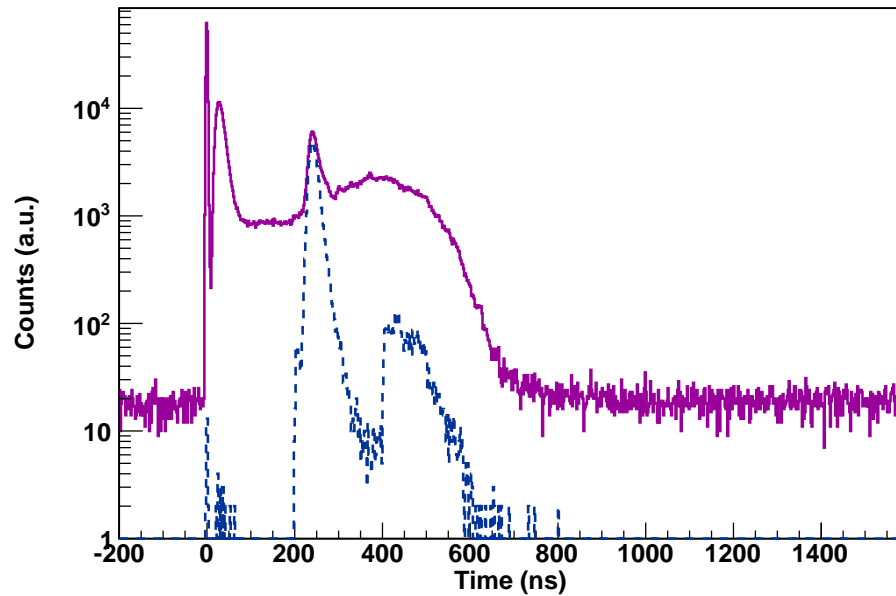
Figure 7.13: Time-of-flight spectrum of events recorded in one 250 μs run, as shown in Figure 7.11, overlaid with time-of-flight spectrum of events occurring 202-216 ns after the previous event. The echo pulses are most prominent around 225 ns, but a second peak in their spectrum is also observed around 430 nm.
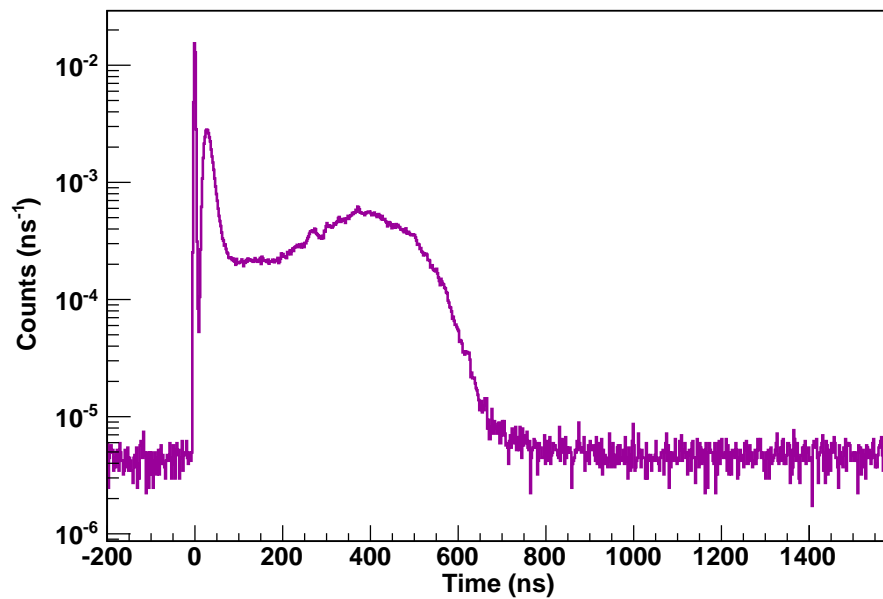
Figure 7.14: Combined spectrum of pulses arriving during one 250 μs run, as shown in Figure 7.11, following the elimination of pulses due to electronic echoes.
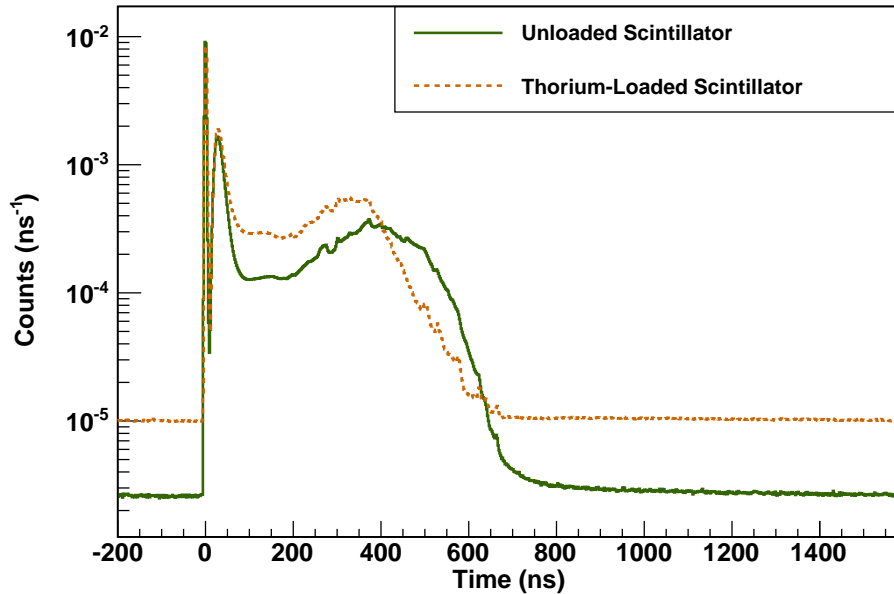
Figure 7.15: Combined time-of-flight spectra for all thorium-loaded and unloaded liquid scintillator runs. The liquid scintillator spectrum has been scaled by 1.066, to compensate for the greater neutron flux measured using the fission chamber during the thorium-loaded detector runs. α-decay events from ^{232}Th result in a higher background count rate in the thorium-loaded detector.

A difference in the areas of pulses produced by the two detectors was clearly seen between $t = -200$ ns and $t = -10$ ns, as shown in Figure 7.16. This region primarily contains background events, but also the beginning of the γ-flash. The hump visible at $Area = 381$ in the thorium-loaded scintillator and $Area$=832 in the unloaded scintillator results from γ-ray events. Based on the location of this peak, the light yield of the thorium-loaded scintillator was only 45.8% of the light yield of the unloaded liquid scintillator.

The area spectrum shown in Figure 7.16 can be adjusted to account for the lower light yield of the thorium-loaded scintillator by multiplying each bin of the thorium-loaded detector spectrum by 218%, the inverse of the reduction in light yield. As shown in Figure 7.17, this results in adjusted areas for events in the thorium-loaded detector that are identical to the areas obtained for events in the unloaded scintillator.

In order to compensate for the reduced light yield of the thorium-loaded scintillator, an adjustment must also be made to the peak-finding algorithm. To avoid misidentifying background fluctuations as scintillation pulses, any potential pulse must rise at least 3 steps (on an 8-bit, or 256-step scale) above the background level
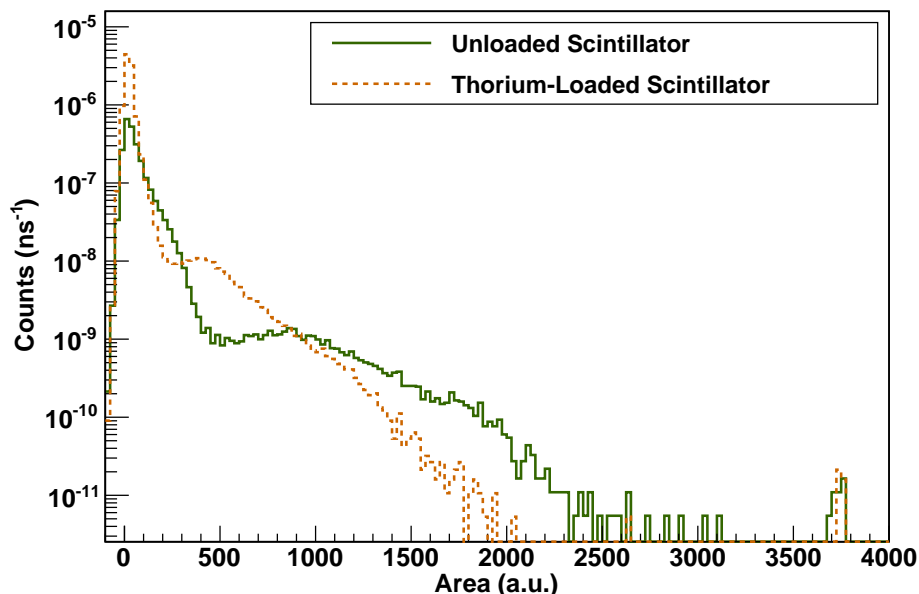
Figure 7.16: Area distribution of pulses arriving between $t = -200$ ns and $t = -10$ ns in the thorium-loaded and unloaded liquid scintillators. In addition to the α-particle events in the thorium-loaded detector and neutron scattering events in both detectors, events from the beginning of the γ-flash are visible in both scintillators. The γ-flash events are centered around $Area = 832$ in the liquid scintillator and $Area = 381$ in the thorium-loaded scintillator, indicative of a 54.2% decrease in light yield.

to be selected. Since the thorium-loaded scintillator emits only 45.8% as much light as the unloaded scintillator, a neutron that results in a pulse in the unloaded scintillator that is just above the cutoff is likely to produce a pulse in the thorium-loaded scintillator that is below the cutoff. Lower-energy pulses could not be added to the thorium-loaded scintillator data without also adding spurious pulses from background fluctuations, so the unloaded scintillator data was modified instead. In order to apply an equivalent pulse height cutoff to the unloaded scintillator, the original cutoff was multiplied by 218%, and all pulses with heights below this new cutoff of 6.54 steps were discarded. Applying this pulse height cut to the unloaded scintillator results in unloaded and thorium-loaded scintillator spectra with similar slopes, as shown in Figure 7.18. This indicates that adjustments in the pulse height cutoff can be used to ensure that observed differences between spectra from the two detectors result from particle interactions, not from differences in the light yield.

The α-background can be calculated by comparing the region immediately preceding the arrival of the γ-flash in the two detectors. In this region, shown between

Figure 7.17: Area distribution of pulses arriving between $t = -200$ ns and $t = -10$ ns in the thorium-loaded and unloaded liquid scintillators. Each bin of the thorium-loaded detector spectrum has been multiplied by 2.18 to compensate for its lower light yield. The features resulting from γ-ray events now fall at the same energy.

$t = -200$ ns and $t = -100$ ns in Figure 7.15, spallation γ-rays are absent and incident neutrons have energies between 232 keV and 262 keV, below the ^{232}Th fission threshold. Therefore, the difference in the event rates in the two detectors should result solely from α-decay in the thorium-loaded detector (other neutron interactions with thorium either result in negligible energy deposition or have very small cross-sections). Integrating the spectrum of the unloaded liquid scintillator from $t = -200$ ns through $t = -100$ ns produced a rate of $(1.53 \pm 0.08) \times 10^{-6}$ counts/ns. In comparison, the thorium-loaded scintillator produced a rate of $(1.004 \pm 0.026) \times 10^{-5}$ counts/ns, an increase of $(8.54 \pm 0.27) \times 10^{-6}$ counts/ns over the unloaded scintillator. The expected α-decay rate for the thorium-loaded scintillator was

$$\frac{dN_{Th}}{dt} = -\lambda_{Th} N_{Th} = \frac{(2 \pm 0.175 \text{ g})(6.022 \times 10^{23} \text{ atoms/mol})}{232.038 \text{ g/mol}} \times \frac{\ln 2}{4.420 \times 10^{17} \text{ s}} \quad (7.9)$$

$$= 8139.820 \text{ decays/s} = (8.140 \pm 0.712) \times 10^{-6} \text{ decays/ns}$$

where the error in the expected decay rate results from uncertainty in the amount of thorium added to the liquid scintillator. Thus, the increased event rate ob-
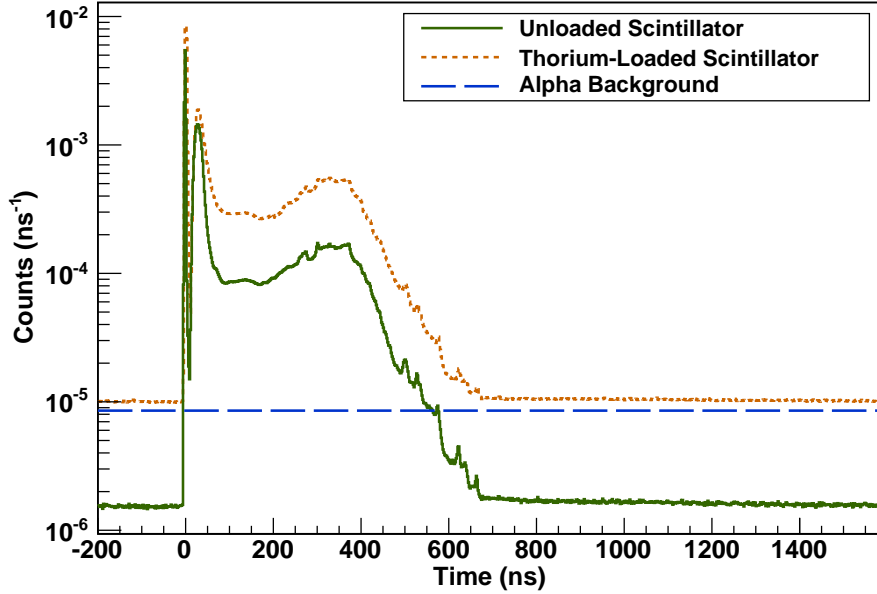
Figure 7.18: Time-of-flight spectra of thorium-loaded and unloaded scintillators, after removing from the unloaded scintillator data all pulses with heights below 6.54 steps. The original pulse height criterion of 3 steps was modified for the unloaded scintillator to compensate for reduced light yield in the thorium-loaded detector. The event rate due to the decay of α-particles, $(8.54 \pm 0.27) \times 10^{-6}$ counts/ns, is also shown.

served in the thorium-loaded detector is within the range expected due to α-decay events in thorium. The amount of thorium required to produce the event rate of $(8.54 \pm 0.27) \times 10^{-6}$ counts/ns shown in Figure 7.18 is (2.098 ± 0.066) g; this number will be used in calculations.

At the 2100 m elevation at which the experiment was performed, the μ^- flux is $\sim$40 m^{-2} s^{-1} sr^{-1} and the μ^+/μ^- ratio is $\sim$1.1, resulting in a predicted total muon flux of 84 m^{-2} s^{-1} sr^{-1}. [Boe00] [Cou00] Applying the liquid scintillator surface area of 20.27 cm^2 and assuming that the detector has a solid angle of 2π produces a flux of 1.070 10^{-9} ns^{-1}. Therefore, muons do not contribute significantly to the spectrum of either detector.

7.7 Analysis of Neutron Energy Spectra

The normalized neutron energy spectra for all runs from the unloaded and thorium-loaded scintillators are shown in Figure 7.19. The background, as measured in the region between $t = 800$ ns and $t = 900$ ns, has been subtracted from each spec-
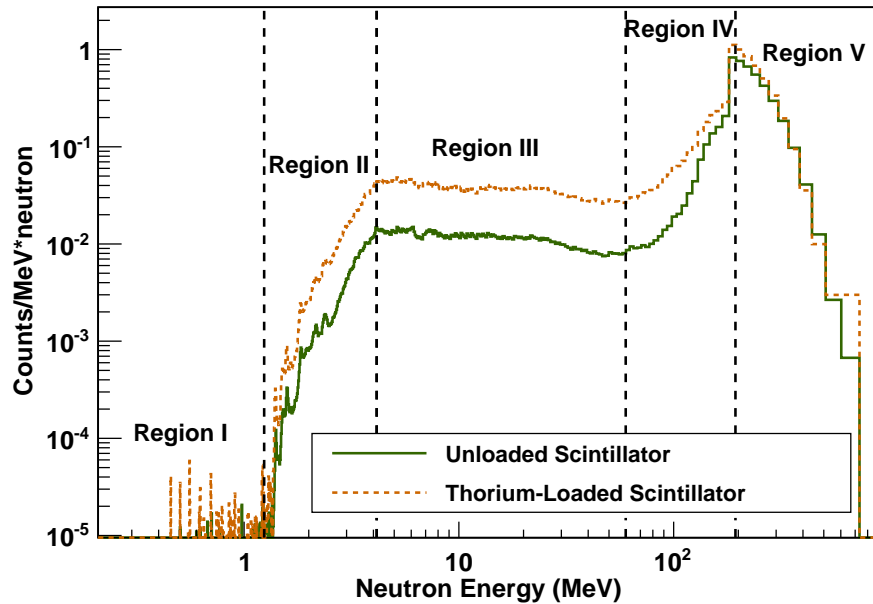
Figure 7.19: Neutron time-of-flight spectra for unloaded and thorium-loaded scintil-
lators. The spectra have been normalized by the energy bin width and
neutron flux profile and the background rate due to α-particles has been
subtracted from the spectrum of the thorium-loaded detector. Both
spectra contain five distinct regions.

trum. In addition, events below the adjusted pulse height cutoff of 6.54 steps have
been removed from the liquid scintillator spectrum. Although neutrons with energies
as high as 800 MeV can be measured at the flight path, the neutron flux spectrum
shown in Figure 7.10 only provides data up to ~194 MeV, because no cross-sections
are available to normalize the flux at higher energies. Therefore, the normalized neu-
tron time-of-flight spectrum is not accurate for neutrons with energies greater than
194 MeV, a region that is indicated as Region V in Figure 7.19. Region IV is also
challenging to analyze. Although the difference between the thorium-loaded and un-
loaded scintillator spectra in this region will be addressed, the shape of the unloaded
scintillator spectrum will not be discussed because most cross-sections have not been
measured for neutron energies higher than a few tens of MeV. Three other regions
may also be distinguished in Figure 7.19 and will be dealt with separately.

Region I features a very low count rate in both spectra, indicating that few neu-
trons in this energy range result in pulses above the cutoff. The energy corresponding
to the pulse height cutoff (3 steps in the thorium-loaded detector, 6.54 steps in the
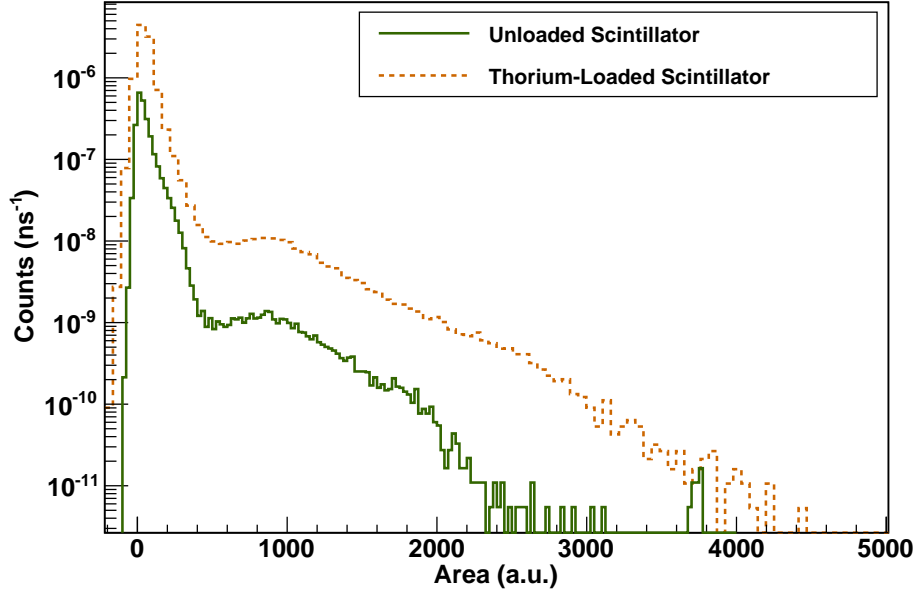liquid scintillator) can be roughly estimated by examining the α-particle energy spec-
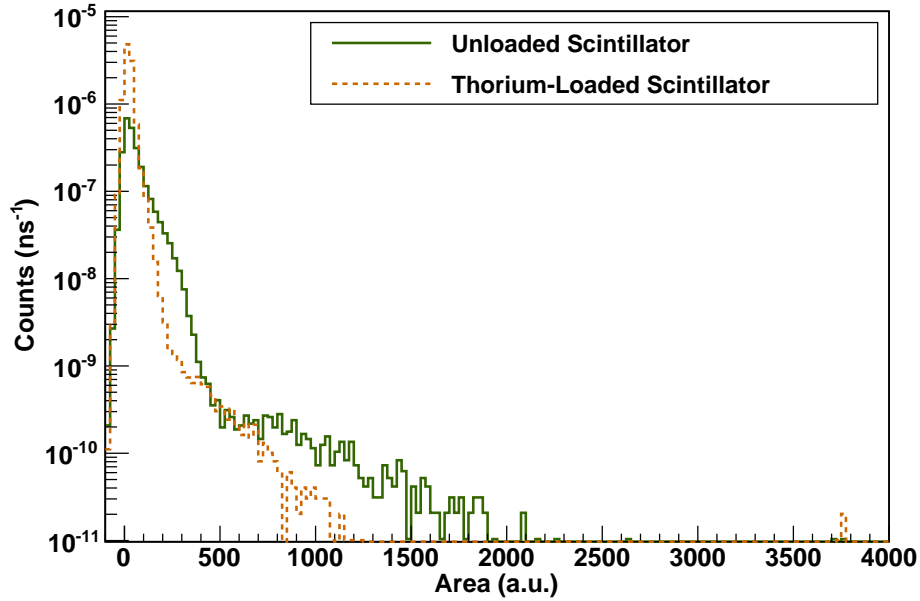
Figure 7.20: Area distribution of pulses arriving between $t = -200$ ns and $t = -100$ ns in the thorium-loaded and unloaded scintillators. Pulses in this region result from the elastic scatter of low-energy (232-262 keV) neutrons and cosmic ray interactions in both scintillators and α-decay events in the thorium-loaded scintillator.

trum. Figure 7.20 shows the area distribution of pulses arriving between $t = $ -200 ns and $t = $ -100 ns. In the thorium-loaded detector, this region is dominated by α-decay events, which result in an area distribution that peaks near $Area = 20$. The α-particles emitted by ^{232}Th have energies of 3.8 MeV (0.7%), 3.9 MeV (21.7%), and 4.0 MeV (78.2%) [1], so events with significantly lower energies must result in pulses with much smaller areas, which would not have been detected. Since a neutron cannot transfer more than its kinetic energy in an elastic scattering event, Region I (incident neutrons below $\sim$1.24 MeV) should have no elastic scattering events. Since the α-background has also been removed from the thorium-loaded scintillator, the few events seen in Region I must result from neutron capture. Region II shows a sharp rise in the count rates of both spectra, as the proportion of events resulting in pulses large enough to be detected increases. The count rate becomes relatively stable for neutrons with energies higher than $\sim$4.2 MeV.

In Regions II, III, and IV, the count rate in the thorium-loaded scintillator is greater than the count rate in the unloaded liquid scintillator. This higher rate of interactions in the thorium-loaded scintillator cannot be explained by an expected in-
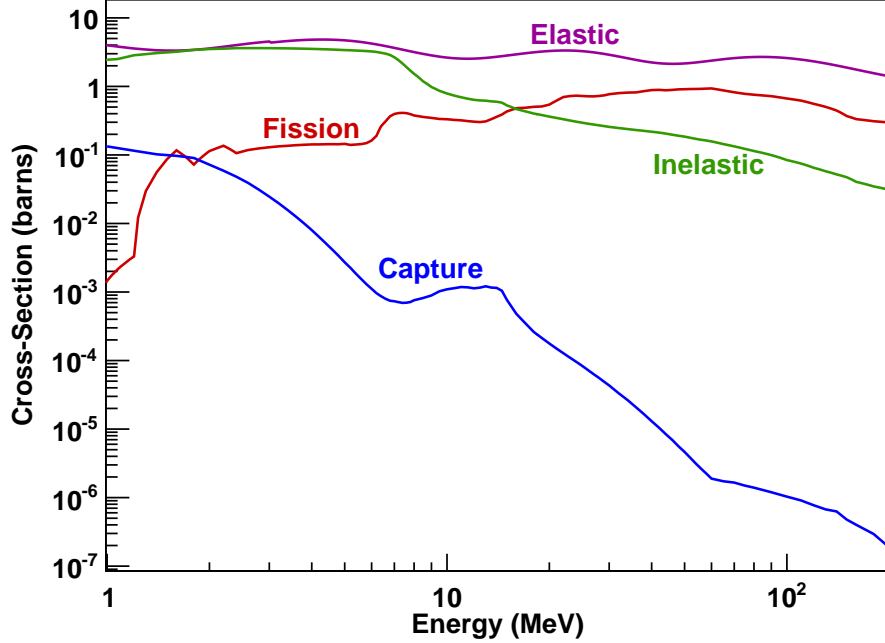
Figure 7.21: Cross-sections for elastic and inelastic scattering, radiative capture, and fission on ^{232}Th between 1 MeV and 200 MeV, or Regions II, III, and IV in Figure 7.19. Cross-sections are from from TENDL-2009. [Kon09]

crease in scattering or radiative capture. Elastic scattering of a neutron on a ^{232}Th nucleus can transfer at most 1.7% of the incident neutron energy. Figure 7.19 shows that an incident energy of greater than ∼1.2 MeV is required to produce a detectable pulse in the unloaded liquid scintillator. Assuming that the events detected at 1.2 MeV result from transfer of the full incident neutron energy to hydrogen nuclei through elastic scattering, we may assume that an identical energy is required to detect a ^{232}Th elastic scattering event, so no increase in detected elastic scattering is expected for neutrons below ∼71 MeV in the thorium-loaded detector. Neutron capture γ-rays from ^{232}Th are also not expected to result in a significant increase in counts. For incident neutrons above ∼1.8 MeV, the cross-section for fission is higher than that for radiative capture, and as shown in Figure 7.21, the radiative capture cross-section decreases substantially for higher-energy neutrons, dropping by more than five orders of magnitude between 4 MeV and 200 MeV. Therefore, the increased count rate in the thorium-loaded scintillator can be best explained by fission.

The difference between the thorium-loaded and unloaded scintillator count rates is shown in Figure 7.22. This difference is assumed to result primarily from the induced fission of ^{232}Th, with the exception of the additional events that cause the
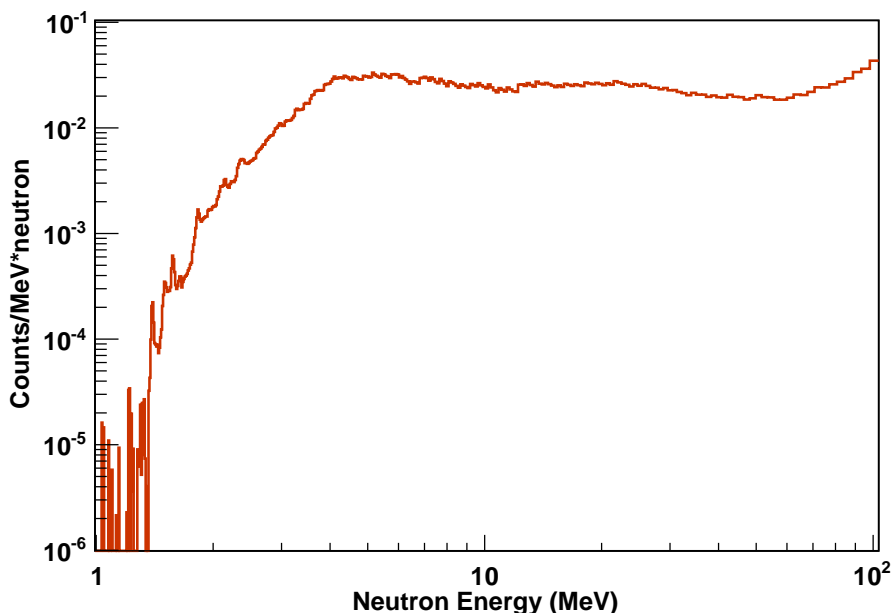
Figure 7.22: Difference in count rate between thorium-loaded and unloaded time-of-flight spectra. Over the energy range shown in Region III of Figure 7.19, from 4.2 MeV to 60 MeV, the fission cross-section, as shown in Figure 7.21, increases by about an order of magnitude, while the difference between the thorium-loaded and unloaded scintillators decreases by ∼40%. This inconsistency was hypothesized to result from increased ionization quenching of fission fragments.

difference to rise for incident neutrons with energies above ∼70 MeV. For incident neutrons with energies above this value, elastic scattering on a ^{232}Th nucleus may be accompanied by a detectable (>1.2 MeV) energy transfer. Setting aside both the region above 70 MeV and the cutoff region below 4.2 MeV, the remaining difference between spectra is roughly constant but decreases slightly, by about 40%, between 4.2 MeV and 70 MeV. However, Figure 7.21 shows that the fission cross-section for ^{232}Th increases by about one order of magnitude across this region, so the difference between spectra would have been expected to increase gradually with energy due to the larger number of fission events. One possible explanation for the failure of the probable fission event rate to increase with incident neutron energy was ionization quenching of fission fragments, which reduces the fraction of energy deposited. If, as the incident neutron energy increases, the rise in the fission cross-section is offset by an increase in the proportion of fission events that deposit too little energy to be detected, then the trend in the fission event rate would be inconsistent with the behavior of the fission cross-section.

7.8 Modeling of Energy Deposition in Unloaded and Thorium-Loaded Liquid Scintillators

To test the hypothesis that the roughly constant profile of probable fission events in the thorium-loaded detector resulted from ionization quenching in the scintillator, a simulation was developed using GEANT4 [Ago03] [All06] In the simulation, a point source shot neutrons towards a detector. The distance between source and detector was 11.5 m, the same as the distance between the spallation source and the detectors in the experiment. The simulation was run for two detectors, one containing a solution of toluene with 2.175 g of thorium in the form of $Th(NO_3)_4(TBP)_2$ and one containing a solution of toluene with the same amount of TBP ligand. The one billion neutrons simulated were randomly sampled from the beam profile shown in Figure 7.10. Multiplying the contents of each bin by the bin width, to compensate for the variable sizes of the energy bins, resulted in a true flux distribution that had less than one order of magnitude difference for the total number of neutrons expected at energies between 200 keV and 100 MeV, so random sampling of the spectrum was expected to produce good statistics across the entire energy range.

Deposited energy spectra for the unloaded and thorium-loaded models are shown in Figure 7.23. Significantly more events were observed in the thorium-loaded detector, 8.11×10^8 compared with 8.06×10^8 events in the unloaded scintillator. Most of the additional events, which resulted from fission, deposited between 70 MeV and 150 MeV. The spectra shown in Figure 7.23 represent the theoretical energy deposited in the detectors. However, the actual energy deposition is also affected by both ionization quenching and statistical broadening. ROOT was used to simulate these effects on the deposited energy.

Scintillation light yield is generally stated for energy deposited by electrons following γ-ray interactions. The scintillation response L of a material to electrons can be described as a function of its absolute scintillation efficiency S and the energy E deposited in the scintillator by an incident particle,

$$\frac{dL}{dx} = S\frac{dE}{dx} \tag{7.10}$$

over the range x of the particle in the scintillator. However, the luminescence of organic scintillators decreases markedly for heavier particles, since their higher dE/dx means that many surrounding particles have already been ionized or excited. [Bir64] To describe the effect of ionization quenching on the scintillation response, Equa-
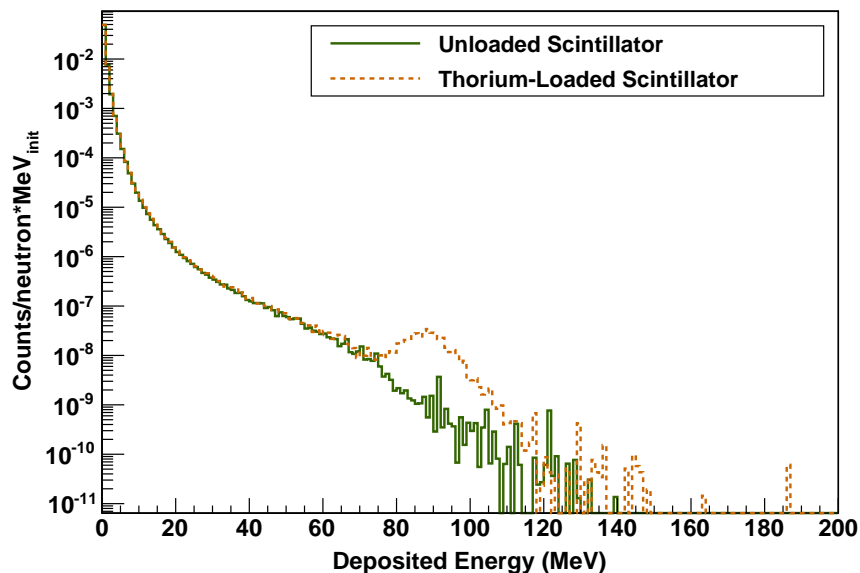
Figure 7.23: Energy deposited by one billion neutrons randomly sampled from the beam profile for 4FP90L. The unloaded and thorium-loaded scintillators were modeled using GEANT4. The thorium-loaded detector spectrum contained 0.66% more events, primarily due to fission, most of which deposited between 70 MeV and 150 MeV.

tion 7.10 can be modified by the addition of another efficiency factor,

$$\frac{dL}{dx} = \frac{1}{1 + kB(dE/dx)} \times S\frac{dE}{dx} \tag{7.11}$$

where k is a quenching parameter and BdE/dx is the specific density of excited and ionized molecules along the path of the incident particle. [Bir64] In order to simulate the effects of ionization quenching on the energy deposited by recoil protons and fission fragments in liquid scintillator, approximate values of kB for liquid scintillator (assumed to be identical to kB for toluene) and dE/dx for protons and fission fragments across the energy range of interest were determined using a combination of values found in the literature and calculations performed using the Stopping and Range of Ions in Matter (SRIM) software. [Zie85]

The dominant interaction of high-energy neutrons in liquid scintillator is elastic scattering. Verbinski et al. measured the light output of an NE-213 liquid scintillator in response to monoenergetic neutrons at 21 energies ranging from 202 keV to 21.81 MeV. [Ver68] The observed quenching was ∼53% for 21.81 MeV neutrons (47% of the expected luminescence was observed) and increased to ∼92% for 202 keV

neutrons. The reported quenching at five energies from across the measured range was compared with calculations of the efficiency factor in Equation 7.11, with kB approximated as a constant value of 0.019 cm/MeV^{-1} based on Peron and Cassette's measurements of a toluene/PPO solution [Per96] and the stopping power, dE/dx, calculated using the SRIM software [Zie85] for hydrogen ions in xylene, the principal component of NE-213. The calculated approximate quenching factor was found to be within 50% of the reported value for all energies. Since the quenching model was designed to provide a qualitative, not a quantitative, picture of the effect of ionization quenching on the unloaded and thorium-loaded scintillators, this accuracy was deemed sufficient.

The deposited energy spectra produced using GEANT4 were modified by multiplying the quenching efficiency, as shown in Equation 7.11, by the deposited energy for each event. The parameter kB was approximated as 0.019 cm/MeV^{-1}. SRIM was used to generate a table giving the energy deposition rate dE/dx for selected values between 100 keV and 200 MeV, and ROOT was used to generate splines allowing dE/dx to be interpolated for intermediate values. For the unloaded scintillator, all energy deposition events were assumed to result from elastic scattering of the incident neutron on a hydrogen nucleus. For the thorium-loaded scintillator, all events resulting in the deposition of less than 80 MeV were assumed to result from elastic scattering of the incident neutron on a hydrogen nucleus. Since ∼95% of events depositing 80 MeV or more in the thorium-loaded scintillator could be attributed to fission, for this approximation they were all treated as fission resulting in the production of Ag fission fragments. As shown in Figure 7.24, ionization quenching has a greater effect on fission fragments than on protons. Compared with the original deposited energy spectra shown in Figure 7.23, events in the unloaded scintillator deposit slightly less energy, but the shape of the distribution is unchanged. Events depositing 80 MeV or more in the thorium-loaded detector, however, which were treated as fission events, have been highly quenched. The energy deposited in the thorium-loaded scintillator remains higher, though. Assuming that only events depositing more than 4 MeV are detected, 3% more energy should be detected from the thorium-loaded detector.

The spectra shown in Figure 7.24 represent the actual energy deposited by neutrons in the detectors. For a given deposited energy, however, the detected energy undergoes statistical broadening due to the resolution of the scintillator and the quantum efficiency of the PMT. To reproduce this effect, the counts for each energy in Figure 7.24 were redistributed as a Gaussian. Assuming that the response of the detector is linear, its standard deviation is a function of the centroid and the number
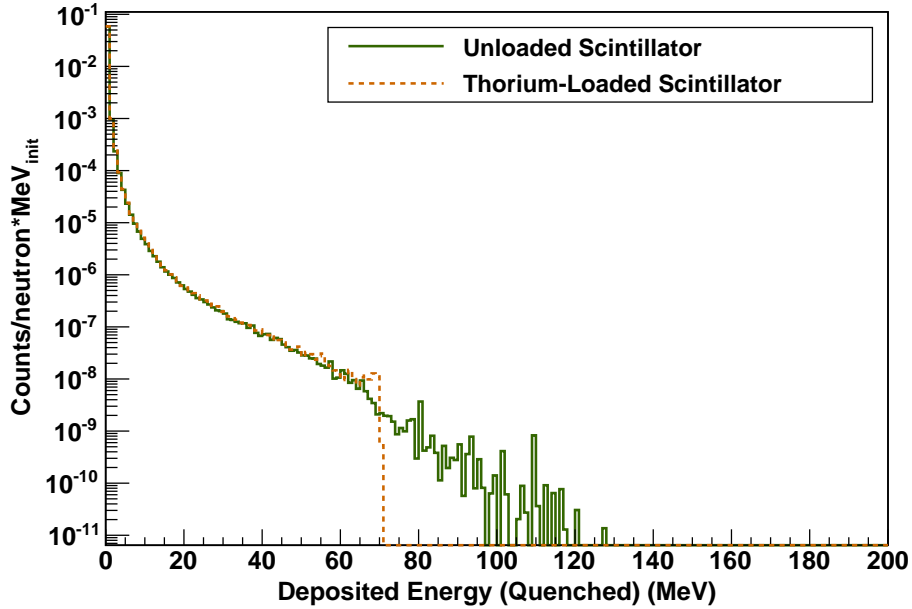
Figure 7.24: Modeled effect of ionization quenching on energy deposition in unloaded and thorium-loaded liquid scintillators. The energy deposited in the unloaded scintillator has decreased, but the effect on thorium-loaded scintillator is even more pronounced. Events depositing more than 80 MeV were assumed to be induced fission of ^{232}Th resulting in Ag fission fragments. The energy deposited by these fragments has been heavily quenched, removing all events depositing more than 72 MeV from the spectrum.

of photons produced for a given deposited energy. The number of photons produced may be calculated relative to a known standard.

$$
\begin{aligned}
\sigma &= \frac{x_0}{\sqrt{N}} \\
&= \frac{x_0}{\sqrt{N_{Cs} x_0 / E_{Cs}}} \\
&= \frac{R_{Cs}}{2.35} \sqrt{\frac{x_0}{E_{Cs}}}
\end{aligned}
\tag{7.12}
$$

Since the model was meant to approximate the behavior of the scintillators, not reproduce it exactly, numerical values were selected from similar experiments. The resolution of both the thorium-loaded and liquid scintillator solutions was assumed to be 22.08%, as measured for the 661.7 keV ^{137}Cs photopeak in the spectrum of a liquid scintillator loaded with 20% CeF_3 nanoparticles. This measurement is described in Chapter V. Smearing the spectra shown in Figure 7.24 with Equation 7.12
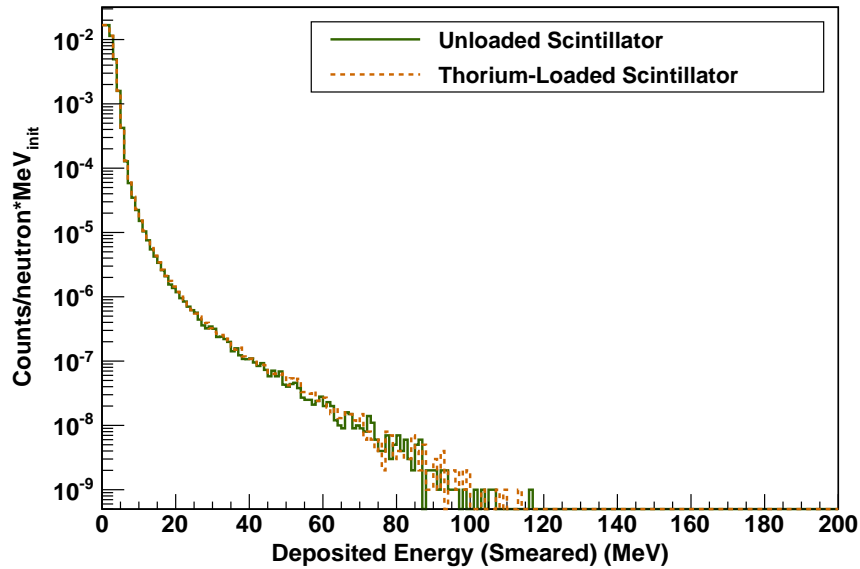
Figure 7.25: Quenched energy deposited in unloaded and thorium-loaded scintillators by one billion neutrons, as shown in Figure 7.24, broadened to simulate the effect of an energy resolution of 22.08% at 661.7 keV.

produces the spectra shown in Figure 7.25. The change in slope seen in the quenched spectrum for the unloaded scintillator has become a more gradual decline in counts with increasing energy. Statistical broadening has also eliminated the sharp edge seen in the quenched spectrum for the thorium-loaded detector, resulting in identical shapes for the two deposited energy spectra. The identical shapes are consistent with the similarities seen between the two area distributions in Figure 7.26, but the lack of an increased count rate in the thorium-loaded detector is in disagreement with the data.

To obtain a neutron energy plot corresponding to those calculated from the neutron time-of-flight, the neutron initial energy was plotted for events resulting in more than 4.0 MeV of quenched deposited energy. The spectra, shown in Figure 7.27, feature no significant difference in shape. The spectrum for the thorium-loaded detector contains 3.7% more counts than the spectrum for the unloaded scintillator, but less than than the 0.5 order-of-magnitude difference observed experimentally. It was concluded that the additional counts seen experimentally in the thorium-loaded detector resulted from interactions that were not modeled by GEANT4, namely the radioactive decay of fission products. The delayed nature of this process would also explain the smearing observed for fission events in the time-of-flight spectrum.
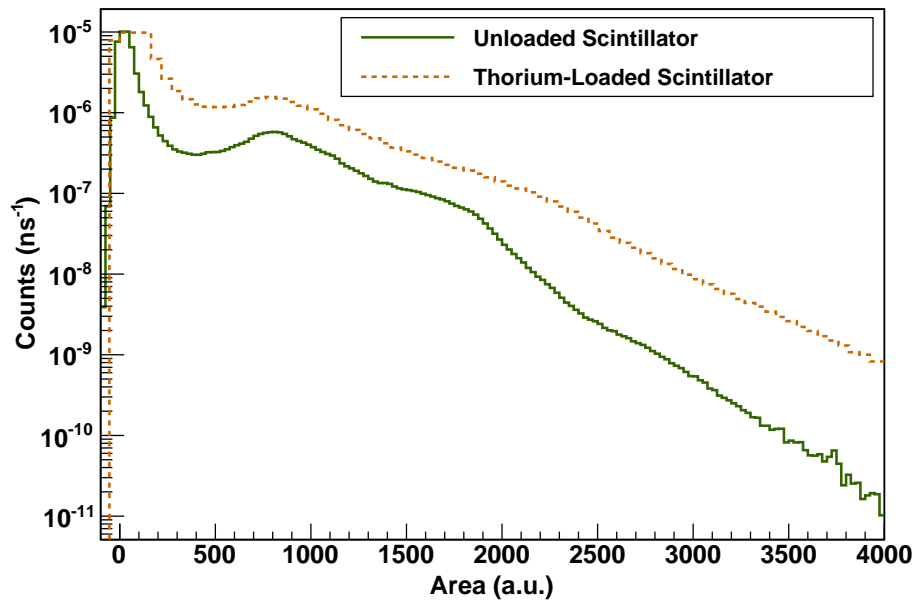
Figure 7.26: Area distributions of all events, excluding the γ-flash, observed experimentally in the unloaded and thorium-loaded scintillators. Each bin in the distribution for the thorium-loaded detector has been multiplied by 2.18 to compensate for the detector's lower light yield. The shapes of the two distributions are similar, with more events observed in the thorium-loaded detector.
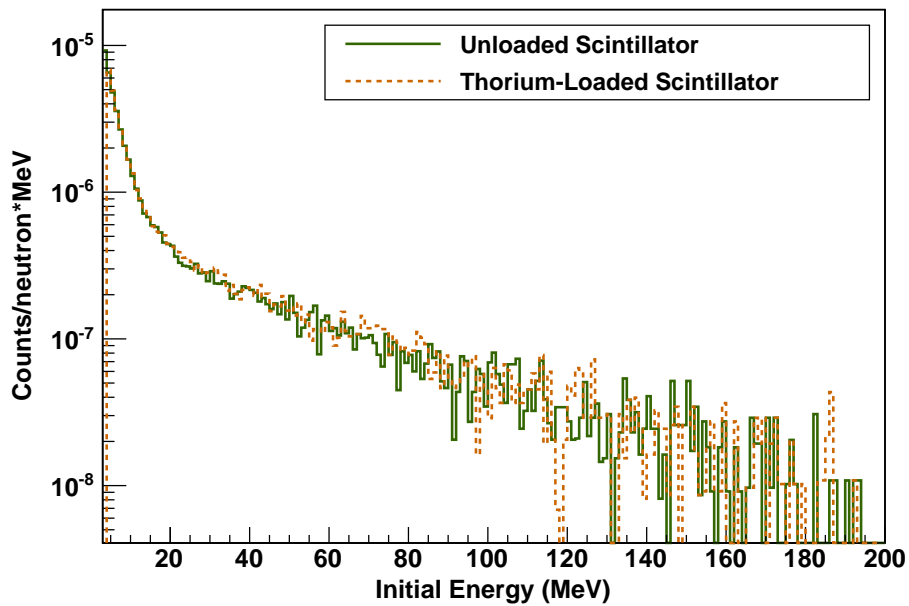
Figure 7.27: Distribution of initial neutron energies for events resulting in the deposition of more than 4.0 MeV following ionization quenching. The spectrum for the thorium-loaded detector contains 3.7% more counts than that for the unloaded scintillator, but this increase is much lower than the experimentally observed difference.

CHAPTER VIII

Conclusions and Future Work

8.1 Summary of CeF$_3$ Experiments

Detectors incorporating CeF$_3$ nanoparticles were developed as a potential substitute for BaF$_2$ single crystals in neutron capture experiments. CeF$_3$ nanoparticles were successfully fabricated using a precipitation technique. A liquid scintillator using toluene and two wavelength-shifting dyes, PPO and POPOP was developed for use as a suspension matrix for nanoparticles and its light output was optimized. TEM, XRD, and Rayleigh scattering fits to UV/Vis data were employed to measure the sizes of CeF$_3$ nanoparticles dispersed in the liquid scintillator. These structural characterization techniques agreed that particles were generally less than 20 nm in diameter. Optical characterization using PL and RL indicated that the luminescence of CeF$_3$ nanoparticles dispersed in liquid scintillator was dominated by the luminescence of the liquid scintillator. Luminescence was observed at 415 nm and 435 nm, rather than the 286 nm, 305 nm, and 340 nm characteristic wavelengths of CeF$_3$, indicating that light emitted by nanoparticles may have been absorbed and re-emitted by the liquid scintillator. RL of CeF$_3$ suspended in liquid scintillator showed a 200% increase in intensity over all wavelengths compared with liquid scintillator alone, due to some combination of CeF$_3$ emission and the increased photoelectric cross-section due to the presence of high-Z material.

Characterization of dispersions using different mass loadings of CeF$_3$ indicated that the light yield decreased as the nanoparticle concentration increased. Experiments involving the dropwise addition of oleic acid, the capping ligand used in the fabrication of CeF$_3$ nanoparticles, to toluene and liquid scintillator revealed that oleic acid quenches the toluene luminescence. While this result was produced too late to be of use in the production of the CeF$_3$ nanoparticles whose characterization is described in this work, oleic acid is a commonly used ligand in nanoparticle production,

150

and knowledge of its deleterious effects on liquid scintillators has already informed our work on the production of other nanoparticles for scintillator use.

Experiments were conducted at flight path 1FP5 at LANSCE on two detector modules containing 20% CeF_3 dispersed in 60 mL liquid scintillator. The detectors were positioned to detect capture γ-rays produced by beam neutron capture on tantalum, cobalt, and gold targets. A BaF_2 detector used for comparison was unable to detect capture γ-rays from neutrons with energies greater than 40 eV due to the time it required to recover from the arrival of the γ-flash. The CeF_3 nanocomposite detector, with its faster decay time and correspondingly short recovery time, was able to detect capture γ-rays with energies more than an order of magnitude higher.

It was demonstrated that an organic scintillating matrix loaded with nanoparticles is capable, due to its faster response time, of detecting neutron capture γ-rays that cannot be detected using conventional BaF_2 scintillators. While poor energy resolution was observed due to the reduced light yield produced by oleic acid quenching, this could be corrected by employing a different capping ligand in the synthesis process. By employing a version of the CeF_3 nanocomposite detector with the same fast time response and improved light yield, and using pulse shape discrimination to remove neutron scattering events, neutron capture cross-sections could be measured for quickly-decaying targets. These measurements could provide useful and currently unavailable information. In addition, the success of the CeF_3 nanocomposite detector suggests that nanocomposite detectors could also be used for other applications that require both a high photoelectric cross-section and a fast time response.

8.2   Summary of Fissionable Scintillator Experiments

Scintillators loaded with fissionable nanoparticles were conceived as neutron flux monitors for nuclear physics experiments. As a proof-of-principle, solutions were prepared of fissionable molecular complexes in the liquid scintillator designed for the CeF_3 work. The first complex chosen for incorporation in the fissionable scintillator was $UO_2(NO_3)_2(TBP)_2$ utilizing ^{238}U. However, the transmission of the liquid scintillator emission through solutions incorporating this complex was hampered by both the yellow coloration characteristic of U^{6+} and excitation and re-emission by uranyl nitrate. The fissionable complex that ultimately was successfully characterized and used for beamline testing was $Th(NO_3)_4(TBP)_2$ utilizing ^{232}Th. Solutions incorporating this complex were found to emit light at the same wavelengths as the liquid scintillator alone and to have a 10% higher response to x-rays due to the presence of

high-Z material. Characterization of their response to γ-rays, however, was difficult due to the large amount of light produced in response to the α-decay of ^{232}Th.

A module containing 2.098 g ^{232}Th in the form of Th(NO$_3$)$_4$(TBP)$_2$ in solution with 150 mL liquid scintillator was tested against a liquid scintillator module and a fission chamber at flight path 4FP90L at LANSCE. Comparing time-of-flight spectra for the thorium-loaded and unloaded scintillators showed a clear additional background of 8,140 decays/s attributable to α-decay events in the thorium-loaded detector. Examination of the area distributions of pulses detected in the scintillators indicated that the thorium-loaded detector emitted only 45.8% as much light as the unloaded liquid scintillator, likely due to energy deposition in the large and non-scintillating thorium complex. After removing α-particle events from the time-of-flight spectra, correcting for the difference in light yield between the two detectors, and converting the spectrum to energy, the detected count rate in the thorium-loaded detector remained ~400% higher. The increased count rate could only be attributed to fission, but its trend with neutron energy did not agree with the cross-section for fission on ^{232}Th. A model was used to simulate the deposition, quenching, and statistical broadening of energy from neutron interactions in unloaded and thorium-loaded scintillators. The model predicted only a 3.7% increase in the count rate observed in the thorium-loaded time-of-flight spectrum due to the energy deposited by fission fragments, suggesting that the higher observed increase resulted from interactions not simulated by the model, namely, the radioactive decay of fission fragments.

Although it was not possible to employ pulse shape discrimination using the existing experimental setup to distinguish between fission and other events, the 400% increase in the thorium-loaded detector event rate indicated the presence of a significant fission rate. This increase proves that a detector loaded with fissionable material could be used to detect neutrons, and it should be possible to develop a pulse shape discrimination technique allowing fission events to be identified. Such a detector would be of interest for nuclear physics experiments requiring measurements of very high or very low neutron flux, for which conventional fission chambers are poorly suited. Being less fragile than a fission chamber, a fissionable scintillator could also be used to detect neutrons in the field. In particular, scintillators incorporating isotopes such as ^{232}Th and ^{238}U, which do not fission in response to thermal neutrons, would be ideal for detection of fast neutrons.

8.3 Directions for Future Work

This work established that CeF_3 nanoparticles can be fabricated and loaded into liquid matrices. However, more work is necessary to understand how the luminescence of a nanocrystal may differ from that of a single crystal and how additional energy transfer mechanisms introduced by the presence of a matrix material may affect the light yield of the composite. The beamline experiments performed on CeF_3 detectors suggested that the presence of high-Z nanoparticles in a liquid scintillator improve its ability to detect γ-rays, irrespective of the nanoparticle luminescence, while retaining the fast response of the liquid scintillator. This suggests that one interesting potential avenue of research would be the effect of non-scintillating, high-Z nanoparticles on the efficiency of organic scintillators.

Non-scintillating nanoparticles were a part of the concept of the fissionable detector, with the goal of benefiting not from an increased photoelectric cross-section, but from introducing a new cross-section, for fission, to an organic scintillator system. The successful detection of induced fission in a liquid scintillator loaded with a fissionable molecular complex indicated the feasibility of this idea, so the development of a synthesis technique for fissionable nanoparticles should be a major part of future work in this area. The 54.2% drop in light yield observed for the thorium-loaded scintillator, compared with the unloaded scintillator, suggests that work also remains to optimize the mass loading of the fissionable component. Finally, the difficulties encountered in identifying fission events among the pulses recorded in beam line experiments show that the data acquisition system must be modified to improve its range and pulse shape discrimination capabilities.

APPENDICES

APPENDIX A

Supplemental Figures for Oleic Acid Quenching
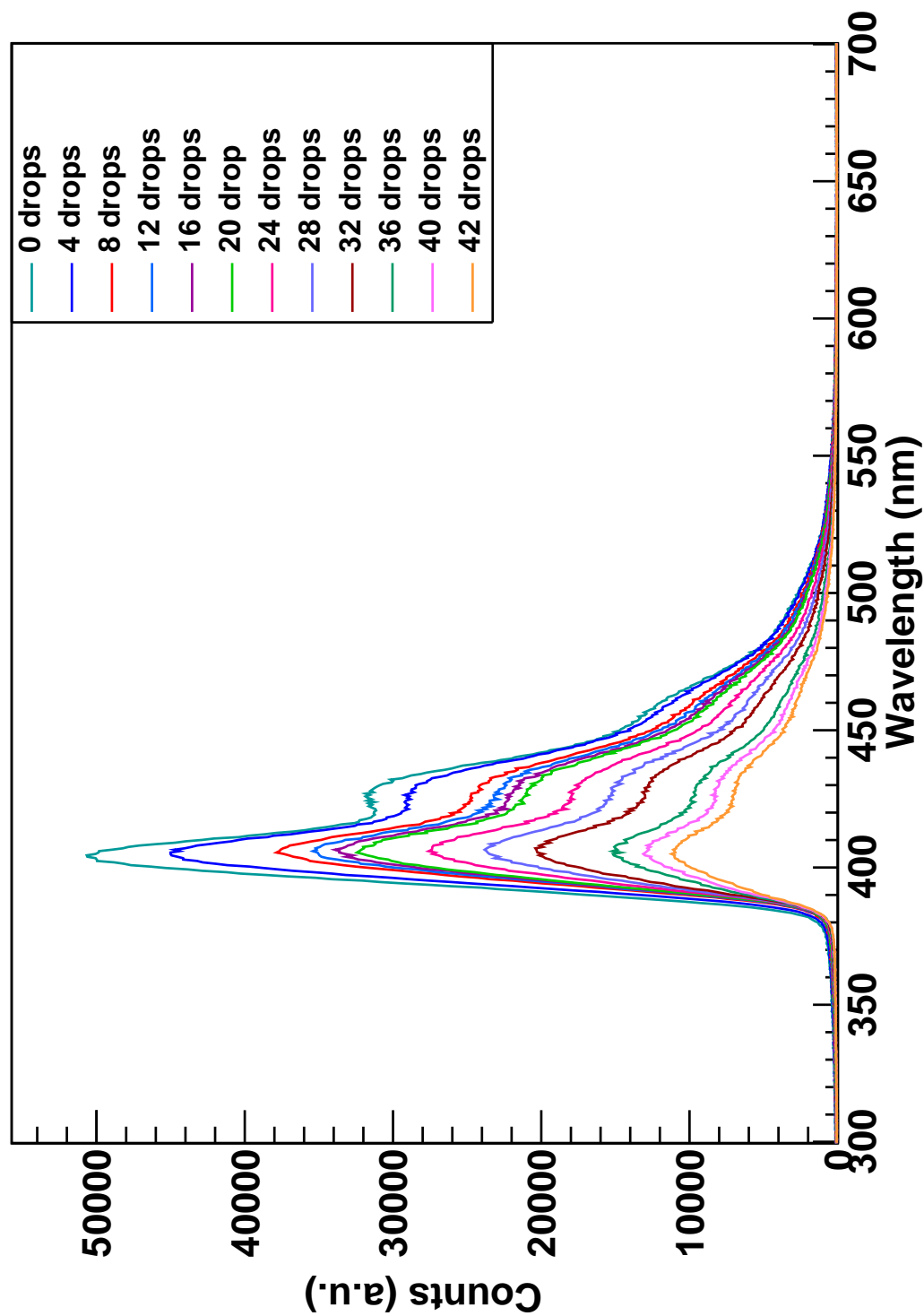
Figure A.1: Quenching of liquid scintillator by 99%-pure oleic acid, added dropwise. An abbreviated version of this figure is shown as Figure 3.19.

APPENDIX B

Photomultiplier Tube Specifications
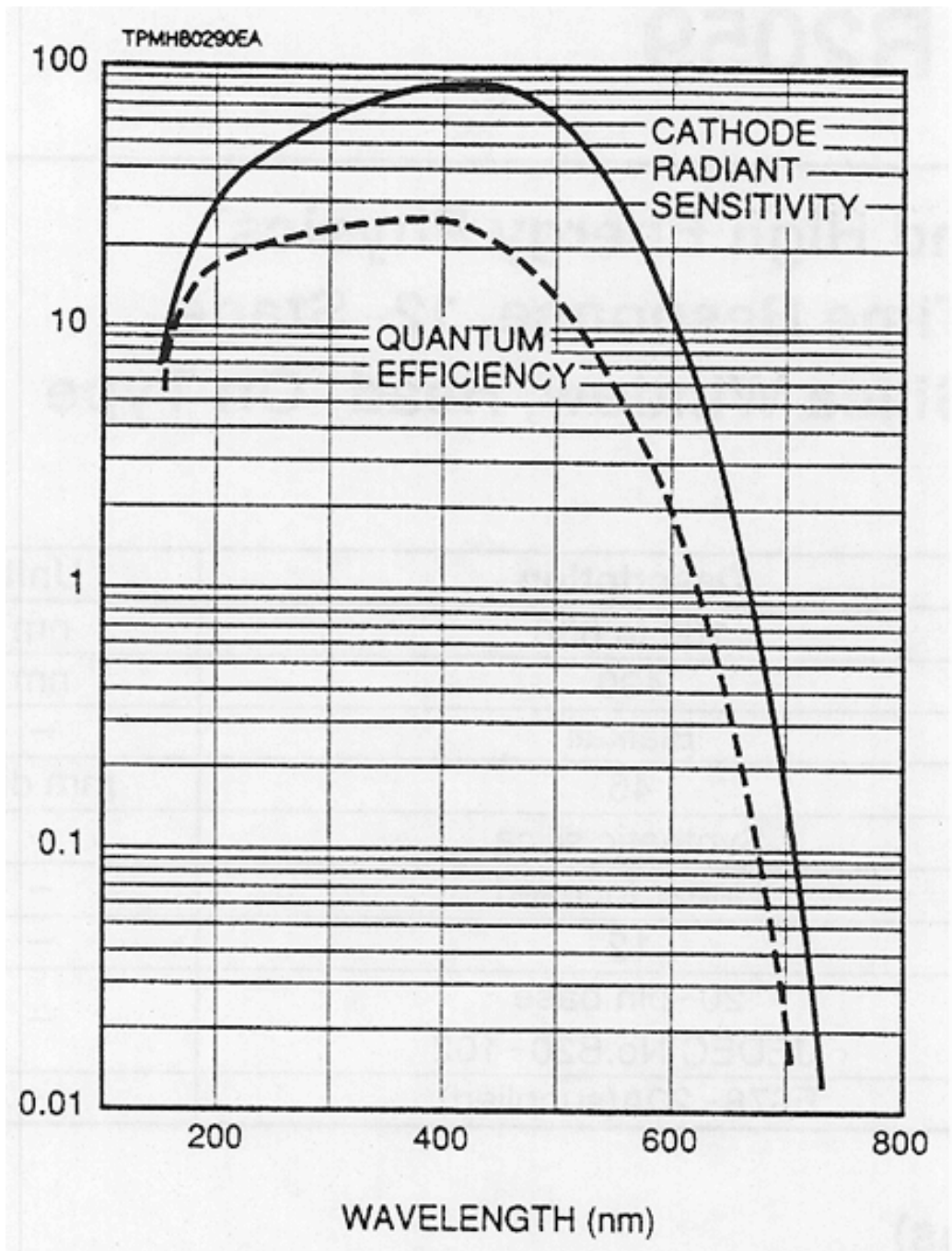
Figure B.1: Cathode radiant sensitivity and quantum efficiency of Hamamatsu R2059 PMT, showing peak sensitivity at 420 nm.

Type	Head on
Size	51 mm
Active Diameter	46 mm
Minimum λ	160 nm
Maximum λ	650 nm
Cathode Radiant Sensitivity	85 mA/W
Window Material	Quartz
Cathode Type	Bialkali
Cathode Luminous Sensitivity	90 mA/lm
Cathode Blue Sensitivity Index	10.5
Anode Luminous Sensitivity	1800 A/lm
Gain	2.0E+7
Dark Current after 30 minutes	50 nA
Rise Time	1.3 ns
Transit Time	28 ns
Transit Time Spread	0.55 ns
Number of Dynodes	12

Table B.1: Characteristics of Hamamatsu R2059 PMT

PMT Type	51 mm head on
Ground Electrode	Anode
Supply Voltage Polarity	Negative
Maximum Insulation Voltage Rating	3000 V
Maximum Supply Voltage	3000 V
Maximum Voltage Divider Current	0.7 mA at 3000 V
Leakage Current in Signal	1.0E-10 A at 1000 V
Total Voltage Divider Resistance	4.31 MΩ
Maximum Linear Output in DC Mode	34 μA at 3000 V
Signal Output	DC/Pulse

Table B.2: Characteristics of Hamamatsu E2979-500 socket

APPENDIX C

Electronics Specifications

Power Supplies and Boards

The power supply used for most characterization measurements and all beamline experiments was a LeCroy 1454 High Voltage Mainframe with two LeCroy 1461 12-Channel High Voltage Boards, one of them a 1461N (factory set to negative polarity) and one of them a 1461P (factory set to positive polarity). A handful of characterization measurements utilized a Caen SY1527 LC Universal Multichannel Power Supply System with a negative Caen A1733 12-channel High Voltage Board. Specifications for these instruments are given in Tables C.1, C.2, C.3, and C.4.

Data Acquisition Electronics for Characterization Measurements

Characterization measurements for CeF_3 and liquid scintillator samples utilized the Caen V812 16-Channel Constant Fraction Discriminator, the Caen V925 Quad Linear Fan In Fan Out Board, and the Caen V965 16-Channel Dual Range Multievent QDC. Specifications for these electronics are given in Tables C.5, C.6, C.7, and C.8.

Capacity	4 HV card slots
Output Power	360 W (15 A at 24 V)
Power	90 V to 260 V AC, 50 to 60 Hz, power factor corrected

Table C.1: Characteristics of LeCroy 1454 High Voltage Mainframe

Output Voltage	0-3 kV
Maximum Current	> 2.5 mA for 2.8-3 kV, > 1.0 mA for 0-1 kV
	linear from 1 to 2.8 kV
Voltage Ripple	< 100 mV pp (< 50 mV pp for < 1 mA)
Voltage Set Resolution	< 1 V (750 mV nominal)
Voltage Output Accuracy	± 0.1% of setting + 1.5 V
	from 5%-100% of full scale at 25° C
Current Measurement Resolution	< 1 μA
Current Measurement Accuracy	± 2% of reading + 12 μA

Table C.2: Characteristics of LeCroy 1461 12-Channel High Voltage Board

Power Requirements	100 V to 230 V AC, 50 to 60 Hz, 3400 W
Capacity	16 boards (3 power supply units)
Output Power	2250 W

Table C.3: Characteristics of Caen SY1527 LC Universal Multichannel Power Supply System

Output Voltage	dual range 0-3 kV / 0-4 kV
Maximum Current	dual range 3 mA / 2 mA
Voltage Ripple	< 30 mV pp
Voltage Set vs. Voltage Monitor Accuracy	± 0.3% ± 0.25 V
Voltage Monitor Accuracy vs. Output Voltage	± 0.3% ± 0.25 V
Current Set vs. Current Monitor Accuracy	± 2% ± 0.2 μA
Current Monitor Accuracy vs. Output Current	± 2% ± 1 μA

Table C.4: Characteristics of Caen A1733 12-channel High Voltage Board

Input Impedance	50 Ω
Gate Width	Programmable from 100 ns to 10 s

Table C.5: Characteristics of Caen V462 Dual Gate Generator

Maximum Input Voltage	-5 V
Minimum Detectable Signal	-5 mV
Threshold Range	-1 mV to -255 mV (1 mV step)
Constant Fraction	20%
Input / Output Delay	Set delay + 4.5 ns
Output Width	Programmable from 15 ns to 250 ns
Dead Time	Programmable from 150 ns to 2.2 μs (± 10%)

Table C.6: Characteristics of Caen V812 16-Channel Constant Fraction Discriminator

Input Impedance	50 Ω
Input Coupling	DC
Reflection	Less than 4% for 2 ns risetime
Zero Adjustment	± 100 mV
Maximum Output Amplitude	± 1.6 V
Input/Output Delay	4 ± 1 ns
Noise	< 300 μV RMS

Table C.7: Characteristics of Caen V925 Quad Linear Fan In Fan Out Board

Input Range	Dual Range 0-900 pC / 0-100 pC
Input Impedance	50 Ω
Input Polarity	Negative
Input Coupling	DC
Gain	High Range 200 fC/count / Low Range 25 fC/Count
Reflections	< 5%
Input Offset	± 2 mV
RMS Noise	0.5 counts typical

Table C.8: Characteristics of Caen V965 16-Channel Dual Range Multievent QDC

Data Acquisition Electronics for Beamline Experiments

Signals from the PMT and the fission chamber were acquired using an Acqiris DC265 board in an Acqiris CC105 crate. Specifications for these electronics are given in Tables C.9.

Input Voltage	100 - 120 V
Maximum Input Power	600 W
Maximum Usable Power	400 W
Output Voltage	+5.1 ± 0.1 V
Maximum Output Current	35 A
RMS Ripple	greater of 0.1% or 10 mV
Peak to Peak Noise	greater of 1% or 50 mV
Dynamic Response	<2% or 100 mV at 25% load step
Recovery Time	To within 1% in <0.3 ms
Slots	5 (1 system, 4 peripheral)

Table C.9: Characteristics of Acqiris 5-slot CC105 cPC1 Crate

Supplemental X-Ray Diffraction Data

Table D.1: Expected peak locations, intensities relative to strongest peak, and Miller-Bravais indices for CeF_3. All values obtained from International Centre for Diffraction Data Joint Committee on Powder Diffraction Standards, except for i, which was calculated using $i = -h-k$.

2θ	Intensity	h	k	i	l
14.365	1	1	0	-1	0
18.862	1	1	0	-1	1
24.459	34	0	0	0	2
25.014	30	1	1	-2	0
27.899	100	1	1	-2	1
28.479	1	1	0	-1	2
28.962	1	2	0	-2	0
31.515	1	2	0	-2	1
35.267	18	1	1	-2	2
38.261	1	2	0	-2	2
38.635	1	2	1	-3	0
39.931	1	1	0	-1	3
40.649	1	2	1	-3	1
44.060	41	3	0	-3	0
45.228	48	1	1	-2	3
46.259	1	2	1	-3	2

Table D.1: *continued*

2θ	Intensity	h	k	i	l
47.699	1	2	0	-2	3
50.130	3	0	0	0	4
51.033	23	3	0	-3	2
51.331	4	2	2	-4	0
52.426	1	1	0	-1	4
52.959	15	2	2	-4	1
53.590	1	3	1	-4	0
54.604	1	2	1	-3	3
55.172	1	3	1	-4	1
56.822	3	1	1	-2	4
57.651	4	2	2	-4	2
58.937	1	3	0	-3	3
–	0	2	0	-2	4
59.747	1	3	1	-4	2
60.016	1	4	0	-4	0
61.489	1	4	0	-4	1
64.982	11	2	2	-4	3
–	11	2	1	-3	4
65.929	1	1	0	-1	5
66.048	1	3	2	-5	0
66.943	1	3	1	-4	3
67.448	1	3	2	-5	1
68.921	7	3	0	-3	4
69.798	6	1	1	-2	5
69.914	4	4	1	-5	0
71.277	10	4	1	-5	1
72.672	1	4	0	-4	3
74.582	1	2	2	-4	4
75.304	3	4	1	-5	2
76.432	1	3	1	-4	4
77.275	1	2	1	-3	5
77.387	1	5	0	-5	0
78.226	1	3	2	-5	3

Table D.1: *continued*

2θ	Intensity	h	k	i	l
78.910	1	0	0	0	6
81.034	3	3	3	-6	0
81.865	9	4	1	-5	3
–	9	4	0	-4	4
82.609	1	5	0	-5	2
82.844	1	4	2	-6	0
84.344	2	1	1	-2	6
86.210	4	2	0	-2	6
–	4	3	3	-6	2
86.334	3	2	2	-4	5
87.306	1	3	2	-5	4
88.004	1	4	2	-6	2
88.127	1	3	1	-4	5
88.236	1	5	1	-6	0
89.057	1	5	0	-5	3
89.522	1	5	1	-6	1

BIBLIOGRAPHY

BIBLIOGRAPHY

[Aar93] Pertti A. Aarnio and Mika Huhtinen. Hadron fluxes in inner parts of LHC detectors. *Nucl. Instrum. Meth. Phys. Res. A*, **336**:98–105, 1993.

[Abb02] U. Abbondanno et al. CERN n_TOF Facility: Performance Report. *Technical Report CERN-SL-2002-053 ECT*, European Organization for Nuclear Research (CERN), 2002.

[Abb03] ——. Measurement of the neutron capture cross sections of ^{233}U, ^{237}Np, ^{240,242}Pu, ^{241,243}Am and ^{245}Cm with a Total Absorption Calorimeter at n_TOF. *Technical Report CERN INTC-2003-036*, European Organization for Nuclear Research (CERN), 2003.

[Ago03] S. Agostinelli et al. GEANT4—a simulation toolkit. *Nucl. Instrum. Meth. Phys. Res. A*, **506**:250–303, 2003.

[Ali06] G. Aliberti, G. Palmiotti, M. Salvatores, T. K. Kim, T. A. Taiwo, M. Anitescu, I. Kodeli, E. Sartori, J. C. Bosq, and J. Tommasi. Nuclear data sensitivity, uncertainty and target accuracy assessment for future nuclear systems. *Ann. Nucl. Energy*, **33**:700–733, 2006.

[All80] R. Allemand, C. Gresset, and J. Vacher. Potential Advantages of a Cesium Fluoride Scintillator for a Time-of-Flight Positron Camera. *J. Nucl. Med.*, **21**:153–155, 1980.

[All06] J. Allison et al. Geant4 Developments and Applications. *IEEE Trans. Nucl. Sci.*, **53**:270–278, 2006.

[An02] Changhua An, Kaibin Tang, Guozhen Shen, Chunrui Wang, and Yitai Qian. Hydrothermal preparation of luminescent $PbWO_4$ nanocrystallites. *Mater. Lett.*, **57**:565–568, 2002.

[And89] D. F. Anderson. Properties of the High-Density Scintillator Cerium Fluoride. *IEEE Trans. Nucl. Sci.*, **36**:137–140, 1989.

[And90] ——. Cerium Fluoride: A Scintillator for High-Rate Applications. *Nucl. Instrum. Meth. Phys. Res. A*, **287**:606–612, 1990.

[Ave54] R. Aves, D. Barnes, and R. B. MacKenzie. Fission Chambers for Neutron Detection. *J. Nucl. Energy*, **1**:110–116, 1954.

[Bar58] V. Bar and A. Weinreb. Influence of Oxygen on the Transfer Efficiency and Fluorescent Yield of Organic Scintillators. *J. Chem. Phys.*, **29**:1412–1414, 1958.

[Bar65] E. Barnard, A. T. G. Ferguson, W. R. McMurray, and I. J. Van Heerden. Time-of-Flight Measurements of Neutron Spectra from the Fission of U^{235}, U^{238}, and Pu^{239}. *Nucl. Phys.*, **71**:228–240, 1965.

[Bay94] G. L. Bayatian et al. The Compact Muon Solenoid Technical Proposal. *Technical Report CERN-LHCC-94-38*, European Organization for Nuclear Research (CERN), 1994.

[Bel03] P. Belli, R. Bernabei, R. Cerulli, C. J. Dai, F. A. Danevich, A. Incicchitti, V. V. Kobychev, O. A. Ponkratenko, D. Prosperi, V. I. Tretyak, and Yu. G. Zdesenko. Performances of a CeF_3 crystal scintillator and its application to the search for rare processes. *Nucl. Instrum. Meth. Phys. Res. A*, **498**:352–361, 2003.

[Ber61] Isadore B. Berlman. Luminescence in a Scintillation Solution Excited by α and β Particles and Related Studies in Quenching. *J. Chem. Phys.*, **34**:598–603, 1961.

[Bir64] J. B. Birks. *The Theory and Practice of Scintillation Counting*. The MacMillan Company, 1964.

[Bir70] John B. Birks. *Photophysics of Aromatic Molecules*. Wiley Interscience, 1970.

[BJ88] C. Budtz-Jørgensen and H.-H. Knitter. Simultaneous Investigation of Fission Fragments and Neutrons in ^{252}Cf (SF). *Nucl. Phys. A*, **490**:307–328, 1988.

[Boe00] M. Boezio et al. Measurement of the flux of atmospheric muons with the CAPRICE94 apparatus. *Phys. Rev. D*, **62**:032007, 2000.

[Boh83] Craig F. Bohren and Donald R. Huffman. *Absorption and Scattering of Light by Small Particles*. Wiley-Interscience, 1983.

[Boy06] John-Christopher Boyer, Fiorenzo Vetrone, Louis A. Cuccia, and John A. Capobianco. Synthesis of Colloidal Upconverting $NaYF_4$ Nanocrystals Doped with Er^{3+}, Yb^{3+} and Tm^{3+}, Yb^{3+} via Thermal Decomposition of Lanthanide Trifluoroacetate Precursors. *J. Am. Chem. Soc.*, **128**:7444–7445, 2006.

[Bro54] J. E. Brolley, Jr. and W. C. Dickinson. Angular Distribution of Fragments from Neutron-Induced Fission. *Phys. Rev.*, **94**:640–642, 1954.

[Bro92] A. D. Bross and A. Pla-Dalmau. Radiation Damage of Plastic Scintillators. *IEEE Trans. Nucl. Sci.*, **39**:1199–1204, 1992.

[Bro93] Alan D. Bross and Anna Pla-Dalmau. Radiation effects in intrinsic 3HF scintillator. *Nucl. Instrum. Meth. Phys. Res. A*, **327**:337–345, 1993.

[Bru97] Rene Brun and Fons Rademakers. ROOT: An object-oriented data analysis framework. *Nucl. Instrum. Meth. Phys. Res. A*, **389**:81–86, 1997. See also http://root.cern.ch/.

[Bud07a] S. V. Budakovsky, N. Z. Galunov, B. V. Grinyov, N. L. Karavaeva, Jong Kyung Kim, Yong-Kyun Kim, N. V. Pogorelova, and O. A. Tarasenko. Stilbene crystalline powder in polymer base as a new fast neutron detector. *Radiat. Meas.*, **42**:565–568, 2007.

[Bud07b] Sergey V. Budakovsky, Nikolai Z. Galunov, Natalya L. Karavaeva, Jong Kyung Kim, Yong Kyun Kim, Oleg A. Tarasenko, and Eugenia V. Martynenko. New effective organic scintillators for fast neutron and short-range radiation detection. *IEEE Trans. Nucl. Sci.*, **54**:2734–2740, 2007.

[Cab10] O. Cabellos, P. Fernández, D. Rapisarda, and N. García-Herranz. Assessment of fissionable material behavior in fission chambers. *Nucl. Instrum. Meth. Phys. Res. A*, **618**:248–259, 2010.

[Chi94] R. Chipaux, J.-L. Faure, P. Rebourgeard, G. Dauphin, and J. Safieh. Behavior of CeF_3 scintillator in an LHC-like environment. *Nucl. Instrum. Meth. Phys. Res. A*, **345**:440–444, 1994.

[Coo74] Malcolm Cooper, Brian Williams, and Philip Pattison. The separation of x-ray doublets. *J. Phys. E. Sci. Instrum.*, **7**:516–518, 1974.

[Coo10] Jonathan Cook, 2010. Personal communication.

[Cou00] S. Coutu et al. Energy spectra, altitude profiles, and charge ratios of atmospheric muons. *Phys. Rev. D*, **62**:032001, 2000.

[Cou07] A. Couture and R. Reifarth. Direct measurements of neutron capture of radioactive isotopes. *Atom. Data Nucl. Data*, **93**:807–830, 2007.

[Cry93] Crystal Clear Collaboration. Further results on cerium fluoride crystals. *Nucl. Instrum. Meth. Phys. Res. A*, **332**:373–394, 1993.

[Cry96a] ———. Extensive studies on CeF_3 crystals, a good candidate for electromagnetic calorimetry at future accelerators. *Nucl. Instrum. Meth. Phys. Res. A*, **383**:367–390, 1996.

[Cry96b] ———. Performance of cerium fluoride crystal matrix measured in high-energy particle beams. *Nucl. Instrum. Meth. Phys. Res. A*, **378**:171–178, 1996.

[Cul56] B. D. Cullity. *Elements of X-Ray Diffraction*. Addison-Wesley, 1956.

[dA03] K. C. S. de Almeida, T. S. Martins, P. C. Isolani, G. Vicentini, and J. Zukerman-Schpector. Uranyl nitrate complexes with diphenylsulfoxide and dibenzylsulfoxide: characterization, luminescence and structures. *J. Solid State Chem.*, **171**:230–234, 2003.

[Dai02] Sheng Dai, Suree Saengkerdsub, Hee-Jung Im, Andrew C. Stephan, and Shannon M. Mahurin. Nanocrystal-based scintillators for radiation detection. *AIP Conf. Proc.*, **632**:220–224, 2002.

[Deu44] M. Deutsch and G. A. Linenberger. Fission and Radiative Capture Cross Section of 25 for Thermal Neutrons. *Technical Report LA Report 100*, Los Alamos National Laboratory, 1944.

[Deu46] Martin Deutsch and Margaret Ramsey. Mass Ratios and Energy Release in the Fission of U^{235}, U^{233}, and Pu^{239} by Thermal Neutrons. *Technical Report LA-510*, Los Alamos National Laboratory, 1946.

[Dow06] David J. Dowsett, Patrick A. Kenny, and R. Eugene Johnston. *The Physics of Diagnostic Imaging*. Hodder Arnold, 2006.

[Du98] Hai Du, Ru-Chun Amy Fuh, Junzhong Li, Andrew Corkan, and Jonathan S. Lindsey. PhotochemCAD: A computer-aided design and research tool in photochemistry. *Photochem. Photobiol.*, **68**:141–142, 1998.

[Ege05] Ray F. Egerton. *Physical Principles of Electron Microscopy: An Introduction to TEM, SEM, and AEM*. Springer, 2005.

[Elj] Eljen Technology. *EJ-200 Plastic Scintillator*.

[Emm54] W. S Emmerich. A fast neutron scintillator. *Rev. Sci. Instrum.*, **25**:69–70, 1954.

[Erd95] S. Erdei, R. Roy, G. Harshe, H. Juwhari, D. Agrawal, F. W. Ainger, and W. B. White. The effect of powder preparation processes on the luminescent properties of yttrium oxide based phosphor materials. *Mater. Res. Bull.*, **30**:745–753, 1995.

[Ern09] Rolf Erni, Marta D. Rossell, Christian Kisielowski, and Ulrich Dahmen. Atomic-Resolution Imaging with a Sub-50-pm Electron Probe. *Phys. Rev. Lett.*, **102**:096101–1–096101–4, 2009.

[Esc08a] E.-I. Esch, R. Reifarth, E. M. Bond, T. A. Bredeweg, A. Couture, S. E. Glover, U. Greife, R. C. Haight, A. M. Hatarik, M. Jandel, T. Kawano, A. Mertz, J. M. O'Donnell, R. S. Rundberg, J. M. Schwantes, J. L. Ullmann, D. J. Vieira, J. B. Wilhelmy, and J. M. Wouters. Measurement of the $^{237}Np(n,\gamma)$ cross section from 20 meV to 500 keV with a high efficiency, highly segmented 4π BaF_2 detector. *Phys. Rev. C*, **77**:034309–1–034309–10, 2008.

[Esc08b] Ernst-Ingo Esch. Analysis of the ^{237}Np neutron capture cross-section at DANCE. *Technical Report LA-UR-08-06630*, Los Alamos National Laboratory, 2008.

[fDDnt] International Centre for Diffraction Data. JCPDF card 72-1436, 1974-present. Joint Committee on Powder Diffraction Standards.

[Fie74] Larry R. Field, Emmerich Wilhelm, and Rubin Battino. The solubility of gases in liquids 6. Solubility of N_2, O_2, CO, CO_2, CH_4, and CF_4 in methylcyclohexane and toluene at 283 to 313 K. *J. Chem. Thermodyn.*, **6**:237–243, 1974.

[Fow47] J. L. Fowler and Louis Rosen. Energy Distribution of the Fragments Resulting from the Fission of U^{235} and Th^{232} by Slow and by Fast Neutrons. *Phys. Rev.*, **72**:926–930, 1947.

[Gag] N. D. Gagunashvili. Comparison of weighted and unweighted histograms. ArXiv:physics/0605123.

[Gag05] ——. χ^2 test for comparison of weighted and unweighted histograms. In *Statistical Problems in Particle Physics, Astrophysics and Cosmology, Proceedings of PHYSTAT05*, 2005.

[Gal09] Nikolai Z. Galunov, Boris V. Grinyov, Natalya L. Karavaeva, Jong Kyung Kim, Yong Kyun Kim, Oleg A. Tarasenko, and Eugenia V. Martynenko. Development of new composite scintillation materials based on organic crystalline grains. *IEEE Trans. Nucl. Sci.*, **56**:904–910, 2009.

[Gol97] E. T. Goldburt, B. Kulkarni, R. N. Bhargava, J. Taylor, and M. Libera. Size dependent efficiency in Tb doped Y_2O_3 nanocrystalline phosphor. *J. Lumin.*, pages 190–192, 1997.

[Ham95] F.-J. Hambsch, J. Van Aarle, and R. Vogt. Is there a pulse height defect for methane? *Nucl. Instrum. Meth. Phys. Res. A*, **361**:257–262, 1995.

[Hei99] M. Heil, R. Reifarth, F. Kaeppeler, K. Wisshak, F. Voss, J. L. Ullmann, R. C. Haight, E. H. Seabury, J. B. Wilhelmy, R. S. Rundberg, and M. M. Fowler. GEANT simulations of neutron captures experiments with a 4π BaF_2 detector. *Technical Report LA-UR-99-4046*, Los Alamos National Laboratory, 1999.

[Hei00] M. Heil, R. Reifarth, M. M. Fowler, F. Käppeler, R. S. Rundberg, E. H. Seabury, J. L. Ullmann, J. B. Wilhelmy, and K. Wisshak. A 4π BaF_2 detector for (n, γ) cross-section measurements at a spallation neutron source. *Nucl. Instrum. Meth. Phys. Res. A*, **459**:229–246, 2000.

[Hna10] Z. Hnatejko, S. Lis, and Z. Stryła. Preparation and characterization of uranyl complexes with phosphonate ligands. *J. Therm. Anal. Calorim.*, **100**:253–260, 2010.

[Hol88] I. Holl, E. Lorenz, and G. Mageras. A Measurement of the Light Yield of Common Inorganic Scintillators. *IEEE Trans. Nucl. Sci.*, **35**:105–109, 1988.

[Hor52] W. F Hornyak. A fast neutron detector. *Rev. Sci. Instrum.*, **23**:264–267, 1952.

[How54] P. R. Howland and W. E. Kreger. Gamma-Ray Absorption Coefficients for NaI, Cu, Ta, and W. *Phys. Rev.*, **95**:407–410, 1954.

[Huh05] M. Huhtinen, P. Lecomte, D. Luckey, F. Nessi-Tedaldi, and F. Pauss. High-energy proton induced damage in $PbWO_4$ calorimeter crystals. *Nucl. Instrum. Meth. Phys. Res. A*, **545**:63–87, 2005.

[Ina00] Takao Inagaki, Yoshio Yoshimura, Yukio Kanda, Yoshikazu Matsumoto, and Kazuhiro Minami. Development of CeF_3 crystal for high-energy electromagnetic calorimetery. *Nucl. Instrum. Meth. Phys. Res. A*, **443**:126–135, 2000.

[Jør82] Christian K. Jørgensen and Renata Reisfeld. Uranyl Photophysics. *Struct. Bond.*, **50**:121–171, 1982.

[Kas50] Michael Kasha. Characterization of Electronic Transitions in Complex Molecules. *Discuss. Faraday Soc.*, **9**:14–19, 1950.

[Kno00] Glenn F. Knoll. *Radiation Detection and Measurement.* John Wiley & Sons, Inc., 2000.

[Kob91] M. Kobayashi, M. Ishii, E. A. Krivandina, M. M. Litvinov, A. I. Peresypkin, Yu. D. Prokoshkin, V. I. Rykalin, B. P. Sobolev, K. Takamatsu, and V. G. Vasil'chenko. Cerium fluoride, a highly radiation-resistive scintillator. *Nucl. Instrum. Meth. Phys. Res. A*, **302**:443–446, 1991.

[Kon09] A. J. Koning and D. Rochman. TENDL-2009: TALYS-based Evaluated Nuclear Data Library including covariance data. *Technical Report JEFF-DOC 1310*, Joint Evaluated Fission and Fusion File (JEFF), 2009.

[Koz04] Peter Kozma and Petr Kozma, Jr. Radiation resistance of heavy scintillators to low-energy gamma-rays. *Radiat. Phys. Chem.*, **71**:705–707, 2004.

[Kub88] S. Kubota, T. Motobayashi, J. Ruan(gen), T. Murakami, and J. Kasagi. A new solid state neutron detector: Particle identification with a barium-fluoride plastic scintillator. *Nucl. Instrum. Meth. Phys. Res.*, **A270**:598–601, 1988.

[LB66] C. Lloyd Braga, D. Lumb, and J. B. Birks. Energy Transfer and Oxygen Quenching in Solutions of 2.5-Diphenyl Oxazole in Benzene, Toluene, p-Xylene and Mesitylene. *Trans. Faraday Soc.*, **62**:1830–1837, 1966.

[Leo94] W. R. Leo. *Techniques for Nuclear and Particle Physics Experiments.* Springer-Verlag, 1994.

[Ler99] S. Leray. Physical aspects of neutron production and related nuclear data. *J. Phys. IV*, **9**:Pr7–57–72, 1999.

[Leu99] A. F. Leung, L. Hayashibara, and J. Spadaro. Fluorescence properties of uranyl nitrates. *J. Phys. Chem. Solids*, **60**:299–304, 1999.

[Lew44] Gilbert N. Lewis and M. Kasha. Phosphorescence and the Triplet State. *J. Am. Chem. Soc.*, **66**:2100–2116, 1944.

[Li] Andy Li. Development and Evaluation of Novel Structured Scintillation Detectors. North Carolina State University Ph.D. dissertation, in preparation.

[Li06] Wei Li. Facile synthesis of monodisperse Bi_2O_3 nanoparticles. *Mater. Chem. Phys.*, **99**:174–180, 2006.

[Lid09] David R. Lide and W. M. Haynes (Editors). *CRC Handbook of Chemistry and Physics.* CRC Press, 90 edition, 2009.

[Lis90] P. W. Lisowski, C. D. Bowman, G. J. Russell, and S. A. Wender. The Los Alamos National Laboratory spallation neutron sources. *Nucl. Sci. Eng.*, **106**:208–218, 1990.

[Lov09] W. Loveland and J. D. Baker. Target preparation for the fission TPC. *J. Radioanal. Nucl. Chem.*, **282**:361–363, 2009.

[Lug03] Maria Lugaro, Falk Herwig, John C. Lattanzio, Roberto Gallino, and Oscar Straniero. S-Process nucleosynthesis in asymptotic giant branch stars: A test for stellar evolution. *Astrophys. J.*, **586**:1305–1319, 2003.

[Maj87] Stan Majewski and Margaret Kathleen Bentley. Gamma radiation induced damage effects in the transmission of barium fluoride and cesium fluoride fast crystal scintillators. *Nucl. Instrum. Meth. A*, **260**:373–376, 1987.

[Mar06] S. Marrone et al. Pulse shape analysis of signals from BaF_2 and CeF_3 scintillators for neutron capture experiments. *Nucl. Instrum. Meth. Phys. Res. A*, **568**:904–911, 2006.

[McK07a] E. A. McKigney, R. E. Muenchausen, D. W. Cooke, R. E. Del Sesto, R. D. Gilbertson, M. K. Bacrania, B. L. Bennett, L. G. Jacobsohn, T. M. McCleskey, K. C. Ott, S. C. Sitarz, J. F. Smith, and S. Stange. LaF_3:Ce nanocomposite scintillator for gamma-ray detection. *Proc. SPIE*, **6706**:67061A, 2007.

[McK07b] Edward A. McKigney, Rico E. Del Sesto, Luiz G. Jacobsohn, Peter A. Santi, Ross E. Muenchausen, Kevin C. Ott, T. Mark McCleskey, Bryan L. Bennett, James F. Smith, and D. Wayne Cooke. Nanocomposite scintillators for radiation detection and nuclear spectroscopy. *Nucl. Instrum. Meth. Phys. Res.*, **A579**:15–18, 2007.

[Mel99] R. S. Meltzer, S. P. Feofilov, B. Tissue, and H. B. Yuan. Dependence of fluorescence lifetimes of Y_2O_3:Eu^{3+} nanoparticles on the surrounding medium. *Phys. Rev. B*, **60**:14012–14015, 1999.

[Miy94] R. S. Miyaoka and T. K. Lewellen. Evaluation of CeF_3 as a scintillator for high speed dynamic PET imaging. *IEEE Trans. Nucl. Sci.*, **41**:2743–2747, 1994.

[Mos89] W. W. Moses and S. E. Derenzo. Cerium Fluoride, a New Fast, Heavy Scintillator. *IEEE Trans. Nucl. Sci.*, **36**:173–176, 1989.

[Mos06] M. Moszyński, M. Kapusta, A. Nassalski, T. Szczęśniak, D. Wolski, L. Eriksson, and C. L. Melcher. New prospects for time-of-flight PET with LSO scintillators. *IEEE Trans. Nucl. Sci.*, **53**:2484–2488, 2006.

[Mou49] W. G. Moulton and C. W. Sherwin. Fast neutron detector. *Rev. Sci. Instrum.*, **20**:766–767, 1949.

[Mul81] Nizar A. Mullani, David C. Ficke, Ross Hartz, Joanne Markham, and Gary Wong. System design of fast PET scanners utilitzing time-of-flight. *IEEE Trans. Nucl. Sci.*, **NS-28**:104–108, 1981.

[Nik94] M. Nikl and C. Pedrini. Photoluminescence of heavily-doped CeF_3:Cd^{2+} single crystals. *Solid State Commun.*, **90**:155–159, 1994.

[1] National Nuclear Data Center (NNDC). Chart of Nuclides. http://www.nndc.bnl.gov/chart/.

[oSa] National Institute of Standards and Technology (NIST). Stopping Power and Range Tables for Electrons (ESTAR). http://physics.nist.gov/PhysRefData/Star/Text/ESTAR.html.

[oSb] ——. Stopping Power and Range Tables for Helium Ions (ASTAR). http://physics.nist.gov/PhysRefData/Star/Text/ASTAR.html.

[oSc] ——. X-ray Transition Energies. http://physics.nist.gov/PhysRefData/XrayTrans/index.html.

[oSd] ——. XCOM: Photon Cross Sections Database. http://www.nist.gov/physlab/data/xcom/index.cfm.

[Pat98] Jacqueline M. Pates, Gordon T. Cook, Angus B. MacKenzie, and Charles J. Passo, Jr. Implications of beta energy and quench level for alpha/beta liquid scintillation spectrometry calibration. *Analyst*, **123**:2201–2207, 1998.

[Pau25] W. Pauli. Über den Zusammenhang des Abschlusses der Elektronengruppen im Atom mit der Komplexstruktur der Spektren. *Z. Phys*, **31**:765–783, 1925.

[Ped92] C. Pedrini, B. Moine, J. C. Gacon, and B. Jacquier. One- and two-photon spectroscopy of Ce^{3+} ions in LaF_3–CeF_3 mixed crystals. *J. Phys.: Condens. Matter*, **4**:5461–5470, 1992.

[Per96] M. N. Peron and P. Cassette. A Compton coincidence study of liquid scintillator response to low-energy electrons. *Nucl. Instrum. Meth. Phys. Res. A*, **369**:344–347, 1996.

[Poz09] S. A. Pozzi, S. D. Clarke, M. Flaska, and P. Peerani. Pulse-height distributions of neutron and gamma rays from plutonium-oxide samples. *Nucl. Instrum. Meth. Phys. Res. A*, **608**:310–315, 2009.

[Pri53] R. W. Pringle, L. D. Black, B. L. Funt, and S. Sobering. A New Quenching Effect in Liquid Scintillators. *Phys. Rev.*, **92**:1582–1583, 1953.

[Pyr08] William D. Pyrz and Douglas J. Buttrey. Particle size determination using TEM: A discussion of image acquisition and analysis for the novice microscopist. *Langmuir*, **24**:11350–11360, 2008.

[Rac48] W. A. Rachinger. A Correction for the $\alpha_1 \alpha_2$ Doublet in the Measurement of Widths of X-ray Diffraction Lines. *J. Sci. Instrum.*, **25**:254–255, 1948.

[Rap09] David Rapisarda, Angela García, Óscar Cabellos, Fernando Mota, Jose M. Gómez-Ros, Ángel Ibarra, Natalia Casal, Vicente Queral, and Javier Sanz. Feasibility of fission chambers as a neutron diagnostic in the IFMIF-Test Cell. *Fusion Eng. Des.*, **84**:1570–1574, 2009.

[Rei03] R. Reifarth, C. Arlandini, M. Heil, F. Käppeler, P. V. Sedyshev, A. Mengoni, M. Herman, T. Rauscher, R. Gallino, and C. Travaglio. Stellar neutron capture on promethium: Implications for the s-process neutron density. *Astrophys. J.*, **582**:1251–1262, 2003.

[Rei04] R. Reifarth, T. A. Bredeweg, A. Alpizar-Vicente, J. C. Browne, E.-I. Esch, U. Greife, R. C. Haight, R. Hatarik, A. Kronenberg, J. M. O'Donnell, R. S. Rundberg, J. L. Ullmann, D. J. Vieira, J. B. Wilhelmy, and J. M. Wouters. Background identification and suppression for the measurement of (n, γ) reactions with the DANCE array at LANSCE. *Nucl. Instrum. Meth. Phys. Res. A*, **531**:530–543, 2004.

[Roz09] C. M. Rozsa, Peter R. Menge, and M. R. Mayhugh. Scintillation Products Technical Note: BrilLanCe^{TM} Scintillators Performance Summary. *Technical report*, Saint-Gobain Crystals, 2009.

[Sai08a] Saint-Gobain Crystals. *Bismuth Germanate Scintillation Material*, 2008.

[Sai08b] ——. *Scintillation Products: Organic Scintillators*, 2008.

175

[Sch94] M. A. Schneegans. Cerium fluoride crystals for calorimetry at LHC. *Nucl. Instrum. Meth. Phys. Res. A*, **344**:47–56, 1994.

[Sen79] Pradeep K. Sengupta and Michael Kasha. Excited State Proton-Transfer Spectroscopy of 3-Hydroxyflavone and Querceptin. *Chem. Phys. Lett.*, **68**:382–385, 1979.

[Shi] K. Shibata et al. JENDL-4.0: A New Library for Nuclear Science and Engineering. To be submitted to *J. Nucl. Sci. Technol.*

[Son03] K. Sonnabend, P. Mohr, K. Vogt, A. Zilges, A. Mengoni, T. Rauscher, H. Beer, F. Käppeler, and R. Gallino. The s-process branching at ^{185}W. *Astrophys. J.*, **583**:506–513, 2003.

[Sto52] G. G. Stokes. On the Change of the Refrangibility of Light. *Philos. T. R. Soc. Lond.*, **142**:463–562, 1852.

[Str76] Andrew Streitwieser, Jr. and Clayton H. Heathcock. *Introduction to Organic Chemistry*. Macmillan Publishing Co., Inc., 1976.

[Tho87] P. Thompson, D. E. Cox, and J. B. Hastings. Reitveld Refinement of Debye-Scherrer Synchrotron X-ray Data from Al_2O_3. *J. Appl. Cryst.*, **20**:79–83, 1987.

[Tov07] F. Tovesson and T. S. Hill. Neutron induced fission cross section of ^{237}Np from 100 keV to 200 MeV. *Phys. Rev. C*, **75**:034610, 2007.

[Tov09] F. Tovesson, T. S. Hill, M. Mocko, J. D. Baker, and C. A. McGrath. Neutron induced fission of ^{240,242}Pu from 1 eV to 200 MeV. *Phys. Rev. C*, **79**:014613–1 – 014613–9, 2009.

[Ull05] J. L. Ullmann, U. Agvaanluvsan, A. Alpizar, E. M. Bond, T. A. Bredeweg, E.-I. Esch, C. M. Folden, U. Greife, R. Hatarik, R. C. Haight, D. C. Hoffman, L. Hunt, A. Kronenberg, J. M. O'Donnell, R. Reifarth, R. S. Rundberg, J. M. Schwantes, D. D. Strottman, D. J. Vieira, J. B. Wilhelmy, and J. M. Wouters. The Detector for Advanced Neutron Capture Experiments: A 4π BaF_2 detector for neutron capture measurements at LANSCE. *AIP Conf. Proc.*, **769**:918–923, 2005.

[Vas03] V. G. Vasil'chenko and A. S. Solov'ev. Properties of Composite Scintillators in Static and Dynamic States. *Instrum. Exp. Tech.*, **46**:35–41, 2003.

[Vas04] ——. New Composite Scintillators (in Static and Dynamic States). *Instrum. Exp. Tech*, **47**:38–47, 2004.

[vE02] Carel W. E. van Eijk. Inorganic scintillators in medical imaging. *Phys. Med. Biol.*, **47**:R85–R106, 2002.

[Ver68]   V. V. Verbinski, W. R. Burrus, T. A. Love, W. Zobel, N. W. Hill, and R. Textor. Calibration of an organic scintillator for neutron spectrometry. *Nucl. Instrum. Methods*, **65**:8–25, 1968.

[vL01]   E. V. D. van Loef, P. Dorenbos, C. W. E. van Eijk, K. Krämer, and H. U. Güdel. High-energy-resolution scintillator: Ce^{3+} activated $LaBr_3$. *Appl. Phys. Lett.*, **79**:1573–1575, 2001.

[Wal07]   Steven A. Wallace, Andrew C. Stephan, Ron Cooper, Hee-Jung Im, and Sheng Dai. Lithiated sol-gel based neutron scintillators. *Nucl. Instrum. Meth. Phys. Res.*, **A579**:184–187, 2007.

[Wen93]   S. A. Wender, S. Balestrini, A. Brown, R. C. Haight, C. M. Laymon, T. M. Lee, P. W. Lisowski, W. McCorkle, R. O. Nelson, W. Parker, and N. W. Hill. A fission ionization detector for neutron flux measurements at a spallation source. *Nucl. Instrum. Meth. Phys. Res. A*, **336**:226–231, 1993.

[Wer74]   G. K. Wertheim, M. A. Butler, K. W. West, and D. N. E. Buchanan. Determination of the Gaussian and Lorentzian content of experimental line shapes. *Rev. Sci. Instrum.*, **45**:1369–1371, 1974.

[Wes68]   L. W. Weston, R. Gwin, G. deSaussure, R. R. Fullwood, and R. W. Hockenbury. Measurement of the Neutron Fission and Capture Cross Sections for ^{233}U in the Energy Region 0.4 to 2000 eV. *Nucl. Sci. Engin.*, **34**:1–12, 1968.

[Wil09]   David B. Williams and C. Barry Carter. *Transmission Electron Microscopy: A Textbook for Materials Science.* Springer U.S., 2009.

[Won84]   Wai-Hoi Wong, Nizar A. Mullani, Gary Wardworth, Ross K. Hartz, and David Bristow. Characteristics of small barium fluoride (BaF_2) scintillator for high intrinsic resolution time-of-flight positron emission tomography. *IEEE Trans. Nucl. Sci.*, **NS-31**:381–386, 1984.

[You82]   R. A. Young and D. B. Wiles. Profile Shape Functions in Rietveld Refinements. *J. Appl. Cryst.*, **15**:430–438, 1982.

[Zha05]   Ya-Wen Zhang, Xiao Sun, Rui Si, Li-Ping You, and Chun-Hua Yan. Single-Crystalline and Monodisperse LaF_3 Triangular Nanoplates from a Single-Source Precursor. *J. Am. Chem. Soc.*, **127**:3260–3261, 2005.

[Zha09]   Chao Zhang, Ji Chen, Xingfu Zhu, Yunchun Zhou, and Deqian Li. Synthesis of Tributylphosphate Capped Luminescent Rare Earth Phosphate Nanocrystals in an Ionic Liquid Microemulsion. *Chem. Mater.*, **21**:3570–3575, 2009.

[Zie85]   J. F. Ziegler, J. P. Biersack, and U. Littmark. *The Stopping and Range of Ions in Solids.* Pergamon, 1985.